Multidimensional Scanning Probe Microscopy Applications for Optoelectronic Charge Carrier Characterizations of Metal Oxides

by

BUGRAHAN GUNER

ARTICLE-BASED THESIS PRESENTED TO ÉCOLE DE TECHNOLOGIE SUPÉRIEURE IN PARTIAL FULFILLEMENT FOR THE DEGREE OF DOCTOR IN PHILOSOPHY
Ph.D.

MONTREAL, JUNE 17TH, 2025

ÉCOLE DE TECHNOLOGIE SUPÉRIEURE
UNIVERSITÉ DU QUÉBEC

BOARD OF EXAMINERS

THIS THESIS HAS BEEN EVALUATED

BY THE FOLLOWING BOARD OF EXAMINERS

Mr. Omur E. Dagdeviren, Thesis Supervisor
Department of Mechanical Engineering at École de technologie supérieure

Ms. Claudiane Ouellet-Plamondon, President of the Board of Examiners
Department of Construction Engineering at École de technologie supérieure

Mr. Antoine Tahan, Member of the jury
Department of Mechanical Engineering at École de technologie supérieure

Ms. Elmira Moosavi Khoonsari, Member of the jury
Department of Mechanical Engineering at École de technologie supérieure

Mr. Ozgur Sahin, Member of the jury
Department of Biological Sciences and Physics at Columbia University

THIS THESIS WAS PRESENTED AND DEFENDED

IN THE PRESENCE OF A BOARD OF EXAMINERS AND PUBLIC

ON JUNE 9TH, 2025

AT ÉCOLE DE TECHNOLOGIE SUPÉRIEURE

ACKNOWLEDGMENT

This research and work is the respective outcome of the cultivation of many people's efforts throughout the last four years. It would be my honor to credit those souls that were an active part of this work. I am deeply grateful to my supervisor, Dr. Omur E. Dagdeviren, for his unwavering support, guidance, and mentorship. His encouragement and insightful advice have made my transition into a new field both enriching and rewarding. Beyond being an exceptional mentor, he has also been a supportive colleague, always available for discussions and offering invaluable wisdom. His dedication and belief in my potential have profoundly shaped my academic journey, and for that, I am truly thankful. Also, I would like to thank my collaborators and contributors Mohammad Safikhani-Mahmoudi, Simon Laflamme, Prof. Ke Zou, Prof. Fengmiao Li and Prof. Vladimir Brailovski; and my academic mentors Prof. Udo D. Schwarz, Prof. Eric Altman, Prof. Mehmet Z. Baykara, and Prof. Özgür Şahin for their valuable contributions and support during this work. Their input and support have been greatly appreciated.

I would like to express my gratitude to the funding agencies who saw the vision in this work and generously supported our research. This work was supported by the Fonds de recherche du Québec – Nature et technologies (FRQNT), the Natural Sciences and Engineering Research Council of Canada (NSERC), Canada Economic Development for Quebec Regions (CED), and the Fonds de recherche en coopération intersectorielle – FRECC. Their generous support is gratefully acknowledged.

To my family, who have been my rock throughout this journey and for the last 26 years, it is a privilege to know and love you all. To my late grandmother Faika Yenal, who was my first teacher and the person who laid the foundation of who I am today with her guidance, love and support; to my late father Dr. Ömer Güner, who was always there with his unwavering support, guidance and love anytime I needed; to my uncle Dr. Umur Yenal, who is my idol/hero and the reason behind my enthusiasm to pursue science as a career and becoming a better version

of myself each day with the beacon he holds to this day; to my grandfather Kaya Yenal who is my absolute best friend, a hero who served as a military pilot for multiple decades and whom I am so proud to be his grandson; and to my lovely mother Ezlam Yenal who is my favorite person in the world, the touchstone of my success, source of the love and perseverance I managed to hold throughout my life; this achievement yet along everything that I achieved in my life would not be possible without any one of you. Thank you so much for being yourselves. I love you so much. To my second family, my dear friends who stood by my side through thick and thin, it is a privilege to know each and every one of you and be able to call you guys family. Your love, support, and the roles each one of you played in my life are irreplaceable and inimitable. To Yiğit Emre Karakoç, Bengisu Şahin, Deniz Şenkutlu, Eray Karakuş, Janset Namlı, Özgür Can Gümüş, Muhammed Fatih Gürbüz, Orçun Dinçer, Ali Alp Alpdoğan, Taha Tell and many others that I could not name here, I love you all profoundly. Thank you for being yourselves and being family.

APPLICATIONS DE LA MICROSCOPIE À SONDE DE BALAYAGE MULTIDIMENSIONNELLE POUR LA CARACTÉRISATION DES PORTEURS DE CHARGE OPTOÉLECTRONIQUES DANS LES OXYDES MÉTALLIQUES

Bugrahan GUNER

RESUME

La caractérisation et l'optimisation des porteurs de charge (par exemple, électrons, trous, ions, lacunes, etc.) dans des systèmes échantillons liés aux énergies renouvelables (en particulier les oxydes métalliques, c'est-à-dire les MOs) dépendent fortement de techniques de mesure adaptées à la bonne échelle physique (c'est-à-dire une résolution temporelle submicroseconde et une résolution spatiale à l'échelle nanométrique) ainsi que de méthodologies appropriées. Des techniques avancées de microscopie à sonde de balayage (SPM), telles que la microscopie à force atomique résolue en temps (tr-AFM) et ses variantes uniques/personnalisées, sont utilisées pour révéler les tendances de migration et les caractéristiques de ces porteurs en fonction de diverses conditions. Dans ce travail, des configurations AFM personnalisées et des techniques de mesure spécifiques sont utilisées pour révéler quantitativement les propriétés électroniques des oxydes métalliques, telles que les différences de potentiel de contact (CPD), la dynamique des porteurs de charge, etc., dans le but d'optimiser la durée de vie des systèmes à base de MOs. En particulier, les propriétés de migration des porteurs de charge dans les oxydes métalliques (par exemple, TiO_2) en lien avec leurs tendances photocatalytiques, via des activités d'ingénierie des défauts et des caractérisations de surface, jouent un rôle crucial dans ces systèmes. Les propriétés des systèmes échantillons sont examinées sous plusieurs dimensions, où la température, l'emplacement et le temps constituent les axes principaux. Les lacunes d'oxygène induites par la lumière (PI-SOVs) créées par irradiation UV de surface jouent un rôle clé dans la modification de la dynamique des porteurs de charge dans les systèmes à base de MOs. En outre, les stimuli externes (par exemple, irradiation UV, impulsions de tension, etc.), les agents de surface (par exemple, le méthanol) et les interfaces diverses (par exemple, Au-TiO_2) ont été étudiés en détail afin d'approfondir l'analyse des caractéristiques clés de la dynamique des porteurs de charge telles que la mobilité, les constantes de temps, les énergies d'activation, les barrières de migration, ainsi que les dépendances spatiales et/ou historiques.

Mots-clés: Microscopie à sonde de balayage (SPM), Microscopie à force atomique résolue en temps (tr-AFM), personnalisation des systèmes, différence de potentiel de contact (CPD), dynamique des porteurs de charge, lacunes d'oxygène de surface photoinduites (PI-SOVs), mobilité des porteurs de charge, barrières de migration

MULTIDIMENSIONAL SCANNING PROBE MICROSCOPY APPLICATIONS FOR OPTOELECTRONIC CHARGE CARRIER CHARACTERIZATIONS OF METAL OXIDES

Bugrahan GUNER

ABSTRACT

Characterization and optimization of charge carriers (e.g., electrons, holes, ions, vacancies, etc.) feature in renewable energy sample systems (particularly metal oxides, i.e., MOs) heavily rely on the right physical scale (i.e., submicrosecond time resolution and nanometer scale distance resolution) measurement techniques and correct methodologies. Advanced scanning probe microscopy (SPM) techniques like time-resolved atomic force microscopy (tr-AFM) and its unique/customized variants are utilized to reveal migration tendencies and characteristics of these carriers. In this work, customized AFM setups and measurement techniques are used to quantitatively reveal electronic properties of metal oxides, like contact potential differences, charge carrier dynamics, etc., to optimize the lifetime of MO-based systems. Particularly, the charge carrier migration properties of metal oxides (e.g., TiO_2) for their photocatalytic tendencies through defect engineering activities and surface characterizations play a significant role in these systems. Sample system properties are investigated from multiple dimensions, where temperature, location, and time are the main variables. Photoinduced surface oxygen vacancies introduced with ultraviolet surface irradiation played a key role in the alteration of the charge carrier dynamics in MO systems. Additionally, external stimuli (e.g., ultraviolet irradiation, voltage pulses, etc.), surface agents (e.g., methanol) and different interfaces (e.g., Au-TiO_2) were explored to extend the investigation of key charge carrier dynamics features like mobilities, time constants, activation energies, migration barriers, distance and/or history dependencies.

Keywords: Scanning probe microscopy, Time-resolved atomic force microscopy, system customization, contact potential difference, charge carrier dynamics, photoinduced surface oxygen vacancies, charge carrier mobility, migration barriers

TABLE OF CONTENTS

Page

LIST OF TABLES

Page

LIST OF FIGURES

Page

LIST OF ABREVIATIONS

3D-AFM	Three-Dimensional Atomic Force Microscopy
AFM	Atomic Force Microscopy
AM-AFM	Amplitude Modulation Atomic Force Microscopy
CB	Conduction Band
c-AFM	Conductive Atomic Force Microscopy
CPD	Contact Potential Difference
EIS	Electrochemical Impedance Spectroscopy
FFT	Fast Fourier Transform
FM-AFM	Frequency Modulation Atomic Force Microscopy
FWHM	Full Width at Half Maximum
GXSM	Gnome-X Scanning Microscopy
HOPG	Highly Oriented Pyrolytic Graphite
KPFM	Kelvin Probe Force Microscopy
MBE	Molecular Beam Epitaxy
MO / MOS	Metal Oxides / Metal Oxide Semiconductors
NP	Nanoparticle
PCE	Photoelectrochemical
PI-SOV	Photoinduced Surface Oxygen Vacancy
PID	Proportional–Integral–Derivative
PL	Photoluminescence
PLL	Phase-Locked Loop

SAM	Signal Access Module
SIMS	Secondary Ion Mass Spectrometry
SPM	Scanning Probe Microscopy
STM	Scanning Tunneling Microscopy
TR / tr-AFM	Time-Resolved Atomic Force Microscopy
UVA / UVC	Ultraviolet-A / Ultraviolet-C
UV	Ultraviolet
VB	Valence Band
VCO	Voltage Controlled Oscillator
XAS	X-ray Absorption Spectroscopy
XPS	X-ray Photoelectron Spectroscopy
XRD	X-ray Diffraction

LIST OF SYMBOLS

w_{o}	Natural Resonance Frequency
w_{d}	Drive Frequency
A and Amp	Cantilever Oscillation Amplitude
ΔA	Change in the Oscillation Amplitude
Q	Cantilever Quality Factor
Δw	Change in the Cantilever Oscillation Frequency
Δf_0 and Δf	Resonance Frequency Shift
f_0 and f	Resonance Frequency
Δf_s	Saturated Frequency Shift
$E(t)$	Time-dependent Electric Field
τ^*	Effective Time Constant of Charge Carrier Relaxation Motion
β	Stretching Factor for Charge Carrier Relaxation Motion
τ	Various Generic Time Constants
T	Time
t_{c}	Cutoff Time
${\tau_{eff}}^*$	Effective Attempt Rate
${E_a}^*$	Effective Activation Energy
E_a	Single Charge Carrier Migration Barrier
k_B	Boltzmann Constant
T	Temperature in Kelvin
E_{BG}	Bandgap

V_o	Surface Oxygen Vacancies
a_{exc}	Excitation Signal of the Cantilever Oscillation
θ	Phase Difference Between the Cantilever Excitation and Oscillation Signals
x_s, y_s, z_s	Cantilever Motion Output Signals
V and V_{bias}	Tip-Sample Bias Voltage
$V_{trigger}$	Trigger Voltages
c_z	Cantilever Spring Constant
F	Tip–Sample Interaction Force
F_{total}	Total Tip–Sample Interaction Force
$F_{long\text{-}range}$	Long-range Tip–Sample Interaction Force
$F_{chemical}$	Chemical Tip–Sample Interaction Force
F_{other}	Combination of Long-range and Chemical Tip–Sample Interaction Forces
D	Nearest Tip–Sample Distance
d	Tip–Sample Distance
Å	Ångström
Cu Kα	X-ray Emission Line of Copper
Co Kα	X-ray Emission Line of Cobalt
λ	Wavelength
2θ	XRD Scan Angle
C	Total Tip-Sample Capacitance
$\frac{\partial C}{\partial d}$	Gradient of the Tip-Sample Capacitance
t_{fp}	Time Constant of Fast Timescale Charge Carrier Relaxation Motion

μ	Charge Carrier Mobility
D_c	Diffusion Coefficient
$< \Delta r^2 >$	Mean-Square Displacement
α	Dimensionality of the Process
l	Jump Length/Hopping Distance
N	Number of Jumps
n	Nearest Neighboring Sites for Potential Jumps
Γ	Hopping Rate of Jumping Events
$\tilde{v}$	Effective Frequency of Defect Vibration at the Saddle Point
ΔF_e	Energy Change Requirement for Defect Movement
ΔE	Change in Diffusion Activation Energy Barrier
ΔS and ΔS_{vib}	Change in Vibrational Entropy
h	Planck Constant
μ_e	Electrical Mobility for a Charged Particle
q	Electric Charge of a Charge Carrier
v_d	Terminal Drift Velocity
F_e	Electrical Force
m	Effective Mass of the Particle

PREFACE

The presented thesis is built on the research conducted at the Dagdeviren Group at École de technologie supériure (ÉTS), Université du Québec. The content of the thesis is published/submitted publications throughout the author's studies at the designated institute. All respective publications are presented in chronological order, based on recency.

Peer-Reviewed Publications

1) Guner, B., Safikhani-Mahmoudi, M., Li, F., Zou, K., and Dagdeviren, O. E., Ultraviolet irradiation penetration depth on TiO_2, Communications Chemistry, 8(1), 83 (2025). **Editor's choice and Cover.**

2) Guner, B., Dincer, O., and Dagdeviren, O. E., Fast and Slow Time-Scale Effects of Photoinduced Surface Oxygen Vacancies on the Charge Carrier Dynamics of TiO_2, ACS Applied Energy Materials, 7(6), 2292-2298 (2024). **Editor's choice and supplemental Cover.**

3) Dincer, O., **Guner, B.,** and Dagdeviren, O. E., Effect of methanol and photoinduced surface oxygen vacancies on the charge carrier dynamics in TiO_2, APL Materials, 12(2), 021125 (2024).

4) Guner, B., Laflamme, S., and Dagdeviren, O. E., Customization of an atomic force microscope for multidimensional measurements under environmental conditions, Review of Scientific Instruments, 94, (6) (2023).

5) Guner, B. and Dagdeviren, O. E., Multidimensionality of the Contact Potential Difference at the Nanoscale in Inorganic Oxides, ACS Applied Electronic Materials, 4(8), 4085-4093 (2022). **Editor's choice and supplemental Cover.**

INTRODUCTION

The pursuit of the fundamental understanding of nature through investigating why materials behave the way they behave has always been a cornerstone interest of humanity. This interest actually stretches back to ancient times. Around the 5th century BCE, Democritus came up with the idea of "atoms" as the building blocks of matter in northern Euro-Asia, which is modern-day Turkey. His statements regarding atoms being small, inseparable and solid particles were a revolutionary idea for his time, although being proven wrong many centuries later. The main transition from thought experiments to actual empirical attempts to investigate the fundamental particles in our universe was only possible with deeper understanding of mathematical formulations/techniques and through the contributions of many special individuals.

From ancient philosophy to medieval age alchemy practices, until the birth of modern chemistry with Robert Boyle [1] in the 17th century, the concept of elements was a vague topic in the science world. In continuation, building up concepts like conservation of mass through Lavoisier's work [2] and the law of definite proportions by Proust [3], John Dalton [4] was the first person to come up with a scientific atomic theory in the 19th century. Following him, J.J. Thomson [5], Ernest Rutherford [6], and Niels Bohr [7] revolutionized our understanding of matter and the actual "building blocks" of them. Advancement of science in the upcoming century shifted the exploration from understanding the "atoms" and their structures to actually visualizing and manipulating them with the rise of "quantum mechanics". [8]

The groundbreaking achievement in this sense was the invention of Scanning tunneling microscopy (STM) in 1981 [9], which is based on quantum tunneling, that won Gerd Binnig and Heinrich Rohrer their Nobel prize in 1986. Together with STM, atomic force microscopy (AFM) [10], which was invented 5 years after STM by Gerd Binnig, Calvin Quate, and Christoph Gerber completely changed the game and revolutionized the probing microscopy field that opened countless new horizons in the scientific world and also the reason behind all the work in this thesis. In the upcoming decades after the invention of STM and AFM, the

ability we gained in terms of manipulating and optimizing the matter at the atomic scale led us to a nanoscale reality, where our macroscopic world almost completely dived into a new path, evolving each day and unlocking countless possibilities for research in energy and semiconductors, materials science and surface engineering, biotechnology and hopefully newly emerging fields like quantum computing, metamaterials and many others.

In this context, the work presented in this thesis is a continuation of the evolution in the last three decades in scanning probe microscopy (SPM) field for investigating material properties from a multidimensional perspective. Various sample systems that can be included in this quest are narrowed down to renewable energy-applicable materials such as metal oxides (MOs) (*e.g.*, TiO_2). Due to the versatile nature, flexible and optimizable properties of MOs, they have a wide range of applicability primarily for renewable energy applications (*e.g.*, batteries, solar cells, etc.), sensing, and biological applications. [11-16]

From the renewable energy perspective, solar-driven sustainable and renewable energy solutions can be prominent replacement options for the highly utilized fossil fuel options that will fail against the supply/demand in the upcoming decades. [17-21] Also, the destructive effects of excess fossil fuel dependency on the environment makes the transition inevitable. [22, 23] TiO_2 as a MO serves in sample systems that are widely utilized in various renewable energy and solar-driven applications that can be the cornerstone of this transition. [24-27] In photocatalytic applications like photoelectrochemical (PEC) water splitting, [28, 29] hydrogen productions, [30] CO_2 reductions, [31] electron transport layer in perovskite solar cells, [32] lithium-ion batteries [33] and supercapacitors, [34] TiO_2 plays a pivotal role from a nanomaterial engineering perspective.

The use and efficiency of MOs, specifically TiO_2, in renewable energy applications can be optimized and enhanced for their targeted sample properties (*e.g.*, electrical, chemical, mechanical). [14, 35-37] Multidimensional investigations like thermodynamically driven intrinsic properties (*e.g.*, contact potential difference (CPD) measurements) and defect engineering activities such as charge carrier dynamics research are necessary perspectives for

understanding and characterizing the effects of surface defects for further charge transfer and migration investigations in many photocatalytic and/or energy applications. [35, 38-42]

Charge carriers are reactive and mobile charged particles that mainly facilitate conductivity and energy transfer within a material system. [14, 35, 41, 43, 44] These carriers play an important role in charge migration, transfer, storage, and photocatalytic efficiency. [45-50] For this purpose, measuring the migration of charge carriers against highly reactive surface defects such as photoinduced surface oxygen vacancies (PI-SOVs), which are indigenous to many MOs, has been a long-term effort. Theoretically, it has been postulated that charge carriers can alter significant material properties like mobilities, time constants, activation energies, migration barriers, distance and/or history dependencies, etc. [14, 35, 41, 43, 44] However, existing knowledge of migration dynamics is macroscopically volume and/or time-averaged at scales that are orders of magnitude larger than the governing physical dimensions (*i.e.*, nanometers, milliseconds). [51-56] Such macroscopic averaging is a fundamental problem in nonequilibrium thermodynamics and engineering applications, as it obscures a deeper understanding of the basic atomic scale principles that govern diffusive dynamics. The main question answered in this work is “Is it possible to characterize and measure the charge carrier dynamics for MOs under representative physical scales and conditions without compromising any valuable information?”.

As a subbranch of AFM, time-resolved atomic force microscopy (tr-AFM) is a key methodology that can be utilized to solve the scale inadequacy in charge carrier characterization and optimization attempts. [41, 43, 57] Existing tr-AFM theories and methods are not sufficient on their own without the inclusion of necessary hardware and software capacities, as well as the combined experimental structures. Specialized and enhanced tr-AFM methods and measurement techniques are utilized for used for examining both fast (*i.e.*, electrons) and slow (i.e., holes) charge carriers under multivarious conditions in this thesis to find an answer to the abovementioned inquiry. [38, 40, 58-60]

Chapter 1 discusses a brief history of the research question, connects the dots in the existing literature while emphasizing the missing points and know-how that triggered this research to its full extent. It puts profound context on why this investigation and the respective work was necessary. Chapter 2-6 are the progressive works that are published as peer-reviewed journal articles. [38-40, 60, 61] These articles demonstrate the fruitful outcomes of the research and how step-by-step we achieved a comprehensive understanding and an extensive measurement capacity to examine charge carrier dynamics from a multidimensional perspective. The final section puts a conclusion on the work and proposes future work to enhance and further the current understanding and know-how we gained for the respective research.

CHAPTER 1

LITERATURE REVIEW

1.1 Atomic Force Microscopy (AFM)

1.1.1 Fundamental AFM Modes & Their Working Principles and Limitations

Atomic force microscopy (AFM) is a powerful tool that can be adapted for multidimensional research under various ambient and experimental conditions. The ability to operate in liquid, air, or vacuum conditions for a wide range of temperatures broadens the application spectrum of the method. [10, 62-70] In addition, the susceptibility and adaptivity of the method for combining it with external stimuli (e.g., voltage pulses, ultraviolet irradiation, etc.) creates opportunities to portray and investigate wide-range physical phenomena. [35, 38, 40, 41, 60, 61]

Historically, major AFM techniques can be examined in two main groups, static mode (i.e., contact mode) and dynamic mode AFM. [10, 63, 71] The first method, contact mode AFM, relies on a constant contact procured between the cantilever tip and the sample surface, which creates several complications during the feedback. Gathered information cannot get ahead of being an averaging for the tip-sample interaction, since the contact area between the tip and the sample remains as a finite surface throughout the process. This situation prevents the users from obtaining information about the behavior of individual atoms, which is vital for furthering the optimization and engineering of different sample systems.

Chronologically, the first dynamic AFM method was amplitude modulation atomic force microscopy (AM-AFM). [10, 72] This method is based on the modulation of the oscillation amplitude of the cantilever during the measurement under ambient conditions for extracting topographic information from the sample surface. The AFM cantilever is driven by an attached piezo, which is controlled by a user-applied voltage. As shown in Figure 1.1, the cantilever has a

natural resonance frequency of "w_o", and the frequency it is driven at is "w_d", which is close to w_o. Excluding any surface interaction with the sample, the cantilever has a constant oscillation amplitude based on the harmonic oscillation principle. Once the cantilever is close enough to the surface as the tip-sample interaction forces (*e.g.*, van der Waals, electrostatic, etc.), their effects result in a shift in the resonance frequency of the cantilever from w_o to w_o'. This shift results in the oscillation amplitude to change as well. The utilized controller detects this shift and adjusts how far our tip is from the sample surface (*i.e.*, tip height) to keep the oscillation amplitude constant. This change implemented in the oscillation amplitude, "ΔA", is used to map the surface from the most simplistic understanding. Once the interaction is going to be converted to the tip-sample interaction forces, as the main oscillation principle of an AFM cantilever, the damped harmonic oscillation principle must be visited.

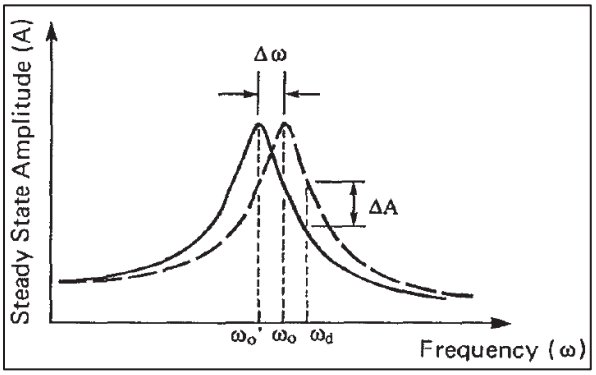

Figure 1.1 Oscillation amplitude and resonance frequency relation for an AFM cantilever
Taken from T. R. Albrecht et al. (1991) [72]

Another significant concept in the AM-AFM method is the quality factor "Q" of the used cantilever. Q is a measure of cantilever oscillation efficiency, which is related to the sharpness of the resonance curve and is defined by the ratio between w_o to the full width at half maximum (FWHM) of the resonance peak from an amplitude vs. frequency curve like the one shown in Figure 1-1. [62, 73-76] The minimum measurable force with the cantilever is directly related to this metric, since as sharp as the amplitude vs. frequency curve is (*i.e.*, as large as the Q is), small changes in the tip-sample interaction force start to demonstrate larger deviations in A. The stability of the cantilever depends on the opposite principle, where a broader resonance

peak results in a higher stability and hence faster imaging/measuring opportunity. There is a significant trade-off between cantilever sensitivity and the cantilever bandwidth based on the sensitivity-stability spectrum. This relation is the main limitation of AM-AFM and is explained in equation 1.1. [72]

$$\tau_c = \frac{2Q}{w_o} \tag{1.1}$$

In equation 1.1, τ_c is the time constant of the cantilever oscillation (*i.e.*, cantilever response time). In this equation, a higher Q value or a lower w_o value results in a higher response time for the cantilever. The main issue in AM-AFM based on the equation is higher Q cantilevers takes a longer time to respond to changes in frequency, even though the sensitivity is increased. Hence, the time resolution of detectable events is hampered due to the mechanical limitations of the cantilevers.

Additionally, potential tip instabilities and amplitude drops due to the inconsistencies at the slight contact between the cantilever tip and sample surface may damage the overall vibrational stability of the setup, which is critical depending on the nature of the research. Thus, to overcome the stated drawbacks, the second dynamic AFM method, which is the frequency modulation atomic force microscopy (FM-AFM) and methods built on this mode are required for the works in this thesis. Figure 1.1 can be used for visualization of the following principle of FM-AFM. [72] The primary variables of an oscillation are amplitude and frequency. In AM-AFM, changes happening to the oscillation were tracked with the change in the amplitude of the cantilever's oscillation. However, as explained above, this case is not as sensitive and "instantaneous" enough to capture desired physical phenomena. In FM-AFM, the oscillation amplitude is kept at a constant level for the cantilever, where the drive voltage is adjusted and the system actively "tracks" resonance. The change in cantilever oscillation frequency, Δw, is the dynamic parameter that is influenced by the external effects and changes. The value of this change, Δw, is the direct outcome of the tip-sample interaction forces (*e.g.*, van der Waals, electrostatic, etc.), and the respective force gradients. As the frequency shift is an

"instantaneous" phenomenon, there is no mechanical limitation and thus the achievable time and event resolution are significantly improved with the FM-AFM-based methods.

FM-AFM control algorithm depends on several feedback loops. [61, 72] The method is based on controlling the frequency/phase feedback loop and oscillation amplitude feedback loop simultaneously for recording the frequency shift changes at a constant oscillation amplitude. The amplitude of the oscillation is controlled for a fixed value and always adjusted by a PID control loop, where the drive voltage is adjusted to keep it at the desired value. For the control of the oscillation frequency in FM-AFM applications, however, a phase-locked-loop (PLL) is required. PLLs are customized PID controllers combined with a phase comparator and a voltage-controlled oscillator (VCO). PLLs are generally used when the phases of the generated output signal and the input signal are correlated with each other as is the case for FM. Additions of a phase comparator and a VCO enable the controller to work in correlation to a phase difference between two signals, which is vital since a 90-degree phase difference between the excitation and oscillation signals of the cantilever is required for FM-AFM. [61, 62]

For the fixed oscillation amplitude in the cantilever's oscillation, simultaneously a PLL continuously adjusts the w_{d}, so the new resonance peak is followed by the system and the difference between the frequency of cantilever's actual oscillation and the resonance frequencies ($w_{\mathrm{o}} - w_{\mathrm{d}}$) is kept at the same predefined value. This adjusted difference, also known as the resonance frequency shift, Δf_0, is the main variable of the oscillation which is capturing the physical phenomena occurring on the sample surface. Tip-sample interactions and their influence cause the value Δf_0 to change and the quantitative change in this value can be converted into many features like the tip-sample interaction forces, potential energies, time constants, etc.

For the work in this thesis, most of the required measurement methods were based on FM-AFM techniques (*vide infra*). Hence, the utilized system required to have FM-AFM capacity. As the existing AFM setup available did not have the FM capacity, a detailed enhancement and upgrade procedure was implemented to gain the necessary features and perks. With the necessary software and hardware implementations, it is possible to convert a contact

mode/AM-AFM setup into a customizable FM-enabled system. In Chapter 2 of this thesis, the respective published journal article is presented in detail.

1.1.2 Traditional Time-resolved AFM Method

One of the pioneer ideas for a "time-resolved" AFM method, time-domain electrostatic force microscopy, was implemented by Schirmeisen [57] and has been successfully implemented for various transport mechanisms over Li, Na and K ions. The technique was based on a similar idea and was the fundamental version of the time-resolved AFM (tr-AFM) methods were utilized in this thesis. tr-AFM and its versions are based on the generation of an electrostatic interaction between the cantilever tip and the sample surface. [35, 41, 43, 58, 59]

The main purpose of these methods is to investigate electrically charged particles (*e.g.*, charge carriers) for their migration dynamics, tendencies and behaviors as it is explained in detail within the upcoming sections (*vide infra*). A designated bias pulse (*i.e.*, a timed voltage pulse) is applied between the conductive (*e.g.*, gold-coated) cantilever tip and the sample surface once the cantilever is at the proximity of the surface while still being away for a defined separation. Given pulse results in a coulombic interaction, which creates a time-dependent electric field within the tip-sample space. Any change happening in the electrical interaction and/or electrostatic force between the sample system and the cantilever is captured by the changes in the resonance frequency shift, Δf_0, of the cantilever's oscillation. The procured electrostatic field is directly correlated with the electrostatic tip-sample interaction force. Equation 1.2 demonstrates the relation between the internal electric field, $E(t)$, and the decay behavior of the charge carriers. The obtained relation follows a stretched exponential decay model from the mathematical aspect. [35, 41]

$$E(t) \propto e^{(\frac{-t}{\tau^*})^{\beta}} \text{ for } t > t_c \tag{1.2}$$

In equation 1.2, $E(t)$ is the time-dependent internal electric field, τ^* is the effective time constant, β is the stretching factor and t_c is the cutoff time which is in picoseconds. For the

relaxation models in materials, cutoff time, t_c, is defined as the smallest time interval until the relaxation dynamics of individual particles (*e.g.*, atoms, molecules, carriers, etc.) are not significantly influenced/altered through their interactions with neighboring particles. [35, 41] Hence, for times shorter than t_c, relaxation behavior was expressed as it was dominated by the intrinsic properties of these particles, *i.e.*, these particles act independently through the influence of their fundamental vibrational, rotational, etc., properties. At time scales longer than this cutoff point, particle interactions start to take place as the nearby particles start to have an influence on others, as well as developing a cumulative effect. Models known as the coupling model [77, 78] and the jump relaxation model [79] explain this phenomenon through different approaches, which yield the same fundamental point in the traditional tr-AFM understanding.

In light of these models and the nature of physical interaction, mathematical modelling of the decay behavior of electrically charged particles under the time-dependent electric field can be expressed in the form of the frequency shift of the cantilever as in equation 1.3. Δf_0 is the initially obtained resonance frequency shift for the cantilever's oscillation at t = 0 seconds, Δf_s is the saturated frequency shift (i.e., additional frequency shift occurring as the system relaxes) with the stretched exponential decay behavior embedded in its change.

$$\Delta f(t) = \Delta f_0 + \Delta f_s \, e^{(\frac{-t}{\tau^*})^{\beta}} \tag{1.3}$$

Replacing reaction rates for relaxation process, Arrhenius law [80, 81] is used to explain the resultant time constant of the particle relaxation process as measured in tr-AFM. Equation 1.4 shows the relation between the relaxation time constant, τ^*, as a function of temperature based on the Arrhenius law.

$$\tau^* = (\tau_{eff}{}^*) \; e^{\frac{E_a{}^*}{k_B T}} \tag{1.4}$$

In equation 1.4, $\tau_{eff}{}^{*}$ is the effective attempt rate for Arrhenius-like models, $E_a{}^{*}$ is the effective activation energy for charged particles in the sample system, k_B is the Boltzmann constant and T is the temperature of the sample. One can express the effective activation energy for the collective particle motion to retrieve the equivalent single particle migration barrier as in equation 1.5, where E_a is the migration barrier for single particle motion and β is the stretching factor for the charge carrier relaxation motion. [77, 78]

$$E_a = (E_a^*)(\beta) \tag{1.5}$$

Further discussion regarding the conventional tr-AFM methodology, setup (i.e., hardware and software implementations), and measurements are discussed in the upcoming sections of this thesis under the respective journal articles presented in Chapters 2-6.

1.1.3 Submicrosecond Time-resolved AFM Method

Traditional tr-AFM is a powerful method for investigating electrically charged particles within a sample system. However, the explanation power for the method is limited through the feedback control speed of the control architecture. [43, 57, 72] Although FM-AFM-based tr-AFM provides almost an "instantaneous" capturing capacity for charged particle dynamics, how fast the cantilever height and resonance frequency shift is adjusted is the limiting factor against this ability. The feedback loop introduces a lag, which hinders the submicrosecond time-scale measurement abilities of the method. Additionally, frequency demodulation required for the control loop smooths out the transient effects which could carry useful information regarding faster time-scale particle motion. The overall issue created here is, that the lowest time-resolution of the traditional tr-AFM is still could be larger than certain electrically charged particles of interest.

Theoretically postulated works of Giridharagopal et al. [59] and Karatay et al. [58] introduced an idea for a feedback-free approach for bypassing the feedback response lag within the traditional tr-AFM idea, while simultaneously introducing "subcycle electrostatic force

microscopy" methodology, where one can obtain submicrosecond time-scale resolution and accuracy. Procuring time-resolution down to low nanoseconds level introduces new possibilities for accurate measurement of microsecond-submicrosecond physical phenomena. Utilizing a feedback-free approach relies on capturing the tip-sample interaction through another data channel. Thus, the oscillation signal of the cantilever is digitized at a high sampling rate for this purpose and undergoes various averaging, numerical filtering (*e.g.*, Butterworth) and mathematical transformations (*e.g.*, Hilbert transform). Eventually, the necessary instantaneous frequency shift for the cantilever is retrieved for the examined tip-sample interaction and the physical phenomenon behind it.

Details of the empirical implementation and enhanced realization of these methods are utilized within the journal article presented in Chapter 5 of this thesis.

1.2 Metal Oxide Sample Systems

1.2.1 Electronic Structure of Metal Oxides and Their Implementation Capacity for Scanning Probe Microscopy Investigations

Metal Oxides (MOs) are widely utilized sample systems with extensive use in different fields, most commonly for renewable energy applications (*e.g.*, batteries, solar cells, etc.), sensing, and biological applications. [82-88] Their versatility and functionality make them suitable for photocatalysis and energy transport/storage applications. Their electronic structure is investigated over the foundation governing charge carrier behaviors and tendencies, their optical absorption capacities and conductivity under the right circumstances. To utilize these sample systems efficiently, a fundamental understanding of their intrinsic and extrinsic features, their band structures and defect and/or dopant influences is critical. [15, 37, 89, 90]

Semiconductor MO systems (e.g., TiO_2) possess a special band structure. [91, 92] Electronic states are divided between a valence band (VB), and a conduction band (CB). The difference between the maximum of the valence band and the minimum of the conduction band makes

the bandgap for the semiconductor. Electron excitation from VB to CB is only possible with photons with energy levels equal to or higher than the bandgap level. Thus, the level of the bandgap, with respect to the type of bandgap is directly related to the optoelectronic properties of the sample systems. Photoexcitation and/or external voltage-based VB to CB electron transitions are fundamental to many processes like photocatalysis and electrochemistry, as it is within the scope of this thesis.

Different types of bandgap structures are bound to different implementations based on the physical tendencies in these systems. Energy separation levels between VB and CB are higher in wide bandgap structures (typically $E_{BG} > 3\,eV$) and hence higher energy photon absorptions (*i.e.*, photons in UV-range) are commonly needed for the required excitation. [93, 94]

As a wide bandgap MO, TiO_2 is a worthy candidate for building tr-AFM-based measurement techniques and methods for charge carrier investigations based on several material features. [93, 94] It is suitable for UV-light-driven photoexcitation applications, where generation of electron-hole pairs under this irradiation and the introduction of photoinduced vacancies to the sample surface is possible. The low intrinsic charge carrier concentration of TiO_2 sample systems amplifies the influence of surface defects and vacancies over the mobility and motion of these particles, which is significant for the optimization attempts for their migration dynamics.

UV-range irradiations result in surface vacancies (*e.g.*, photoinduced surface oxygen vacancies (PI-SOVs)) that can act as charge carrier traps and/or donors, which is vital for examining defect-influenced charge transport optimization methods. [95-101] These defect states are both stabilizable and reversible under correct circumstances and enables a profound reaction characterization for the PI-SOV introductions and charge carrier excitations.

TiO_2 consists of various electrically charged carriers (*e.g.*, holes, electrons, ions etc.) acting at different time scales (*i.e.*, fast and slow time scales). [38] Observing both slower and faster

recombination and migration mechanisms for charge carrier dynamics is critical for building instrumental methods to quantify and characterize their influences over the electronic features of the sample systems.

Additionally, TiO_2 has thermodynamically driven intrinsic tendencies based on doping and vacancy formations. [35, 41] Thus, it demonstrates variations in its properties as a function of temperature even without any phase change over the sample surface. Phase transformation aspect of TiO_2 is a tunable property on a structural basis and is a requirement for stability at device/application levels. [39, 102, 103] Hence, as an important dimension to the optoelectronic optimization works for these sample systems, temperature-dependent behaviors at nanoscale have been a point of interest.

One of the significant examples of these temperature-dependent features is the work functions of sample systems and coated cantilevers. Work function is the minimum energy requirement for removing an electron from a material surface to the vacuum level. [91, 104, 105] It is an important intrinsic property that can vary from sample to sample and even from surface to surface and/or defect site to defect site over the same material system. Various SPM methods like scanning tunneling microscopy (STM), atomic force microscopy (AFM), kelvin probe force microscopy (KPFM), are sensitive to the variations of the work functions and their differences. If the work function differences between the sample and the cantilever when they are at proximity (*i.e.*, contact potential difference (CPD); a.k.a volta potential [39, 106]) are not characterized or known against the varying environmental conditions (*e.g.*, temperature, etc.) measurement issues arise.

For STM, uncontrolled or tracked CPD changes result in tunneling barrier alterations, local ban bending problems and spectroscopy issues. For KPFM, the whole method is based on the measurement of these differences and mapping material properties respectively. For AFM, specifically for the electrostatic and optoelectronic investigations like the charge carrier studies, quantification of the measured tip-sample interaction forces, correlated frequency shifts and many outcomes are altered and hindered. Potential temperature-dependent variations

may affect charge carrier distributions and interfacial charge migration dynamics, shift Fermi levels and alter external electric fields. Thus, the ability to characterize intrinsic doping-based material features like CPD variations under external influences and unique to the sample system is vital. It is possible to characterize these properties with SPM-based measurement techniques and build a foundation for the extensive tr-AFM method developments. [39, 61]

1.2.2 Charge Carrier Dynamics and Their Characterization in Metal Oxides

1.2.2.1 Charge Carrier Transport Mechanisms in TiO_2

Charge carriers are electrically charged particles (*e.g.*, electrons, holes, ions, vacancies, etc.) that influence and alter the electronic properties of semiconductor metal oxides (*e.g.*, TiO_2). [91, 92, 104] Their transport mechanisms are mainly based on either drift or diffusion mechanics. [107, 108] These mechanics as a result of the carrier concentrations are highly dependent on surface defects.

Drift transport is based on the movements of these charged particles under an applied external electric field. Diffusion transport on the other hand is based on carrier concentration gradients and generally anisotropic (directionally dependent; based on Einstein's random walk [109]) rather than a continuous diffusion based on the classical Fick's Law. [110, 111] For n-type semiconductors like TiO_2, surface oxygen vacancies as carrier donors, localization effects, trapping mechanisms and diffusion characteristics of both surface oxygen vacancies and photoexcited carriers have a direct influence on the charge carrier mobilities. [35, 38, 60, 95-98]

Under representative conditions, both transport mechanisms are observed for a TiO_2 sample system, where the stronger influence over the measured migration behaviors and tendencies are based on the external effects like applied external electric fields and surface irradiation-based vacancy generations. Overall, controlled charge displacement requirement in different applications (*e.g.*, transistors, memristors, etc.) require a drift transport dominant charge carrier

motion, where the diffusion features like diffusion length, relaxation times and collectivity of charge motions are critical for charge separation and storage activities. [107, 108]

1.2.2.2 Influence of Surface Defects on Charge Carriers

Most influential surface defects in TiO_2 for charge carrier dynamics are the surface oxygen vacancies (V_o) as they influence charge carrier mobilities, recombination and trapping mechanisms and transport/storage efficiencies. [112-115] These vacancies exist with and without external influences either due to intrinsic thermodynamic and kinetic features or external stimuli like UV irradiation. They have multiple possible charge states (V_o^0, V_o^+,V_o^{+2}, and V_o^{+3}), where the most favorable one is V_o^+ based on former theoretical work with the most significant influence on the conductivity of the TiO_2 sample systems. [35, 41] Defect densities, formation energy and sample conductivity play important roles on the systems' tendency to favor one charge state to others. [112-115]

Dynamic interaction of V_o, as well as the possibility to tune and control their introduction to the system through optical manipulations (*i.e.*, UV irradiation generated PI-SOVs). High-energy UV photons are proven to eject oxygen atoms from the sample surface and introduce PI-SOVs to TiO_2 surface. [42, 48, 93, 104] PI-SOVs can alter electric potential landscapes, introduce charge traps and recombination centers for charge carriers. They can be tuned for various metal interfaces (e.g., TiO_2/Au), [38] environmental conditions (e.g., temperature variations) [39] and photocatalytic surface agents (e.g., methanol). [40] These conditions propose strong pathways to quantify and optimize the charge carrier migration dynamics from a defect engineering point of view.

1.2.2.3 Existing Deficiencies and Limiting Factors for Charge Carrier Dynamics Quantification and Characterization

Despite the significant and numerous attempts to characterize and optimize the charge carrier dynamics properties in MO systems, existing methods remain insufficient for explaining the

charge carrier migration and transport phenomena with high-end temporal and spatial resolution. Traditional techniques, while significantly valuable for various purposes in material characterization, mainly suffer from two issues. These methods are either macroscopically volume and/or time-averaged at scales that are orders of magnitude larger than the governing physical dimensions (i.e., nanometers, microseconds) or lack the capacity to simultaneously isolate and quantify the local charge migration tendencies at nanometer and submicrosecond scales simultaneously. [51-56]

Raman spectroscopy is one of the strongest optical methods to gain insights into charge carrier recombination, phonon-carrier interactions and significant defect generations in materials. [44, 116] It is commonly used to examine oxygen vacancies and "indirectly" tracking the charge carrier localizations, as it is not designed to directly track electronic motion of these particles, in sample systems. [13, 44, 116] The main drawback to Raman methods is the achievable spatial resolution, which is diffraction limited and generally orders of magnitude larger than the SPM methods. Thus, spatial characterization of localized charge carrier migration tendencies and patterns is not directly feasible. Additionally, the achievable time resolutions are limited and insufficient to track sub-microsecond carrier recombination or trapping events. [117]

Photoluminescence (PL) spectroscopy is another significant method used to measure charge carrier recombination and trapping states. [118] It is based on photoexcitation, where the radiative recombination is captured through emitted photon detections. However, it is possible for the charge carriers to recombine through both radiative and nonradiative paths. [119] It is a critical drawback for the PL spectroscopy method when it comes to investigating defect and trapping effects over these paths for MO systems like TiO_2. In addition to suffering from real-time temporal resolution and capturing power, similar to Raman methods, the spatial resolution of PL spectroscopy, where the averaging of the spatial resolution is more drastic and a couple of magnitudes larger than the attainable levels in SPM techniques. [120, 121]

Electrochemical Impedance Spectroscopy (EIS) is a method that can be utilized to investigate similar charge carrier phenomena to SPM methods, where the mobility, storage (accumulation) and recombination features and tendencies of these particles, defect states and trapping sites, etc. are within the scope. [122] The method is sensitive to conductivity changes and can measure bulk properties for material systems. However, the locality of the measurements and the spatial resolution, as well as the ability to distinguish between bulk and surface charge transport phenomena are limited compared to SPM methods. Additionally, EIS, as it is not exactly a dynamic method, assumes a quasi-stationary system and the system evolution throughout an event may interfere with the ability of the method to capture fast time-scale events. [123, 124]

In addition to the discussed methods, there are various conventionally accepted methods that can be countered against advanced SPM techniques for measurement activities. Methods like secondary ion mass spectrometry (SIMS), [125, 126] surface reactivity studies, [127] flexoelectricity, [128] hall effect measurements, [129] X-ray Photoelectron Spectroscopy (XPS), [130] X-ray Absorption Spectroscopy (XAS) [131] and even other traditional atomic force microscopy (AFM) methods like conductive AFM (c-AFM) [132, 133] can be used in attempts to characterize and optimize charge carrier dynamics but hindered due to various issues (i.e., necessary temporal and spatial resolution capacities, bulk measurement averaging, surface destructions, not having direct electronic property quantification, lacking data for charge migration and transport phenomena, etc.)

Given the limitations in existing methodologies (*vide supra*) within the literature that are used to establish a fundamental understanding for transient charge carrier dynamics from a multidimensional perspective, techniques built over the foundation of AFM-based spectroscopy with time-resolved frame are necessary. tr-AFM offers wide-range abilities to quantify charge carrier dynamics with the possibility of high-resolution real-time data acquisition. Methods based on the tr-AFM idea can be utilized for examining migration, trapping, recombination and storage aspects of these carriers with respect to various external influences, environmental factors, surface chemistries and agents. [35, 38, 40, 41, 58-60]

To fully exploit the capacity of tr-AFM idea, it must be converted into a standardized and customizable tool with future enhancement capacity. This can only be procured with instrumental refinement for theoretical potentials and empirical realizations of various measurement combinations and possibilities. With its versatility, adaptivity, spatial precision and high temporal responsiveness, tr-AFM idea could be cornerstone technique in not only the abovementioned fields but in many others as well. Main issue with the method was the generalizability of the tr-AFM idea and its applicability to answer real physical problems. Goal of this thesis is to lay out a profound tr-AFM based physical characterizations for an existing gap in the literature, while developing and integrating enhanced tr-AFM measurement techniques with the high-end system characterization guidelines to eventually propose tr-AFM as a fundamental characterization tool.

The following section in this thesis addresses the given problem at hand. Chapter 2 revolves around how to enhance and customize a basic AFM system without any advanced features to gain high-resolution measurement capabilities and application power for various time-resolved measurement techniques. [61] Chapter 3 focuses on how this system can be used to investigate intrinsic material properties under varying environmental conditions to disclose MO system tendencies. [39] Chapters 4-6 include high spatial and temporal resolution charge carrier dynamics investigations for demonstrating the potential of measurement techniques and methods developed over tr-AFM idea. [38, 40, 60] In these chapters, conducted works demonstrate realization of theoretically postulated fast scale tr-AFM methods for different interfaces, investigate surface agent and chemistry influences through traditional techniques and examine decades-old optical behavior inconsistencies in the literature.

CHAPTER 2

CUSTOMIZATION OF AN ATOMIC FORCE MICROSCOPE FOR MULTIDIMENSIONAL MEASUREMENTS UNDER ENVIRONMENTAL CONDITIONS

Bugrahan Guner[a], Simon Laflamme[a], and Omur E. Dagdeviren[a]

[a]Department of Mechanical Engineering, École de Technologie Supérieure,
1100 Notre-Dame West, Montreal, Quebec, Canada H3C 1K3

Paper published in *Review of Scientific Instruments*[1], June 2023

2.1 Abstract

Atomic force microscopy (AFM) is an analytical surface characterization tool that reveals the surface topography at a nanometer length scale while probing local chemical, mechanical, and even electronic sample properties. Both contact (performed with a constant deflection of the cantilever probe) and dynamic operation modes (enabled by demodulation of the oscillation signal under tip–sample interaction) can be employed to conduct AFM-based measurements. Although surface topography is accessible regardless of the operation mode, the resolution and the availability of the quantified surface properties depend on the mode of operation. However, advanced imaging techniques, such as frequency modulation, to achieve high resolution, quantitative surface properties are not implemented in many commercial systems. Here, we show the step-by-step customization of an atomic force microscope. The original system was capable of surface topography and basic force spectroscopy measurements while employing environmental control, such as temperature variation of the sample/tip, etc. We upgraded this original setup with additional hardware (e.g., a lock-in amplifier with phase-locked loop capacity, a high-voltage amplifier, and a new controller) and software integration while utilizing its environmental control features. We show the capabilities of the customized system

---

[1] Bugrahan Guner (2023, *p.* 063704)

with frequency modulation-based topography experiments and automated voltage and/or distance spectroscopy, time-resolved AFM, and two-dimensional force spectroscopy measurements under ambient conditions. We also illustrate the enhanced stability of the setup with active topography and frequency drift corrections. We believe that our methodology can be useful for the customization and automation of other scanning probe systems.

2.2 Introduction and Background

Atomic force microscopy (AFM) is a surface characterization method. [134] The key element in AFM is a sharp probe tip, attached to a force-sensing transducer. [70, 134] The tip is scanned relative to a sample while the resultant interaction force is measured. Mapping as a function of the sample position allows, in principle, imaging of surface structures. [62, 70] In addition, many other interactions, such as the local chemical and electrostatic forces, can be accessed. [135] Moreover, the ability to integrate different stimuli into AFM measurements (e.g., temperature dependence, ultraviolet irradiation, etc.) enables the investigation of diverse experimental effects. [35, 41] Chronologically, AFM operation can be grouped into two: static (aka, contact) and dynamic modes. [10, 70, 72] The contact mode of operation relies on the direct deflection measurement of the probe. [63, 136] With the knowledge of the force-sensing transducer's (i.e., cantilever) spring constant, forces can be recovered directly. [136] For this reason, the contact mode is easy to operate, and the results are intuitive. However, the degree of locality is defined by the established contact area between the tip and the sample, which can be as many as hundreds of nanometer squares. [70, 137, 138] In addition, there are mechanical instabilities where the attractive tip–sample interaction overcomes the stiffness of the cantilever, also known as jump-in to contact. [139, 140] Dynamic operation modes have been introduced to resolve the limitations of the contact mode. [62, 70] The fundamental idea of the dynamic mode of operation relies on the demodulation of the otherwise harmonic oscillation of the cantilever to control tip–sample separation. [62, 70, 72] Amplitude modulation (AM) is one of the most widely used dynamic operation modes. [70] The AM is based on the demodulation of the oscillation amplitude and/or the phase difference between the excitation and the oscillation signals while driving the cantilever with a constant excitation signal. Only

one control loop is involved to control the tip–sample separation for the constant excitation signal in AM-AFM. [70, 73] For this reason, AM-AFM is relatively straightforward to use. Although the AM-AFM is easy to implement, it is mechanically limited, particularly under vacuum conditions. More specifically, the settling time of the oscillation amplitude is proportional to the quality factor of the cantilever. [72, 141] For this reason, due to the lack of viscous damping under vacuum conditions, the use of AM modulation is not feasible. In addition, mechanical instabilities and amplitude variations beyond the capabilities of existing AFM hardware hamper the use of conventional AM-AFM under vacuum conditions. [142] The alternative to AMAFM is frequency modulation atomic force microscopy (FM-AFM), which is based on the demodulation of the resonance frequency of the cantilever under tip–sample interaction. [62, 72] The FM-AFM eliminates the limitations of the AM-AFM; however, it requires a relatively complex control architecture as the excitation signal changes due to tip–sample interaction. [62, 72, 142] FM-AFM is usually employed under vacuum conditions as the signal-to-noise ratio improves with a high-quality factor; however, it can also be used under ambient and even in liquid environments. [62, 73-76, 143-147] FM-AFM enables the measurement of tip–sample interaction forces with high resolution, i.e., piconewton in force and picometer in distance. [148-152] In addition, with recent advances in atomically engineered tips, it is possible to assess direct chemical characterization at distinct atomic sides. [150, 152-154] In addition to FM-AFM's precise force and distance control, FM-AFM also overwrites AM-AFM with its potential for time-resolved measurements, where the tip–sample interaction force is measured as a function of time. [35, 41, 43, 57] Nevertheless, it has been theoretically shown and experimentally verified that the time resolution of FM-based measurements is not mechanically limited. [155-157] Here, we demonstrate the customization of a commercial atomic force microscopy system with new hardware and software integration. Although the initial setup, VEECO's EnviroScope scanning probe microscope (SPM) with a NanoScope® IIIa controller, had user-friendly features (e.g., easy access to sample and tip and temperature control of the sample and/or tip), it was only capable of contact mode and AM-AFM-based topography measurements and a primitive force spectroscopy ability. We implemented a phase-locked-loop, a high-voltage amplifier, and a new microscope controller for automated measurements with FM-AFM. We illustrate our customization with experiments

under ambient conditions. More specifically, we performed FM-AFM topography experiments, contact potential difference measurements, FM-AFM-based force spectroscopy measurements, time-resolved atomic force microscopy measurements, and two-dimensional force spectroscopy measurements across step edges. Although each commercial system has its own peculiarities (e.g., driving step motors for rough approach, ability to access all data signals as well as high-voltage signals, and camera connection for sample localization), similar upgrades/customizations are possible for many (commercial) systems. For this reason, we believe that our methodology will be useful for other scanning probe microscopes.

2.3 Experimental Methods

The initial system had a NanoScope IIIa controller, which is capable of contact mode and AM-AFM-based topography measurements and primitive distance spectroscopy measurements, as Figure 2.1 illustrates. We employ this configuration for the initial approach to the sample (*vide infra*). This eliminates the necessity of the implementation of step motor drivers, a built-in camera, and a laser diode signal amplifier to the original system without sacrificing its performance (*vide infra*).

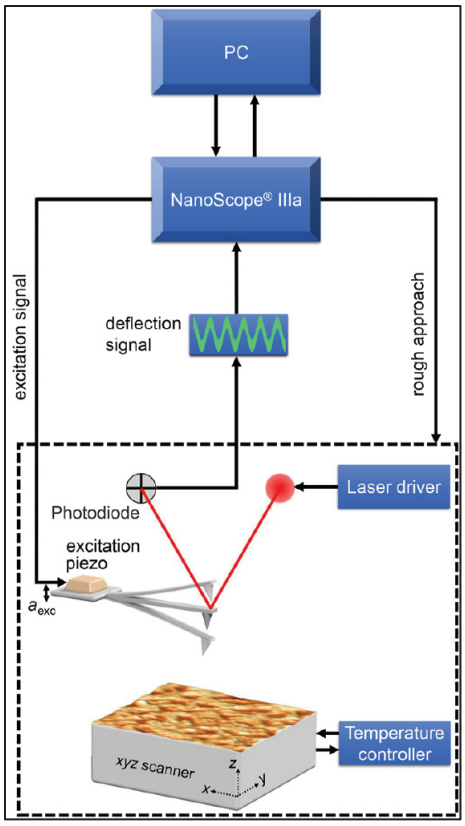

Figure 2.1 The illustration of the original control architecture of the microscope

Figure 2.1 caption continued: We use the original hardware for the initial approach to the sample either with contact mode or with amplitude-modulation atomic force microscopy. For the dynamic mode of operation, the excitation signal, a_{exc} is controlled/modulated by the NanoScope IIIa controller. The use of existing hardware eliminates the necessity of the implementation of step motor drivers, an amplifier for the laser diode, and a built-in camera for rough sample manipulation.

As Figure 2.1 shows, the deflection signal is used as an input for the NanoScope IIIa controller, where it is demodulated to control tip–sample separation. As the NanoScope IIIa controller is incapable of demodulating the deflection signal for its resonance frequency shift, Δf_0, the implementation of the additional hardware, i.e., a phase-locked loop (PLL), is essential. To

integrate any additional hardware, signals that go in and out of the microscope must be accessed. For this purpose, the Signal Access Module™ (SAM) was employed. As Figure 2.2 demonstrates, the cantilever deflection signal is directed to a lock-in amplifier with a PLL capability (Zurich Instrument's MFLI lock-in amplifier) to demodulate Δf_0. The excitation signal, a_{exc}, created by the lock-in amplifier, is also directed to the microscope with SAM (see APPENDIX I.A and I.B for details). With this configuration, it is possible to employ FM-AFM for topography imaging while using the NanoScope software (version V5.31r1). [158] Although this upgrade enables the FM-AFM imaging with the microscope, due to the limitations of the NanoScope software, the customization of measurements is impeded.

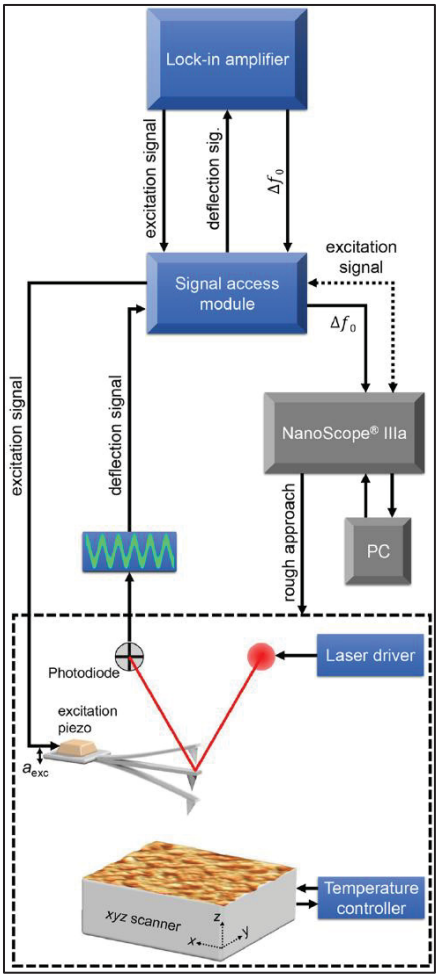

Figure 2.2 The control architecture to enable frequency modulation atomic force microscopy

Figure 2.2 caption continued: The deflection signal has been accessed via the Signal Access Module (SAM). A lock-in amplifier with phase-locked-loop (PLL) capacity is employed to demodulate the resonance frequency shift of the cantilever, Δf_0. The excitation signal of the cantilever is modulated by the PLL. Signals, i.e., Δf_0, and a_{exc}, are exchanged via SAM. The tip–sample distance is established by the NanoScope IIIa controller while using NanoScope software (version V5.31r1) in "contact mode" as Δf_0 is a constant voltage output of the PLL.

To conduct customized and/or automated experiments, we implemented a second microscope controller to the microscope [SoftdB's microscope controller with Gnome X Scanning Microscopy (GXSM) software]. [159] As Figure 2.3 shows, the deflection signal is accessed via the SAM. The outputs of the PLL, i.e., Δf_0, demodulated oscillation amplitude, the phase difference between the excitation and the oscillation signal, θ, and a_{exc}, are directed to the GXSM to achieve tip–sample distance control and/or data recording. The small signal outputs of the GXSM (x_s, y_s, z_s) for the x, y, and z motion of the piezo are amplified with a separate high-voltage amplifier (PiezoDrive TD250-INV). The tip–sample bias, V, is also controlled via GXSM. The amplified piezo signals, a_{exc}, and V are used as inputs to the microscope and are exchanged via the SAM (see APPENDIX I.A and I.B for details). The GXSM and PLL have continuous MATLAB® and/or Python™ communication for control, automation, and drift corrections (see APPENDIX I.C and *vide infra*). We implemented a new sample approach procedure with this updated configuration (see APPENDIX I.A and I.B for details). Briefly, we approach the surface with a NanoScope IIIa controller to avoid the implementation of additional step motor drivers, a built-in camera, and a laser diode amplifier. Upon approach, we fully retract the scanner piezo and switch from the NanoScope IIIa controller to SoftdB controller with GXSM software. After switching to GXSM, the scanner re-engages to the surface and experiments can be conducted.

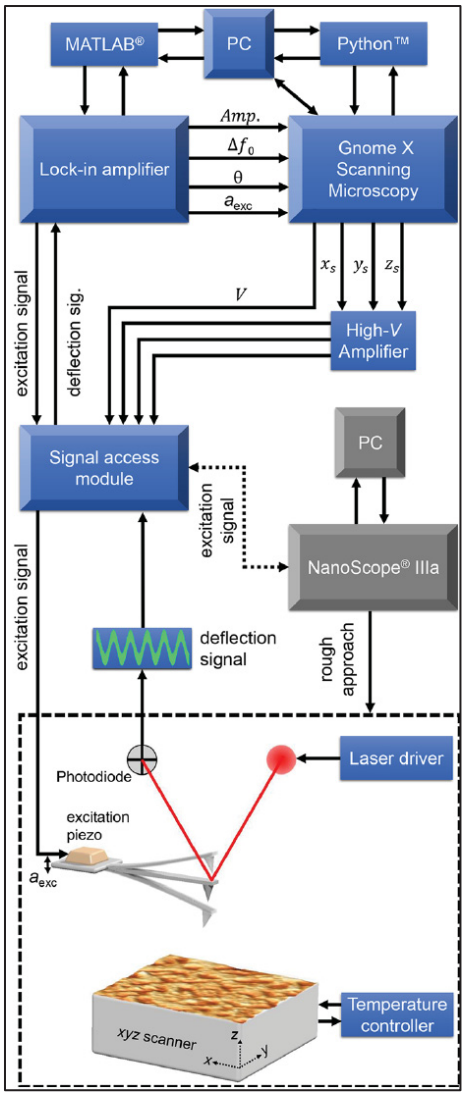

Figure 2.3 The updated control architecture for customized/automated experiments with frequency modulation atomic force microscopy (FM-AFM) capability

Figure 2.3 caption continued: The FM-AFM has been enabled by the lock-in amplifier with phase-locked loop (PLL) capability while experiment customization and automation have been rationalized with the SoftdB controller with Gnome X Scanning Microscopy (GXSM) software. The deflection signal of the cantilever is accessed via the Signal Access Module (SAM). The outputs of the PLL, i.e., the resonance frequency shift, Δf_0, demodulated oscillation amplitude, the phase difference between the excitation and the oscillation signal, θ,

and the excitation signal, a_{exc}, are directed to the GXSM. The small signal outputs of the GXSM (x_s, y_s, z_s) for the piezo motion are amplified with a high-voltage amplifier. The tip–sample bias, V, is defined with GXSM. The amplified piezo signals, a_{exc}, and V are inputs of the microscope and are exchanged via the SAM. The PLL and GXSM have continuous communication with MATLAB and Python for control and automation. We approach to the surface with NanoScope IIIa and then switch to GXSM with a well-defined procedure.

2.4 Results and Discussions

We conducted experiments under ambient conditions to show the performance and capability of the updated control architecture. First, we performed a thermal spectra measurement under ambient conditions to reveal the noise floor of the microscope for a specific cantilever as well as to calibrate for the oscillation amplitude. [160, 161] The Fast Fourier Transform (FFT) of the photodiode signal under thermal excitation has been recorded far from the surface. [162] We recorded and calculated the FFT of the photodiode signal with the plotter of our MFLI by Zurich Instruments (see APPENDIX I.A and I.B for connections). Figure 2.4 shows the voltage noise density of our cantilever under ambient conditions (OPUSTIPS, 4XC-GG, spring constant, $c_z \approx 8.1$ N/m, resonance frequency, $f_0 = 146.620$ kHz, quality factor, $Q \approx 244$, sensitivity ≈ 118.3 nm/V, and noise floor ≈ 0.13 nm/√Hz).

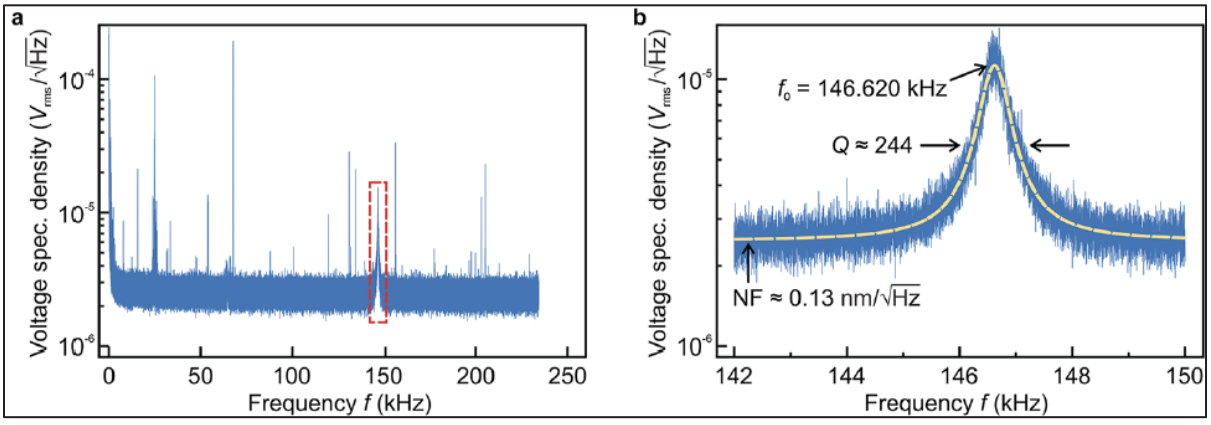

Figure 2.4 Thermal spectra measurement of a cantilever probe

Figure 2.4 caption continued: (a) The complete voltage noise density of the cantilever. (b) The resonance frequency is calculated with a Lorentzian curve (dashed line) to fit the region presented with the red rectangle in (a). Voltage noise density presented in this figure was recorded at room temperature (27 °C) under ambient conditions and averaged 50 times. The bandwidth of the measurement was 469 kHz, and a built-in Hanning window filter has been employed.

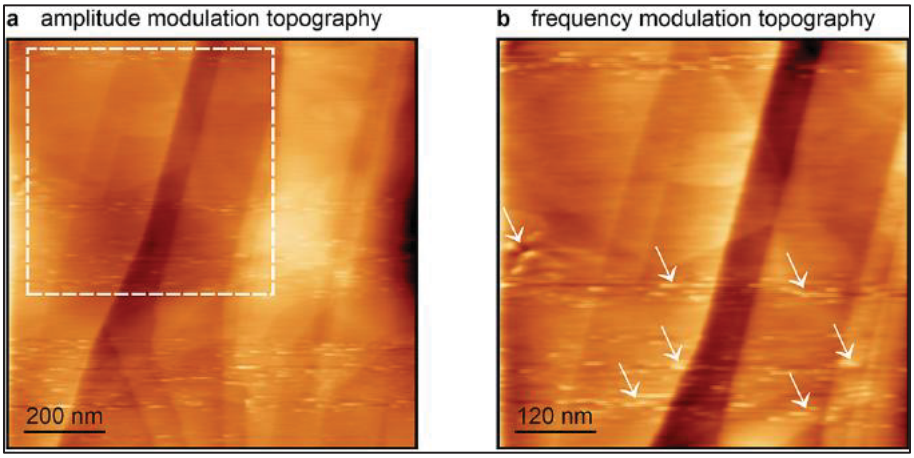

Figure 2.5 Topography measurements of highly ordered pyrolytic graphite (HOPG) under ambient conditions with amplitude modulation (AM) and frequency modulation (FM) atomic force microscopy (AFM)

Figure 2.5 caption continued: (a) AM-AFM-based topography image presents unit cell steps as well as buried steps, which are common for HOPG samples (see the main text for details). (b) We performed FM-AFM-based topography measurements on the region highlighted by the square. Surface adsorbates, shown with arrows, are visible on the freshly exfoliated HOPG sample. The free oscillation amplitude was ~10 nm (peak-to-peak) for AM-based measurements. The oscillation amplitude was kept constant at ~10 nm for FM-based measurements for a resonance frequency shift, Δf_0, set point of −8 Hz. The z-scale of the topography images (from black to white) is 0–2.65 nm for Figure 2.5(a) and 0–1.05 nm for Figure 2.5(b).

We performed topography measurements to illustrate the capabilities of our updated setup. As Figure 2.5 shows, we conducted AM-AFM and FM-AFM topography measurements on HOPG (supplied by NanoAndMore Corp.) under ambient conditions in the same region. We were able to switch the modulation method from AM to FM without full retraction from the surface and successfully image with both. Unit cell steps as well as buried steps, which are common on HOPG samples, are evident. [163-165] The operation of the PLL may suffer from surface adsorbates and the inherently low-quality factor of the oscillating probe due to ambient conditions. As shown in Figure 2.5(a), we first performed AM-AFM measurements over a larger region to confront such instabilities. As presented in Figure 2.5(b), we then conducted FM-AFM-based topography measurement while avoiding clusters of surface contaminants in the region highlighted by the dashed square in Figure 2.5(a). We want to note the stability of FM-based measurement despite measuring under ambient conditions. Moreover, the stability of FM AFM has been preserved over adsorbates, which is inevitable even for freshly exfoliated samples due to ambient conditions. Generally, the operator should pay attention to the surface region and take necessary actions (e.g., automatic tip retraction with a sudden change in the drive signal) to avoid oscillation instabilities and potential tip crashes while operating the microscope with FM-AFM under ambient conditions.

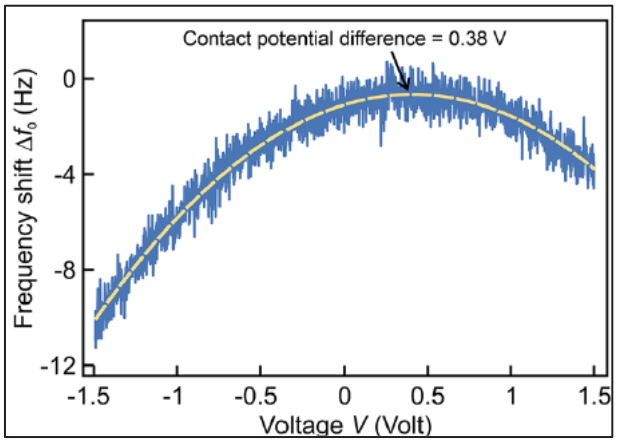

Figure 2.6 Voltage spectroscopy measurement of a rutile-terminated, single-crystal TiO_2 (100) sample at 65 °C

Figure 2.6 caption continued: The resonance frequency shift, Δf_0, vs tip–sample bias, V, measurements were performed 20 nm away from the surface (see the main text for details). The difference between the Fermi levels of the tip and the sample, aka, the contact potential difference, is revealed as 0.38 V with a second-order polynomial fit to experimental data (shown with a dashed line). 2625 data points were recorded under ambient conditions in ~8.3s for the experiment presented in this figure. The oscillation amplitude was kept constant at ~8 nm peak-to-peak (resonance frequency, f_0 = 144.248 kHz, quality factor, $Q \approx 240$).

With the completion of topography measurements, we illustrated the capability of our customized system with spectroscopy experiments. As Figure 2.6 shows, we first performed voltage spectroscopy measurements on a rutile-terminated, single-crystal TiO_2(100) sample (supplied by MSE Supplies LLC). [39] After engaging to the surface with FM-AFM, the tip has been retracted from the surface by a controlled amount, e.g., 20 nm, and the tip–sample bias, V, has been tuned. As detailed elsewhere, the electrostatic interaction is minimized when the difference between the Fermi levels of the tip and the sample, aka, the contact potential difference (CPD), is equal to the tip–sample bias voltage. [106] As Figure 2.6 reveals, the CPD between the TiO_2 sample and a gold-coated cantilever probe is 0.38 V.

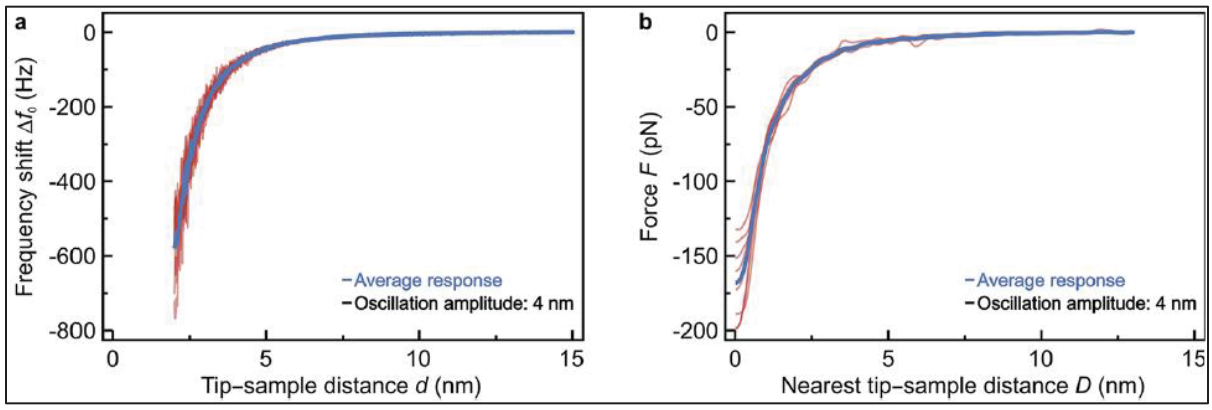

Figure 2.7 Frequency modulation atomic force microscopy-based force spectroscopy measurements of a highly ordered pyrolytic graphite under ambient conditions

Figure 2.7 caption continued: (a) The resonance frequency shift, Δf_0, vs distance, d, measurements were performed. The experiment has been repeated for ten times while keeping the tip around the same lateral position across the sample (blue shows an average of 8 different measurements, and red curves are individual datasets). (b) The measured Δf_0 vs d data were used to reconstruct tip–sample interaction force, F, as a function of the nearest tip–sample distance, D (blue shows an average of 8 different measurements, and red curves are individual datasets). We used a constant oscillation amplitude of 4 nm peak-to-peak with a cantilever with a free resonance frequency, $f_0 = 125.091$ kHz, spring constant, $c_z \approx 5.2$ N/m, and quality factor, $Q \approx 197$.

In addition to voltage spectroscopy measurements, we also performed FM-AFM-based force spectroscopy measurements to access the tip–sample interaction forces. As Figure 2.7 shows, we recorded Δf_0 as a function of tip–sample separation on the HOPG sample (*vide supra*). The tip–sample interaction force was recovered from the experimental data. [166] Figure 2.7 discloses the reproducibility and stability of spectroscopy measurements deep into the attractive regime under ambient conditions.

We also performed FM-AFM-based experiments to reveal the electrical properties of samples to illustrate the capability of the customized system. More specifically, we combined voltage and force spectroscopy measurements to reveal the distance dependence of CPD for a TiO_2 sample (*vide supra*). As Figure 2.8 illustrates, we performed automated force spectroscopy measurements at different tip–sample biases. As detailed elsewhere, the resulting two-dimensional array of Δf_0 as a function of d and V is employed to reveal the distance dependence of the CPD, which is associated with the electrical properties of the sample. [39, 167, 168] We also repeated such measurements at different sample temperatures to access the temperature dependence of the CPD on TiO_2. As explained in detail elsewhere, the intrinsic n-type doping of the TiO_2 sample resulted in a decrease of the CPD (−3.8 mV/○C) with the Fermi level shifted toward the conduction band. [39]

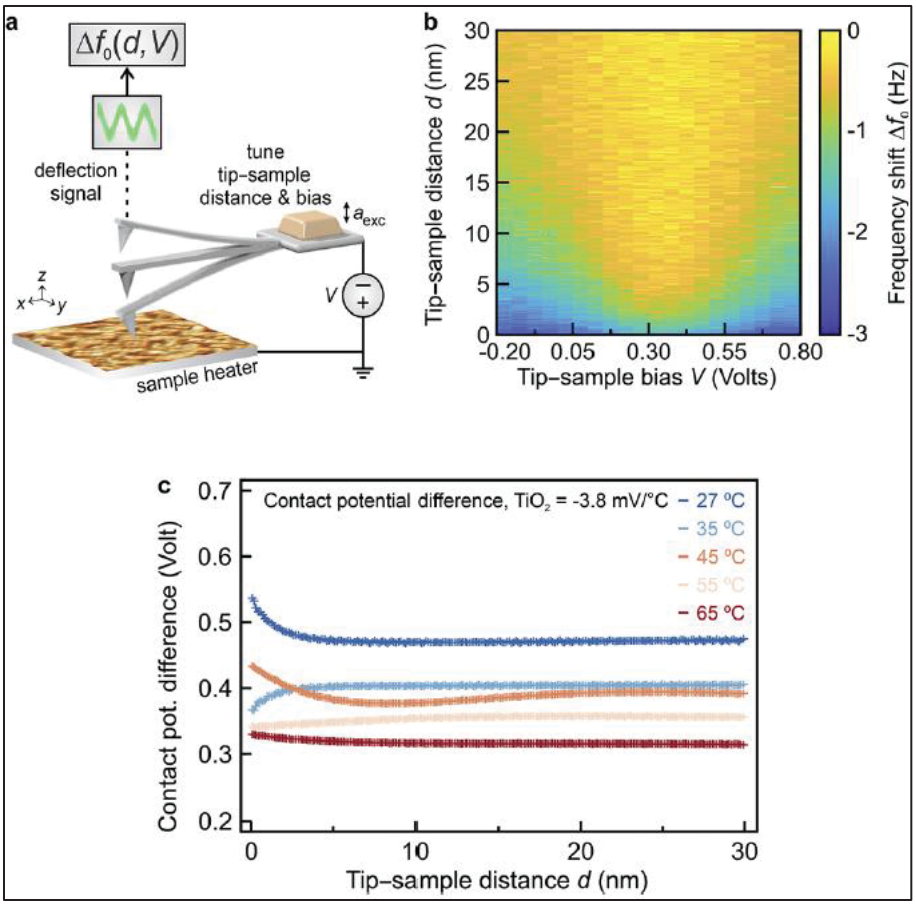

Figure 2.8 Experiments to measure the resonance frequency shift, Δf_0, as a function of the tip-sample distance, *d,* and tip-sample bias voltage*, V*

Figure 2.8 caption continued: (a) The *d* was tuned while the deflection signal was demodulated for Δf_0 at different *V*. (b) This procedure results in a two-dimensional array of Δf_0 as a function of *d* and *V*. Measurements were repeated ten times for each *V* to cross-validate measurements and achieve an adequate signal-to-noise ratio. We used this two-dimensional array to reconstruct the tip–sample interaction force as a function of *d* and *V* to access the distance dependence of the contact potential difference. (c) We repeated the measurement at different temperatures (shown with different colors) to reveal the distance dependence and temperature dependence of a rutile-terminated, single crystal TiO_2 (100) sample. We employed the active drift control module of Gnome X Scanning Microscopy to preserve the sample position of the

sample. We used an oscillation amplitude of 10–12 nm (peak-to-peak) for all our measurements with a cantilever with a free resonance frequency, f_0 = 146.620 kHz, and quality factor, $Q \approx 244$. Experimental results presented in (b) are for a TiO_2 sample at 65 °C.

To further illustrate the capability and stability of our customization for advanced electrical measurements with FM-AFM, we performed time-resolved AFM measurements to reveal the charge carrier dynamics of a TiO_2 sample (vide supra). Figure 2.9 schematically explains that a voltage pulse is applied in proximity to the surface. As explained elsewhere in detail, the applied voltage pulse results in a time-dependent Coulomb interaction, which reflects as Δf_0. [43, 57] The time constant of Δf_0 decay as a function of temperature, i.e., Arrhenius plot, reveals the energy barrier associated with charge carrier migration. With our customized setup, we performed automated, temperature-dependent measurements at more than 64 different points across the surface and repeated the measurement 40 times at each point of the grid to enhance the confidence level of our measurements. We corrected the lateral drift with the active drift correction of GSXM. As our automated measurements were longer than ten hours for each temperature, we also corrected the resonance frequency drift of our cantilever probe with the MATLAB integration of the MFLI lock-in amplifier with phase-locked loop capacity (see APPENDIX I.C for details). More specifically, we measured the free resonance frequency of the cantilever at 20 nm away from the surface and corrected the drift accordingly before we applied the voltage pulse. With our resonance frequency drift correction, the stability of our microscope has enhanced significantly, particularly for measurements at elevated temperatures.

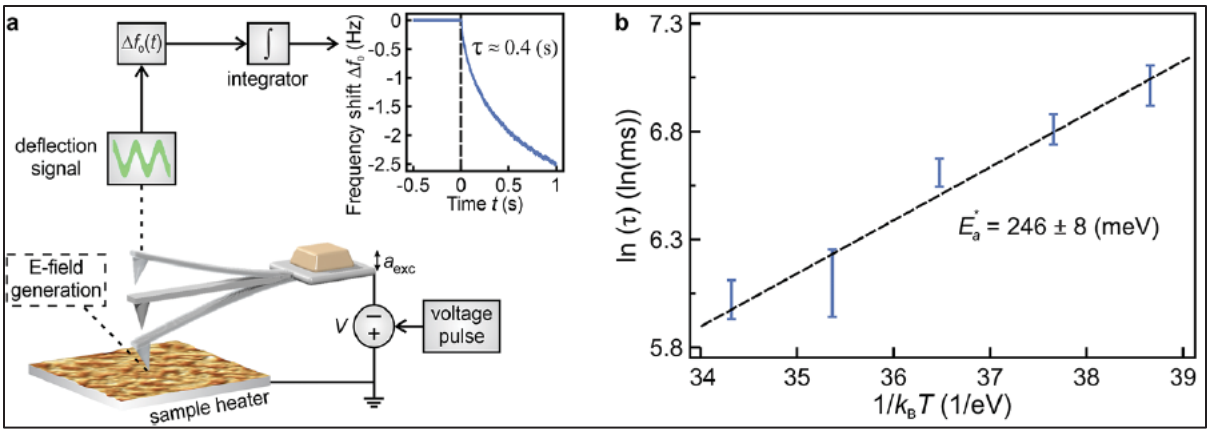

Figure 2.9 Explanation of time-resolved atomic force microscopy measurements and main findings

Figure 2.9 caption continued: (a) A voltage pulse is applied between the sample [a rutile-terminated, single-crystal TiO_2(100) sample] and the cantilever probe. The applied pulse results in a time-dependent Coulomb interaction between the probe and the sample, which leads to a time-dependent resonance frequency shift, Δf_0(t). The time constant of the Δf_0 is related to the dynamics of charge carrier migration. (b) Temperature-dependent measurement of the decay time of the Δf_0 reveals the activation barrier of the charge carrier migration. More specifically, the Arrhenius plot for the natural logarithm of time constant vs $1/k_BT$ (k_B is the Boltzmann constant, and T is the temperature) delivers the effective activation energy as $E_a^* = 246 \pm 8$ meV.

Finally, we performed two-dimensional force spectroscopy measurements across a cluster of three-unit cell steps on HOPG. To this end, we conducted automated topography measurements with Python integration at different resonance frequency shift set points while utilizing active drift control of the GXSM controller, i.e., at different tip–sample separations. For this purpose, resonance frequency shifts were used with 0.28 Hz increments, starting from −23 Hz, i.e., 85 consecutive topography measurements. We minimized the drift/creep along lateral directions (x and y, *vide supra*) by measuring at the same region for more than four hours before data acquisition. A vertical drift rate of 1.2 Å/min was measured during

experiments and corrected in post-processing. The measured topography data have been used to reconstruct tip–sample interaction potential. [148] The vertical and lateral forces acting on the tip can be revealed by the negative gradient of the tip–sample interaction potential. [148] As Figure 2.10(a) illustrates (see APPENDIX I.D for additional measurements), the tip first experiences an attractive lateral force for a step-up motion across step edges, i.e., −75 pN at the smallest tip–sample separation. Upon further approach to the step edge, the tip is repelled by the step edge and experiences a total repulse force, i.e., 109 pN at the smallest tip sample separation. We also conducted measurements along the backward direction, i.e., step- down motion. Figure 2.10(b) shows that the tip is experiencing an assistive lateral force, i.e., 58 pN at the smallest tip–sample separation, for step-down motion upon approach to step edges, which has been reported elsewhere. [163-165, 169, 170] After moving down across step edges, the tip experiences an attractive lateral force as step edges “attract” the tip toward themselves, i.e., −63 pN at the smallest tip–sample separation. The frictional force acting on the tip across the flat regions of the upper and lower terrace is around 20–30 pN and inverse to the scan direction.

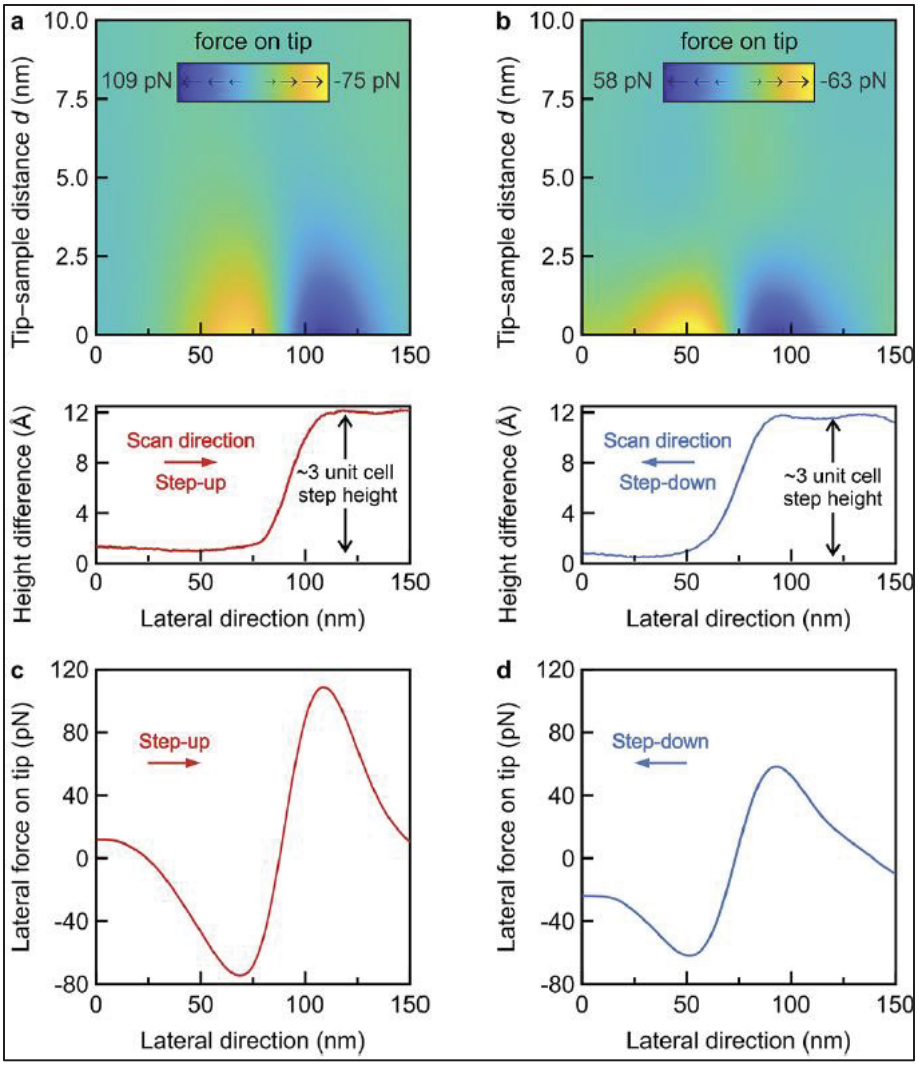

Figure 2.10 Two-dimensional force spectroscopy measurements of highly ordered pyrolytic graphite under ambient conditions across a cluster of three-unit cell steps for forward (step-up) and backward (step-down) directions

Figure 2.10 caption continued: (a) and (c) The tip experiences an attractive force upon approach to the step edge; however, upon further approach to the step edge, the tip experiences a repulsive force during step-up motion. (b) and (d) shows the corresponding step-down motion. The tip has an assistive step-down motion upon approach to step edges. At the lower terrace, the tip is attracted by step edges. On flat regions of the lower and upper terrace, i.e., lateral position at around 0 and 150 nm, the tip experiences a net friction force of around 20–

30 pN. The vertical tip–sample interaction was in the attractive region for measurements presented in this figure. The drift along the z direction (1.2 Å/ min) has been measured during experiments and corrected in the post-processing. We used a constant oscillation amplitude of 10 nm peak-to-peak with a cantilever with a free resonance frequency, f_0 = 130.231 kHz, spring constant, $c_z \approx 7.8$ N/m, and quality factor, $Q \approx 281$.

2.5 Summary and Conclusions

We presented the customization of an atomic force microscopy (AFM) system to enable automated, multidimensional measurements under ambient conditions. The initial setup, VEECO's EnviroScope SPM with a NanoScope IIIa controller, was limited to contact and amplitude modulation-based topography measurements and primitive distance spectroscopy. We customized this setup with new hardware (e.g., Signal Access Module, a lock-in amplifier with phase-locked loop capability, a separate microscope controller, and a high-voltage amplifier) and software integration. Our measurements illustrate the capability of the customized setup for a wide range of applications, including quantitative force spectroscopy and multidimensional (electrical) characterization of samples. More specifically, we illustrated the performance of the customized setup with voltage noise density, frequency-modulation-based AFM topography, voltage and/or distance spectroscopy, time-resolved AFM, and two-dimensional force spectroscopy measurements. We also enhanced the stability of our setup with topography and frequency drift corrections, which significantly improved the quality of long term, automated measurements at elevated temperatures. Finally, we want to note that a new scanning probe microscopy system may deliver some of these capabilities; however, upgrading an operational system is a more economical option. In addition, system upgrade enables aim-specific customization and automation for well-defined experimental needs. We believe that our methodology will be useful for other scanning probe microscopes as similar upgrades/customizations are possible for many (commercial) systems.

CHAPTER 3

MULTIDIMENSIONALITY OF THE CONTACT POTENTIAL DIFFERENCE AT THE NANOSCALE IN INORGANIC OXIDES

Bugrahan Guner[a] and Omur E. Dagdeviren[a]

[a]Department of Mechanical Engineering, École de Technologie Supérieure,
1100 Notre-Dame West, Montreal, Quebec, Canada H3C 1K3

Paper published in *ACS Applied Electronic Materials*[2], July 2022

3.1 Abstract

Inorganic oxide-based sample systems are popular for applications in catalysis, sensing, renewable energy, and fuel cells in which electronic properties play important roles. Environmental conditions, e.g., temperature, can greatly impact the electronic properties and thereby the performance. The lack of basic knowledge of the local variation of electronic properties as a function of temperature limits the fundamental understanding of systems and hampers their robustness. Here, we present temperature-dependent scanning probe microscopy experiments to reveal the variation of contact potential difference (CPD) across different length scales. Our measurements demonstrate that the CPD of inorganic perovskites (e.g., $SrTiO_3$) and metal-oxide semiconductors (e.g., TiO_2) evolve significantly with temperature. We show that CPD variation depends on the locality of the measurement and originates from a thermodynamically driven intrinsic doping state. These results will facilitate a fundamental understanding of the electronic properties of oxides and thus ease emerging technologies, rationalized by engineering temperature-dependent electronic properties.

---

[2] Bugrahan Guner (2022, *p.* 4085−4093)

Keywords: Inorganic oxides, perovskites, metal-oxide semiconductors, temperature-dependent electronic properties, strontium titanate ($SrTiO_3$), titanium dioxide (TiO_2), contact potential difference, scanning probe microscopy

3.2 Introduction and Background

Inorganic oxide-based sample systems (e.g., perovskites, metal-oxide semiconductors (MOS), i.e., semiconductors consisting of metal and oxygen) are widely utilized for a broad spectrum of applications, such as solar cells, [24-27, 171-174] high-temperature superconducting films, [175-180] oxygen separation membranes and advanced oxidation water treatments, [181-186] and memristive devices. [187-190] Their common use can be explained by the competence to tune their electronic and physical properties to the desired application. [51, 54, 191] For this reason, it is vital to understand the properties of perovskites and MOS for a range of conditions and temperatures. Nevertheless, even without any external manipulation, characteristics of such sample systems evolve due to their thermodynamically driven intrinsic doping and vacancy formation. [112, 192] Therefore, revealing the properties of inorganic oxides at the nanoscale as a function of temperature is essential. Temperature-dependent characterization of perovskites and MOS mainly focuses on structural and phase transformation studies, as well as the stability at the device level. [87, 175, 181, 193] Recently, we explained how ergodic (i.e., history-dependent) and non-ergodic (i.e., history-independent) charge carrier dynamics of perovskites change with temperature by revealing the effective migration barrier of intrinsic oxygen vacancies. [41] In another recent work, we experimentally investigated the effect of ultraviolet irradiation on the surface oxygen vacancies and their effect on the bulk charge carrier dynamics for MOS. [35]

Here, we demonstrate the multidimensionality of contact potential difference (CPD, i.e., the difference in the work functions of the gold-coated probe and the sample when they are in proximity and under thermodynamic equilibrium, a.k.a., volta potential) [106] at the nanoscale in inorganic perovskites and MOS with scanning probe microscopy (SPM) measurements. We concentrated on single-crystal, inorganic perovskites (e.g., strontium titanate, $SrTiO_3$) and

MOS (e.g., titanium dioxide, TiO_2) to have the least amount of uncertainty of sample properties. [191] We employed an undoped $SrTiO_3$ and TiO_2, as they are vastly utilized due to their ideal lattice match for similar systems, cost efficiency, stability, and technological and scientific importance. [194-205] Our experiments reveal three important results: (I) the CPD of both $SrTiO_3$ and TiO_2 evolve with temperature, (II) the measured CPD is dominated by the local surface state at small tip-sample separations (i.e., tip-sample distance < 10 nm), and (III) the thermodynamically driven intrinsic doping of the material is the governing mechanism of the variation of the CPD for these sample systems. These results clearly show that care must be given to identify the temperature-dependent change of electronic properties to attain and preserve the desired performance of inorganic oxide-based sample systems.

3.3 Sample Preparation and Experimental Methods

3.3.1 Sample Preparation of $SrTiO_3$

We followed a previously established sample preparation recipe, details of which can be found elsewhere. [41, 206] We employed single-crystal, undoped $SrTiO_3$ (100) samples which were supplied by CrysTech GmbH, Germany. Samples were etched at the company with a buffered HF solution. To avoid fluorine residuals that may have been introduced due to HF etching, samples were cleaned with deionized water. [207] We also annealed samples in an oxygen flux furnace in 1270 K for 30 minutes to remove contaminants, plus heating up and cool down times of 45 minutes each. We controlled the annealing temperature with a thermocouple beneath the sample in the oxygen flux furnace. The sample was introduced in the high vacuum (10-7 mbar) within 10 minutes after cooling to 470 K. The sample was annealed up to 400 K for 30 minutes under high vacuum conditions. Our recipe, i.e., cleaning the sample with deionized water and annealing in 1270 K, ensures the elimination of fluorine residuals. [207] Our sample preparation and annealing conditions maintained a non-conducting $SrTiO_3$ sample and results in atomically flat SrO and TiO_2 surface phases with no evidence of clusters of carbon contamination at the length scale and sample area in which we performed our experiments. [41, 206]

3.3.2 Sample Preparation of TiO_2

We annealed a single-crystal, undoped TiO_2 (100) sample (supplied by MSE Supplies LLC) at 1270K for ten hours, plus heating up and cool down times of one hour each. It is well-known that this previously established sample preparation recipe results in a rutile surface phase with no trace of anatase. [35] Our sample preparation recipe preserved a non-conducting, single-crystal, atomically flat TiO_2 surface phase with no evidence of clusters of carbon contamination at the sample area and the length scale that we performed our experiments. [41]

We concentrated on the rutile surface phase for our TiO_2 experiments. The rutile phase of TiO_2 has advantages over the anatase phase of the material due to its excess stability under ambient conditions, for all temperature ranges. [208-211] Additionally, the tendency of the anatase phase for irradiation-based adsorption of surface radicals influenced the mentioned choice. Encountering surface radical adsorption correlated with irradiation is more probable in the anatase phase. [212, 213] Thus, the rutile phase is preferred over the anatase phase of the sample.

3.3.3 Preparation of Template-stripped Gold Substrate

We prepared the template-stripped gold substrate by using an already established recipe, details of which can be found elsewhere. [102, 103] In summary, template-stripped gold substrate was prepared by employing a silicon wafer. A gold film with a thickness of ~ 100 nm was thermally evaporated (Thermionics Vacuum Products model VE-90) under a vacuum (10^{-5} mbar) at a rate of 0.1 nm/s. The silicon substrate was thoroughly cleaned with acetone, isopropanol, and then ethanol with an ultrasonic cleaner and then dried with nitrogen. Another clean piece of clean silicon was glued on the evaporated gold (EPO-TEK® 377 epoxy, one hour of curing at 150 °C in an oven in the air). The silicon/epoxy/gold sandwich was scraped with a razor blade and then a freshly cleaved gold surface was utilized for measurements.

3.3.4 Scanning Probe Microscopy Measurements

The SPM measurements for $SrTiO_3$ were conducted employing a customized JSPM-5100 system. The microscope was upgraded with a custom-design sample heater stage operating in a high vacuum (i.e., 10^{-7} mbar). The microscope was controlled with the Gnome X Scanning Microscopy (also known as GXSM) control module [159] with active drift control while employing a Nanosurf® EasyPLL Plus for frequency shift detection). We employed a modified Veeco EnviroScope SPM system for our TiO_2 and template-stripped gold samples under ambient conditions. The Veeco EnviroScope has also been controlled with a GXSM control module [159] with active drift control while employing Zurich Instrument's MFLI lock-in amplifier for frequency shift detection. For all our experiments, we utilized gold-coated microcantilever tips by OPUSTIPS (4XC-GG, tip radius = 40 nm, stiffness = 9.0 N/m, resonance frequency = 150 kHz). The standard frequency-modulation atomic force microscopy technique, which relies on the resonance frequency shift, Δf_0, of the oscillation cantilever due to tip-sample interaction, was used. [72] We used an oscillation amplitude of 10 to 12 nm peak-to-peak for our measurements.

3.3.5 X-ray Diffraction Measurements

Temperature-dependent X-ray diffraction (XRD) measurements were conducted with "X'Pert³ XRD from Panalytical" operating with a Cu anode at 8.05 keV as the X-ray source, which provides Cu Kα_1 (λ=1.540598 Å) and Cu Kα_2 (λ=1.544426 Å) for 45 kV tension and 40 mA current inputs with an 'Anton Paar HTK 2000' stage, to assess the existence of phase transfer of $SrTiO_3$ sample. As Figure-A II.1 (see APPENDIX II.A) shows, we conducted temperature-dependent XRD measurements at 25 °C, 45 °C and 85 °C. Successive XRD measurements were performed while keeping the sample and the beam at the same spatial position. The 2θ angle was scanned from 10° to 120° to cover a wide enough range of structural information of $SrTiO_3$. [214-219] As Figure-A II.1 (see APPENDIX II.A) illustrates, our XRD measurements clearly show the absence of any phase transformation between 25 °C and 85 °C. Our result is in good agreement with the existing literature as structural and phase transformations of $SrTiO_3$

are not encountered in the utilized range of temperatures, i.e., for temperatures between 25 °C to 85 °C. [220-226]

3.3.6 Background of Experimental Technique

As details of which can be found elsewhere, the measurement of the CPD with SPM is a well-established experimental technique. [106, 227-229] Here, we briefly explain the overview of CPD measurements. The electrostatic interaction force between the tip and the sample has a parabolic dependence with respect to the total electrical potential. [106, 228, 229] The main idea of CPD measurements is to find the electrical potential difference between the tip and the sample that compensates and minimizes the electrostatic portion of the tip-sample interaction force. [106, 228, 229] There are multiple ways to measure this minimum electrostatic force between the tip and the sample. [106, 228, 229] One of the main methods is to scan the surface while applying a small oscillating tip-sample electrical potential. With the demodulation of the probe's response, the CPD can be assessed. It is possible to implement this oscillating bias voltage approach both for frequency and amplitude modulation atomic force microscopy. [106, 228, 229] Alternatively, Δf_0 can be measured as a function of tip-sample bias voltage, i.e., the so-called bias spectroscopy technique, while the tip is positioned at the same spatial position.

Conventional techniques implemented to measure the CPD with SPM have certain advantages (e.g., ease of implementation, applicability under different environmental conditions, etc.) and disadvantages (e.g., the dependence of tip and probe geometry, difficulty to disentangle the contribution of the probe capacitance, etc.). [106, 228, 229] Beyond these mainstream SPM-based measurement principles, there have been relatively recent SPM-based methodologies to reveal the CPD. [167, 229] For example, the G-mode-based method, which relies on the fast, real-time data acquisition of the oscillation can be implemented. [167] The main advantage of this real-time technique is the time scale of the experimental technique. Alternatively, the CPD can also be measured with the direct measurement of the tip-sample interaction force as a function of tip-sample distance, d, and tip-sample interaction potential, V. [167, 168, 230] This technique is also known as the force-volume technique, which has originally been developed

by Stomp, and details can be found at ref. [168]. We utilized the force-volume technique in this work, which was successfully implemented for different sample systems. [167, 168, 230] As illustrated in Figure 3.1, the probe is kept at the same spatial position, while d and V are tuned successively. As a result, Δf_0 as a function of d and V is measured. The experimental data, Δf_0 as a function of d and V, was used to recover the tip-sample interaction force. [166] We repeated the experiment at least at three different positions to verify the reproducibility of the measurement results (*vide infra*).

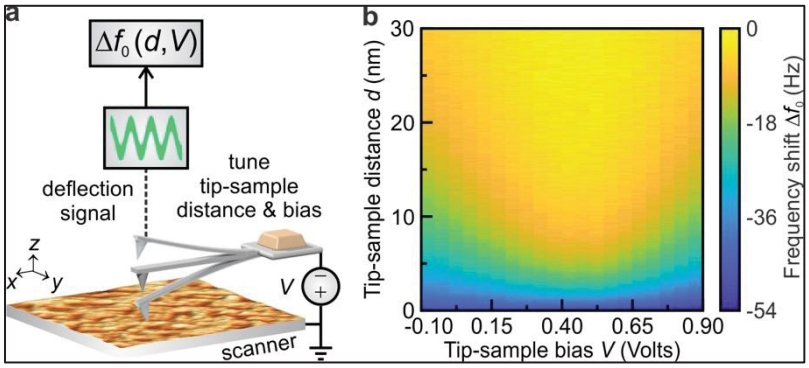

Figure 3.1 Schematic explanation of the experimental procedure to measure the resonance frequency shift, Δf_0 as a function of tip-sample distance, d, and bias voltage, V

Figure 3.1 caption continued: (a) The distance was tuned while the deflection signal was demodulated for Δf_0. The measurement was repeated by changing V 0.05 Volts. (b) This procedure leads to a two-dimensional array of Δf_0 as a function of d and V. Measurements were repeated ten times for each V to achieve an adequate signal-to-noise ratio and cross-validate measurements. We utilized the active drift control module of Gnome X Scanning Microscopy to preserve the sample position of the sample. We used an oscillation amplitude of 10 to 12 nm peak-to-peak for all our measurements. The experimental data presented in this figure was recorded on $SrTiO_3$ at 55 °C.

As Figure 3.2a illustrates, we reconstructed the tip-sample interaction potential. [166, 231] The numerical derivative of the reconstructed tip-sample interaction potential as a function of d

was used to calculate the tip-sample interaction force, F, as presented in Figure 3.2b. It is expected that the conventional force reconstruction technique does not result in an unphysical tip-sample interaction force, as we utilized large oscillation amplitudes. [75]

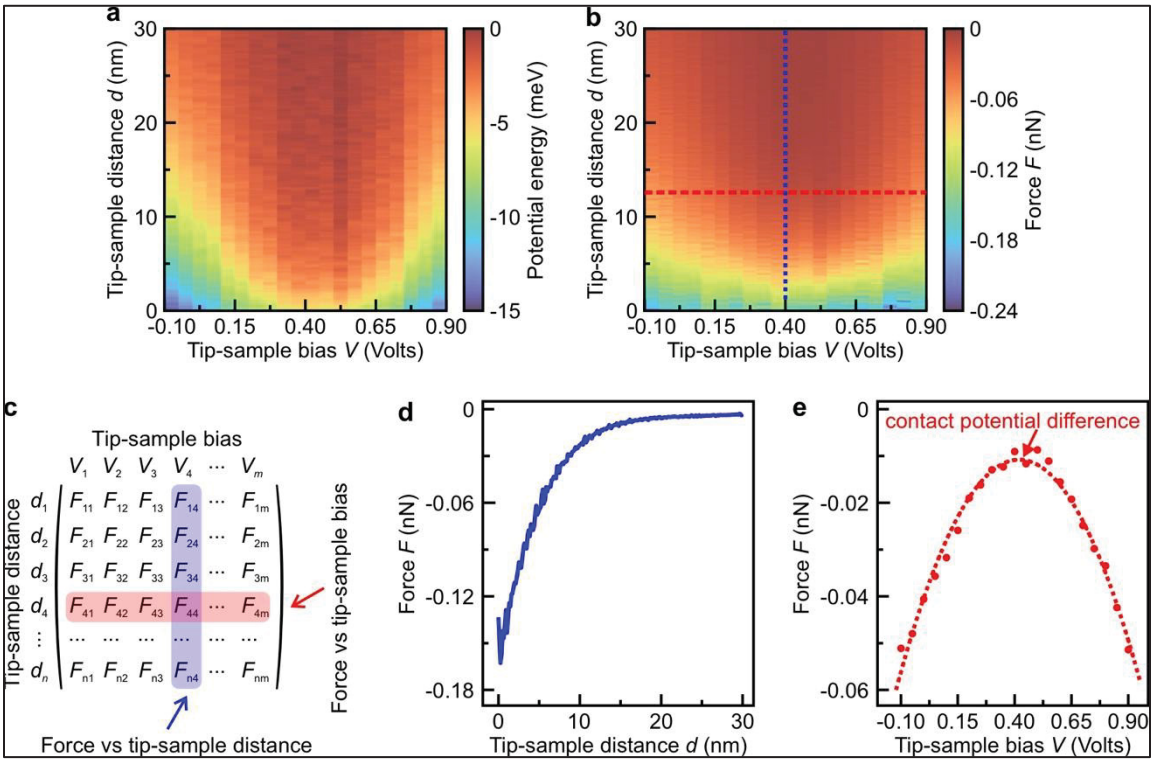

Figure 3.2 Mathematical assessment of contact potential difference (CPD) with tip-sample spectroscopy measurements

Figure 3.2 caption continued: (a) The resonance frequency shift, Δf_0, as a function of tip-sample distance, d, was used to recover the tip-sample interaction potential as a function of d. We repeated this reconstruction procedure for each tip-sample bias voltage, V. (b) The negative gradient of the tip-sample interaction potential as a function of d reveals the tip-sample interaction force, F. (c) Replicating this mathematical conversion for each V results in a two-dimensional array of F. Columns of this array reveals F as a function of d, while rows of this array disclose F as a function of V. (d) An example, the reconstructed F as a function of d for a constant V is shown across the blue dashed line presented in b. (e) Similarly, F, as a function

of *V*, is disclosed across the red dashed curve shown in b. A two-dimensional polynomial was fitted to *F*(*V*) for each d to extract the CPD value as a function of *d*. As explained in the main text, further physical quantities such as the derivative of the tip-sample capacitance, and total tip-sample force are accessible via this fitted polynomial. The experimental data presented in this figure was recorded at 55 °C on $SrTiO_3$.

The recovered *F* forms a two-dimensional array (Figure 3.2c). The columns of this two-dimensional array reveal *F* as a function of *d* at a constant *V* (Figure 3.2d), while the rows show the dependence of *F* as a function of *V* at a constant *d* (Figure 3.2e). The total *F* superimposes chemical, long-range van der Waals, and capacitive forces between the tip and the sample. As Figure 3.2e discloses, *F* as a function of *V* has a parabolic dependence. Therefore, it is possible to fit a second-order polynomial to *F* (i.e., $F(V) = aV^2 + bV^2 + c$), as detailed elsewhere. [168] For this reason, the measurement of the total force and its parabolic dependence, as presented in Figure 3.2e, can reveal important physical quantities. As explained in detail in ref [168], the coefficients of this second-order polynomial deliver the gradient of the tip-sample capacitance (i.e., $\frac{\partial C}{\partial d} = 2a$), CPD (i.e., $V_{CPD} = {}^{-b}/_{2a}$), and the contribution of chemical forces and long-range forces to the total tip-sample interaction force (i.e., $F_{other} = c\,{}^{-b}/_{2a}$).

There are different SPM-based measurement methodologies in order to reveal the CPD of sample systems (*vide supra*). [106, 227-229] The oscillating *V* approach, i.e., a small oscillating tip-sample bias is added to a constant component of *V*, is one of the most employed SPM-based measurement techniques to determine the CPD of the sample. To get the CPD as a function of tip-sample distance, the operator must record images of the surface region at different *d*. However, when the oscillating *V* approach is employed, the correlation of CPD with other physical quantities such as total tip-sample interaction force, non-electrical tip-sample interaction force, and tip-sample capacitance will not be easily accessible. In addition, the operator needs to correct the height frequently to adjust for piezo and resonance frequency drifts, and such corrections build up the total duration of the experiment. Another mainstream

SPM-based CPD measurement is conducting V spectroscopy measurements at different d. [106, 227-229] The recorded parabolas, e.g., Δf_0 as a function of V, at different d can technically be used to reconstruct Δf_0 as a function of V and d. This two-dimensional array, like the array presented in Figure 3.2c, can directly deliver the CPD as a function of d and can then be used to reconstruct F as a function of d similar to the mathematical procedure that we employed (*vide supra*). Although V spectroscopy measurement at the same spatial position across the sample at different d has the same mathematical origin and can theoretically deliver the same physical information, the number of V spectroscopy measurements at different d and the necessity of tip-sample separation correction in between each measurement scales up the measurement time, as the operator has to approach and retract from the surface at rates comparable to force spectroscopy measurements to avoid piezo creep and dangerous fast approach to the sample. For these technical and experimental reasons, we utilized the force volume technique.

The main advantage of the force-volume technique is its flexibility to deliver CPD as a function of tip-sample distance. Although this technique offers a robust methodology to deliver CPD as a function of distance, the total measurement time is relatively long compared to a single CPD measurement with the oscillating bias technique or a single V spectroscopy measurement. To achieve an adequate signal-to-noise ratio and cross-validate our results, we repeated the force spectroscopy measurements ten times at each bias voltage. In addition, we increased the tip-sample bias with increments of 0.05 Volts while measuring the bias range of ± 0.5 Volt with respect to CPD. This leads to two hundred and ten force spectroscopy measurements at the same spatial position. Considering it takes around thirty seconds to conduct a single force spectroscopy measurement, the total duration of the experiment is around two hours. We utilized active drift control of Gnome X Scanning Microscopy to ensure measurements at the same spatial position. Finally, we repeated the experiment in at least three different spatial positions for each temperature. We changed the temperature of the sample with increments of 10 °C while controlling the temperature of the sample and the room where we conduct the measurement better than 0.5 °C.

3.4 Results and Discussions

Our temperature-dependent force volume measurements on $SrTiO_3$ show that CPD has a linear dependence with a negative slope with respect to the temperature of the sample, i.e., with increasing temperature the CPD decreases, as shown in Figure 3.3. More specifically, at $d >$ 10 nm, CPD decrease by 3.6 ± 0.1 mV/°C with increasing temperature (Figure 3.3a). It is well-known that undoped $SrTiO_3$ has intrinsic doping due to thermodynamically driven oxygen vacancies (V_O), which reveal free electrons and V_O. [112] With increasing temperature, both the number of n-type (e.g., free electrons in the conduction band) and V_O are expected to increase. The charge state of the V_O can, theoretically, be neutral (V_O^N), +1-charge state (V_O^{1+}), or +2-charge state (V_O^{2+}). It has been shown by different groups that at low electronic conductivity values, V_O^+ vacancies are thermodynamically favoured. [41, 112] We want to note that oxygen vacancies are different from holes in the valance band and are not mobile unless a strong external stimulus is applied to the sample. [41, 51] Towards this end, with increasing temperature, n-type charge carriers, i.e., additional electrons in the conduction band, become available, and as a result, the Fermi level shifts towards the conduction band. The shift of the Fermi level of the sample towards the conduction band decreases the difference between the work functions of the sample and the gold-coated probe, which ultimately results in an inverse dependence of the CPD as a function of the sample. We conducted temperature-dependent X-ray diffraction measurements on $SrTiO_3$, which show the absence of phase or structural transition at the temperature range of our SPM measurements (see APPENDIX II.A). We also want to discuss the potential effect of the desorption of H_2O, OH, and oxygen on the observed variation of CPD measurements. H_2O desorption of $SrTiO_3$ and TiO_2 is expected to happen at a much lower temperature range. [232, 233] In addition, OH desorption of such sample systems has been associated with the interaction of water under ultra-violet irradiation. [35, 234] It has also been previously shown that $SrTiO_3$ and TiO_2 terminated $SrTiO_3$ samples desorb oxygen at much higher temperatures and oxygen concentration does not change even under ultra-high vacuum annealing up to 470 K. [206, 235] Finally, we want to underline that we conducted our $SrTiO_3$ measurements under vacuum conditions, while TiO_2 and template

stripped gold sample measurements were performed under ambient conditions (vide supra). Under ambient conditions and even under vacuum conditions the surface is expected to be covered with monolayers of adsorbates in seconds. As a result, the desorption of H_2O, OH, or oxygen is not a strong candidate for the observed temperature-dependent variation of the CPD. Due to the nonexistence of phase or structural transition and the existence of intrinsic doping, we believe that the temperature-dependent variation of the CPD has a thermodynamic origin for $SrTiO_3$ due to intrinsic doping (*vide supra*).

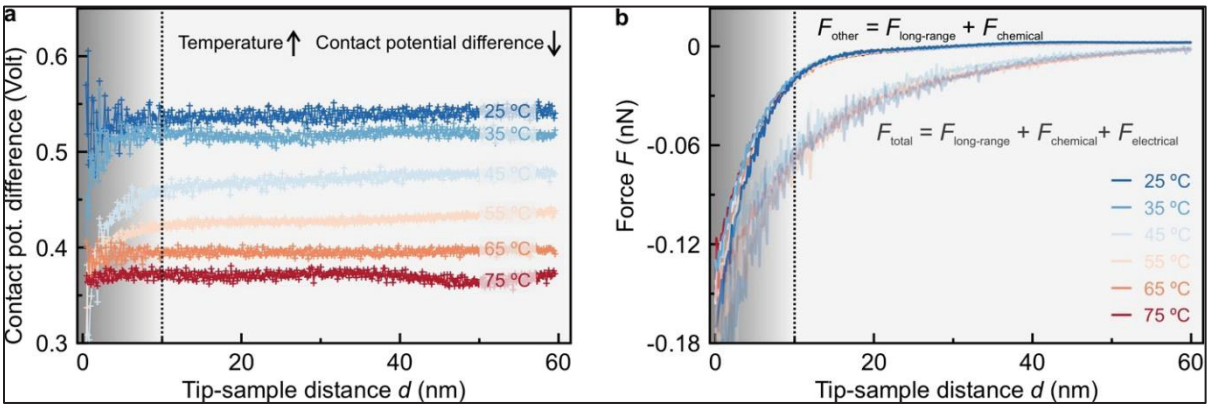

Figure 3.3 Measurement of the contact potential difference (CPD) and the reconstruction of tip-sample interaction force, F, for each CPD measurement for a single crystal $SrTiO_3$ sample

Figure 3.3 caption continued: (a) The measurement of CPD is presented as a function of the tip-sample distance, d, and temperature of the sample. Our experimental results at different temperatures clearly show that CPD decreases with increasing temperature. More specifically, CPD decreases by 3.6 ± 0.1 mV/°C with increasing temperature at $d > 10$ nm. At $d < 10$ nm, shown with a dashed line, the CPD has rather a chaotic dependence on d and temperature due to local variations of F. (b) The total tip-sample interaction force, F_{total}, and contributions of long-range and chemical forces ($F_{other} = F_{long\text{-}range} + F_{chemical}$) have been reconstructed by using mathematical methods described in the main text, to systematically link those with the observed changes in CPD. Our experimental results show that F_{other} starts to have a significantly enhanced contribution to F_{total} at $d < 10$ nm, which is consistent with the observed

chaotic dependence of CPD at this tip-sample separation. For data presented in this figure, we performed our force spectroscopy experiments at three different sample locations while performing ten distance spectroscopy measurements for each tip-sample bias voltage, as explained in the main text.

As presented in Figure 3.3a, at $d < 10$ nm, the temperature and distance dependence of the CPD are less pronounced and rather chaotic. Different phenomena may govern the observed chaotic behaviour of the CPD measurements at $d < 10$ nm. For instance, $SrTiO_3$ (100) will be ill-defined for 1×1 reconstruction, unless cleaved in situ. [236, 237] It is also well-known that our sample preparation recipe reveals both SrO and TiO_2 terminations. [41, 206] A variation of the dominant surface termination may lead to the observed chaotic behaviour for $SrTiO_3$. In addition, the measurements of the TiO_2 sample were conducted under ambient conditions. Due to this reason, the surface is covered with at least a monolayer of adsorbates. These adsorbates may chemically react due to charge injection or diffuse to the electric field at small tip-sample distances, i.e., $d < 10$ nm. [238, 239] As expected, these potential mechanisms, i.e., the change of surface termination, reaction with the surface, or diffusion of adsorbates are less dominant for a simple template-stripped gold sample. Beyond these mechanisms, it is possible that the tip may pick up adsorbates and it may change its electrical properties. However, the reproducibility of measurements and the monitoring of the excitation signal nullify the change due to a tip artifact caused by picking up material from the surface (see APPENDIX II.D). Another alternative explanation is the change of the spatial position across the surface. Although it is certain that the locations of different data sets had different local chemistries, we believe that the drift cannot be the source of the observed variation, as chemically different regions are expected to have different energy dissipation levels, which would have shown up in the excitation channel (see APPENDIX II.D). Finally, significant capacitance changes upon approach may alter the CPD measurements; however, our measurements do not reveal such a significant change in the tip-sample capacitance at small tip-sample separations, i.e., $d < 10$ nm (vide infra).

To further investigate the effect of local tip-sample interaction on the CPD measurement, we calculated the contribution of chemical forces and long-range forces on total tip-sample interaction force, i.e., F_{other}, by using the parameters of the second-order polynomial fit, as explained above (*vide supra*). As Figure 3.3b illustrates, at $d \leq 10$ nm, chemical forces, and long-range forces start to dominate the tip-sample interaction. Normally, long-range forces may have a contribution of van der Waals forces, which presents the interaction well for a continuum. At small distances, however, individual atoms and/or local surface states may dictate the interaction and result in a spatial dispersion effect with the failure of the continuum assumption. [240-242] Although it is still long-range compared to the range of chemical forces, which normally dominate the interaction up to a few Angstroms, [62] the tip-sample distances of less than 10 nm, the local chemical variations are expected to gradually become the governing interaction mechanisms. For this reason, the spatial dispersion effect, i.e., the interaction between individual atoms, and local variations of the surface chemistry may dominate the tip-sample interaction. [240-242] It is well-known that the contribution of different atomic sides to the chemical force may change significantly with distance. [243] Towards this end, the pronounced variation of the CPD at small separations is expected to be associated with the varying contribution of different surface phases and reconstructions, and their interaction with the tip (see APPENDIX II.B for further details).

We want to note that, as both n-type, i.e., electrons in the conduction band and p-type charge carriers, i.e., holes in the valance band, may become available with increasing temperature, the measurement of the CPD at large distances (e.g., $d > 10$ nm) as a function of temperature may be utilized as an experimental technique to trace the charge state of intrinsic carriers. If more p-type charge carriers are induced with temperature compared to n-type charge carriers, the Fermi level will shift towards the valance band and the CPD will increase with temperature. However, if both n-type and p-type charge carriers are induced with equal numbers due to increased temperature in a semiconductor, the shift of the Fermi level, i.e., the variation of the CPD would be dictated by the effective masses of electrons and holes. Nevertheless, for a metal surface with free electrons, the Fermi level is expected to stay still, i.e., no change in CPD shall be observed. As a result, this SPM-based methodology may be an alternative

experimental technique to electron spectroscopy measurements [244] and can be used as a complementary tool for computational models and to reveal the intrinsic doping state of complex material systems and interphases or for non-conducting sample systems. As Table 3.1 summarizes, we conducted experiments on TiO_2 and template-stripped gold samples (see APPENDIX II.B, II.C, and II.D for further experimental data). For a single-crystal TiO_2 sample with a rutile surface phase, the CPD of the sample decreases by 3.8 ± 0.1 mV/°C. TiO_2 is an n-type material with intrinsic doping. [89, 245] For each intrinsic doping, excess electrons in the conduction band become available and as a result, the Fermi level shifts towards the conduction band. [245] The temperature-dependent variation of the CPD of TiO_2 is in good agreement with the $SrTiO_3$, as both sample systems have intrinsic n-type doping states. However, template-stripped gold substrate reveals a much weaker temperature dependence of the CPD between 25 °C and 65 °C, i.e., -0.5 ± 0.1 mV/°C, as for a metal surface, free electrons are the main charge carriers, and the intrinsic doping is absent. The observed weak dependence of the CPD on temperature for the template-stripped gold may be due to the limited thickness of the gold coating both on the tip and the substrate. More specifically, it has been previously shown that the electrical properties of gold films approximate the properties of single-crystal samples at a film thickness of ~ 200 nm. [246, 247] For this reason, the observed temperature-dependent variation of the CPD of the template-stripped gold sample may have contributions both from the substrate of the sample and the limited thickness of the probe's gold coating. As a result, we did not subtract the CPD measurements of the template stripped gold sample with an aim to find the absolute CPD values of our $SrTiO_3$ and TiO_2 samples. The CPD measurement of a gold single crystal may enable disentangling the contributions of the probe and the sample. However, such a measurement is beyond the scope of this work, as it does not change/add to the main findings presented.

Table 3.1 Result summary of the contact potential difference values for sample systems

Sample Type	Intrinsic Doping	CPD Variation
$SrTiO_3$	n-type ([41, 112])	-3.6 ± 0.1 (mV/°C)
TiO_2	n-type ([89])	-3.8 ± 0.1 (mV/°C)
Template-stripped gold	N.A.	-0.5 ± 0.1 (mV/°C)

The total tip-sample capacitance (i.e., C) and its derivative as a function of d ($\frac{\partial C}{\partial d}$) can also be retrieved by using the parameters of the polynomial fit. Figure 3.4a presents the dependence of C on d. As Figure 3.4a shows, at d > 70 nm, C is inversely proportional to d and therefore can be approximated with an effective area of $4.0 \pm 0.6 \times 10^{-14}$ m^2 by using the parallel plate approach. As explained in ref [168], an effective surface area in the order of 10^{-14} m^2 may be deemed high; however, the effective surface area fitted by the experimental data may include contributions not only from the apex of the probe but also from the side of the probe as well as the cantilever. For this reason, it is not easy, if not impossible, to disentangle such secondary contributions with the analytical model of parallel plates. A sphere-plate model can also be used to approximate the observed capacitance at small separations. [168] At d < 10 nm, the value of C saturates (11.8 ± 1.1 aF) and can be assessed as the experimental capacitance between a sphere (radius of the sphere = 106 ± 10 nm) and a flat surface. Although the calculated tip radius approximates the expected tip radius of the commercial tip (~ 40 nm, see Section 2.2 for further details), the effect of the side of the tip apex and long-range capacitive contributions may still affect the measured capacitance value.

In passing, we want to mention that our experiments did not reveal a monotonic temperature dependence of C (see APPENDIX II.E). The main reason for the absence of such a temperature dependence is the assumption behind its calculation, which can be assessed with the numerical integration of the parameter of the polynomial fitting, i.e., $\frac{\partial C}{\partial d} = 2a$. A capacitance value of zero is assumed for this numerical integration at large d, i.e., d ≈ 90 nm. Although C approximates very low values at large d, the actual capacitance can be non-zero and is prone to change due to the total number of effective charge carriers, which may differ at different

locations on the surface due to different surface terminations of $SrTiO_3$ and TiO_2. [41, 206] As a result, the non-zero C and the local charge carrier variations across the surface make the comparison of the total capacitance irrelevant at different temperatures and even at different locations. Figure 3.4b shows that $\frac{\partial C}{\partial d}$ represents a similar variation for each measurement temperature. However, at d < 10 nm (or equivalently F_{other} < -0.01 nano newtons, as shown in Figure 3.4c), the monotonic variation $\frac{\partial C}{\partial d}$ diminishes. The observation of such a chaotic trend at d < 10 nm is consistent with the CPD measurements, which are expected to be dominated by local tip-sample interaction forces, as explained above (*vide supra*). Similarly, for the template-stripped gold sample, the variation of the CPD at close tip-sample separations is much weaker due to the absence of the variation of surface terminations (*vide supra*, also see APPENDIX II.B for further details).

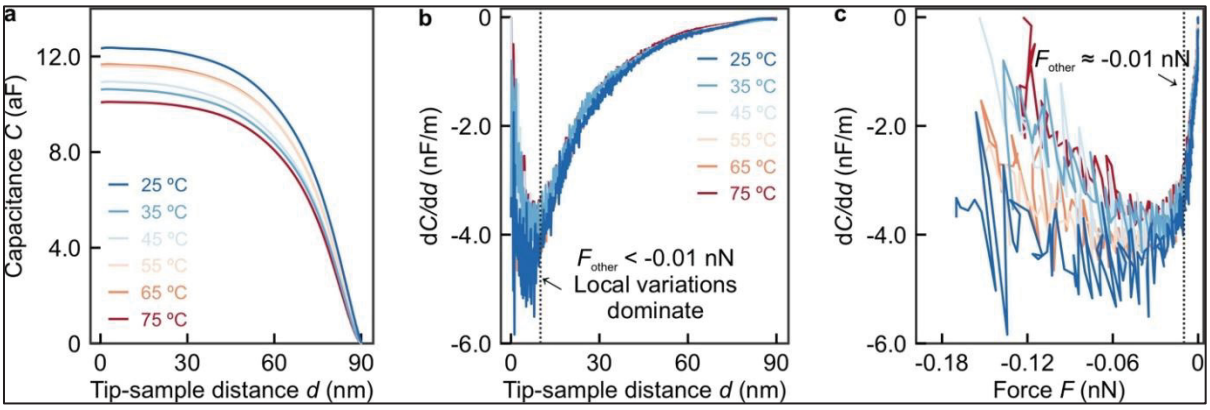

Figure 3.4 Measurement of the tip-sample capacitance, C, and the derivative of the tip-sample capacitance as a function of tip-sample distance, d, and/or F_{other} (i.e., long-range, and chemical forces) for a single crystal $SrTiO_3$ sample

Figure 3.4 caption continued: (a) C was reconstructed with the numerical integration of tip-sample capacitance, $\frac{\partial C}{\partial d}$. Monotonous temperature dependence is absent for C measurements, which may be due to the local variations of charge carriers and surface phases (see the main text for details). (b) $\frac{\partial C}{\partial d}$ vs. d reveals the same trend for each temperature and has rather a chaotic

trend at $d < 10$ nm, which corresponds to $F_{other} < -0.01$ nN highlighted with a dashed line. This chaotic trend is consistent with our contact potential difference measurements. (c) $\frac{\partial C}{\partial d}$ vs F_{other} clearly shows that with the onset of attractive local forces, $\frac{\partial C}{\partial d}$ displays strong variations with d.

3.5 Summary and Conclusions

The temperature-dependent variation of contact potential difference (CPD) was monitored with scanning probe microscopy (SPM) experiments. By measuring the tip-sample interaction force, F, as a function of temperature, tip-sample bias distance, d, and tip-sample bias voltage, V, the temperature-dependent variation of CPD have been assessed for a single-crystal strontium titanate sample ($SrTiO_3$), for a single crystal titanium dioxide (TiO_2), and a template-stripped gold sample. In addition, the variation of the tip-sample capacitance, C, and its derivative with respect to the tip-sample distance, $\frac{\partial C}{\partial d}$, have been revealed. Our measurements clearly show that the CPD of the $SrTiO_3$ and TiO_2 sample decrease with increasing temperature at $d > 10$ nm, as the Fermi level of the sample shifts towards the conduction band with increasing temperature due to excess electrons in the conduction band, while the CPD of the template-stripped gold sample is inert to the temperature variations, as expected. For $d < 10$ nm, both the CPD, C, and $\frac{\partial C}{\partial d}$ as a function of d have rather chaotic variations, due to local F. As such, these findings are directly relevant to the design and understanding of emerging technologies for which inorganic oxides are utilized either as the main compound or substrate of thin films. We believe our results also build up the scientific basis of future SPM experiments involving the critical role of temperature variations in these applications.

CHAPTER 4

FAST AND SLOW TIME-SCALE EFFECTS OF PHOTOINDUCED SURFACE OXYGEN VACANCIES ON THE CHARGE CARRIER DYNAMICS OF TiO_2

Bugrahan Guner[a], Orcun Dincer[a], and Omur E. Dagdeviren[a]

[a]Department of Mechanical Engineering, École de Technologie Supérieure,
1100 Notre-Dame West, Montreal, Quebec, Canada H3C 1K3

Paper published in *ACS Applied Energy Materials*[3], March 2024

4.1 Abstract

The migration of charge carriers (e.g., electrons, holes) in metal oxides, such as TiO_2, plays a vital role in (photo)catalytic applications. Nevertheless, photoinduced surface oxygen vacancies (PI-SOVs), prompted by high-energy ultraviolet irradiation, can significantly alter the dynamics of charge carriers. Here, we performed time-resolved atomic force microscopy measurements to quantitatively deliver the effect of such surface defects on the dynamics of fast (i.e., electrons) and slow (i.e., holes) charge carriers of TiO_2 and TiO_2/gold nanoparticle interface. Our results show that time constants and/or energy barriers associated with the migration of charge carriers change across the sample landscape due to PI-SOVs.

Keywords: metal oxides, titanium dioxide, gold nanoparticles, time-resolved atomic force microscopy, electron dynamics, hole dynamics, high-energy ultraviolet irradiation, photo-induced surface oxygen vacancies

---

[3] Bugrahan Guner (2024, *p.* 2292-2298)

4.2 Introduction and Background

Metal oxides (MO) have been used for a wide range of environmental [11] and industrial applications such as electronics, [12] sensing, [13-15] catalysis, etc. [16, 248] The widespread use of MO exists thanks to the ability to manipulate properties at will. Defect engineering is a common technique to achieve desired properties without radically altering other characteristics, such as biocompatibility, toxicity, etc. [11, 36, 37, 42] Particularly, oxygen vacancy (V_O) defects can act as highly reactive sites, even in small concentrations (i.e., a few ppm), altering the functional properties of MOs. [93, 249, 250] Although V_O has high reactivity, experimental identification of such defect states under realistic conditions, e.g., ambient conditions, is particularly challenging due to low concentrations of V_O. [250] Thus, the experimental investigation of real-time dynamics is essential, as these defects dominate the properties of MO in many catalytic and electronic applications. [113]

The photoinduced surface oxygen vacancies (PI-SOVs), caused by high-energy ultraviolet (UV) irradiation, have been explored for many years. [115, 248] Enhanced Raman spectroscopy under photocatalytic conditions has enabled an in-depth understanding of the formation of such defect states. [13, 14] Although many photocatalytic interactions depend on the dynamics, mobility, and movement of both fast (e.g., electrons) and slow (e.g., ions, vacancies) charge carriers, the fast and slow timescale effects of surface V_O on the charge carrier dynamics and the quantitative effect of metallic nanoparticles (enhancing the stability/density of defects) on these dynamics remain unclear. In a recent work, [35] we explored the effect of PI-SOVs on the hole migration barrier on a pristine TiO_2 surface. More specifically, in the former work, we solely concentrated on how surface V_O alters the dynamics and migration barrier of holes. [35]

Here, we study the effect of PI-SOVs (prompted by high-energy UV irradiation) on fast and slow charge carriers via time-resolved atomic force microscopy (TR-AFM) measurements, while simultaneously exploring the effect of gold nanoparticles (Au-NPs). We conducted our measurements on Au-NP deposited titanium dioxide, i.e., TiO_2, (see APPENDIX.III.A). Our measurements illustrate that the induced VO defects result in a decrease in time constants

associated with the migration of electrons. In addition, we quantified the effect of induced defects on the migration barrier of slow charge carriers, i.e., holes. Our respective measurements show that PI-SOVs lower the migration barrier of holes for both the TiO_2 and TiO_2/Au-NP interface. We believe that the observed statistical difference is caused by the effect of defects over the recombination and trapping mechanisms of fast and slow charge carriers. Our results express the important effect of V_O on charge migration dynamics, which underlines the need for further studies of defects under realistic conditions.

4.3 Experimental Methods

The time-dependent, transient response of photogenerated charge carriers has been examined before. [114, 115, 251] The nature of our TR-AFM measurements does not allow the access to this transient response both due to the timescale of events as well as the amount of the tip-sample interaction force induced by the transient recombination of charge carriers (see APPENDIX.III.B, III.D, III.E, and III.F). [114, 115, 120, 251, 252] Instead, we measure the collective motion of fast (i.e., electrons) and slow (i.e., holes) charge carriers due to an externally applied electric field with and without the UV irradiation of the sample.

We used template-stripped gold, [39, 102, 103] TiO_2 (single crystal, (100) surface, rutile-terminated), [35, 39, 41] and Au-NP deposited TiO_2 samples for our experiments (as illustrated by Figure 4.1, also see APPENDIX.III.A and III.H). TiO_2 is a wide bandgap semiconductor (E_{bg} > 3eV), which absorbs photons within the UV region (λ < 375 nm). [93, 94] As a result, we sealed the microscope to avoid external light. Previous studies have shown that low-energy irradiation (i.e., λ > 280 nm) is not capable of the formation of PI-SOVs, which are very sensitive to the wavelength of surface irradiation. [253] For this reason, in the former work, [14, 35, 44] high-energy UV irradiation (λ = 254 nm and λ = 255) was employed. To this end, we used a high-energy UV source (λ = 255 nm, OP255-10P-SM by Crystal IS) and irradiated the sample with a power density of 1.3 mW/cm^2 (see APPENDIX.III.G).

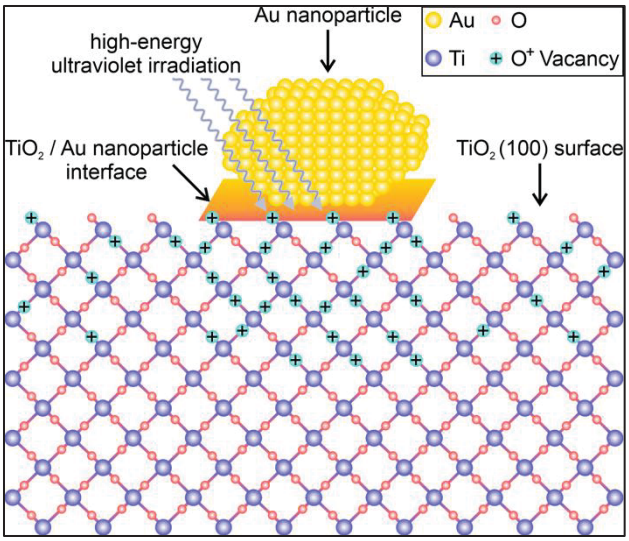

Figure 4.1 The schematic representation of the sample system illustrates the TiO_2 (100) surface, deposited gold nanoparticle (Au-NP), and TiO_2/Au-NP interface formed at the overlapping surface area. Oxygen vacancies are formed due to high-energy surface irradiation and are more stable across the interface

The penetration depth of high-energy UV is estimated to be in the order of 10 - 30 nanometers, [90] even though some photons can reach larger depths. [254] For this reason, the absorption of UV is a surface phenomenon, which alters the charge carrier and defect concentration at and near the surface of the TiO_2 sample. The major change across the surface is introducing surface V_O, which can be either neutral (i.e., V_O^0) or charged (e.g., V_O^{1+}, V_O^{2+}). [255, 256] The charge state of the surface V_O is determined by the formation energy, defect density, and the conductivity of the TiO_2. [35, 41, 112] Former theoretical work has revealed that V_O^+-type oxygen vacancies are the most favourable ones and have the greatest effect on the conductivity of semiconducting TiO_2 samples; crucial to many applications, ranging from electrical transport to photo/electrocatalysis. [255] To this end, V_O^{1+} is expected across the surface within the penetration depth due to surface irradiation, as illustrated in Figure 4.1. Moreover, the TiO_2 forms an interface with deposited Au-NPs across the overlapping section, where induced V_O^{1+} is more stable as explained in detail elsewhere. [44, 257]

4.4 Results and Discussion

We employed two different TR-AFM techniques for fast and slow timescale events. Slow timescale events were measured by conducting classical TR-AFM, which can deliver dynamics of charge carriers with time constants from a few ms up to 100s of ms, as explained elsewhere. [35, 41, 43, 258] To summarize, we applied a voltage pulse between the sample and the tip. The applied bias led to a time-dependent Coulombic interaction, which results in a time-dependent tip-sample interaction force. This force induced a corresponding time-dependent resonance frequency shift, Δf. The time dependence of the demodulated Δf delivers the dynamics of slow timescale charge carriers. Repeating this measurement as a function of temperature reveals the effective activation energy, E_a^*, associated with the collective motion of charge carriers. The migration barrier of a single carrier, E_a, can be extracted by $E_a = E_a^* \times \beta$ equation, where β is the stretching factor of the exponential fit for Δf as a function of time.

For fast timescale events, we used an extended version of sub-microsecond electrostatic force microscopy, originally developed by Giridharagopal et al. [59] and Karatay et al., [58] by employing commercial triggering and detection electronics. Figure 4.2 summarizes the experimental procedure that we used for the measurement of fast time-scale events. Fast time-scale TR-AFM measurements require optimization of the experimental parameters (e.g., tip-sample separation, tip-sample bias, sampling frequency, and number of measurements at each spatial point). [58, 59] As summarized in Figure 4.2a, a tip-sample bias with an amplitude, i.e., V_{bias} = 7 Volts, and time constant, e.g., τ = 20 μs, is applied to the sample at an exact phase of the deflection signal (see APPENDIX.III.B, III.D, and III.E). Similar to the classical TR-AFM, applying a localized electric field at a proximity to the sample (i.e., optimized tip-sample separation = 15 nm, see APPENDIX.III.E for details) causes charge carriers in the sample to move. [258] As presented in Figure 4.2b, the resulting interaction leads to an almost 'instantaneous' variation of the deflection signal due to time-dependent, attractive tip-sample interaction. [58] Figure 4.2c shows that this procedure is repeated and integrated at each measurement point across the surface with a 20 MHz sampling rate to enhance the signal-to-noise ratio (see APPENDIX.III.B and III.D). [58, 59] As represented in Figure 4.2d, the

recorded time versus deflection signal data is filtered with a numerical, 8th-order Butterworth filter, as explained elsewhere. [58, 59] Figure 4.2d also shows that the Hilbert transform is applied to the numerically filtered data, and the time derivative of the Hilbert transform data (i.e., instantaneous phase, Figure 4.2e) leads to the instantaneous resonance frequency shift, Δf, versus time. As Figure 4.2f shows the time to the first frequency shift peak, i.e., t_{fp}, is associated with the movement of fast timescale charge carriers, as explained in detail elsewhere [58, 59] (see APPENDIX.III.B, III.D, III.E, and III.F). It is important to note that the t_{fp} is associated with the charge carrier dynamics; however, it is also a function of the time constant of the applied bias voltage (i.e., τ, see APPENDIX.III.D and III.E). For this reason, the relative variation of the t_{fp} is informative rather than its absolute value (*vide infra*, also see APPENDIX.III.B, III.D, III.E, and III.F).

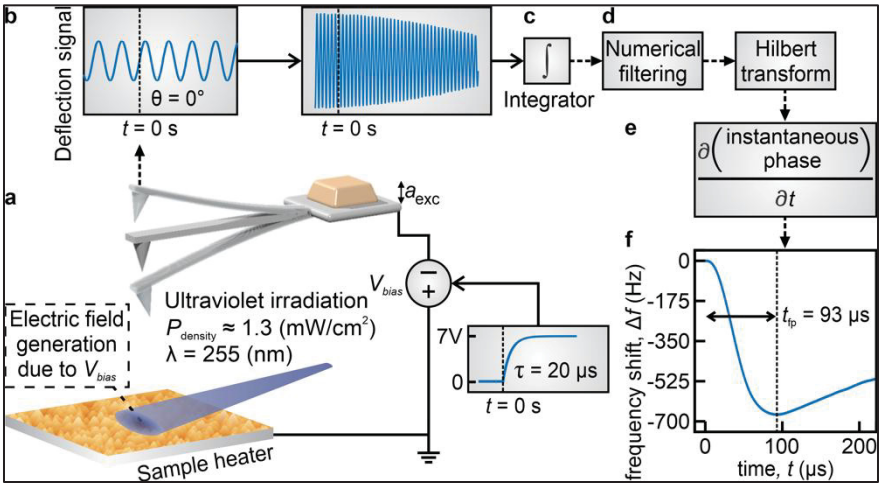

Figure 4.2 Schematic explanation of the experimental procedure for the measurement of fast timescale carrier dynamics

Figure 4.2 caption continued: (a) To measure the time constants associated with the fast charge carriers, a tip-sample bias voltage, V_{bias}, with a well-defined amplitude (7 Volts) and time constant (τ = 20 µs) is applied to the sample at an exact phase difference ($\theta = 0^o$) between the deflection and the excitation signal, a_{exc}. To investigate the effect of photoinduced surface oxygen vacancies, the sample is irradiated with an ultraviolet source (λ = 255 nm, $P_{density} \approx 1.3$

mW/cm^2) and under ambient conditions. (b) The applied bias voltage, V_{bias}, results in an instantaneous change of the deflection signal. (c) The measurement is integrated, i.e., repeated, at the same spatial position across the surface to enhance the signal-to-noise ratio. (d) The averaged signal is filtered with an 8th-order Butterworth filter. The Hilbert transform is applied to the numerically filtered data. (e, f) The numerical derivation as a function of time is applied to the output of the Hilbert transform data (i.e., instantaneous phase) which delivers the instantaneous resonance frequency shift, Δf, versus time, t. (f) The time to the first peak of the resonance frequency shift, t_{fp}, delivers the time constant associated with the charge carrier dynamics. As detailed elsewhere, [58, 59] the measured t_{fp} is a convolution of charge carrier dynamics and τ of V_{bias}. For this reason, the relative variation of t_{fp} is important rather than its absolute value. We used a single crystal, rutile terminated TiO_2 (100) sample for the data presented in this figure.

The fast charge carriers (e.g., electrons) move freely in metallic surfaces (e.g., template-stripped gold); however, in a MO sample (e.g., TiO_2) they encounter frequent recombination centers (e.g., surface, and sub-surface defects), which ultimately results in a shorter mean-free path and slower effective displacement. [105] For this reason, although the time difference between the dynamic properties of fast charge carriers is minuscule on a metallic and semiconducting sample, there is a measurable difference, as Figure 4.3 shows. We also performed measurements to optimize the τ of V_{bias}. It is important to note that $\tau \leq 5$ μs is smaller than one full oscillation cycle of the cantilever. We believe that this amplifies measurement uncertainty and hampers the Δf calculation. However, for $\tau \geq 100$ μs, slow timescale events, e.g., migration of holes, may contribute to the measured signal. Finally, the measured t_{fp} value is inert to the sampling rate for $\tau \geq 20$ μs (Figure-A III.5). For these reasons, we employed an intermediate value, i.e., $\tau = 20$ μs. Besides, the difference of the measured t_{fp} value of fast charge carriers is maximized ($\Delta t_{fp} \approx 3.6$ μs) between metallic template-stripped gold and semiconducting TiO_2 samples for $\tau = 20$ μs.

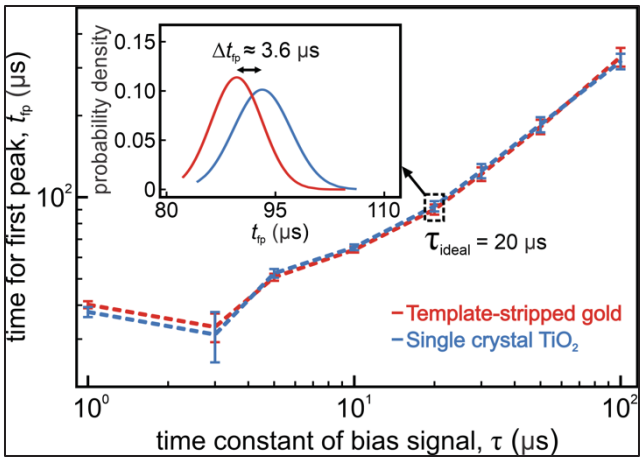

Figure 4.3 The measurements to optimize the time constant of the tip-sample bias voltage, τ

Figure 4.3 caption continued: We performed sub-microsecond time-resolved atomic force microscopy measurements on a template-stripped gold sample (i.e., ideal conductor with metallic surface states) and a metal oxide sample (i.e., TiO_2) to measure the difference of the time for the first peak, t_{fp}. τ= 20 µs avoids sub-cycle and slower timescale events (see text for details). Our measurements also show that, for τ = 20 µs, the difference of t_{fp} values is maximized, $\Delta t_{fp} \approx 3.6$ µs, as shown in the inset. For these reasons, we employed an ideal time constant of 20 µs for our measurements, τ_{ideal}= 20 µs.

Materials such as gold and TiO_2 are influenced by electric fields created by V_{bias}. The resulting strong electric field mobilizes charge carriers both on the surface and in the bulk. Although charge carriers can recombine rapidly (i.e., nanoseconds), [45, 251] adsorbed water molecules [48] and local defect densities can alter charge recombination rates. [94, 259] Charge carriers exist in metal oxides under their intrinsic conditions and their interactions with each other and defects alter their migration barriers. [35, 41, 258] More specifically, the time-dependent electric field within the probing volume of the scanned probe, across the surface towards the bulk of the substrate, leads to a time-dependent tip-sample interaction force, which results in Δf of the oscillating probe as a function of time. [35, 41, 58, 59, 258] For this reason, TR-AFM-based measurements deliver an average within a probing volume, which is determined by the

shielding of the applied electric field in the substrate. Specifically, the shielding of the applied electric field is linked to its magnitude, direction, and permittivity of the material, which is defined by the polarization of charges. [260] For this reason, the amplitude of V_{bias} and tip-sample separation are optimized for TR-AFM experiments.

Electrons, holes, and ions may govern the charge transfer in a material. [105, 261] For materials like $LiFePO_4$ and $LiAlSiO_4$, Li+ ions and electrons dominate the charge transfer. [262-264] Similarly, in $K_2O.2CaO.4SiO_2$ and $Na_2O.GeO_2$ glasses, K+ and Na+ ions are prominent charge carriers. [57] Nevertheless, in TiO_2 electrons and holes are major charge carriers even without photogeneration, [114, 115, 251] as well as ions which can contribute to electrical conductivity, especially for the high oxygen partial pressures. [265] Carrier and defect concentrations, together with the surface phase, determine the charge mobility in TiO_2. [41] The recombination of electrons and holes upon UV irradiation is a rapid effect in TiO_2 with recombination rates in the order of nanoseconds or faster. [114, 115, 251]

Figure 4.4 shows that we imaged the same area of the sample with and without UV irradiation. The blue shift of the t_{fp} values for the same color scale in Figure 4.4b implies a decrease with respect to Figure 4.4a. Moreover, the histogram analysis based on TR-AFM measurements (Figure 4.4c) demonstrates that upon UV irradiation, the time constant associated with electron dynamics (i.e., t_{fp}) decreases across the sample landscape by ~1.3 μs. Nevertheless, the numerical difference of measured t_{fp} values is rather small. For this reason, the significance of the measured difference can only be justified with a statistical test. To this end, we performed the one-sided equality of means test (a.k.a, t-test) with a confidence level of 99.9%. [266, 267] The result of the statistical test robustly illustrated that the measured t_{fp} distributions with and without UV irradiation (i.e., due to PI-SOVs) were statistically different.

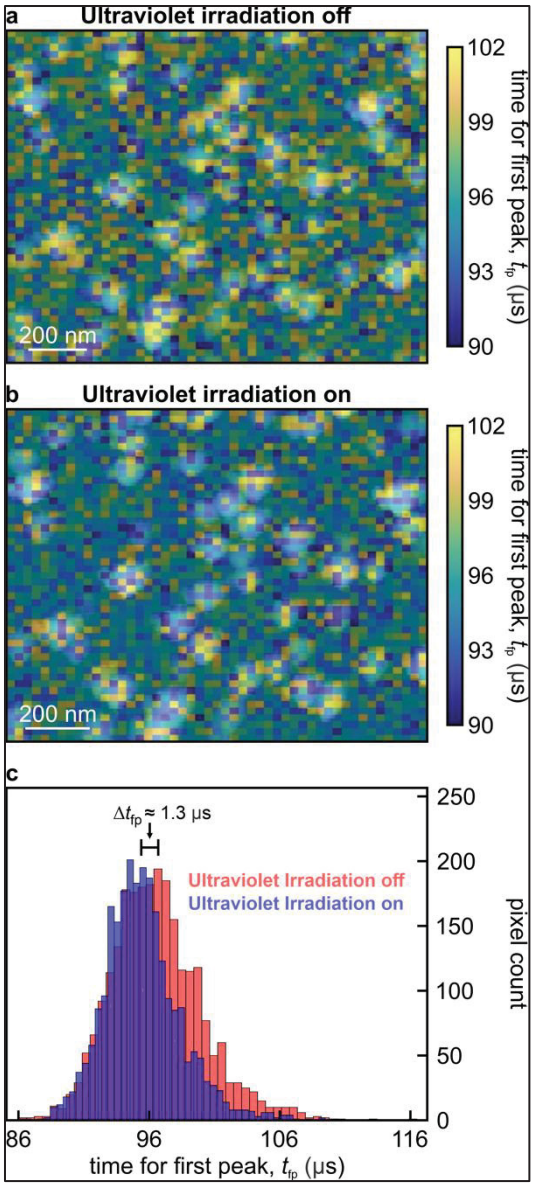

Figure 4.4 Mapping of time constants (i.e., time for the first peak, t_{fp}) associated with the migration of fast charge carriers (i.e., electrons) across the TiO_2 (100) and TiO_2/gold nanoparticle (Au-NP) interface with and without ultraviolet (UV) irradiation

Figure 4.4 caption continued: The t_{fp} values were spatially mapped and superimposed over the topography image of the Au-NP-deposited TiO_2 (a) without UV irradiation and (b) with UV irradiation under ambient conditions. (c) The distribution of t_{fp} values shows that they decrease for both TiO_2 and TiO_2/Au-NP interface differ due to UV irradiation. The observed decrease

is associated with the photoinduced surface oxygen vacancies due to UV irradiation, which is expected to alter the charge carrier's migration and trapping mechanisms (as discussed in detail in the text).

The time-resolved data were superimposed to topography data in Figures 4.4a and 4.4b, which enabled the identification of Au-NPs and TiO_2 regions. (see APPENDIX.III.A and III.H, Figure-A III.2 and III.9). For the TiO_2/Au-NP interface and TiO_2 regions, t_{fp} values are proven to be statistically different (t-test, confidence level = 99.9%). Moreover, our analysis showed that the t_{fp} decrease is more dominant at the TiO_2/Au-NP interface (a drop of ~1.4 μs, from 97.1 ± 0.8 μs to 95.7 ± 0.7 μs) compared to TiO_2 regions (a decrease from 96.4 ± 0.6 μs to 95.4 ± 0.5 μs, i.e., a drop of ~1 μs.). As former studies illustrate, the TiO_2/Au-NP interface forms a Schottky junction which stabilizes PI-SOV formation and reduces their formation energy. [44, 257] Our results imply that the increased PI-SOV density at the interface leads to a statistically more prominent decrease in the time constants of electrons. This decrease can be explained by the increasing number of charge recombination centers. Nevertheless, the TiO_2 region, i.e., regions without Au-NP coverage, has a larger formation energy of PI-SOVs, and the decrease of t_{fp} values is less pronounced compared to the TiO_2/Au-NP interface. In passing, we want to note that, although reported t_{fp} variations upon UV irradiation were mathematically justified, the comparison of t_{fp} values for metallic and semiconducting surfaces is the benchmark for the maximum observable difference. Figure 4.3 discloses the difference of t_{fp} between a metallic and semiconducting surface as ~3.6 μs. Thus, the variation of t_{fp} values of TiO_2 and TiO_2/Au-NP interface due to PI-SOVs is within the expected physical limits. The mobility and the drift velocity of electrons have a direct relationship for an externally applied electric field (see APPENDIX.III.I). Moreover, the drift velocity of electrons is correlated with their decay time constants, i.e., t_{fp}. [268, 269] For this reason, the decrease in the measured t_{fp} of electrons also implies a decrease in their mobility. To this end, one can speculate that the t_{fp} can be used as a gauge to reveal the relative variation of mobility, locally across the sample landscape as a function of defect density.

We performed conventional TR-AFM measurements to reveal the effect of PI-SOVs on the migration barrier of slow charge carriers with the presence of Au-NPs. As Table 4.1 summarizes, the energy barriers associated with the migration of holes decrease both for the TiO_2 and TiO_2/Au-NP interface. The observed decrease in the single charge carrier migration barrier, E_a, can be explained by its relationship with mobility (see Equation AIII.13 in APPENDIX.III.I). The relative positions of defects, e.g., V_O, may promote recombination and an increase in carrier separation. [93, 270, 271] Both recombination and carrier separation can alter mobility, as Equation AIII.13 illustrates. An increase in carrier separation increases mobility. However, it is known that with increased defect density, the mobility decreases in MOs. [105] For this reason, the decrease in E_a is expected to be compensated by other factors including the carrier separation.

It is known that small polarons (electron polarons and hole polarons) are common in TiO_2 originating from oxygen vacancies. [272, 273] Holes as part of small polarons, can be confined in low-energy traps, which can alter their lifetime and mobility. [95, 250, 272, 273] Also, at around room temperature, holes have enough time to recombine for the migration towards stable trapping sites and to localize around defects. [96, 97] To this end, V_O and surface-bridging oxygen can form high-energy traps and alter the dimensionality of the motion of charge carriers, which decreases mobility. [95, 98, 99] Table 4.1 demonstrates that the E_a for the TiO_2/Au-NP interface is higher compared to the pristine TiO_2 region both with and without UV irradiation. This can be explained by the enhanced stability of V_O due to Au-NPs. [44, 257] The enhanced stability of V_O can act as trapping sites which results in a higher E_a at the TiO_2/Au-NP interface. Moreover, Au-NPs can alter the trapping of electrons and holes. [97, 100] In other words, positive self-trapping energy for polaronic hole formation, e.g., small polarons with oxygen vacancies, can further contribute to trapping of charge carriers at the V_O across the TiO_2/Au-NP interface. [101]

Table 4.1 The migration barriers of slow charge carriers (i.e., holes) in TiO_2 and TiO_2/gold nanoparticle (Au-NP) interface and their variation due to photoinduced surface oxygen vacancies (PI-SOVs) prompt by high-energy ultraviolet (UV) irradiation

	Effective Activation Energy, E_a^*	**Stretching factor, β**	**Single Charge Carrier Migration Barrier, E_a**
TiO_2 region (UV OFF)	132.6 ± 27.2 meV	0.64 ± 0.09	85.0 ± 21.4 meV
TiO_2/Au-NP interface (UV OFF)	225.6 ± 7.2 meV	0.65 ± 0.08	145.7 ± 18.4 meV
TiO_2 region (UV ON)	30.6 ± 14.8 meV	0.70 ± 0.04	21.3 ± 10.4 meV
TiO_2/Au-NP interface (UV ON)	147.3 ± 18.8 meV	0.70 ± 0.05	102.7 ± 15.0 meV

Table 4.1 caption continued: We performed conventional time-resolved atomic force microscopy measurements across Au-NP-deposited TiO_2 surface, as a function of sample temperature (25 °C to 65 °C, with 10 °C increments). Spatially correlated measurements were retrieved for both TiO_2 and TiO_2/Au-NP interface, which disclose the effective activation energy (i.e., E_a^*), stretching factor of the exponential fit (i.e., β), and the single charge carrier migration barrier (i.e., E_a) associated with the migration of holes in TiO_2 and TiO_2/Au-NP interface. [35, 41, 43, 258] Our results show that upon UV irradiation, energy barriers associated with the migration of charge carriers decrease across the sample landscape. However, the decrease among the TiO_2/Au-NP interface is less compared to TiO_2 regions. We believe that the enhanced stability of PI-SOVs plays a role in this observation.

4.5 Summary and Conclusions

The effect of photoinduced surface oxygen vacancies (PI-SOVs), due to high-energy ultraviolet (UV) irradiation, in fast (i.e., electrons) and slow (i.e., holes) charge carrier relaxation lifetimes and/or related migration barriers were disclosed in TiO_2 and TiO_2/gold nanoparticle (Au-NP) interface. Our results statistically show that the time constant associated with the migration of electrons decreases upon UV irradiation. Moreover, the decrease in the TiO_2/Au-NP interface is more significant compared to TiO_2 regions due to the enhanced stability of PI-SOVs, which plays a role in charge transfer and recombination mechanisms. Moreover, the mobility of holes decreases upon defect generation due to UV irradiation. To

this end, we believe that the decrease in the migration barrier of holes is compensated by carrier separation, hole trapping, and dimensionality of charge transfer. We also observed a higher migration barrier of holes at the TiO_2/Au-NP interface compared to bare TiO_2 regions. It is expected that the enhanced stability of PI-SOVs and polaronic electron trapping contribute to the higher migration barrier. Our findings are critical to the understanding and the design of emerging (photo)catalytic systems which rely on the migration and mobility of charge carriers in metal oxides. Moreover, we also believe that our results structure the scientific basis of time-resolved measurements that account for the important impact of PI-SOVs in (photo)catalytic applications.

CHAPTER 5

EFFECT OF METHANOL AND PHOTOINDUCED SURFACE OXYGEN VACANCIES ON THE CHARGE CARRIER DYNAMICS IN TiO_2

Orcun Dincer[a], Bugrahan Guner[a], and Omur E. Dagdeviren[a]

[a]Department of Mechanical Engineering, École de Technologie Supérieure,
1100 Notre-Dame West, Montreal, Quebec, Canada H3C 1K3

Paper published in *APL Materials*[4], February 2024

5.1 Abstract

The migration of holes in metal-oxide semiconductors (MOS) such as TiO_2 plays a vital role in (photo)catalytic applications. The dynamics of charge carriers under operation conditions can be influenced by both methanol addition and photoinduced surface oxygen vacancies (PI-SOVs). Nevertheless, the existing knowledge of the effect of methanol as a function of PI-SOVs solely concentrates on the chemical reduction process. For this reason, the fundamental understanding of the time-dependent charge carrier-vacancy interactions with the presence of methanol is impaired. Here, we conducted time-resolved atomic force microscopy measurements to quantitatively disclose the effect of methanol adsorption on the dynamics of hole migration in TiO_2. Our results show that time constants associated with the migration of charge carriers significantly change due to methanol adsorption. Moreover, the energy landscape of the hole migration barrier was dominated and lowered by PI-SOVs. Our findings contribute to the physics of charge carrier dynamics by enabling the engineering of charge carrier-vacancy interactions.

---

[4] Orcun Dincer (2024, *p.* 021125)
Bugrahan Guner's contributions: Experiment design (lead), Sample preparation (equal), Conceptualization (lead); Data curation (equal); Formal analysis (lead); Investigation (equal); Methodology (equal); Software (lead); Validation (equal); Visualization (equal); Writing – original draft (supporting); Writing – review & editing (equal).

5.2 Introduction and Background

The solar-light-driven sustainable energy is a viable alternative for reducing the dependence on fossil fuels. [19-21] Integration of light harvesting and redox functionalities is important for solar energy conversion. [115, 274, 275] Semiconductor photocatalysis initiates upon the absorption of a photon with energy exceeding the bandgap energy, which triggers photoexcitation and an interband transition that gives rise to conduction band electrons and valence band holes. [276, 277] Although the formation of electron/hole pairs occurs swiftly on a timescale of femtoseconds, they rapidly recombine, either within the bulk or at the surface. [48] The low efficiency of semiconductor-based systems is generally attributed to the disparity in lifetimes between photogenerated charge carriers (i.e., femtoseconds to nanoseconds), and the slow kinetics of the redox reaction (i.e., milliseconds to minutes). [49, 50] This difference results in a significant amount of electron/hole recombination. Therefore, it is essential to understand the dynamics of charge carriers, as well as their interaction with surface redox processes, to enhance the performance of photocatalytic systems. [45-47] Metal-oxide semiconductors (MOS) attracted significant interest due to their tunable properties, which enable precise control over surface characteristics and electronic configurations, thereby enhancing their catalytic performance. Nevertheless, TiO_2 has emerged as a focal point in photochemical studies. [45, 278-280] The effectiveness of TiO_2 for applications relies on the interaction between its surface and the adsorbate, influenced by its electronic structures. [87, 281] To this end, recent work investigated charge carrier dynamics of the TiO_2. [35, 39, 45, 48, 282, 283]

Moreover, the surface structure of TiO_2 is strongly affected by organic solvents, surface hydroxyls, and adsorbed water due to the presence of a passivation layer. [259, 284, 285] Being the simplest form of organic alcohol, methanol is utilized in various applications in photocatalytic systems, e.g., hole scavenger, hydrogen production, and reduction of CO_2. [286-288] Even though the interaction between the TiO_2 and methanol has been heavily investigated to reveal its effect on photocatalytic activity, [279, 284, 289-292] a fundamental understanding of the dynamics of the charge carriers is still lacking. Likewise, the efficiency of photochemical

processes is determined by the fraction of photogenerated charge carriers that reach the surface of the catalyst to react with adsorbed electron acceptors and donors. [46, 293] Nevertheless, both methoxy and formaldehyde can be produced due to the photocatalytic reaction of methanol. Their formation kinetics is based on the methanol's tendency to react with photogenerated agents, i.e., electrons and holes. [294, 295] More specifically, the adsorption of methanol molecules on the TiO_2 surface can result in their reduction to methoxy anions through interaction with photogenerated electrons, while holes act as oxidizing agents, leading to the formation of formaldehyde molecules under irradiation. [289, 291] Therefore, it is essential to understand the dynamics of the charge carrier variations under representative conditions, i.e., at a wide range of operating temperatures and under high-energy ultraviolet (UV) irradiation which leads to photoinduced surface oxygen vacancies (PI-SOVs). [14, 35, 44]

Here, we employed time-resolved atomic force microscopy (TR-AFM) to investigate the impact of methanol and UV irradiation on the charge carrier dynamics of a single-crystal, rutile-terminated TiO_2 (100) sample. We have three major findings: (I) The addition of methanol decreased the time constant, and hence, the mobility of the charge carriers. (II) The energy barrier within the system was decreased by UV irradiation; however, the presence of methanol did not alter the corresponding barrier. (III) The reversibility of the charge carrier dynamics was observed upon the termination of UV irradiation. Our findings express the variation of charge migration dynamics of MOS in the presence of methanol as a function of UV irradiation. We believe that our results will pave the way for both quantitative measurements of charge carrier dynamics and their industrial applications.

5.3 Experimental Methods and Sample Preparation

We used a single-crystal, undoped, TiO_2 (100) sample (by MSE Supplies LLC). A well-established procedure was followed, as detailed elsewhere. [35] In brief, we annealed the sample at 1270 K for 10 hours, including ~3 hours for both heating and cooling. Resulting in a rutile-terminated surface, this process yielded atomically flat terraces devoid of clusters of

carbon contamination. [35] Surface stoichiometry and defect density of wide-bandgap semiconductors such as TiO_2 are very sensitive to irradiation (*vide infra*). For this reason, the microscope was sealed to avoid external light. Nevertheless, the surface was irradiated with a built-in halogen lamp. Moreover, it was shown by some previous studies that low-energy irradiation (i.e., $\lambda > 280$ nm) is not capable of the formation of PI-SOVs, which are very sensitive to the wavelength of surface irradiation. [253] In former work, [14, 35, 44] high-energy UV irradiation ($\lambda = 254$ nm and $\lambda = 255$) was employed. For this reason, the high-energy UV component (i.e., $\lambda = 255$ nm) of the light source was measured with a power meter (Slim Photodiode Power Sensor, S130VC by THORLABS) as 2.6 ± 0.1 mW/cm^2, which is a similar power density employed in the former TR-AFM studies. [35] ~2.5 μL of methanol (≥ 99.8% purity, ACS Grade, by Fisher Chemical) was added to the surface of the sample with a micropipette. We waited for 15 minutes for the complete evaporation of methanol before UV irradiation. Darker regions/spots on the TiO_2 surface under a light microscope were evident upon methanol exposure.

Measurements were carried out using a customized VEECO EnviroScope equipped with new hardware and software components, as detailed elsewhere. [61] We used gold-coated microcantilever probes (OPUSTIPS, 4XC-GG, tip radius < 30 nm, stiffness ~9.0 N/m, and resonance frequency ~150 kHz) with an oscillation amplitude of ~8 nm peak-to-peak. We employed the standard frequency-modulation atomic force microscopy technique, which relies on the resonance frequency shift, Δf, of the cantilever due to tip-sample interaction. [72] We performed TR-AFM on the TiO2 sample to measure the charge carrier dynamics. [43] As Figure 5.1 illustrates, the bias voltage, V_{bias}, was applied between the probe and the sample. The V_{bias}, (a voltage step with a peak-to-peak amplitude of 5 Volts) induces a time-dependent Coulombic interaction within the probing volume of the tip across the sample. The time-dependent interaction was accessed by demodulating Δf of the cantilever probe. The exponential variation of Δf with time delivers the time constant associated with the migration of charge carriers, τ^*. The measurement of τ^* as a function of sample temperature, T, reveals the energy barrier associated with the migration of charge carriers, E_a^*. [43] The migration barrier of a single carrier, E_a, can be disclosed by $E_a = E_a^* \times \beta$, where β is the stretching factor

of the exponential fit, which is associated with the collective motion of charge carriers. [35, 43]

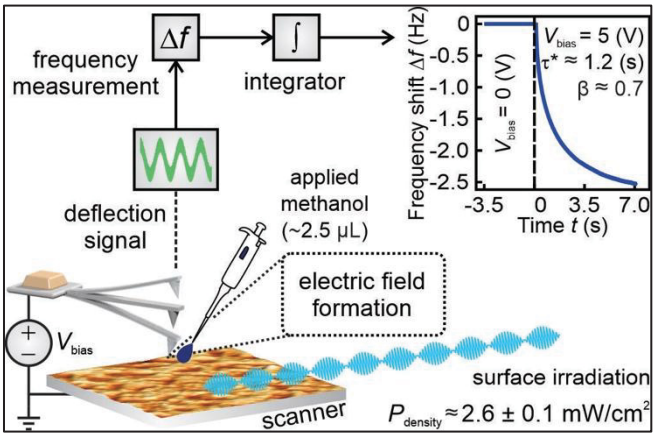

Figure 5.1 Schematic explanation of the experimental setup and the local measurement of charge carrier dynamics as a function of methanol, ultraviolet (UV) irradiation, and temperature of the sample

Figure 5.1 caption continued: A bias voltage, V_{bias}, (i.e., a voltage step with an amplitude of 5 Volts) was applied between the tip and the sample, which results in a time-dependent Coulombic interaction force. This time-dependent force induces a resonance frequency shift, Δf, which was demodulated. We repeated the measurement at each data point to enhance the signal-to-noise ratio. A stretched exponential fit was applied to Δf as a function of time, t. The decay of the stretched exponential fit, τ^*, is associated with the migration dynamics of charge carriers. The stretching factor, β, is linked to the collective motion of charge carriers. To investigate the effect of charge carrier recombination and trapping mechanisms, methanol was applied to the surface and the sample was irradiated by a light source with a high-energy UV component ($P_{density} \approx 2.6 \pm 0.1$ mW/cm^2 at $\lambda = 255$ nm). Repeating measurements as a function of sample temperature reveals the migration barrier of charge carriers.

UV can penetrate the bulk for tens of nanometers; [35, 90] however, some phonons can reach larger depths. [115, 254, 296] For this reason, UV absorption is a surface phenomenon that

alters the charge carrier and defect concentration at and near the surface of the TiO_2 sample by introducing surface oxygen vacancies. [35, 114, 115] Although the transient response of the photogenerated charge carriers was examined before, [114, 115] our measurements solely concentrate on the variation of charge carrier dynamics with the presence of methanol as a function of UV irradiation. The recombination rate of charge carriers is in the order of nanoseconds for TiO_2. [45, 251, 297] However, sample imperfections such as defects, and strongly bounded chemical species as well as interaction with other charge carriers can alter the migration barrier. [41, 259, 298] TR-AFM delivers the dynamics of charge carrier migration within a probing volume, which is determined by the shielding of the applied electric field within the substrate.

5.4 Results and Discussion

Charge transfer in a material can be governed by electrons, holes, and ions. [299-301] Electrons and holes dominate the charge transfer in TiO_2. [114, 115, 251] The charge mobility in TiO_2 is governed by carrier and defect concentrations, together with the surface phase and stoichiometry. [93, 114, 251, 271] The dynamics of electron migration happen in relatively short lifetimes beyond the capability of conventional TR-AFM. [35, 93, 115, 271] For this reason, τ^* measured in our experiments corresponds to the migration of holes, which are orders of magnitude slower, as previously studied in similar sample systems. [35, 41]

Figure 5.2 shows the natural logarithm of τ^* values in milliseconds (i.e., vertical axes) as a function of sample temperature, and illustrates that TiO_2 exhibited an E_a^* of 177 ± 27 meV under dark conditions. TiO_2 is a wide bandgap semiconductor (E_{bg} = 3 eV). [302] For this reason, TiO_2 absorbs light in the UV region (< 420 nm). [303] To this end, we irradiated the surface with a built-in halogen lamp containing high-energy UV components (i.e., λ = 255 nm) to reveal the effect of PI-SOVs (vide supra). Upon UV irradiation, E_a^* decreases to 86 ± 5 meV (~50% decrease compared to dark conditions), while exhibiting a statistically justified (by t-test), robust decrease of ~50% in τ^* values (as can be seen by direct comparison of the

vertical axes of Figure 5.2a and 5.2b). The E_a decreases from 129 ± 21 meV to 62 ± 6 meV (~50% decrease) upon UV irradiation, while the corresponding β values are ~0.73.

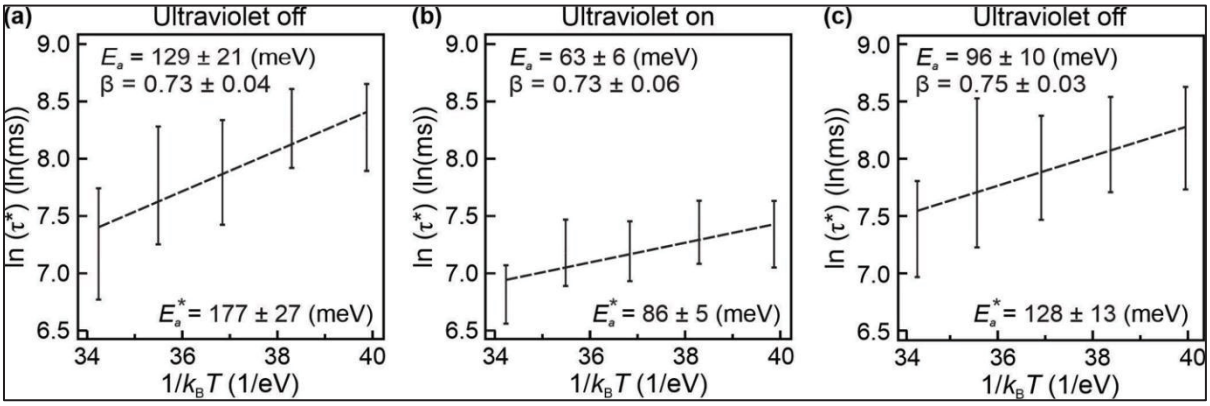

Figure 5.2 Measurement of the effective activation energy barrier of holes in a rutile-terminated, single-crystal, TiO_2 (100) sample

Figure 5.2 caption continued: We measured the time constant associated with the migration of holes, τ^*, as a function of sample temperature, T. The corresponding migration barrier, E_a^*, was obtained from the slope of the Arrhenius plot of the natural logarithm of τ^* in milliseconds, ms, versus $1/(k_BT)$, where k_B is the Boltzmann constant, and T is in Kelvin. The migration barrier of a single carrier, E_a, was disclosed by $E_a = E_a^* \times \beta$, where β was the stretching factor of the exponential fit, associated with the collective motion of charge carriers. (a, b) Our measurements show that E_a^* and E_a decrease with ultraviolet (UV) irradiation. In addition, upon surface irradiation, τ^* decreases for all temperature ranges, which highlights a decrease in the charge carrier mobility. (c) The decrease in E_a^* and E_a recover (partially) over time (i.e., 2 hours) with the termination of the surface irradiation. The vertical error bars show the variation of τ^* across the surface (i.e., 18 different measurement points spaced 40 nanometers apart with 20 repetitions at each point to enhance the signal-to-noise ratio).

The decrease in the charge carrier mobility, μ, is expected due to an increased concentration of defects induced by surface irradiation with UV components. [35, 41] The μ is linearly

correlated with τ^*, i.e., the decrease in τ^* implies a decrease in the μ. Although the decrease in μ is expected and justified by a decrease in τ^*, the decrease in E_a is expected to promote an increase in μ. [41] Former studies [41] show that μ also depends on the distance between individual holes and vacancies as well as the dimensionality of the charge transfer, which was defined as the number of dimensions that charge carriers can move along. Both the number of physical dimensions of the material (e.g., two-dimensional films versus bulk) and local electronic effects such as electron traps can alter the number of dimensions that charges can move. To this end, the dimensionality of the charge transfer and the distance between individual holes and vacancies can also alter μ via low-energy traps and differences in charge recombination and trapping mechanisms induced by PI-SOVs. [95, 304] Nevertheless, positive self-trapping energy for polaronic hole formation and electron trapping effect can contribute to the dimensionality of the process and contribute to the decrease in μ. [101] We believe that these other factors (*vide supra*) compensate for the decrease in E_a.

Formerly, it has been shown that PI-SOVs fully recover after ~90 minutes by employing TR-AFM and Raman studies. [14, 35, 44] Here, our statistical analysis (by t-test) confirms a robust recovery of τ^*, as presented by the vertical axes of Figure 5.2a and Figure 5.2c. In addition, we tested the effect of PI-SOVs on E_a^*. Although τ^* was mainly recovered under dark conditions, our measurements illustrate a partial recovery of the barrier after two hours ($E_a^* = 128 \pm 13$ meV, corresponding $E_a = 96 \pm 10$ meV and $\beta = 0.75 \pm 0.03$). This occurrence may be attributed to the density of surface irradiation with UV components and the necessity of a longer waiting time under dark conditions, as it is well-known that very small concentration variations of PI-SOVs can alter charge recombination and trapping mechanisms. [45, 298]

We performed TR-AFM measurements to quantify the effect of methanol combined with UV irradiation on the charge carrier dynamics of TiO_2. Figure 5.3 illustrates the variation of τ^* (the natural logarithm in milliseconds presented in the vertical axes), E_a^*, and E_a as a function of UV irradiation on a TiO_2 sample with methanol coverage. Although E_a^* and E_a values increase by ~15 and ~12% respectively for pre-covered TiO_2 under dark conditions when compared to results presented in Figure 5.2, τ^* values exhibit a decrease up to ~30% (the natural logarithm

of τ^* values in milliseconds presented in the vertical axes both Figure 5.2 and 5.3) due to exposing the surface to methanol. These statistical differences were justified statistically by the t-test. The statistical decrease in τ^* indicates that methanol alters the hole mobility, which is consistent with methanol's tendency to induce a trapping effect on holes. The decrease in τ^* values was amplified to ~42% by surface irradiation, as can be seen by the comparison of the vertical axes of Figures 5.3a and 5.3b. Nevertheless, the surface irradiation dominates the variation of E_a^* and E_a, ~60% decrease as shown by Figures 5.3a and 5.3b. Moreover, the surface recovers upon the termination of the irradiation as shown in Figure 5.3c, similar to results obtained under the absence of methanol (i.e., Figure 5.2).

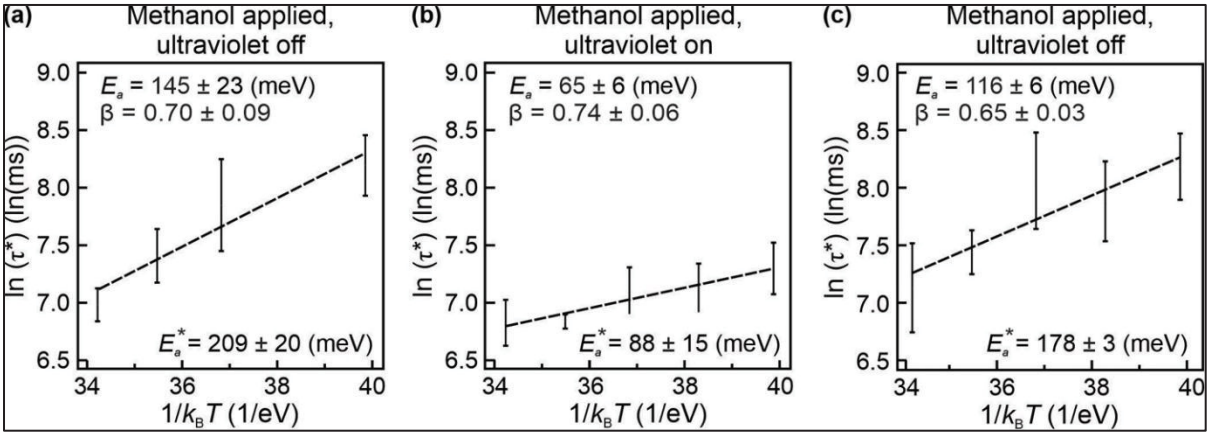

Figure 5.3 Measurement of the effective activation energy barrier of holes in a rutile-terminated, single-crystal, TiO_2 (100) sample in the presence of methanol as a function of ultraviolet (UV) irradiation

Figure 5.3 caption continued: We measured the time constant associated with the migration of holes, τ^*, as a function of sample temperature, T. The corresponding migration barrier, E_a^*, was obtained from the slope of the Arrhenius plot of the natural logarithm of τ^* in milliseconds, ms, versus $1/(k_BT)$, where k_B is the Boltzmann constant, and T is in Kelvin. The migration barrier of a single carrier, E_a, was disclosed by $E_a = E_a^* \times \beta$, where β was the stretching factor of the exponential fit, associated with the collective motion of charge carriers. (a, b, c) Our measurements illustrate that E_a^* and E_a values increase by ~15 and ~12% respectively for pre-

covered TiO_2 when compared to E_a^* and E_a values presented in Figure 5.2a, and the UV irradiation dominates the variation of E_a^* and E_a. Nevertheless, τ^* values decrease up to ~30% for the pre-covered sample under dark conditions. The vertical error bars show the variation of τ^* across the surface (i.e., 18 different measurement points spaced 40 nanometers apart with 20 repetitions at each point to enhance the signal-to-noise ratio).

The stability and mechanism of methanol adsorption are affected by the surface orientation, termination, defect density, and temperature. [279, 289, 305] Methanol can be adsorbed both molecularly and dissociatively on a TiO_2 (001) surface at 200 K. [306] However, at relatively higher temperatures, e.g., room temperature, molecular methanol is desorbed from the surface. [281, 307] Nevertheless, it was shown that surface defects increase the coverage of methanol on the (100) and (110) TiO_2 surfaces. [308]

Previous works indicate that surface methoxy groups interact with uncoordinated Ti_{5c}^{4+} sites, [291, 309-311] and in many cases, primary adsorbate species are methoxy groups on TiO_2 when exposed to methanol. [291, 312-315] Although it was reported that methoxy adsorbates are highly stable at room temperature, it is possible to induce molecular desorption from the surface with increasing temperature. Studies on the thermal stability of methanol on TiO_2 surfaces show that molecular and recombinative desorption of defective rutile TiO_2 (110) surfaces occurs around 320 K – 380 K. [316, 317] However, our statistical analysis shows a decrease in τ^* due to methanol addition (*vide supra*). For this reason, we believe that the methanol did not desorb from the rutile terminated, TiO_2 (100) surface at temperatures up to ~340 K. The observed variation in τ^* can be explained by the reaction of methanol as a hole-scavenging agent. Interaction of methanol with the 5-coordinated titanium (Ti_{5c}) sites results in formaldehyde upon UV radiation. [275, 281, 318] This reaction involves the relocation of dissociated hydrogen atoms to the adjacent bridging oxygen sites and therefore inducing interfacial hole transfer. [291] The adsorption of methanol on the surface in the form of methoxy promotes charge separation by hole trapping in the depletion region and increases the density of accessible surface electrons. [289, 291] While methoxy anions are investigated on the charge separation phenomena, the molecular form of the methanol was reported to be an

effective hole scavenger agent. [319, 320] Especially in the photocatalytic splitting of water into hydrogen by consuming the excess holes, the photogenerated electrons are trapped to the surface of TiO_2 instead of reducing the H^+ ions. [321] Therefore, conversion of methanol in any state, whether reduced (i.e., methoxy), oxidized (i.e., formaldehyde), or chemically adsorbed can exist on the surface simultaneously and potentially contribute to the variation of the charge carrier dynamics. Hence, our focus is to disclose the overarching influence of methanol on the TiO_2 surface, rather than exploring the intrinsic contributions of photocatalytic products of methanol. Disentangling the contributions of the products of methanol upon UV irradiation requires an investigation of temperature-dependent photochemical reactions, which is beyond the scope of this work.

5.5 Summary and Conclusions

In conclusion, our study explored the dynamics of charge carriers in a rutile-terminated, single-crystal TiO_2 (100) sample under the influence of methanol as a function of surface irradiation. Given the pressing need for sustainable energy solutions, our investigation revealed three major findings. First, the application of methanol to the TiO_2 surface resulted in a decrease in time constant (τ^*) and subsequent reduction in charge carrier mobility, emphasizing methanol's significant impact on charge migration. Second, surface irradiation effectively lowered the migration barrier (E_a^*). Nevertheless, the presence of methanol altered this barrier slightly, highlighting the distinct influence of irradiation on the energy landscape of charge carriers. Third, upon termination of the irradiation source, a partial recovery of the activation energy barrier was observed over time, correlated with the reversibility of the charge carrier dynamics. Finally, our analysis of methanol's role in hole mobility as a function of surface irradiation contributes to the understanding of surface interactions and charge carrier dynamics, offering valuable insights for (photo)catalytic applications.

CHAPTER 6

ULTRAVIOLET IRRADIATION PENETRATION DEPTH ON TiO_2

Bugrahan Guner[a], Mohammad Safikhani-Mahmoudi[a], Fengmiao Li[b,c], Ke Zou[b,c], and Omur E. Dagdeviren[a]

[a]Department of Mechanical Engineering, École de Technologie Supérieure, 1100 Notre-Dame West, Montreal, Quebec, Canada H3C 1K3

[b]Department of Physics and Astronomy, University of British Columbia, Vancouver, British Columbia, Canada, V6T 1Z1

[b]Quantum Matter Institute, University of British Columbia, Vancouver, British Columbia, Canada, V6T 1Z4

Paper published in *Communications Chemistry*[5], March 2025

6.1 Abstract

High-energy ultraviolet (UVC) irradiation of metal oxides (MOs, e.g., TiO_2) results in photoinduced surface oxygen vacancies (PI-SOVs), which can change the charge carrier (e.g., electrons and holes) migration dynamics. Although PI-SOVs alter the electronic and chemical properties of MOs, there is no consensus on the penetration depth of the UVC irradiation, which induces PI-SOVs and is an important variable for the design and operation of MO-based systems. Here, we performed optical transmission and time-resolved atomic force microscopy measurements on back-illuminated TiO_2 samples. Our experiments show that the effect of UVC irradiation on MOs can be observed hundreds of micrometers across the bulk, i.e., orders of magnitude larger than previously postulated values. We believe that our findings would be important both for the fundamental understanding of UVC irradiation/penetration and for device design/fabrication processes.

---

[5] Bugrahan Guner (2025, *p.* 83)

6.2 Introduction and Background

Metal oxides (MOs), e.g., TiO_2, are widely used for solar energy, battery, sensor, and biomedical applications. [82-88] The ability to tune their properties (e.g., electrical, chemical) without altering desired characteristics and their relatively low cost are major reasons for their widespread use. [12, 14, 15, 42] To this end, it is known that the ultraviolet (UV) irradiation of MOs plays an important role in many applications. [37, 249, 250] More specifically, high-energy UV (a.k.a., UVC) irradiation can change surface stoichiometry and chemistry by introducing photoinduced surface oxygen vacancies (PI-SOVs) and through resulting chemical reactions (e.g., formaldehyde formation of methanol on Ti_{5c} sites). [14, 35, 40, 44, 273]

TiO_2, a wide bandgap semiconductor (E_{bg} > ~3 eV), absorbs light (λ < ~400 nm). [42, 93, 94] However, PI-SOVs are sensitive to irradiation wavelength and are induced only by UVC irradiation (λ < 280 nm). [14, 35, 44, 253] Although the existence of PI-SOVs is well-supported, there is no agreement on the penetration depth of the UVC. [90, 115, 254, 296, 322-325] Being the nucleus of a decades-old interest, the claims of the penetration depth of UVC range between 10-30 nm up to the micrometer level. [90, 115, 254, 296, 322-325] The uncertainty of the UVC penetration depth not only hinders the complete understanding of UVC-sample interaction but also impedes the longevity of sample systems where TiO_2 is used as an electron transfer and/or UV protection layer. [326] Formerly, Raman spectroscopy and time-resolved atomic force microscopy (TR-AFM) were utilized to explore the effect of PI-SOVs. [14, 35, 38, 40, 44] In our previous works, we performed TR-AFM measurements to understand the influence of UVC irradiation and/or photocatalytic reactions on the charge carrier dynamics of TiO_2 and similar sample systems. [35, 38, 40]

Here, we measured the transmission and the effect of back illumination of UVC (λ = 255 nm) irradiation on a polycrystalline TiO_2 film and a single-crystal TiO_2 sample. Our measurements show two major findings, which are important for the basic understanding of UVC-MO interaction and potentially, for MO-based device design. First, even though the majority of incident UVC is absorbed within the first few tens of nanometers, the UVC irradiation has a

measurable transmission even through 500 μm-thick samples. Moreover, as expected, the measured transmission is inversely proportional to the TiO_2 thickness and the illumination density. Second, the effect of back illumination of UVC has a dominant influence on the charge carrier dynamics, which has been quantified via TR-AFM measurements as a function of UVC illumination density for the single crystal TiO_2 sample. We believe that the observed variation of charge carrier dynamics and its dependence on back illumination power density originates from the PI-SOVs and their collective motion. Our results reveal that the effect of UVC irradiation on MOs can extend through hundreds of micrometers and alter carrier dynamics in TiO_2 across the bulk. We believe our results are important for a fundamental understanding of the interaction of UVC with MOs and for the design of sample systems utilizing MOs in which TiO_2 is employed either as an electron transfer or UV protection layer.

6.3 Experimental Methods and Sample Preparation

6.3.1 Preparation of Polycrystalline TiO_2 Films

46 nm-thick polycrystalline TiO_2 film was prepared on a fused silica glass substrate using molecular beam epitaxy (MBE). [327, 328] The silica glass (by MTI Corporation, UV Grade Fused Silica Glass) was cleaned at 500 °C in a 2.0×10^{-6} Torr O_2 atmosphere for 60 mins in the ultra-high vacuum chamber before the growth. The TiO_2 film was later prepared in the same MBE chamber. The substrate temperature was at 500 °C during the growth. The Ti flux of $\sim 1.1 \times 10^{13}$ atoms$\cdot$cm$^{-2}\cdot$s^{-1} (measured using quartz crystal microbalance) was employed. The O_2 partial pressure was 2.0×10^{-6} Torr during the growth. The film thickness was confirmed by fitting X-ray diffraction reflectivity measurements.

6.3.2 Preparation of a TiO_2 (100) Single Crystal

We utilized a 500 μm-thick, undoped TiO_2 single crystal (by MSE Supplies LLC). We followed an established recipe, as detailed elsewhere. [35, 38, 40, 41, 206] Briefly, TiO_2 crystal was annealed at 1000 °C for 10 hours, in addition to heating and cooling periods (~3 hours

each). This method creates rutile-terminated, atomically flat terraces that are free of carbon clusters (see APPENDIX IV.A for further details). [35] Avoiding large clusters of contamination is important both for the stability of the TR-AFM measurements and to be able to extract intrinsic properties of MBE-grown thin films (*vide supra*) and single crystals.

We used a rutile-terminated surface, as the anatase termination is more susceptible to particles in the air under UVC irradiation and ambient conditions. [208-212] For this reason, adsorbed, undesired particles could impede the characterization of charge carrier dynamics and their variation with PI-SOVs.

Being a slightly more stable configuration compared to the (100) surface, in TiO_2 (110), Ti atoms can have either five or six coordination numbers, while the coordination number of the (100) surface is constant and five. [329-331] Our focus in this work is to understand the penetration depth of the UVC irradiation and its electronic effects across the sample, rather than revealing site-dependent variation of charge carrier dynamics. For these reasons, to eliminate any coordination number-dependent variation of time-resolved properties, we employed a TiO_2 (100) surface as our single crystal sample.

6.3.3 Back Illumination of Samples with Ultraviolet Illumination

We used a constant wavelength (λ = 255 nm), UVC light-emitting diode (LED, OP255-10P-SM by Crystal IS). As Figure 6.1 shows, the UVC source was shielded to ensure that the surface was only back illuminated via the cavity underneath the sample. The power density of the transmitted light was measured with a power meter (Slim Photodiode Power Sensor, S130VC by Thorlabs). The measurement setup was optically isolated to ensure no external light affected the measurement. We tuned the power of the UVC source to understand the effect of illumination density. The distance between the power meter and the sample was kept constant for each measurement. The back illumination of the sample is uniform and covers the entire back side of the sample, as the illumination angle of the UVC diode is 120°, and the optical cavity is ~1 cm away and right above the UVC diode.

We positioned the UVC diode on a large stainless steel heatsink with an embedded thermocouple (PT-1000 with a temperature resolution of 0.01 °C) right under. The maximum power dissipation of the diode is 0.8 Watts, and we did not observe any meaningful temperature variation due to the operation of the LED. Moreover, the temperature in the laboratory was 19.6 ± 0.4 °C, while the corresponding relative humidity level was 38 ± 3% with active temperature and humidity controls to avoid confounding contributions on samples and measured quantities. Finally, as the concentration of PI-SOVs stabilizes within ~90 minutes, we waited for the stabilization of the formation and recovery of PI-SOVs for our measurements. [35, 44]

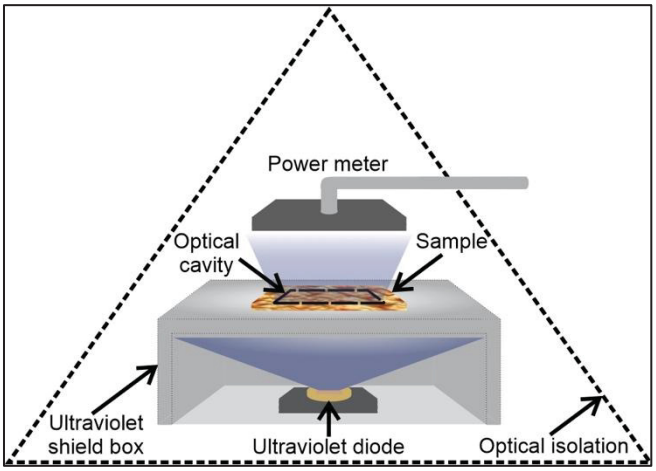

Figure 6.1 Schematic explanation of high-energy ultraviolet (UVC) transmission measurements

Figure 6.1 caption continued: A UVC diode (λ = 255 nm) was employed to back illuminate samples, as a function of metal oxide (MO) thickness and illumination density. The UVC transmission was measured with a power meter. The UVC diode was shielded within a metal box with an optical cavity under the sample, eliminating any UVC leak to the optical power meter. Additionally, the entire measurement setup was optically isolated to prevent any external influence on measurements.

6.3.4 Time-Resolved Atomic Force Microscopy Measurements

Integrated with new hardware and software, we employed a customized VEECO EnviroScope system for our TR-AFM measurements. Details of microscope customization and principles of TR-AFM measurements can be found elsewhere. [61] Briefly, as summarized in Figure 6.2, a voltage pulse, V_{bias}, was applied between the sample and the oscillating cantilever probe after the tip was retracted away (e.g., 15 nm) from the surface. The applied V_{bias} results in a time-dependent Coulombic interaction, which causes the migration of charge carriers. The migration of charge carriers leads to a time-dependent tip-sample interaction force, which induces the time-dependent resonance frequency shift of the cantilever probe, Δf. For conventional TR-AFM measurements, the Δf is demodulated with a phase-locked loop and the stretched exponential function is fitted to the time, t, versus Δf data. [57, 262-264] The time constant associated with the Δf decay, τ^*, corresponds to the charge carrier dynamics of ions, holes, or vacancies depending on the sample system.Schirmeisen, 2004 #220} [77-79, 262-264] This measurement principle was formerly employed for Li^+ transport in $LiAlSiO_4$, K+ transport in $K_2O.2CaO.4SiO_2$ glass, and Na+ transport in $Na2O.GeO_2$ glass, hole migration in TiO_2, and oxygen vacancy migration in $SrTiO_3$. [35, 38, 40, 41, 43, 57, 262-264] The stretched exponential term, β, can have a value between zero and one while representing the collective motion of charge carriers. [77-79] Specifically, decreasing β values imply enhanced collective motion, i.e., stronger particle-to-particle interaction.

We repeated measurements at least 25 different sample locations and at each position 40 times to ensure that the back illumination of the surface covers the entire sample and to enhance the signal-to-noise ratio. [41, 43] For all of our measurements, we implemented a gold-coated, conductive microcantilever (OPUSTIPS, 4XC-GG, tip radius < 30 nm, stiffness ~9.0 N/m, and resonance frequency ~150 kHz). To secure the back illumination, the sample was attached to a shielding box with an opening underneath and positioned directly on the UVC source (*vide supra*). The microscope chamber was also isolated optically. Finally, it was previously shown

that the UVC illumination does not change the sensitivity or the temperature of the oscillating cantilever. [38]

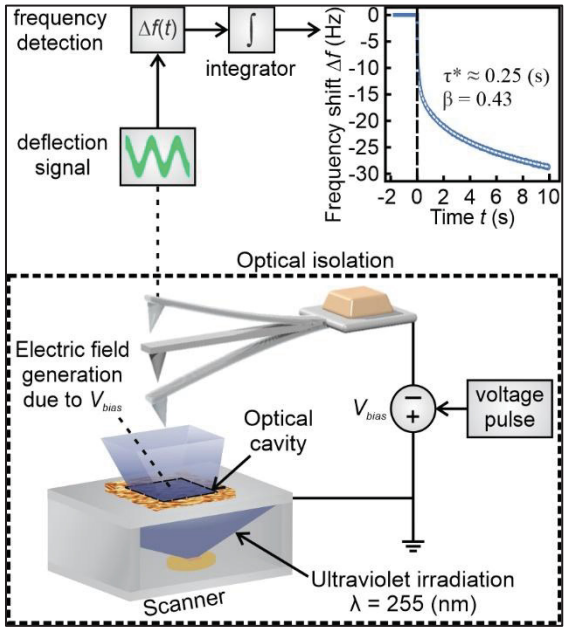

Figure 6.2 Schematic explanation of the time-resolved atomic force microscopy setup and the local measurement of charge carrier dynamics as a function of high-energy ultraviolet (UVC) illumination and metal oxide sample thickness

Figure 6.2 caption continued: A voltage pulse, V_{bias} (e.g., a voltage step with an amplitude of 5 V), was applied between the tip and the sample, which results in a time-dependent Coulombic interaction. The variation in the induced electric field introduces a time-dependent tip-sample interaction force, which leads to the resonance frequency shift of the oscillating cantilever probe, Δf (demodulated with a phase-locked loop). The experiment was repeated on the same lateral position to enhance the signal-to-noise ratio. A stretched exponential fit was applied to the Δf as a function of time, t, as presented with a dashed line. The decay of the stretched exponential fit, τ^*, is related to the migration dynamics of charge carriers. The stretching factor, β, is associated with the collective motion of charge carriers. A UVC source ($\lambda = 255$ nm) was employed to back illuminate samples with different illumination densities to explore the effect of back illumination on charge carrier dynamics. The microscope chamber was optically

isolated from the outside to eliminate any external UVC contributions. The UVC source was also isolated in a metal box to ensure the back illumination of samples via an optical cavity that was at least 50% smaller than the sample area. The data presented in this figure were recorded at room temperature on a TiO_2 (100) single crystal with a back illumination density of 0.47 mW/cm^2.

6.4 Results and Discussion

We performed measurements to reveal the penetration depth of UVC irradiation and its effect on charge carrier dynamics. First, we performed optical transmission measurements via back illumination (*vide supra*) on a fused silica glass substrate, polycrystalline TiO_2 film, and 500 μm-thick, undoped TiO_2 (100) single crystal. The optical transmission measurements of fused silica reveal ~90% of UVC transmission, as classified by the manufacturer. Figure 6.3 summarizes that the optical transmission is inversely proportional to the luminance of the UVC source, i.e., with increasing illuminance, the UVC transmission of both polycrystalline TiO_2 film, and 500 μm-thick, undoped TiO_2 (100) single crystal decreases asymptotically. We believe that this inverse relation with illuminance is associated with the PI-SOV density. It is well-known that UVC irradiation results in oxygen vacancies on the surface (vide supra). [14, 35, 44, 253] With increasing PI-SOV and electron/hole concentration, mid-gap states are introduced, and as our experiments show, the absorption of UVC irradiation increases. [97, 332, 333] Normally, defect engineering is performed in TiO_2 to enhance the optical absorption in the visible spectrum for enhanced photocatalytic performance. [265, 334-337] However, our measurements demonstrate that the optical absorption of TiO_2 increases (i.e., optical transmission decreases) even for UVC irradiation. We also experimentally measured the relation between film thickness and optical transmission. Although the 46 nm-thick TiO_2 film absorbs almost 99% of UVC irradiation, the 500 μm-thick TiO_2 (100) single crystal has a measurable UVC transmission across the sample (0.6 – 1 % depending on the illuminance). For this reason, our optical transmission measurements show that even though a major part of UVC irradiation (~99%) is absorbed within the first tens of nanometers, the rest can penetrate through the entire crystal for hundreds of micrometers. Even though the optical transmission

decreases with increasing illumination density monotonically, at very low illumination density levels, i.e., closer to zero, the error propagation is dominated by the operation principle of the UVC diode, as the power consumption, so the illumination of the diode oscillates for voltages closer to the threshold voltage of the diode.

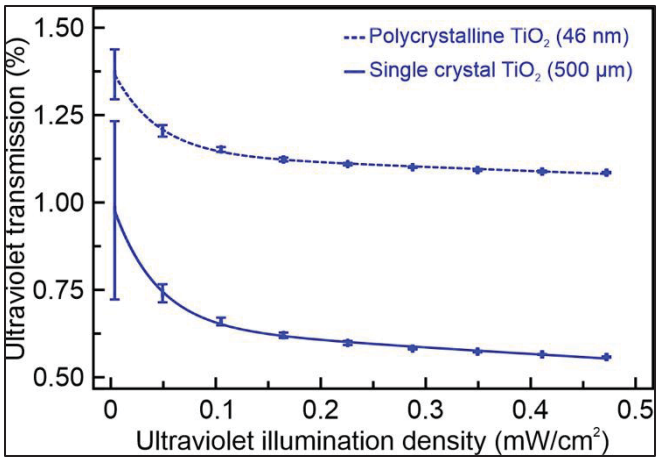

Figure 6.3 High-energy ultraviolet (a.k.a., UVC) irradiation (λ = 255 nm) transmission measurements on a 46 nm-thick polycrystalline TiO_2 film and a 500 µm-thick TiO_2 (100) single crystal as a function of UVC illumination density

Figure 6.3 caption continued: Our measurements on 46-nm thick TiO_2 polycrystalline film show that ~99% of UVC irradiation was absorbed within the first tens of nanometers. However, the optical transmission measurements of the 500 µm-thick TiO_2 (100) single crystal show that the rest of the UVC (~1%) can penetrate through the entire crystal for hundreds of micrometers. Our measurements for both 46-nm thick and 500 µm-thick samples display that with increasing UVC illumination power density, the optical transmission decreases, i.e., absorption increases. We believe that the enhanced absorption is associated with mid-gap states introduced by the photoinduced oxygen vacancies generated by UVC irradiation.

We also performed TR-AFM measurements on a TiO_2 single crystal and a 46 nm-thick polycrystalline film as a function of the back illumination density of UVC irradiation, as shown in Figure 6.4. Surface oxygen vacancies in TiO_2 (Vo) can have multiple different charge states,

where they can be neutral (i.e., Vo^0) or charged (e.g., Vo^{1+} and Vo^{2+}). [255, 256] Former theoretical work showed that the Vo^+ state is the thermodynamically most favourable state and has the greatest influence on the TiO_2 sample conductivity. [35, 41, 255] Thus, we are expecting to mainly induce the Vo^+ vacancies and measure their effect on the charge carrier migration dynamics. [273]

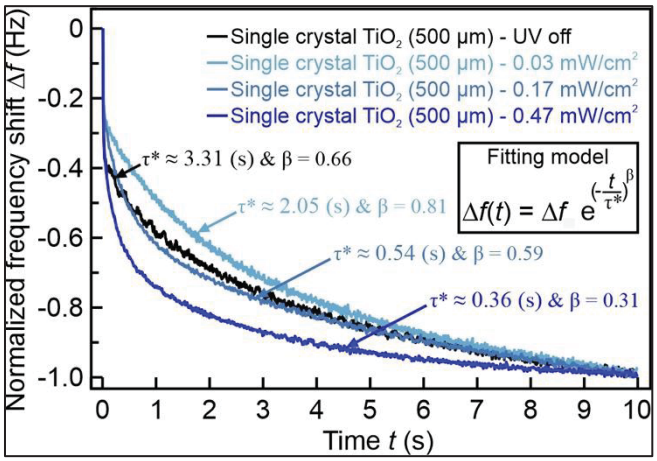

Figure 6.4 Measurement of charge carrier dynamics on a 500 µm-thick, undoped TiO_2 (100) single crystal, which was back illuminated using a high-energy ultraviolet (UVC, λ = 255 nm) source with different irradiation levels

Figure 6.4 caption continued: Charge carrier dynamics were accessed by fitting a stretched exponential function to the resonance frequency shift, Δf, as a function of time, t, $\Delta f(t)=\Delta f \times \exp^{-(t/\tau^*)^\beta}$. The time constant, τ^*, is associated with the decay of the electrostatic interaction within the probing volume and is linked to the charge carrier migration. The stretching factor of the exponential fit, β, is related to the collective motion of charge carriers. We normalized the resonance frequency shifts to enable the comparison of decays for different back illumination levels. Data shows that with increasing back illumination irradiation density, measured τ^* values decrease monotonically. The decrease of τ^* implies a decrease in charge carrier migration velocity and mobility, which can be associated with enhanced vacancy concentration. The variation of β implies that charge carriers interact more collectively at high

irradiation levels. Data presented in this figure was recorded on the same sample region, i.e., the only change between different data points is the UVC illumination densities.

Our TR-AFM measurements on TiO_2 single crystal show that the time constant associated with charge carrier migration, τ^*, decreases with the existence of UVC illumination. The charge transfer of MOs is mainly governed by holes, electrons, and ions. [87, 105, 261, 273] For TiO_2 samples, in addition to a supplemental ion influence, mainly, electrons and holes govern the sample conductivity. [87, 114, 115, 251, 273, 338] Based on the timescale of the measurement (from hundreds of milliseconds to a few seconds), it is expected that we are measuring the migration of slow charge carriers in the sample, i.e., holes as part of small polarons. [38, 95, 224, 250, 273] More specifically, for a single point measurement, τ^* values decrease from 3.31 $\pm$ 0.87 seconds to 2.05 $\pm$ 0.19 seconds even for the lowest illuminance density of 0.03 mW/cm^2. In addition, with increasing UVC illuminance, however, τ^* decreases almost an order of magnitude compared to UVC off case, i.e., decreases to 0.36 $\pm$ 0.08 seconds from 3.31 $\pm$ 0.87 seconds for UVC illumination density of 0.47 mW/cm^2. It is known that the mobility and velocity of charge carriers are linearly correlated to the measured time constant. [38] For this reason, the decrease in the τ^* implies a decrease in the mobility of charge carriers. Moreover, we observed a prominent decrease in β values with increasing UVC illuminance, i.e., β decrease from 0.66 $\pm$ 0.05 (no UVC illumination) to 0.31 $\pm$ 0.06 (UVC illumination density of 0.47 mW/cm^2). The decrease in β values implies that the charge carriers move more collectively with increasing PI-SOV density. Hence, we believe that the enhanced collective motion can be explained by the increased density of charge traps formed by PI-SOVs. [98, 339-341] Nevertheless, as Figure 6.3 shows, ~99% of incident UVC were observed within the first few tens of nanometers, i.e., only ~0.6% of the incident UVC reaches the front side of the 500 μm-thick sample. For this reason, it may be claimed that the transmitted UVC may be responsible for the observed variation of τ^* and β by introducing PI-SOVs on the front side. Even though the transmitted UVC, i.e., ~0.6% of the back illumination density (~2.4 μW/cm^2) may be capable of promoting PI-SOVs on the front side of the sample, the former study has shown that the variation of τ^* is linearly correlated with the illumination density and even for significantly higher front illumination densities, the variation of τ^* was significantly lower.

[40] For this reason, in this study, the strong variation of τ^* (i.e., 10-fold variation) implies that the remaining UVC density is, potentially, not responsible for the observed change. Also, for the back-illuminated sample, the value of β, a parameter for collective motion, decreases by 50%. However, for front-illuminated samples, the variation of β is inert to UVC irradiation. Hence, driven by the concentration variations, we propose that PI-SOVs at the back side of the sample may migrate across the bulk. Nevertheless, back-surface-illuminated X-ray photoelectron spectroscopy measurements or atomic resolution scanning probe microscopy measurements under ambient conditions are required to directly quantify the diffusion of PI-SOVs. However, such measurements are beyond the scope of this work. To distinguish the contribution of PI-SOVs and holes as part of small polarons, we performed complementary back illumination measurements with a low-energy UV (UVA) irradiation ($\lambda = 375$ nm), which only introduces electrons and holes but not PI-SOVs. [14, 35, 44, 253] Our optical transmission measurements for UVA show that, similar to the UVC case, UVA transmission decreases with increasing illumination density asymptotically. However, UVA measurements revealed that the τ^* decreases only 50% upon back illumination of the single crystal TiO_2 sample, and the corresponding β change is only 10%. To this end, the comparison of UVA and UVC measurements also implies that PI-SOVs dominate the dynamic properties of holes as part of small polarons.

We challenged the reproducibility of our TR-AFM results on a single-crystal TiO_2 sample by performing measurements over a span of two weeks under different UVC illumination levels, as Table 6.1 summarizes. To this end, we conducted successive measurements on ten different sample regions. We performed measurements at a minimum of 25 different points at each region and repeated measurements 40 times at each point, i.e., a total of a thousand measurements for each region. Our repetitive experiments on different sample regions and/or under different illumination levels undoubtedly showed that the observed variation originates from high-energy UVC irradiation.

Table 6.1 Time-resolved atomic force microscopy measurements on a 500 μm-thick, undoped TiO_2 (100) single crystal at different ultraviolet (UVC) back illumination levels

High-energy Ultraviolet (UVC) Irradiation of Single Crystal TiO_2 (100) Sample	**Time Constant, τ^*, (ms)**	**Stretching factor, β**
UVC OFF	3077.8 ± 751.4	0.68 ± 0.05
UVC ON – 0.03 mW/cm^2	2053.3 ± 193.7	0.81 ± 0.04
UVC ON – 0.17 mW/cm^2	626.6 ± 71.0	0.65 ± 0.06
UVC ON – 0.47 mW/cm^2	301.4 ± 81.9	0.35 ± 0.07

Table 6.1 caption continued: The data presented in this table were recorded at different regions across the sample in a mixed order on different days. We performed 25 different point measurements with 40 repetitions for each experimental set. Our measurements show that the effect of back illumination of UVC is reproducible across the sample.

Our measurements on 46 nm-thick polycrystalline film show that the τ^* values are significantly smaller compared to the single crystal sample regardless of the UVC irradiation, as shown in Figure 6.5. Former TR-AFM measurements on similar TiO_2 films also disclosed smaller time constants compared to single crystals. [35] We measured the average grain size of our polycrystalline film as 8.7 ± 4.0 nm. The significantly smaller time constants may be associated with the grain size, orientation, and the (degree of) polycrystallinity of the films. [342-348] The grain size and orientation may affect the formation of PI-SOVs and electron/hole pairs, altering the charge carrier migration dynamics. [344, 345, 348] However, the identification of the intrinsic contribution of such effects is beyond the scope of this work.

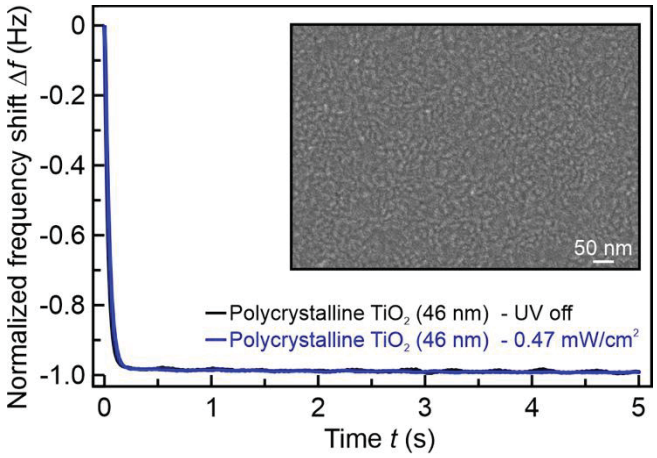

Figure 6.5 Measurement of charge carrier dynamics on a 46-nm thick polycrystalline TiO_2 film grown on a fused silica glass substrate, which was back illuminated with a high-energy ultraviolet (UVC, $\lambda = 255$ nm) source

Figure 6.5 caption continued: The data presented in this table were recorded at different regions across the sample in a mixed order on different days. We performed 25 different point measurements with 40 repetitions for each experimental set. Our measurements show that the effect of back illumination of UVC is reproducible across the sample. Our measurements show that the time constant associated with the charge carrier migration is significantly smaller than the single crystal TiO_2, regardless of the existence of UVC irradiation. As the measured time constant is very close to the detection limit, we do not deliver a numerical value. As shown in the inset, we performed scanning electron microscopy measurements, which revealed that the average grain size has an equivalent circular diameter of 8.7 ± 4.0 nm. We believe that the smaller time constant is related to the grain size, orientation, and degree of polycrystallinity of the film.

Even though oxygen vacancy formation due to UVC irradiation is expected to be a surface phenomenon, as ~99% of incident UVC is absorbed within the first tens of nanometers, our TR-AFM measurements show that the effect of UVC irradiation can penetrate deep into the bulk and can alter electronic properties for hundreds of micrometers across the sample. This result is important not only for the basic understanding of the variation of charge carrier

dynamics due to PI-SOVs in MOs but also for sample systems that employ MOs as a charge transfer layer or protecting layer for underlying photocatalytic activities.

6.5 Summary and Conclusions

We performed optical transmission and time-resolved atomic force microscopy (TR-AFM) measurements on back-illuminated (with high-energy ultraviolet (UVC) irradiation, λ = 255 nm) metal oxide (MO) samples, i.e., a 500 μm-thick, undoped TiO_2 (100) single crystal and a 46 nm-thick polycrystalline TiO_2 film grown on fused silica glass. Our optical transmission measurements show that even though ~99% incident UVC was absorbed within the first tens of nanometers, the residual illuminance (i.e., ~1%) can penetrate through the bulk for hundreds of micrometers. Moreover, we revealed that the optical transmission is inversely correlated with the illumination density. We think that this inverse relation between the optical transmission and the illumination density arises from the enhanced concentration of mid-band gap states prompted by photoinduced surface oxygen vacancies. Our TR-AFM measurements show that the time constant associated with the charge carrier migration is strongly affected by the back illumination density and can decrease almost by an order of magnitude with increasing UVC irradiation density. Moreover, the collective nature of charge carrier migration is more pronounced with increasing irradiation density. Also, the charge carrier migration dynamics and its control are important for other oxides such as $SrTiO_3$ and $KTaO_3$. [349-351] It is important to note that atomic scale identification of oxide-based devices and correlating the measured dynamic characteristics at the interface of different material systems as a function of their intrinsic properties (e.g., bandgap, intrinsic and extrinsic doping, roughness), external stimulation (e.g., temperature variation, chemicals), and transient formation/recovery of PI-SOVs remain to be explored. For this reason, we believe our results will lay the foundation for a more fundamental understanding of UVC penetration and MO-based sample systems.

CONCLUSIONS AND RECOMMENDATIONS

Multidimensional (i.e., location, history, temperature, etc.) measurement and characterization of charge carrier dynamics for renewable energy materials, i.e., metal oxides (MO), e.g., TiO_2, with advanced spectroscopy applications, is a significant attempt to revolutionize renewable energy (e.g., batteries, solar cells, etc.), sensing, and biological applications. In this thesis, complex and dynamic migration features and patterns of MO sample systems have been thoroughly investigated with advanced scanning probe microscopy (SPM) methods. Addressing shortcomings of traditional macroscopically averaged, spatially and/or temporally insufficient methods, this work laid a profound foundation for accurate and extensive charge carrier investigations.

The work in this thesis introduced a step-by-step guideline for upgrading available archaic atomic force microscopy (AFM) setups to level up their capacities and convert them into high-end spectroscopic tools. Frequency modulation AFM (FM-AFM) is the basis of most time-resolved measurement methods in SPM field. For any method application and/or upgrade, base system should include a solid in situ measurement capacity for customized and automized measurements. Our work, as detailed in Chapter 2 (*vide supra*), built the system foundation and demonstrated site testing with common AFM methods like cantilever characterization with thermal spectra, basic topography measurements, force spectroscopies, contact potential difference (CPD) measurements, traditional time-resolved AFM (tr-AFM) measurements, and 3D-AFM measurements.

The thermodynamically driven intrinsic properties of sample systems are influential material properties for characterizing dynamic tendencies. Their variations across different length scales and temperature levels lay an interesting foundation for building temperature-dependent characterization for charge carrier investigations. Our work, as detailed in Chapter 3 (*vide supra*), demonstrated the capabilities of custom AFM systems and measurement techniques for multidimensional electronic property characterizations of inorganic oxide-based sample

systems by revealing an inverse relation of CPDs with increasing temperature levels and Fermi level changes, all with respect to the sample locality.

High-quality time and distance resolution directly determines which properties can be revealed and which ones are going to be kept buried within the measurements. With advanced hardware and software, applying traditional and fast-scale submicrosecond tr-AFM techniques to investigate charge carrier migration parameters, mobilities, and transport/storage characterizations introduces a new point of view to the existing literature and methods. Defect engineering these properties against reactive surface defects such as photoinduced surface oxygen vacancies (PI-SOVs) and capturing external effects induced by high energy ultraviolet (UVC) irradiations, temperature variations and surface agents are all possible with the correct instrumentation and application of these methods in correct governing physical scales and dimensions. Our work, as detailed in Chapter 4 (*vide supra*), reveals the influences of methanol, as a highly utilized surface agent in photocatalytic activities, and UV irradiation over charge migrations, mobility and activation barriers. Methanol's role in hole mobility as a function of surface irradiation was revealed. Work in Chapter 5 (*vide supra*) discussed the fast time scale (*e.g.*, electrons) and slow time scale charge carriers (*e.g.*, holes) with specialized methods to investigate influences of MO-metal interfaces, UV irradiation and their possible combinations at different time resolutions. This way, stabilization and optimization of surface defects (*e.g.*, PI-SOVs) against charge carrier mobilities, migration barriers, and trapping mechanisms are revealed. Finally, work in Chapter 6 (*vide supra*) discussed how these involved measurement methods can be utilized to characterize the external effects such as UV irradiation and disclosing its respective penetration depth through introducing PI-SOVs to sample systems and reverse characterizing charge carrier dynamics based on the influences of the defect density changes under UV.

Future works to implement, mainly the tr-AFM-based works in Chapters 4-6 can be extended into deeper investigations and various other points. As much as other photocatalytic surface agents like formic acid and glycerol can be investigated with the same principle in Chapter 4, methanol in its reduced state (i.e., methoxy), oxidized state (i.e., formaldehyde), or chemically

adsorbed state as a molecule can be explored for their individual and isolated intrinsic contributions as photocatalytic products through the investigation of temperature-dependent photochemical reactions. For Chapters 5 and 6, extending the tr-AFM measurements to other MO-metal interfaces in addition to the MO-AuNP and focusing on revealing the fast and slow scale dynamics as functions of intrinsic properties (*e.g.*, bandgap, intrinsic and extrinsic doping, roughness) and defect diffusions rates/ratios are high-impact future work options. Combining the tr-AFM techniques with X-ray photoelectron spectroscopy measurements or atomic resolution scanning probe microscopy measurements could procure interesting results from that retrospect. UVA variations and UVA-UVC comparisons are good candidate influences to be combined with MO-metal interface-based fast and slow-scale charge carrier recombination and trapping mechanism investigations. Our introduced and optimized measurement techniques and capabilities are very well within their abilities to follow up on these mentioned possible future works. The instrumental update discussed in Chapter 2 is almost applicable to all commercial AFM systems to gain necessary experimental abilities as long as the system has the option to access necessary signals.

ANNEX I

PSEUDO CODE FOR THERMAL SPECTRA MEASUREMENT ANALYSIS

```
<%How to use this code: Change the name of the file accordingly. Also,
%depending on the change in the cantilever, cantilever dimensions like
%length and width should be corrected. Additionally, the resonance
%frequency range should be adjusted for the expected value from the used
%cantilever

clc
clear all
close all
addpath('...')

%We need a data file to insert below so that the filename is going to
%contain the file info and it can be opened in the other code script.
file='trial.mat';

[filepath,name,ext] = fileparts(file);
filename=name;
%constants
um=10^(-6);
kb = 1.3806488*(10^(-23)); %Boltzmann constant (m^2kgs^-2 K-1)

%Cantilever Dimensions
L=175*um;%cantilever length in meters
b=40*um;%cantilever width in meters
T=299;%ambient temp in Kelvin

%range of fit
fbegin=141000;%in Hz
fend=144500;%in Hz
init_hwhm=250;% f0/(2Q)

% # Cantilever parameter spring constant obtained in air

file_pll_psd=load (file);
data_input=file_pll_psd.dev5408.scopes.wave{1, 1}.wave;
%data=data_input.^(2);
Sampling_Rate=file_pll_psd.dev5408.scopes.wave{1, 1}.dt^(-1);
Max_freq=Sampling_Rate/2;
Array_size=size(data_input);
Total_PSD_Sample_measurements=Array_size(1);
Freq_increment=Max_freq/Total_PSD_Sample_measurements;%The resolution can be
checked from the 'Advanced tab of Zurich PLL scope as well.

% #inital guess
init_amp=5*mean(data_input);
init_base=mean(data_input);
```

```
fcenter=(fbegin+fend)/2; %in Hz


for z=1:Total_PSD_Sample_measurements
    freq(z,:)=Freq_increment*z;
end


% wide range spectrum
subplot(2,1,1);%211 is equivalent to nrows=2, ncols=1, plot_number=1 for the plot
loglog(freq, data_input);%defines both log scales for freq and data
xlabel('Frequency (Hz)');
ylabel("PSD (V/(sqrt(Hz))");


% For Lorentzian Curve fitting
initial_guess=[init_base,fcenter,init_amp,init_hwhm];

% Removing unused freq range data for fitting
t=1;
for i=1:length(freq)
if freq(i) > fbegin && freq(i) < fend
    freq_fit(t)=freq(i);
    data_input_fit(t)=data_input(i)*(10^(9));
    t=t+1;
end
end

% zoomed spectrum
subplot(2,1,2);
semilogy(freq_fit,data_input_fit*10^(-9));
xlabel('Frequency (Hz)');
ylabel("PSD (V/(sqrt(Hz))");
figure1=sprintf('%s.fig',filename);
savefig(figure1);

data_fit2=log10(data_input_fit);

% Fit: 'lorentz_curve'.
[xData, yData] = prepareCurveData( freq_fit, data_fit2 );

% Set up fittype and options.
ft = fittype( 'log10(height/(1+((x-center)/hwhm)^2)+base)', 'independent', 'x',
'dependent', 'y' );
opts = fitoptions( 'Method', 'NonlinearLeastSquares' );
opts.Display = 'Off';
opts.Lower = [0 0 0 0];
opts.StartPoint = initial_guess;

% Fit model to data.
[fitresult, gof] = fit( xData, yData, ft, opts );

% Plot fit with data.
```

```
figure( 'Name', 'lorentz_curve' );
h = plot( fitresult, xData, yData );
legend( h, 'data_fit2 vs. freq_fit', 'lorentz_curve', 'Location', 'NorthEast',
'Interpreter', 'none' );
% Label axes
xlabel( 'freq_fit', 'Interpreter', 'none' );
ylabel( 'data_fit2', 'Interpreter', 'none' );
grid on

a=coeffvalues(fitresult);
Amplitude=a(3);
f0=a(2);
hwhm=a(4);
base=a(1);

semilogy(freq_fit,data_input_fit*10^(-9));
xlabel('Frequency (Hz)');
ylabel("PSD (V/(sqrt(Hz))");
hold on
fitted_data = Lorentz(freq_fit,Amplitude,f0,hwhm,base);
semilogy(freq_fit,fitted_data*10^(-9));
figure2=sprintf('%s_2.fig',filename);
savefig(figure2);


Amplitude=Amplitude*(10^(-9));
fwhm=2*hwhm;
Q=f0/fwhm;
base=base*(10^(-9));

%%%%%%%%%%%%%%%%%%%%%%%%%%%%%%%%%%%%%%%%%%%%%%%%%%%%%%%%%%%%%%%%%%%%%%%%%%%
% Determining spring constant with Sader's method
rho=1.18;%in kg/m3 for air density (sea level-15°C)
eta=1.868*(10^(-5)); %# viscosiy of air kg/(mxs)=Pa.s
w0=2*pi*f0;%Radial Resonant Freq.
%Reynold's number
Ren=rho*w0*b^2 /(4*eta);
j^2==-1;
Gamma=omega(Ren)*(1+4*1j*besselk(1,-1j*sqrt(1j*Ren))/(sqrt(1j*Ren)*besselk(0,-
1j*sqrt(1j*Ren))));

kc=0.1906*rho*b*b*L*Q*imag(Gamma)*(w0)^2;
%%%%%%%%%%%%%%%%%%%%%%%%%%%%%%%%%%%%%%%%%%%%%%%%%%%%%%%%%%%%%%%%%%%%%%%%%%%
%%%%

% # peak thermal noise amplitude
Nth_peak=sqrt(2*kb*T*Q/(kc*pi*f0));   %# thermal noise at peak [m/sqrtHz]

Sens=1/((Amplitude)/Nth_peak);  %# sensitivity [m/V]

basenoise=(base)*Sens;      %# baseline noise [fm/sqrtHz]

fprintf('fitting results\n')
```

```
fprintf('Amplitude =%d' ,Amplitude)
fprintf('(V(rms)/(sqrt(Hz))\n')
fprintf('Resonance frequency = %d' ,f0)
fprintf('(Hz)\n')
fprintf('FWHM =%d ' ,fwhm)
fprintf('(Hz)\n')
fprintf('Q factor = %d\n' ,Q)
fprintf('Baseline noise = %d' ,base)
fprintf('(V(rms)/(sqrt(Hz))\n')
fprintf('kc= %d' ,kc)
fprintf('[N/m]\n')
fprintf('Nth= %d',Nth_peak*1e15)
fprintf(' [fm/sqrtHz]\n')
fprintf('Sensitivity_p2p= %d' ,Sens*1e9*sqrt(2))
fprintf(' [nm/V]\n' )
fprintf('Noise = %d' ,basenoise*1e15)
fprintf(' [fm/sqrtHz]\n')

% #saving the fitting results
filename2=sprintf('%s_fitting_result.txt',filename);
fid=fopen(filename2, 'w');

fprintf(fid,'Fitting Results\n');
fprintf(fid,'Amplitude =%d' ,Amplitude);
fprintf(fid,'(V(rms)/(sqrt(Hz))\n');
fprintf(fid,'Resonance frequency = %d' ,f0);
fprintf(fid,'(Hz)\n');
fprintf(fid,'FWHM =%d ' ,fwhm);
fprintf(fid,'(Hz)\n');
fprintf(fid,'Q factor = %d/n' ,Q);
fprintf(fid,'Baseline noise = %d' ,base);
fprintf(fid,'(V(rms)/(sqrt(Hz))\n');
fprintf(fid,'kc= %d' ,kc);
fprintf(fid,'[N/m]\n');
fprintf(fid,'Nth= %d',Nth_peak*1e15);
fprintf(fid,' [fm/sqrtHz]\n');
fprintf(fid,'Sensitivity_p2p = %d' ,Sens*1e9*sqrt(2));
fprintf(fid,' [nm/V]\n' );
fprintf(fid,'Noise = %d' ,basenoise*1e15);
fprintf(fid,' [fm/sqrtHz]\n');

fclose(fid);

% #saving data with text format
freq_data = cat(2,freq,data_input);
filename3=sprintf('%s_values.txt',filename);
fid2=fopen(filename3, 'w');
fprintf(fid2,'Freq.Values ||| PSD Values\n');
fprintf(fid2,'%i\t%i\n',freq_data);
fclose(fid2);

%Reynold's number Functions
function omre=omre(x)
```

```
omre=(0.91324-0.48274*x+0.46842*x^2-0.12886*x^3+0.044055*x^4-
0.0035117*x^5+0.00069085*x^6)/(1-0.56964*x+0.48690*x^2-0.13444*x^3+0.045155*x^4-
0.0035862*x^5+0.00069085*x^6);
end
function omimag=omimag(x)
omimag=(-0.024134-0.029256*x+0.016294*x^2-0.00010961*x^3+0.000064577*x^4-
0.000044510*x^5)/(1-0.59702*x+0.55182*x^2-0.18357*x^3+0.079156*x^4-
0.014369*x^5+0.0028361*x^6);
end
function om=om(x)
om=omre(x)+1j*omimag(x);
end
function omega=omega(x)
omega=om(log10(x));
end

%Lorentzian Fit Function
function Lorentz= Lorentz(x,amplitude,center,hwhm,base)
    Lorentz=(amplitude./(1+((x-center)./hwhm).^2)+base);
end
```

ANNEX II

PSEUDO CODE FOR SINGLE PULSE TIME-RESOLVED MEASUREMENTS ANALYSIS

```
clc
clear all
close all
addpath('...')

I_lower=1200;
I_upper=2180;
master_counter=1;
data_directory=dir;
num_of_size=size(data_directory);
counter=1;
voltage2hertz=100;

a=1;
for i= 1:+1:num_of_size(1)
    if data_directory(i).bytes>400000

    point = SPM.load(data_directory(i).name);%Specialized Data Loading for GXSM
VP Data

    X_coordinate(a)=point.PtLoc.XS+point.Offset.X0;
    Y_coordinate(a)=point.PtLoc.YS+point.Offset.Y0;
    if round(X_coordinate(a)/10)==0 && round(Y_coordinate(a)/10)==0
        fprintf('Trial Data Ignored!')
    else
    X_coordinate_round(a)=round(X_coordinate(a)/10);
    Y_coordinate_round(a)=round(Y_coordinate(a)/10);

    time_all(:,a)=point.Channel(6).Data;
    deltaf_all(:,a)=point.Channel(1).Data*voltage2hertz;

    index=1;
        for jj=I_lower:+1:I_upper
            time(index,a)=time_all(jj,a);
            deltaf(index,a)=deltaf_all(jj,a);
            index=index+1;
        end
    end
    a=a+1
    end

clear time_all deltaf_all
    fclose('all')
end
```

```
save fileloads2.mat

[sortedX_coordinate_round, sortIndex] = sort(X_coordinate_round);
sortedY_coordinate_round=Y_coordinate_round(sortIndex);
sortedTime=time(:,sortIndex);
sorteddeltaF=deltaf(:,sortIndex);
sortedX_coordinate_round_pre=sortedX_coordinate_round(1);
sortedY_coordinate_round_pre=sortedY_coordinate_round(1);

counter=1;
i=1;
data_number=0;
coordinate_points_pre=0;
data_size=size(sortedX_coordinate_round);

while data_number < data_size(2)-1

    check_counter=1;

    while sortedX_coordinate_round_pre==sortedX_coordinate_round(counter) &&
sortedY_coordinate_round_pre==sortedY_coordinate_round(counter)
    time_temp=(sortedTime(:,counter)-sortedTime(1,counter));
    deltaf_temp=(sorteddeltaF(:,counter)-sorteddeltaF(1,counter));
    [fitresult, gof] = noise_ellimination(time_temp, deltaf_temp);
    deltaf_temp_fit=fitresult(time_temp);

    [fitPt_temp, gof] = SexpFit(time_temp, deltaf_temp)
    check_fit=confint(fitPt_temp);
    if fitPt_temp.T<1000 && fitPt_temp.T>10 &&  fitPt_temp.C<1.0 &&
fitPt_temp.C>0
        time_avg(:,check_counter)=time_temp;
        deltaf_avg(:,check_counter)=deltaf_temp;
        deltaf_avg_fit(:,check_counter)=deltaf_temp_fit;
        check_counter=check_counter+1;
    end
    sortedX_coordinate_round_pre=sortedX_coordinate_round(counter);
    sortedY_coordinate_round_pre=sortedY_coordinate_round(counter);

    end
    x_positions(i)=sortedX_coordinate_round_pre;
    y_positions(i)=sortedY_coordinate_round_pre;

    sortedX_coordinate_round_pre=sortedX_coordinate_round(counter);
    sortedY_coordinate_round_pre=sortedY_coordinate_round(counter);

    data_number=counter-1;

    coordinate_points(i)=counter-1-coordinate_points_pre;
    coordinate_points_pre=coordinate_points(i);
    i=i+1;

    if check_counter~=1
    if check_counter>2
```

```
 avg_time=mean(time_avg');
 avg_deltaf=mean(deltaf_avg');
 avg_deltaf_fit=mean(deltaf_avg_fit');
     end

     if check_counter==2
 avg_time=(time_avg');
 avg_deltaf=(deltaf_avg');
 avg_deltaf_fit=(deltaf_avg_fit');
     end


 [fitresult, gof] = noise_ellimination(avg_time, avg_deltaf);
 avg_deltaf_spline=fitresult(avg_time);

 [fitresult_fit, gof] = noise_ellimination(avg_time, avg_deltaf_fit);
 avg_deltaf_fit=fitresult_fit(avg_time);

 [fitPt_avg, gof] = SexpFit(avg_time, avg_deltaf)
 [fitPt_avg_spline, gof] = SexpFit(avg_time, avg_deltaf_spline)
 [fitPt_avg_fit, gof] = SexpFit(avg_time, avg_deltaf_fit)
 fitPt_avg_backup=fitPt_avg;
 end
 if check_counter==1
     fitPt_avg=fitPt_avg_backup;
 end
 data_group=coordinate_points(end);
if  mod(master_counter,data_group)~=0
 x=mod(master_counter,data_group);
end
if mod(master_counter,data_group)==0
        x=coordinate_points(end);
end

y=floor((master_counter-1)/data_group)+1;
 tao(x,y)=fitPt_avg.T
 beta(x,y)=fitPt_avg.C

 tao_spline(x,y)=fitPt_avg_spline.T
 beta_spline(x,y)=fitPt_avg_spline.C

 tao_fit(x,y)=fitPt_avg_fit.T
 beta_fit(x,y)=fitPt_avg_fit.C

log_useful(x,y)=check_counter
close all
 plot(avg_time,fitPt_avg(avg_time))
 hold on
 plot(avg_time,fitPt_avg_spline(avg_time))
 plot(avg_time,fitPt_avg_fit(avg_time))
 plot(avg_time,avg_deltaf)

 figname= strcat(num2str(x),'_',num2str(y),'.jpeg');
```

```
    saveas(gcf,figname)
    master_counter=master_counter+1;
    close all
    clear  time_all deltaf_all fitPt_avg deltaf_smooth time_avg deltaf_avg
deltaf_avg_fit check_counter
    clear point
    fclose('all')
    save Temp.mat
    clear all
    load Temp.mat
end

    save Result_grid5
```

Codes for the functions within the main code

```
function [fitresult, gof] = SexpFit(avg_time, avg_deltaf)
%CREATEFIT(AVG_TIME,AVG_DELTAF)
%  Create a fit.
%
%  Data for 'untitled fit 1' fit:
%      X Input : avg_time
%      Y Output: avg_deltaf
%  Output:
%      fitresult : a fit object representing the fit.
%      gof : structure with goodness-of fit info.
%
%  See also FIT, CFIT, SFIT.


%% Fit: 'untitled fit 1'.
[xData, yData] = prepareCurveData( avg_time, avg_deltaf );

% Set up fittype and options.
ft = fittype( 'A+B*exp(-((x/T)^C))', 'independent', 'x', 'dependent', 'y' );
opts = fitoptions( 'Method', 'NonlinearLeastSquares' );
opts.Display = 'Off';
opts.Lower = [-Inf -Inf 0 10];
opts.Upper = [Inf Inf 1 10000];
opts.Robust = 'Bisquare';
opts.StartPoint = [0.547215529963803 0.138624442828679 0.5 500];

% Fit model to data.
[fitresult, gof] = fit( xData, yData, ft, opts );

% Plot fit with data.
%figure( 'Name', 'untitled fit 1' );
h = plot( fitresult, xData, yData );
legend( h, 'avg_deltaf vs. avg_time', 'untitled fit 1', 'Location', 'NorthEast'
);
% Label axes
xlabel ('time (ms)')
ylabel ('deltaf (Hz)')
```

```
grid on


function [fitresult, gof] = noise_ellimination(time_temp, deltaf_temp)
%CREATEFIT(TIME_TEMP,DELTAF_TEMP)
%  Create a fit.
%
%  Data for 'noise_ellimination' fit:
%      X Input : time_temp
%      Y Output: deltaf_temp
%  Output:
%      fitresult : a fit object representing the fit.
%      gof : structure with goodness-of fit info.
%
%  See also FIT, CFIT, SFIT.


%% Fit: 'noise_ellimination'.
[xData, yData] = prepareCurveData( time_temp, deltaf_temp );

% Set up fittype and options.
ft = fittype( 'smoothingspline' );
opts = fitoptions( 'Method', 'SmoothingSpline' );
opts.Normalize = 'on';
opts.SmoothingParam = 0.995;

% Fit model to data.
[fitresult, gof] = fit( xData, yData, ft, opts );

% % Plot fit with data.
% figure( 'Name', 'noise_ellimination' );
% h = plot( fitresult, xData, yData );
% legend( h, 'deltaf_temp vs. time_temp', 'noise_ellimination', 'Location',
'NorthEast', 'Interpreter', 'none' );
% % Label axes
% xlabel( 'time_temp', 'Interpreter', 'none' );
% ylabel( 'deltaf_temp', 'Interpreter', 'none' );
% grid on
```

APPENDIX I

SUPPLEMENTAL INFORMATION OF THE ARTICLE "CUSTOMIZATION OF AN ATOMIC FORCE MICROSCOPE FOR MULTIDIMENSIONAL MEASUREMENTS UNDER ENVIRONMENTAL CONDITIONS"

Bugrahan Guner[a], Simon Laflamme[a], and Omur E. Dagdeviren[a]

[a]Department of Mechanical Engineering, École de Technologie Supérieure,
1100 Notre-Dame West, Montreal, Quebec, Canada H3C 1K3

Paper published in *Review of Scientific Instruments*[6], June 2023

Appendix I.A - Wiring Diagram and Pin Locations

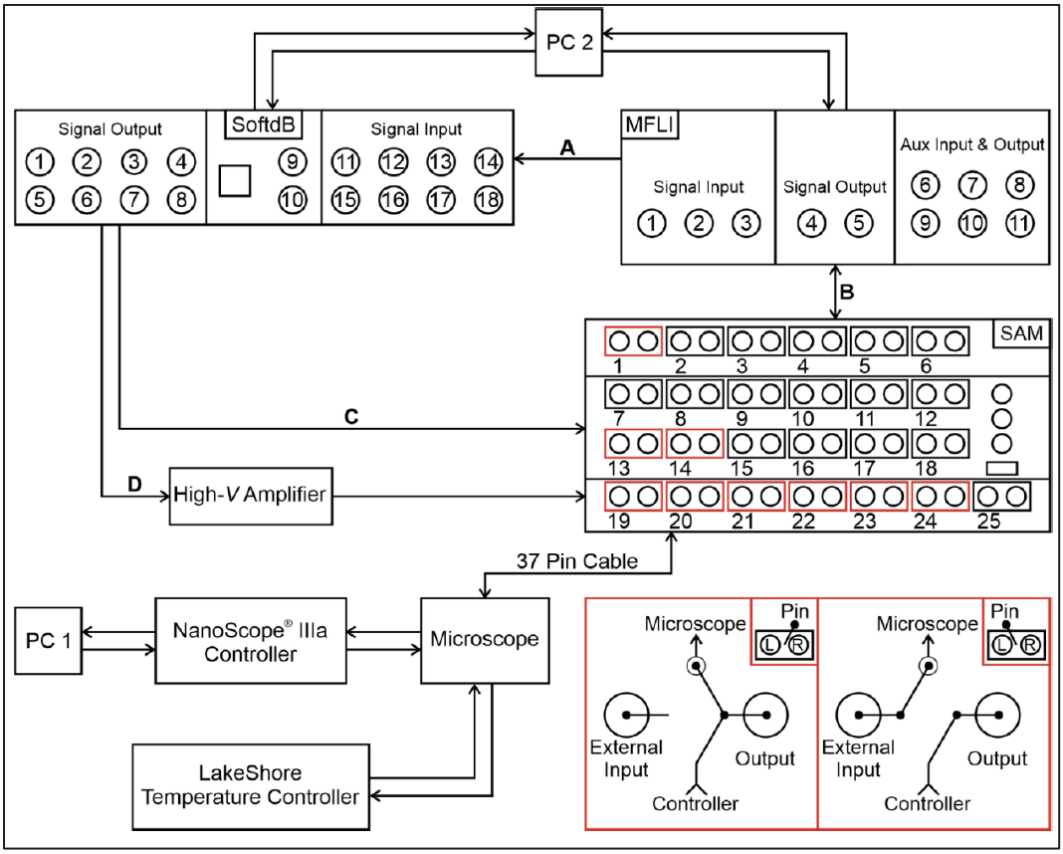

Figure-A I.1 The wiring diagram for the customization of the atomic force microscopy system

---

[6] Bugrahan Guner (2023, *p.* 063704)

An external lock-in amplifier with phase-locked loop capacity (i.e., MFLI by Zurich Instruments), a controller (i.e., SoftdB controller with Gnome X Scanning Microscopy software), a high-voltage amplifier and a Signal Access Module™ (SAM) has been integrated to the system to enable customized and automated experiments (see Figure-A I.2 for details). Main hardware connections have been illustrated with A, B, C, and D junctions (used pins in SAM highlighted with red, see Figure-A I.3 for details). The legend, i.e., red squares, refers to the SAM pin positions. Pins are switched from the right (R) to the left (L) to make the transition for customized experiments.

Capabilities	Nanoscope® IIIa Controller	Signal Access Module™	MFLI lock-in amplifier	SoftdB SPM controller (+GXSM software)	MATLAB® and/or Python™	Lakeshore Temperature Controller
Contact mode	✓	✓	✓	✓		
AM-AFM	✓	✓	✓	✓		
Primitive force spectroscopy	✓	✓	✓	✓		
Signal access and manipulations		✓				
FM-AFM			✓	✓		
Custom tip-sample distance control				✓		
Automated measurement in progress corrections					✓	
Temperature control						✓

Figure-A I.2 Hardware/software integration and additional experimental capabilities

Junctions Presented in Figure S1	Output Port	Input Port	Signal Definition	SAM Pin Locations (Nanoscope®)	SAM Pin Locations (GXSM controller)
A	MFLI-7	SoftdB-13	Amplitude signal	N/A	N/A
	MFLI-8	SoftdB-12	Frequency shift signal	N/A	N/A
	MFLI-10	SoftdB-15	Phase signal	N/A	N/A
	MFLI-11	SoftdB-14	Excitation signal	N/A	N/A
B	SAM-1 (R)	MFLI-3	Photodiode signal	R	L
	SAM-13 (L)	MFLI-4	Drive signal	R	L
	MFLI-7	SAM-1 (L)	Oscillation amplitude	R	L
C	SoftdB-4	SAM-14 (L)	Bias Voltage	R	L
D	SoftdB-5	SAM-19 (L)	$+X_s$ signal	R	L
	SoftdB-5	SAM-20 (L)	$-X_s$ signal	R	L
	SoftdB-6	SAM-21 (L)	$+Y_s$ signal	R	L
	SoftdB-6	SAM-22 (L)	$-Y_s$ signal	R	L
	SoftdB-7	SAM-23 (L)	$+Z_s$ signal	R	L
	SoftdB-7	SAM-24 (L)	$-Z_s$ signal	R	L

Figure-A I.3 Detailed pin connections of the hardware implementation for the operation of the microscope with the Nanoscope® IIIa Controller and SoftdB controller with Gnome X Scanning Microscopy (GXSM) software, where the Signal Access Module™ (SAM) pins are switched from the right (R) to the left (L) to enable the SoftdB controller

Appendix I.B - Step-by-step procedure of the Sample Approach and Controller Transition

As Figure-A I.4 shows, the initial approach to the sample is done by using Nanoscope® IIIa Controller. After engaging the sample, e.g., with amplitude-modulation atomic force microscopy, the scanner is retracted from the sample by using a large set point, e.g., 10 Volt for the amplitude of oscillation. As the scanner is fully retracted from the surface, the tip-sample separation is a couple of micrometres. While the tip is retracted, the user will switch pins from right to left as detailed in Figure-A I.1 and Figure-A I.3. Once the pins are switched, the SoftdB controller with Gnome X Scanning Microscopy software is employed to control tip-sample separation and for customized experiments.

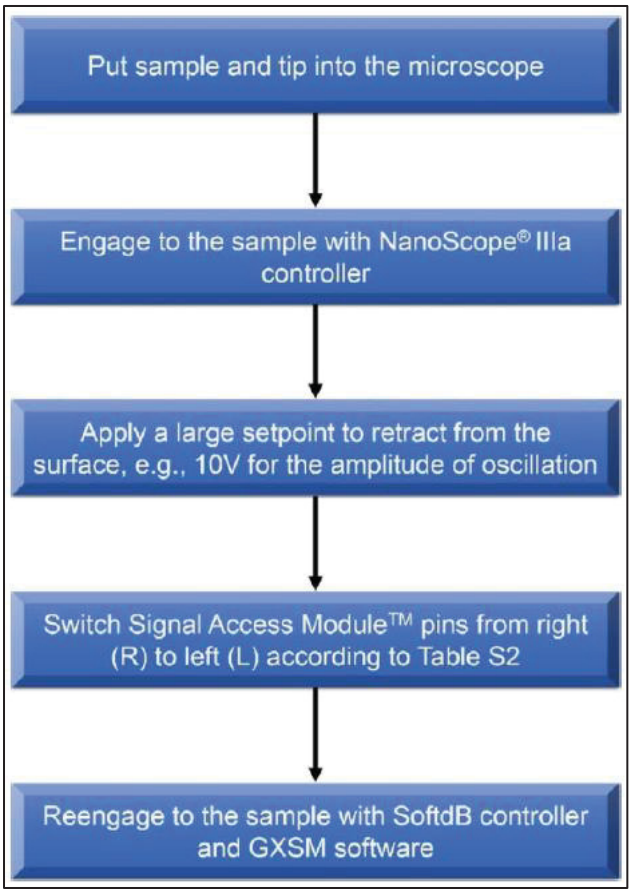

Figure-A I.4 Algorithm to approach the sample and conduct customized measurements with the updated control architecture

Nanoscope® IIIa controller is employed to complete the rough and initial approach to the surface while Signal Access Module™ (SAM) pins are on the right side (see Figure-A I.3 for details). Upon approach to the surface, the user retracts with the scanner by applying a large set point, e.g., 10 Volts for the amplitude of oscillation and changing pin locations to the left to direct signals to the SoftdB controller and the lock-in amplifier (see Figure-A I.3 for details). The SoftdB controller with Gnome X Scanning Microscopy software and the lock-in amplifier with the phase locked-loop capability enables customized and automated experiments.

Appendix I.C - Procedure of the Resonance Frequency Drift Corrections

The resonance frequency of the cantilever may drift over time, particularly during experiments conducted at high temperatures. Figure-A I.5 illustrates the resonance frequency drift

correction for time-resolved measurements. Before applying the tip-sample pulse for time-resolved measurements (at t = 0), the cantilever was retracted 20 nm from the engaged position. At this distance, the cantilever is expected to be at its free resonance frequency. Therefore, any non-zero frequency shift value is due to the resonance frequency drift, which is corrected with the MATLAB® integration of the lock-in amplifier with phase-locked loop capacity (i.e., MFLI by Zurich Instruments). For each measurement, we corrected the resonance frequency drift automatically. To this end, all measurements were completed for the same frequency shift setpoint, while the relative tip-sample distance was kept the same.

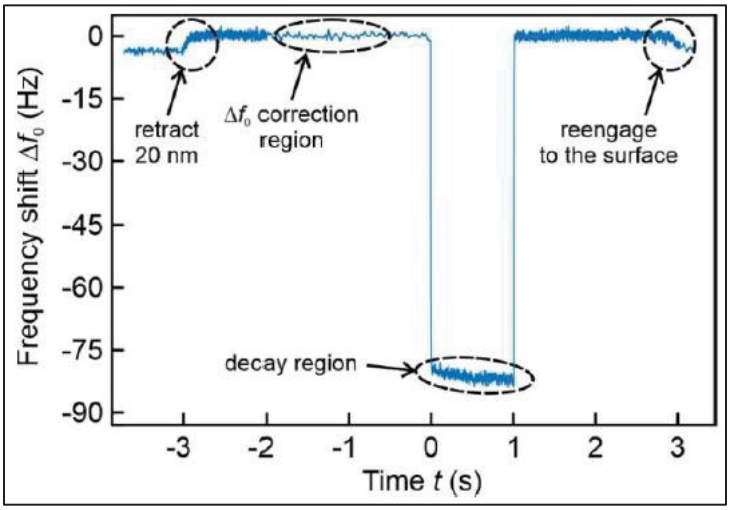

Figure-A I.5 Resonance frequency drift correction analogy for frequency modulation atomic force microscopy-based time-resolved measurements

The frequency shift correction is completed after the tip is retracted from the surface, e.g., 20 nm. At large tip-sample separations, the resonance frequency shift, Δf_0, is expected to be zero. For this reason, the resonance frequency drift can be measured and corrected by using a lock-in amplifier with phase-locked loop capability. As discussed in the main text, the resonance frequency drift correction enhanced the stability of the time-resolved measurements, particularly at high temperatures

.

Appendix I.D - Additional Two-Dimensional Force Spectroscopy Measurements Across Step-Edges of Highly Ordered Pyrolytic Graphite

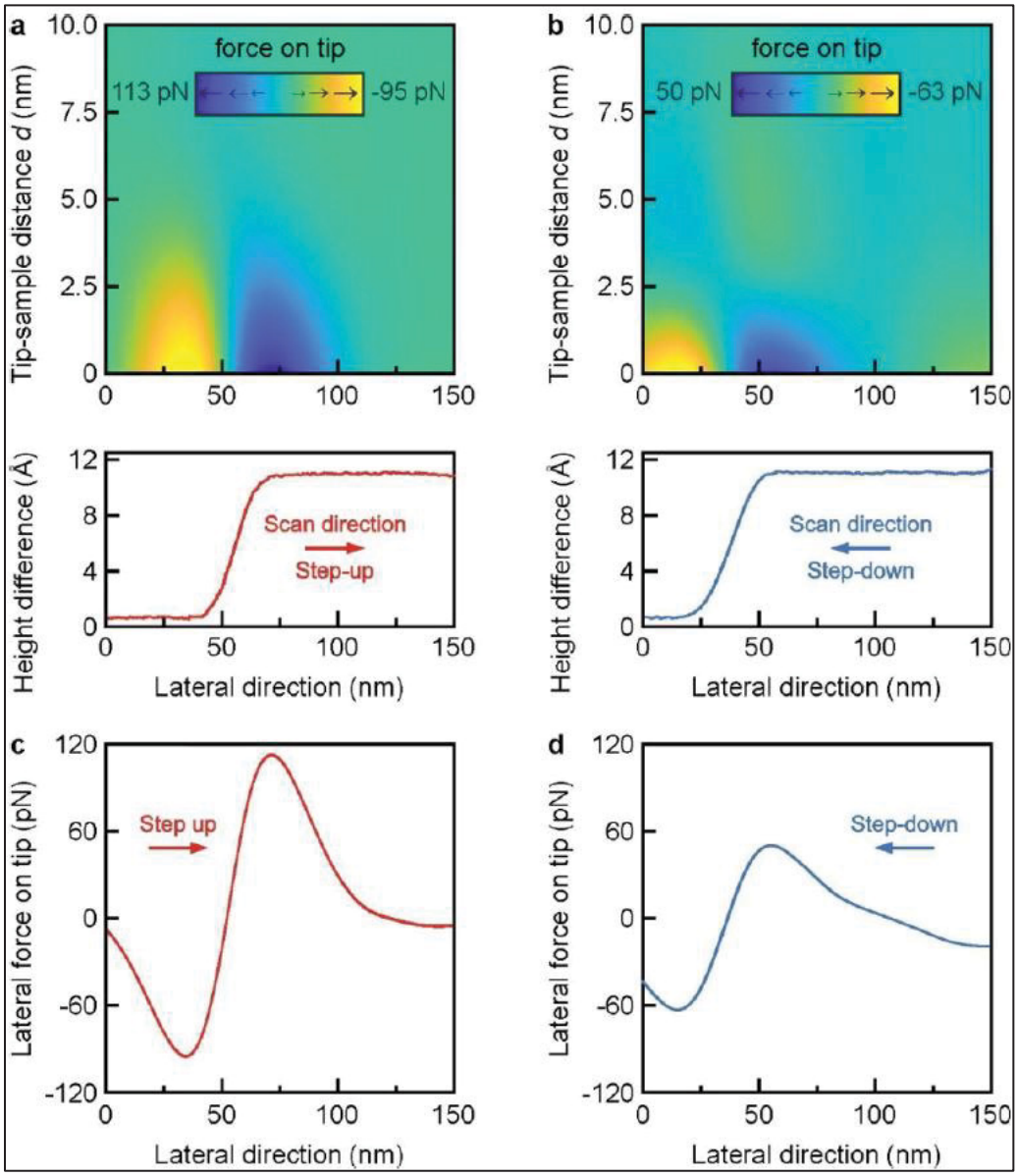

Figure-A I.6 Additional two-dimensional force spectroscopy measurements of highly ordered pyrolytic graphite under ambient conditions across a cluster of three unit-cell steps for forward (step-up) and backward (step-down) directions

The tip experiences an attractive force upon approach to the step edge; however, upon further approach to the step edge, the tip experiences a repulsive force during step-up motion (see Figure-A I.6a and Figure-A I.6c). Figure-A I.6b and Figure-A I.6d show the corresponding

step-down motion. The tip has an assistive step-down motion upon approach to step edges. At the lower terrace, the tip is attracted by step edges. The vertical tip-sample interaction was in the attractive region for measurements presented in this figure. The drift along the z direction (1.2 Å/minute) has been measured during experiments and corrected in the post-processing. We used a constant oscillation amplitude of 10 nm peak-to-peak with a cantilever with a free resonance frequency, f_0 = 130.231 kHz, spring constant, $c_z \approx 7.8$ N/m, and quality factor, $Q \approx 281$).

APPENDIX II

SUPPLEMENTAL INFORMATION OF THE ARTICLE "MULTIDIMENSIONALITY OF THE CONTACT POTENTIAL DIFFERENCE AT THE NANOSCALE IN INORGANIC OXIDES"

Bugrahan Guner[a] and Omur E. Dagdeviren[a]

[a]Department of Mechanical Engineering, École de Technologie Supérieure,
1100 Notre-Dame West, Montreal, Quebec, Canada H3C 1K3

Paper published in *ACS Applied Electronic Materials*[7], July 2022

Appendix II.A - X-ray Diffraction Measurements

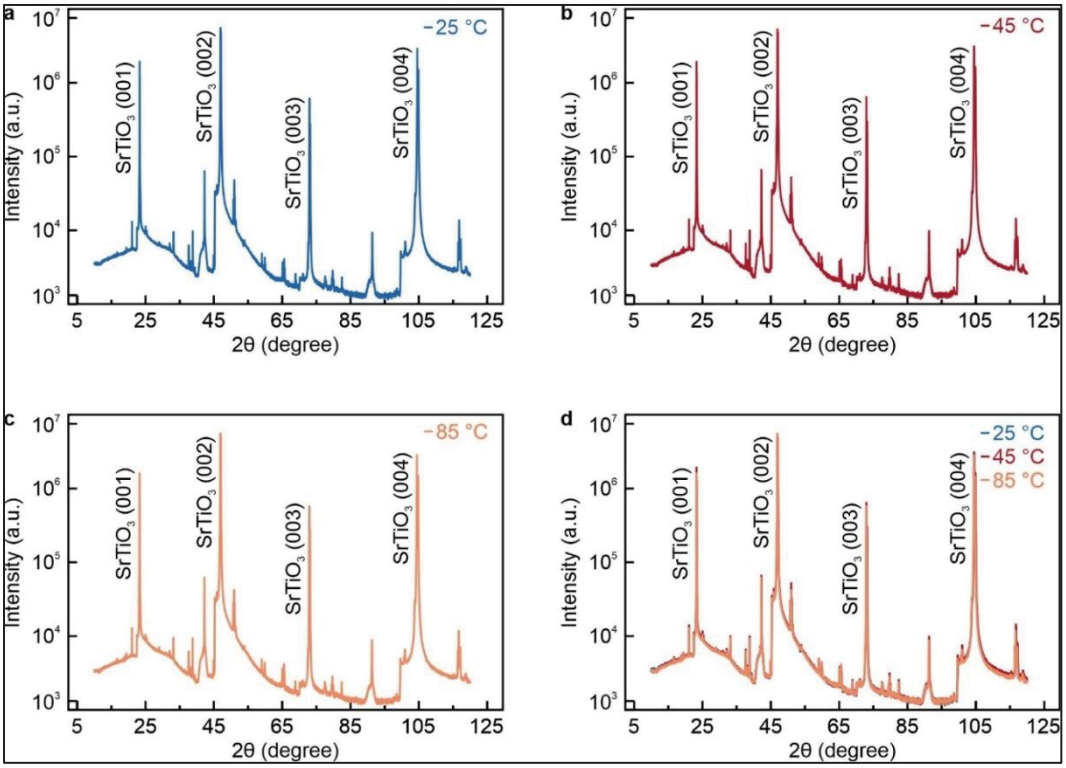

Figure-A II.1 Temperature-dependent X-ray diffraction (XRD) measurements of a single-crystal, undoped $SrTiO_3$ (100) sample

[7] Bugrahan Guner (2022, *p.* 4085−4093)

XRD measurements for a $SrTiO_3$ sample at 25 °C, 45 °C, and 85 °C are shown at the same spatial position. Peak locations are consistent with the literature (see Figure-A II.1a, Figure-A II.1b, and Figure-A II.1c). [214-219] To ease the comparison of structural peaks, we merged XRD results presented in Figure-A II.1d. Our experimental results clearly show that there is no structural change or phase transformation between 25 °C and 85 °C, which is consistent with the existing literature. [220, 221]

To quantify our results, we calculated the full-width half maxima (FWHM) values for four major peaks presented in Figure-A II.1, i.e., Peak I ≈ 23°, Peak II ≈ 47°, Peak III ≈ 73°, Peak IV ≈ 105°. As Table-A II.1 clearly shows, there is no correlation between the temperature and the FWHM values. The nonexistence of such a correlation supports the absence of a phase or structural transformation of $SrTiO_3$ for the temperature range in which we conducted our measurements.

Table-A II.1 Full-width half maxima (FWHM) values of four major peaks of $SrTiO_3$

Temperature	Peak I FWHM	Peak II FWHM	Peak III FWHM	Peak IV FWHM
25 °C	0.03°	0.06°	0.05°	0.08°
45 °C	0.03°	0.07°	0.05°	0.08°
85 °C	0.03°	0.06°	0.05°	0.07°

Appendix II.B - Experimental Results of TiO_2 and Template-stripped Gold

Figure-A II.2 summarizes our temperature-dependent contact potential difference (CPD) measurements on a single-crystal, undoped TiO_2 (100) and template-stripped gold sample by using the force-volume technique, as explained in detail in the main text. As Figure-A II.2a shows, the CPD value of TiO_2 has a linear dependence on the temperature with a negative slope, i.e., CPD decreases with increasing temperature. The variation of the CPD of the TiO_2 originates from intrinsic doping of the sample, as explained in detail in the main text. The CPD of the template-stripped gold sample changes significantly less (-0.5 ± 0.1 mV/°C) compared to TiO_2 (-3.8 ± 0.1 mV/°C) and $SrTiO_3$ (-3.6 ± 0.1 mV/°C) samples. Although ideally, the CPD value of the template-stripped gold was supposed to be independent of the temperature of the sample due to the absence of intrinsic vacancies, the limited thickness of the gold coating

and/or the effect of the silicon cantilever and the sample substrate may contribute to the measured value.

As Figure-A II.2 shows, at distances, $d < 10$ nm, the CPD has a rather chaotic trend compared to $d > 10$ nm. We believe that this variation originates due to the local tip and sample effects, as detailed in the main text. We calculated average values of maximum variation at $d < 10$ nm with respect to the mean value of the mean CPD value for $d > 10$ nm. The template-stripped gold sample has a smaller variation (~ 23 mV) compared to TiO_2 (~ 36 mV) and $SrTiO_3$ (~ 178 mV) samples at $d < 10$ nm. This observation is consistent with the complex surface terminations of TiO_2 and $SrTiO_3$ compared to the template-stripped gold sample. [87, 102, 206]

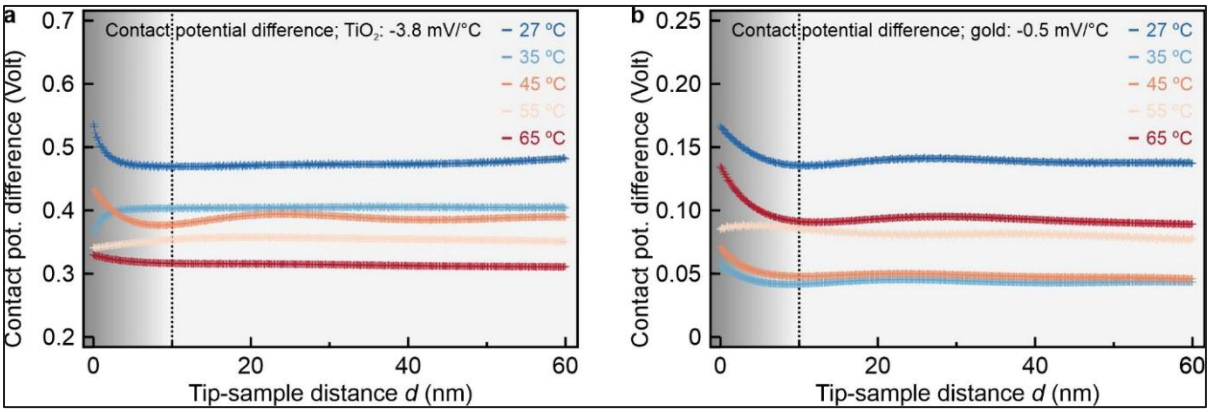

Figure-A II.2 Measurements of the contact potential difference (CPD) for a single-crystal, undoped TiO_2 (100) and template-stripped gold samples as a function of tip-sample distance, d, and temperature of the sample

The measurements of CPD for TiO_2 illustrate a decrease of 3.8 ± 0.1 mV/°C with increasing temperature at $d > 10$ nm. Additionally, the measurements of CPD for the template-stripped gold sample present a change of -0.5 ± 0.1 mV/°C. At $d < 10$ nm, shown with a dashed line, the variation of the CPD is rather chaotic due to local contributions, as explained in detail in the main text.

Appendix II.C - Temperature-Dependent Variation of Contact Potential Difference for $SrTiO_3$, TiO_2, and Template-stripped Gold

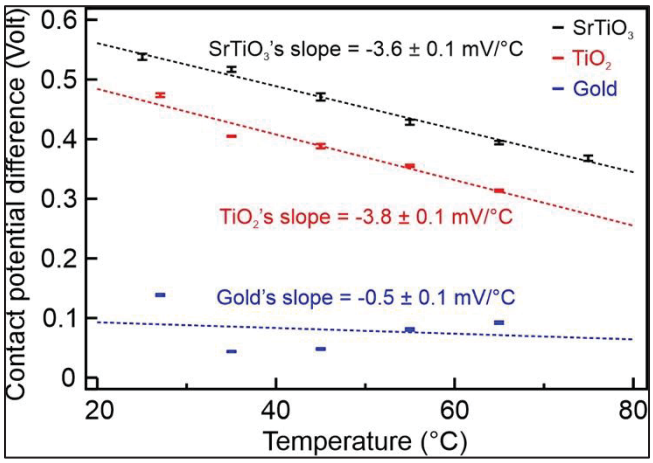

Figure-A II.3 Variation of contact potential difference (CPD) for $SrTiO_3$ (single-crystal, undoped, (100)), TiO_2 (single-crystal, undoped, (100)), and template-stripped gold at tip-sample separations larger than 10 nm

The slope of the first-order polynomial, presented with the dashed line, delivers the temperature-dependent variation of the CPD. The vertical error bar represents the standard variation of the CPD between tip-sample separations of 10 nm to 60 nm, while the horizontal error bar represents the confidence level of the temperature measurement. Please note that some error bars cannot be seen clearly due to their small size.

Appendix II.D - Reproducibility of Contact Potential Difference Measurements

As explained in the main text in detail, the contact potential difference (CPD) is the difference in work functions between the sample and the probe while they are in proximity. For this reason, a change in the work function of the probe is expected to affect the measurement of the CPD. To eliminate this confounding variable, we ensured to protect the tip by approaching samples while keeping the tip-sample interaction in the attractive regime, i.e., far from the surface. Towards this end, for $SrTiO_3$ experiments (i.e., JSPM-5100 system), we utilized a very small and negative resonance frequency shift while setting the tip-sample bias voltage far from the expected range of the CPD value during the initial fine approach to the sample. Similarly, we protected the tip by applying a significantly different tip-sample bias voltage compared to

the expected range of CPD values for the fine initial approach to TiO_2 and template-stripped gold (i.e., VeecoEnviroscope system).

Figure-A II.4 illustrates the reproducibility of the CPD measurements. The orange curve illustrates the CPD measurement at 65 °C, the first experimental set of TiO_2. After decreasing the temperature of the sample down to room temperature with steps of 10 °C and conducting multiple force-volume measurements at each temperature setpoint, we increased the temperature of the sample back to 65 °C and repeated the CPD measurement, the red curve in Figure-A II.4. As Figure-A II.4 clearly illustrates, the first and last CPD measurements at 65 °C are in good agreement and both are significantly different compared to the CPD measurement of the TiO_2 at 55 °C. This cross-validation demonstrates that the tip structure is well-protected during measurements.

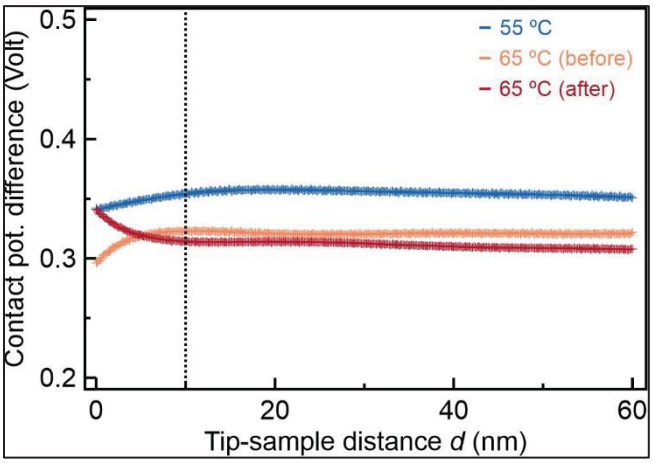

Figure-A II.4 Reproducibility of the contact potential difference measurements

As explained (*vide supra*), we took necessary actions to protect the probe during the fine approach to the sample to eliminate the unintentional variation of the work function of the probe. The orange curve shows the CPD measurement of the TiO_2 sample at 65 °C, 321 ± 1 mV for $d > 10$ nm, presented with the dashed line. After completing the experimental set, i.e., decreasing the temperature of the sample down to room temperature with 10 °C decrements and conducting multiple force-volume measurements at each temperature, the temperature of the sample was set to 65 °C. We repeated the CPD measurement at 65 °C, i.e., the red curve,

311 ± 2 mV. As our experimental results clearly illustrate both measurements at 65°C are in good agreement for tip-sample distances larger than 10 nm, and considerably different compared to the CPD measurement at 55 °C, 355 ± 2 mV.

We also verified the stability of the excitation signal, which is associated with the energy dissipation of the tip-sample interaction. [71, 72] It is well-known that the change of the excitation signal is an indication of a major location/ tip-sample interaction change. [71, 72] For example, a lateral change in the order of a few 10s of nms is expected to result in an interaction change between the probe and the sample. This change in the local interaction mechanism will eventually lead to a significant/apparent variation of the excitation signal. When our excitation signals were analyzed over the course of our experiments, any sudden or gradual change with time was not observed. More specifically, when Figure-A II.5 shows the example of the excitation and amplitude signals over two different experimental sets, which were conducted at different spatial positions across the surface. Each experimental set contains two hundred and ten force spectroscopy measurements, as explained in the main text. The excitation signal changes ~ 0.4% both for experiments 1 and 2, in order to keep the oscillation amplitude of the probe constant, 85.3 mV, i.e., ~ 10 nm (peak-to-peak). However, the excitation signal changes by ~ 2.0% between experiments 1 and 2, which were conducted at different spatial positions across the sample. The significantly larger difference in the excitation signal between two spatial positions across the surface, compared to the variation in experimental sets themselves, implies that the drift rate over the course of an experiment was minimized and we also avoided unrepresentative surface areas, areas with clusters of surface contaminants, or any sudden or major tip changes.

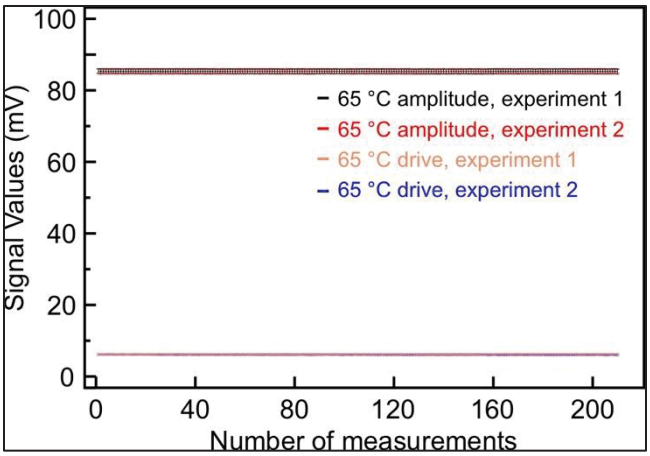

Figure-A II.5 The excitation and the oscillation amplitude signals of two different experimental sets were recorded at different spatial positions across the sample

Each experimental set contains two hundred and ten different force spectroscopy measurements recorded at the same spatial position. The excitation signal changes statistically less during a complete experimental set (i.e., ~ 0.4%), compared to the difference of the excitation signal for two different spatial positions (i.e., ~ 2.0%). This implies that the clusters of surface contaminations and any sudden/major tip changes were avoided while successfully controlling the drift during our experiments.

Appendix II.E - Analysis of the Tip-sample Capacitance as a Function of Temperature

The analysis of the variation of the tip-sample capacitance, *C*, has revealed that the measured *C* does not have a monotonic temperature dependence. Towards this end, we present the *C* of the $SrTiO_3$ sample at different tip-sample separations. As Figure-A II.6 illustrates, although the *C* decreases with increasing tip-sample separation, any temperature-dependent correlation could not be seen. Although *C* decreases with increasing tip-sample separation, i.e., from 10 nm to 60 nm, as shown with different colors, the correlation of the temperature with *C* is absent.

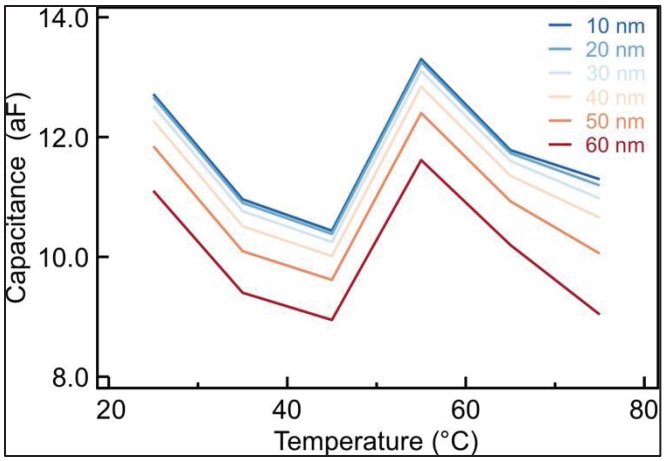

Figure-A II.6 Variation of the tip-sample capacitance, *C*, for the $SrTiO_3$ sample as a function of the sample temperature

APPENDIX III

SUPPLEMENTAL INFORMATION OF THE ARTICLE "FAST AND SLOW TIME-SCALE EFFECTS OF PHOTOINDUCED SURFACE OXYGEN VACANCIES ON THE CHARGE CARRIER DYNAMICS OF TiO_2"

Bugrahan Guner[a], Orcun Dincer[a], and Omur E. Dagdeviren[a]

[a]Department of Mechanical Engineering, École de Technologie Supérieure,
1100 Notre-Dame West, Montreal, Quebec, Canada H3C 1K3

Paper published in *ACS Applied Energy Materials*[8], March 2024

Appendix III.A – Sample Preparation

Appendix III.A.1 – Preparation of the Template-Stripped Gold

We followed a well-established methodology to produce the template-stripped gold sample. [102, 103] A gold film with a thickness of ~100 nm was evaporated (by Thermionics Vacuum Products, model VE-90) with a rate of ~0.1 nm/s under vacuum conditions (i.e., 10^{-5} mbar) on a silicon wafer. The silicon substrates were cleaned by using acetone and isopropanol followed by an ultrasonic cleaning with ethanol and eventually dried by using nitrogen. Clean silicon pieces (5 mm x 10 mm) were glued on the evaporated gold with epoxy (EPO-TEK 377) and cured for one hour at 150 °C forming a silicon/gold/epoxy/silicon structure. The clean gold surface attached to small silicon pieces was scraped off from the silicon wafer before measurements.

Appendix III.A.2 – Preparation of TiO_2

We employed a single crystal, undoped TiO_2 (100) sample (by MSE Supplies LLC). We applied an established recipe, as explained elsewhere. [35] In summary, we annealed the sample at 1270K for 10 hours, in addition to the cooling down and heating periods, ~3 hours

---

[8] Bugrahan Guner (2024, *p.* 2292-2298)

each. This results in atomically flat terraces with no clusters of carbon contamination and leads to a rutile surface. [35]

The anatase phase is more prone to adsorption of substances in air, particularly under irradiation. [212, 352] For this reason, unintentional radicals on the surface are expected to hamper the intrinsic sample properties by altering the extraction of surface oxygen vacancy effects over charge carrier dynamics. [35] As a result, we employed the rutile surface rather than anatase, as the rutile is more stable for all temperatures under ambient conditions. [208-211]

We performed our measurements on the (100) surface rather than the (110) surface. The (110) surface is a more stable configuration compared to the (100) surface. [329, 330] However, the coordination number of Ti atoms can be either five or six on the (110) surface, while Ti atoms on the (100) surface have only a coordination number of five. [331] We wanted to exclude different potential contributions of different Ti sites to the charge carrier dynamics. For this reason, we employed the (100) surface for our measurements. In passing, as an outlook, we want to note that performing similar experiments on the (110) surface with high spatial resolution, i.e., atomic resolution can be interesting to disclose the intrinsic contributions of five and six-coordinated Ti sites; however, this is beyond the scope of this work.

Appendix III.A.3 – Preparation of Gold Nanoparticles-deposited TiO_2

We deposited gold nanoparticles (Au-NPs) on the TiO_2 (100) surface by implementing a well-established recipe, as detailed elsewhere. [14] Here, we summarize the procedure. Citrate-capped Au-NPs (nominal diameter = 40 nm, produced by Sigma-Aldrich, PubChem substance number = 329765547) were functionalized with 4-mercaptobenzoic acid (i.e., 4-MBA, produced by Tokyo Chemical Industry, Chemical Abstracts Service registry number = 1074-36-8). The final solution was centrifuged at 6000 rpm for 6 minutes and washed with deionized water to separate Au-NPs. ~2 µl of the solution was applied to the TiO_2 sample with a micropipette. The TiO_2 sample was heated for ~30 seconds on a hot plate (100 °C) to evaporate the solution. The regions with Au-NP coverage were visually visible. As Figure-A III.1a

exemplifies, the deposition was evident under the light microscope. We also performed scanning electron microscopy (Figure-A III.1b and III.1c) and energy-dispersive X-ray measurements (Figure-A III.1d) to verify the deposition of Au-NPs. Our energy-dispersive X-ray measurements illustrate that we have an Au presence on the surface. Nevertheless, the observation of additional peaks such as carbon, oxygen, etc. can be linked to the exposure of the sample to ambient conditions, as well as the vacuum level of the electron microscopy system (~10^{-6} mbar). Moreover, the thickness of the sample and the energy level of the energy-dispersive X-ray measurements impede the stoichiometric assessment of results. [353, 354]

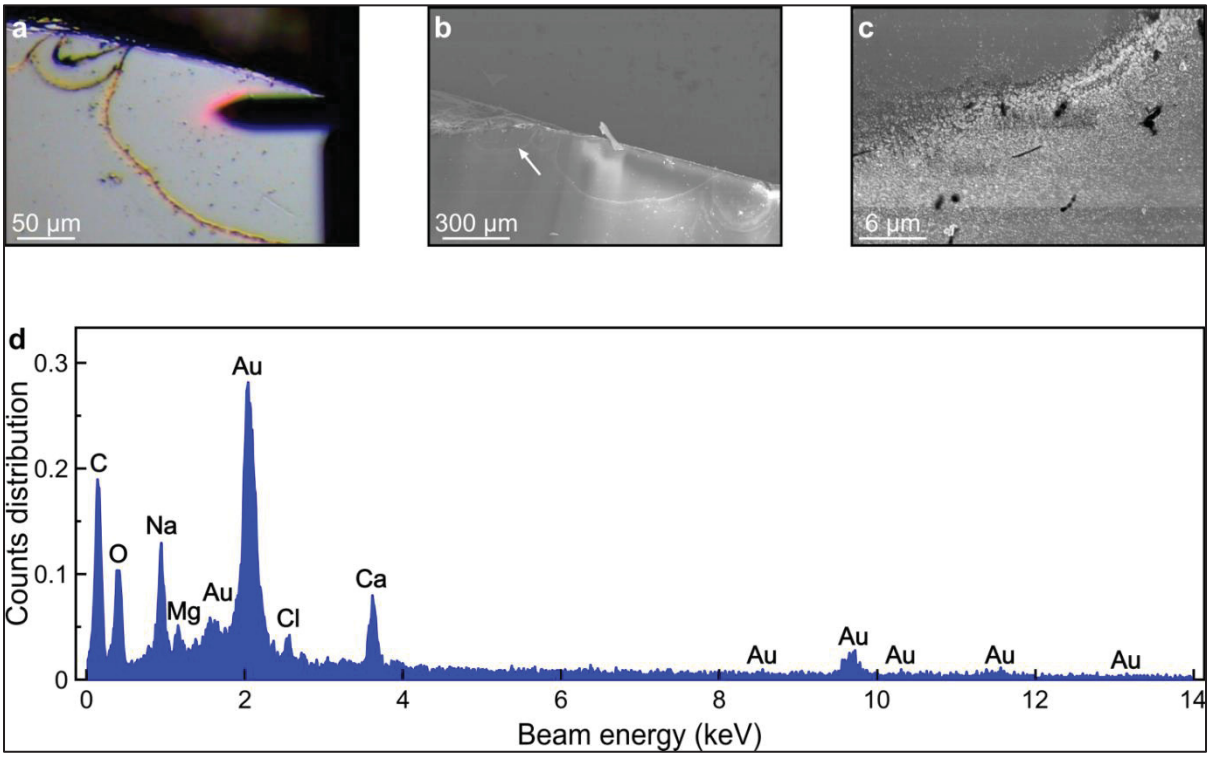

Figure-A III.1 Measurements to illustrate the presence of gold nanoparticles (Au-NPs) on the TiO_2 surface

The optical image shows a transition region as a diffraction pattern, the boundary of the evaporation of 4-mercaptobenzoic acid-functionalized Au-NP solution upon deposition (see Figure-A III.1a). The same region was imaged with a scanning electron microscope (Hitachi S-3600N). The small white arrow in Figure-A III.1b shows the region presented in Figure-A

III.1c. In Figure-A III.1d, the energy-dispersive X-ray measurements were performed in a zoomed-in region within Figure-A III.1c, employing 15 kV with 97 counts in ~450 seconds.

To overcome the limitations of the energy-dispersive X-ray measurements, we performed high-resolution, atomic force microscopy-based topography measurements to ensure a successful deposition of Au-NPs across the regions where we performed our experiments, as presented in Figure-A III.2. Our topography measurement in Figure-A III.2c covers the exact region where we performed our time-resolved atomic force microscopy experiments. In Figure-A III.2c, Au-NPs cover ~37% of the surface area. Figure-A III.2d illustrates that we identified 56 complete/unshielded (i.e., no overlapping) Au-NPs within the region and excluded the partial Au-NP at the borders. The average size of Au-NPs in the measurement region is 7977 ± 1870 nm2 (measured by employing 56 complete Au-NPs within Figure-A III.2d) with a height of 46.4 ± 8.5 nm (measured by the height difference of the peak point of each Au-NPs versus TiO_2 substrate along the fast scan direction), which is consistent with the specifications of deposited Au-NPs (*vide supra*).

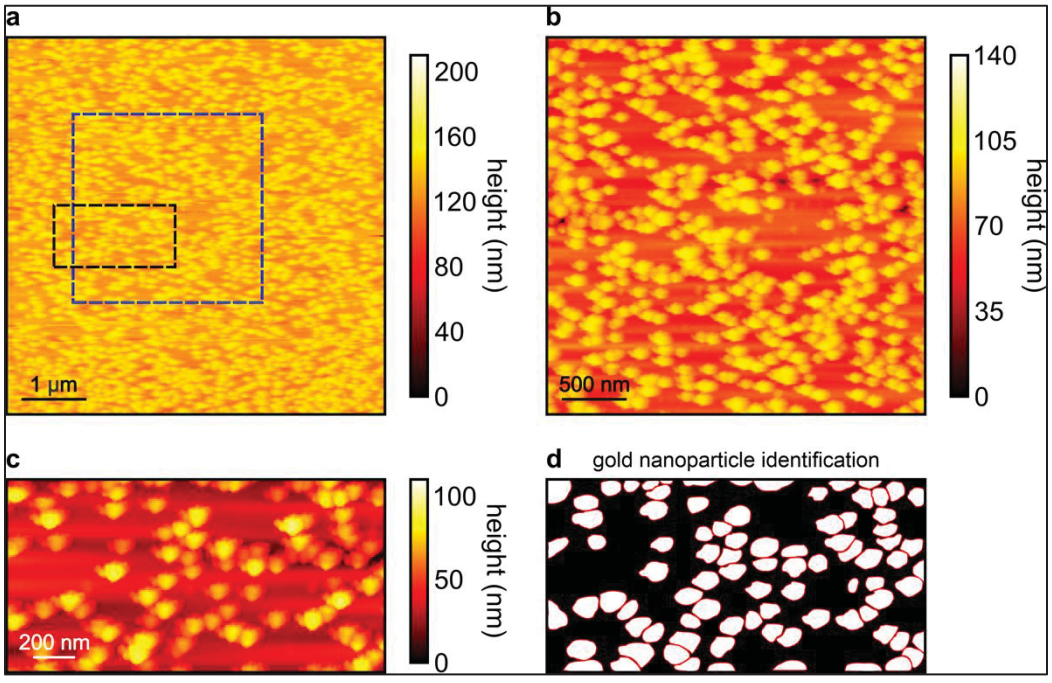

Figure-A III.2 Atomic-force microscopy-based topography measurement of gold nanoparticle (Au-NP)-deposited TiO_2 sample

In Figure-A III.2a, the topography image shows deposited Au-NPs over the TiO_2 surface.In Figure-A III.2b and Figure-A III.2c are zoomed-in regions presented with blue square and black rectangle in Figure-A III.2a. Figure-A III.2c shows the exact region where the time-resolved measurements were performed. Employing image processing, we identified Au-NPs and quantified their physical properties, e.g., average size, and height, across the region where we performed time-resolved measurements.

Appendix III.B – Time-resolved Scanning Probe Microscopy Measurements

The time-resolved scanning probe microscopy measurements were conducted employing a customized VEECO Enviroscope system. [61] As detailed elsewhere, [61] we integrated new hardware (e.g., a lock-in amplifier with phase-locked loop capacity, a high-voltage amplifier, and a new controller) and software into the microscope while utilizing its environmental control features. The microscope was controlled with the Gnome X Scanning Microscopy (also known as GXSM) control module [159] with active drift control while employing an MFLI-lock-in amplifier (by Zurich Instruments) with phase-locked loop capability for frequency shift detection. For all our experiments, we utilized gold-coated microcantilever tips by OPUSTIPS (4XC-GG, tip radius < 30 nm, stiffness ≈ 9.0 N/m, resonance frequency ≈ 150 kHz). The standard frequency-modulation atomic force microscopy technique, which relies on the resonance frequency shift, Δf, of the oscillation cantilever due to tip-sample interaction, was used for conventional time-resolved atomic force microscopy measurements. [72] We used an oscillation amplitude of ~10 nm peak-to-peak for our measurements.

To successfully record the real-time oscillation signal of the cantilever, we further upgraded the microscope electronics, with a digitizer (PicoScope 4824A) and arbitrary function generator (Tektronix AFG31051), as shown in Figure-A III.3. As mentioned in the main text and detailed in the supplemental information (*vide infra*), the probe was retracted away from the surface to perform time-resolved measurements. The GXSM control module retracts the tip away from the surface based on the topography line profile. More specifically, for each scan line, first, the topography was measured, and the tip was lifted by 15 nm at each point

while performing sub-microsecond TR-AFM measurements, ~40 times at each pixel (100 pixels/line, 18 nm/pixel). A voltage pulse was applied by the GXSM controller to the digitizer to inform/trigger the digitizer, V_{trigger1}. Upon triggering, the digitizer outputted another triggering signal, V_{trigger2}, to the lock-in amplifier when the phase of the oscillation signal was 0° with respect to the excitation signal, a_{exc}. With the receipt of the triggering signal, V_{trigger2}, the lock-in amplifier turned off the phase-locked loop operation and outputted another signal to trigger the function generator, V_{trigger3}. The output of the arbitrary function generator, V_{bias}, was applied to the sample. The delays due to cabling and data processing were optimized experimentally to ensure that the tip-sample bias voltage was applied to an exact phase of the oscillation signal.

The oscillation data was recorded for 750 microseconds in total (125 microseconds before the initial trigger of the GXSM (i.e., V_{trigger1}) and 625 microseconds after the start of the pulse) with a 20 MHz sampling rate (*vide infra*). Upon the completion of the measurement, the phase-locked loop was turned on, as V_{trigger2} was off, and then the probe approached the surface with active feedback control based on Δf or amplitude setpoint.

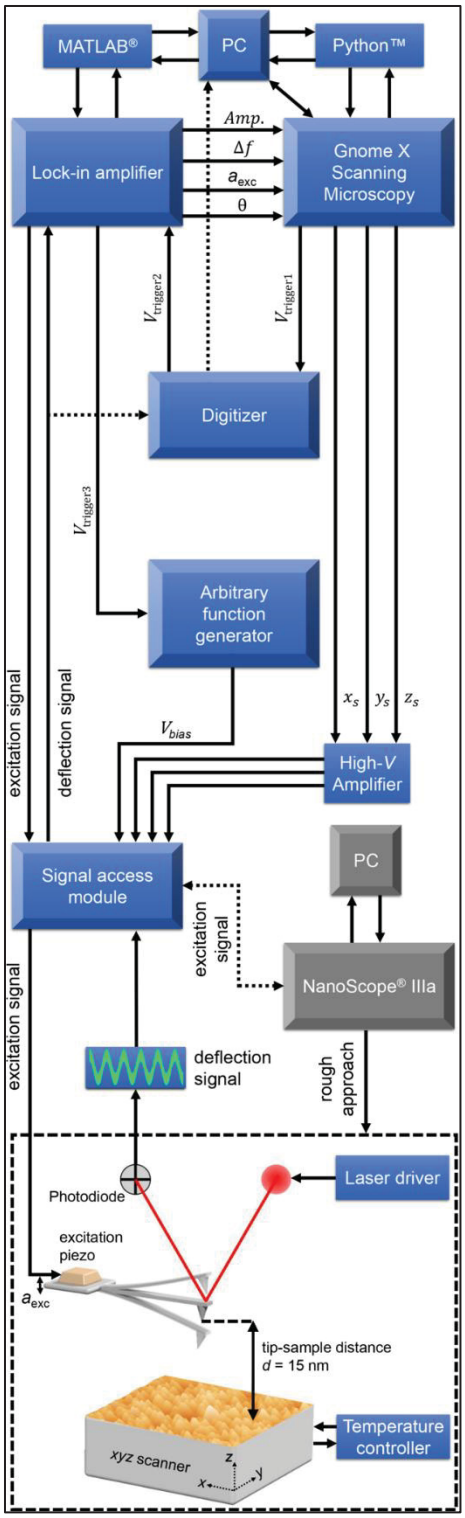

Figure-A III.3 The utilized control architecture for sub-microsecond time-resolved atomic force microscopy measurements

The experiment customization and automation have been rationalized through SoftdB controller with Gnome X Scanning Microscopy (GXSM) software. The deflection signal of the cantilever was accessed via the Signal Access Module™ (SAM). The outputs of the phase-locked loop, i.e., the resonance frequency shift, Δf, demodulated oscillation amplitude, the phase difference between the excitation and the oscillation signal, θ, and the excitation signal, a_{exc}, are directed to the GXSM to control tip-sample separation. The small signal outputs of the GXSM (x_s, y_s, z_s) for the piezo motion are amplified with a high-voltage amplifier. The voltage output of the GXSM is employed as the triggering signal of the digitizer, $V_{trigger1}$. As detailed in the text, the output of the digitizer triggers the lock-in amplifier, i.e., $V_{trigger2}$ and the signal output from the lock-in amplifier, $V_{trigger3}$, triggers the arbitrary function generator. The amplified piezo signals, a_{exc}, and the tip-sample bias voltage generated by the arbitrary function generator, V_{bias}, are inputs of the microscope and are exchanged via the SAM. The lock-in amplifier with phase-locked loop capability, GXSM, and digitizer have continuous communication with MATLAB® and Python™ for control and automation. As explained in detail elsewhere, [61] we approach the surface with Nanoscope® IIIa and then switch to the GXSM controller.

Appendix III.C – Thermal Stability

Appendix III.C.1 – Thermal Stability of the Laboratory and the Sample

We controlled the thermal stability of the system before, during, and after measurements. The temperature of the microscopy laboratory was regulated with a controlled heating, ventilating, and air conditioning (a.k.a., HVAC) system continuously. The temperature in the laboratory was 19.6 ± 0.7 °C, while the corresponding relative humidity level was 37.4 ± 2.3 % with the active temperature and humidity control. This level of temperature and humidity stability is important for the performance of electronic hardware, which may be sensitive to temperature variations due to integrated circuit elements.

To measure and control the microscope and the sample temperature, we employed two thermocouples (PT-1000) with a temperature resolution of 0.01 °C. One of the thermocouples

was within the sample holder and the other one was right under the sample itself. The temperature of the sample was regulated with the thermocouple underneath the sample by employing a LakeShore 331 controller. However, the second thermocouple, i.e., the one within the sample holder, was monitored to observe temperature stability. Once we set the temperature of the sample, we waited overnight for the thermal equilibrium of the entire microscope chamber. It is important to note that we did not observe any temperature or heating power change in the sample upon high-energy ultraviolet irradiation.

Appendix III.C.2 – Thermal Stability of the Cantilever Probe

The temperature of the cantilever was not actively controlled. However, we waited overnight to stabilize the temperature of the system for our temperature-dependent measurements. During this period, the cantilever was ~5 millimeters away from the sample. For this reason, the thermal equilibrium was reached before we performed our measurements. The other factor that may alter the temperature of the cantilever is high-energy ultraviolet (UV) irradiation. As we did not measure the temperature of the cantilever, we monitored parameters, e.g., resonance frequency, that would directly change due to temperature, to ensure the thermal stability of the cantilever upon UV irradiation. We did not observe any resonance frequency change in the cantilever due to UV irradiation. Nevertheless, as Figure-A III.4 shows, we performed thermal spectrum measurements of the cantilever without and with UV irradiation (power density = 2.5 mW/cm^2, ~two times the UV power density that we normally employed during our time-resolved atomic force microscopy measurements). Figure-A III.4 illustrates that the thermal spectrum of the cantilever is inert to UV irradiation, which implies that the temperature of the cantilever does not change (at a measurable amount) due to UV irradiation.

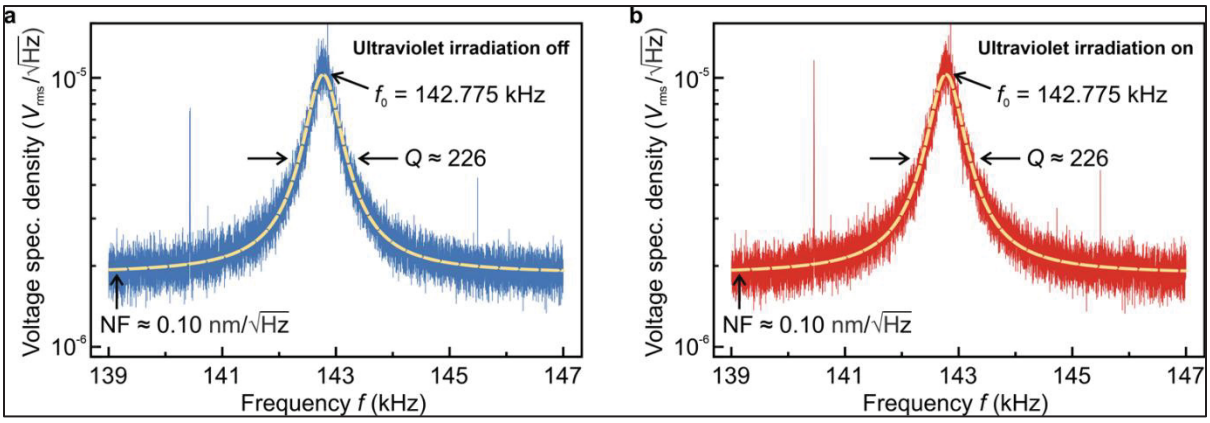

Figure-A III.4 Thermal spectra measurement of a cantilever for ultraviolet (UV) irradiation off (a) and UV irradiation on (b) cases

The resonance frequency was calculated with Lorentzian curves (dashed lines) in Figure-A III.4. Figure-A III.4a and Figure-A III.4b demonstrate that there was no measurable effect of UV irradiation on the cantilever's thermal spectra. The voltage spectral densities presented in this figure were recorded at room temperature (19.5 °C) under ambient conditions and averaged 50 times. The bandwidth of the measurement was 469 kHz, and a built-in Hanning window filter was employed.

Appendix III.D – Optimization of the Sampling Rate

The digitizer that we employed, i.e., PicoScope 4824A, has 256 mega samples buffer memory. As Figure-A III.5 shows, we collected data at 10 MHz, 20 MHz, 40 MHz, and 80 MHz sampling rates on a template-stripped gold sample. We varied the decay times of the tip-sample bias voltage, i.e., τ, 1 μs-100 μs, to optimize the sampling rate. Our measurements illustrate that decay times larger than 20 μs, result in statistically the same decay time for the first peak, i.e., t_{fp}, for all sampling rates; however, for faster decay times the response is limited by the measurement system. [58, 59] Moreover, with increasing sampling rates, i.e., 40 and 80 MHz, the computation cost to post-process data increases significantly. In addition, higher sampling rates limit the number of repetitions per pixel due to the limited storage capability of the digitizer. For these reasons, we used a sampling rate of 20 MHz for our sub-microsecond time-resolved atomic force microscopy measurements, which enabled us to maximize the number of repetitions per pixel and optimize the signal-to-noise ratio.

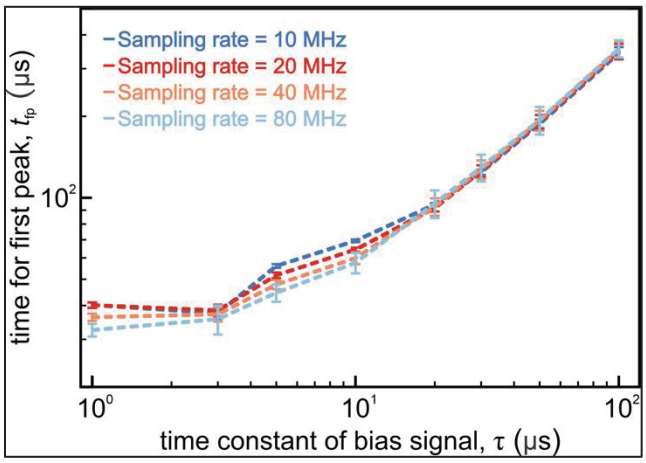

Figure-A III.5 The measurements to optimize the sampling rate

We performed sub-microsecond time-resolved atomic force microscopy measurements on a template-stripped gold sample to optimize the sampling rate of the data digitizer, i.e., PicoScope 4824A. Our measurements show that sampling rates higher than 20 MHz yield the same time for the first peak, t_{fp}, for the time constant of the bias signal, τ, larger than 20 µs. However, higher sampling rates limit data repetition at each pixel (required to enhance the signal-to-noise ratio) and increase the cost of computation required for post-processing. For these reasons, we used a 20 MHz sampling rate for our measurements.

Appendix III.E – Optimization of the Tip-Sample Separation

We performed experiments for two different tip-sample bias voltages, V_{bias}, to check the effect of the tip-sample separation, d, on the time for the first peak, t_{fp}, measurements over template-stripped gold samples. As Figure-A III.6 shows, for $d < 10$ nm, the t_{fp} values have strong variations due to excess tip-sample interaction upon the applied electric field. More specifically, at small tip-sample separations, $d \leq 10$ nm, the cantilever was exposed to very strong, attractive Coulombic forces which constrained the motion of the cantilever and restrained the oscillation at the free end of the probe while promoting non-linear oscillations. Employing an oscillation amplitude of 10 nm peak-to-peak, this effect did not fully fade away at $d = 10$ nm. Nevertheless, our measurements also reveal that the variation of the measured t_{fp} increases monotonically for $d \geq 20$ nm due to weakening tip-sample interaction force with

increasing distance. For these reasons, we employed a $V_{bias} = 7\ V_{pp}$ with a $d = 15$ nm for our measurements.

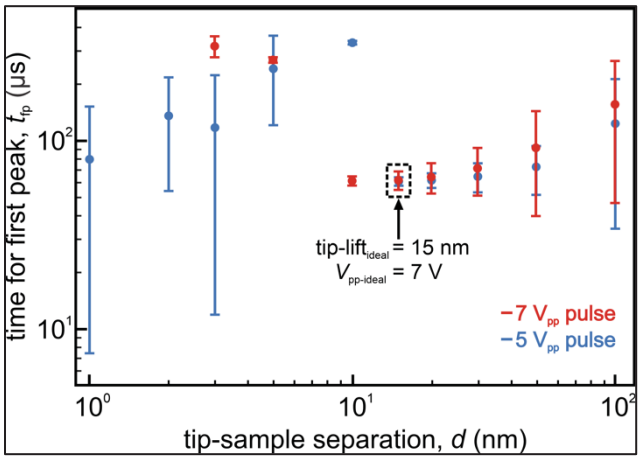

Figure-A III.6 The measurements to optimize the time constant of the tip-sample bias voltage

We performed sub-microsecond time-resolved atomic force microscopy measurements on a template-stripped gold sample with different tip-sample bias voltages (7 V_{pp} and 5 V_{pp}) and tip-sample separations, 1 nm < d < 100 nm. Our measurements show that, for $d \leq 10$ nm, the time for the first peak, t_{fp}, has strong variations due to excess tip-sample interaction of the applied electric field. Nevertheless, for $d \geq 20$ nm, the variation of t_{fp} increases monotonically with decreasing tip-sample interaction. As a result, we employed $V_{pp\text{-}ideal} = 7\ V_{pp}$ with a tip-lift$_{ideal}$ = 15 nm for our measurements.

Appendix III.F – Fast Timescale, Temperature-Dependent Measurements

We performed temperature-dependent sub-microsecond time-resolved atomic force microscopy measurements at 25 °C and 66 °C, as presented in Figure-A III.7. Differences in the measured time for the first peak, t_{fp}, values are minute, 92.74 ± 0.64 μs and 92.42 ± 0.68 μs respectively; however, our statistical analysis (one-sided equality of means test, i.e., t-test) showed that t_{fp} values at different temperatures are statistically different. For this reason, we believe that the measured difference is physical. However, it would be better to measure the temperature-dependent dynamics of fast charge carriers for a wider temperature range to reveal their migration barrier. Nevertheless, this is beyond the scope of this work. Comparing our

results/methods with the literature, we want to note that with our time-resolved experiments, we measured the migration dynamics of charge carriers, which is different than the transient electron injection measured with time-resolved X-ray photoelectron spectroscopy. [252] Being two physically different phenomena, the time scale of migration dynamics and electron injection are different.

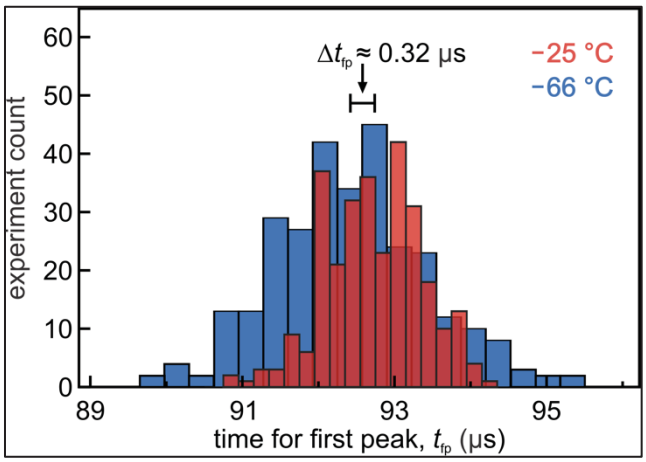

Figure-A III.7 The temperature-dependent time constant (i.e., time for the first peak, t_{fp}) measurements of fast charge carriers (i.e., electrons) across pristine TiO_2 (100) sample

The t_{fp} values were measured at 25 °C (red histogram) and 66 °C (blue histogram). Our results illustrate that t_{fp} values decreased with increasing temperature and the decrease was justified with a statistical test (i.e., t-test); however, the measured difference, Δt_{fp}, was minuscule numerically. As the measured difference was rather small, we repeated measurements 800 times instead of 40 times for ~300 data points to further enhance the signal-to-noise ratio.

Appendix III.G – Effect of Surface Irradiation Power Density

Figure-A III.8 shows measurements at different high-energy ultraviolet (UV) irradiation levels to reveal the effect of surface irradiation power density on migration time constants, τ^*. Our results illustrate that with increasing power density of surface irradiation, the measured time constants for slow charge carriers (*i.e.*, holes) decrease. In addition, our successive measurements show that the surface recovers upon termination of surface irradiation.

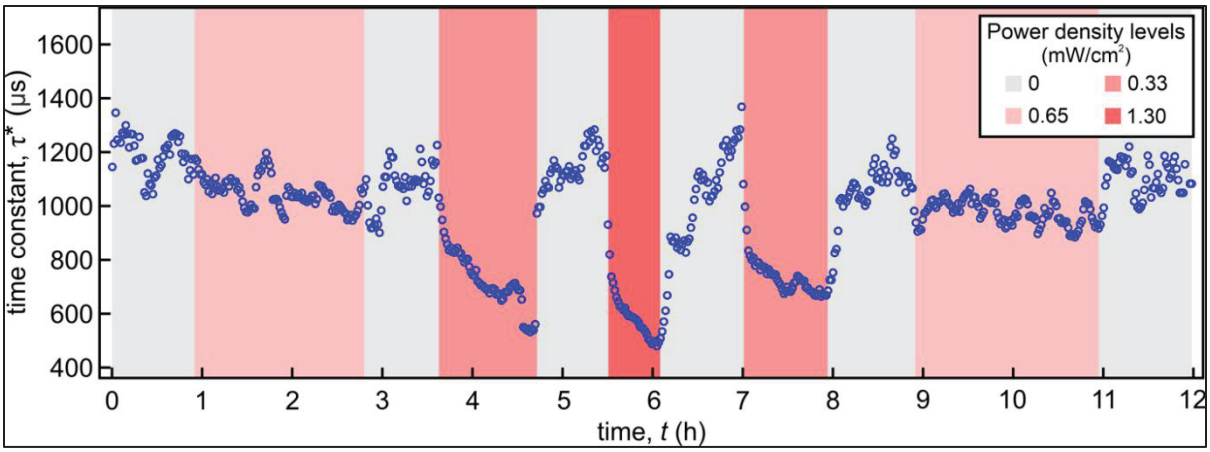

Figure-A III.8 Successive measurements of the effect of surface irradiation power density on the time constant of slow charge carriers, τ^*

Conventional time-resolved atomic force microscopy measurements were performed on a pristine TiO_2 (100) sample under different high-energy ultraviolet (UV) irradiation levels. Our measurements show that with increasing UV power density, τ^* decreases. Moreover, the surface recovers upon termination of UV irradiation.

Appendix III.H – Identification of Gold Nanoparticles

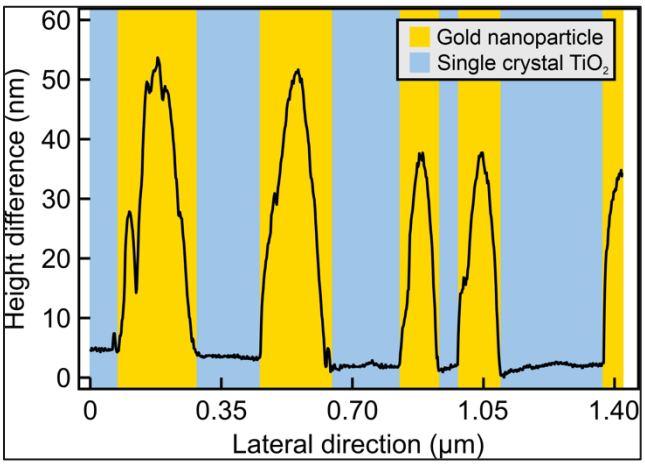

Figure-A III.9 Identification of regions with gold nanoparticles (Au-NPs)
We identified Au-NPs on each scan line automatically by applying the height difference of the Au-NPs with respect to the single-crystal TiO_2 (100) surface.

Appendix III.I – Relation Between Activation Energy and Charge Carrier Mobility

Charge carrier motion in the bulk of a material can be simulated through Einstein's random walk relation. The diffusion coefficient, D_c, is extracted from Einstein's random walk relation as: [109]

$$D_c = \frac{<\Delta r^2>}{2\alpha t} \quad \text{(AIII.1)}$$

Where the mean-square displacement, $< \Delta r^2 >$, refers to the displacement of a particle's diffusion, t is the duration of the diffusion and α is the dimensionality of the process. Also, the mean-square displacement can be represented by using the jump length (l) and number of jumps (N).

$$< \Delta r^2 > = N l^2 \quad \text{(AIII.2)}$$

As given through Equations AIII.1 and AIII.2, total jump events can be represented through the nearest neighboring sites for potential jumps, n, hopping rate (frequency of the jump occurrence phenomenon) associated with jumping events, Γ.

$$N = n\Gamma t \quad \text{(AIII.3)}$$

The individual defect jump rate is given as: [355]

$$\Gamma = \tilde{\nu} e^{\frac{-\Delta F_e}{k_B T}} \quad \text{(AIII.4)}$$

In Equation AIII.4, T is the absolute temperature, k_B is the Boltzmann's constant, $\tilde{\nu}$ is the effective frequency of defect vibration at the saddle point, ΔF_e is the energy needed for the defect movement from initial equilibrium to the saddle point, *i.e.*, the free energy change between the initial equilibrium (charge carrier position) and kinetic barrier (energy required

for the hopping event). By rearranging Equation AIII.4, the hopping rate equation is obtained and expressed as: [41, 105]

$$\Gamma \approx \frac{k_B T}{h} e^{\frac{-\Delta F_e}{k_B T}} \tag{AIII.5}$$

where h is the Planck's constant. If the free energy is divided into its total energy and entropic components, it can be expressed as: [356]

$$\Delta F_e = \Delta E - T\Delta S \tag{AIII.6}$$

where ΔE corresponds to the diffusion activation energy barrier (ΔE=E_a) and ΔS refers to the vibrational entropy. Regarding the charge carrier mobility approximation, comparatively, the local vibrational frequency component is negligible concerning the initial state vibrational frequency for the temperature range that we performed our measurements (i.e., at around room temperature). [357] Thus, the entropy component approximates to zero. For crystalline materials within a similar temperature range, this assumption is regularly utilized. [41, 358]

$$\Delta S = \Delta S_{vib} \cong 0 \tag{AIII.7}$$

To connect the diffusion coefficient to mobility, one can express the diffusion coefficient for a charged particle within Einstein's diffusion relation concept. [109]

$$D_c = \frac{\mu_e k_B T}{q} \tag{AIII.8}$$

In Equation AIII.8, μ_e is the electrical mobility for a charged particle, where q is the electric charge of a charge carrier. To retrieve the mobility in our case, one can combine given equations. If Equation AIII.1 is rewritten by substituting Equation AIII.2 and AIII.3:

$$D_c = \frac{<\Delta r^2>}{2\alpha t} = \frac{Nl^2}{2\alpha t} = \frac{n\Gamma t l^2}{2\alpha t} = \frac{n\Gamma l^2}{2\alpha} \tag{AIII.9}$$

Inserting Equation AIII.5 into Equation AIII.9 results in:

$$D_c = \frac{n\Gamma l^2}{2\alpha} = \frac{nl^2}{2\alpha}\frac{k_B T}{h} e^{\frac{-\Delta F}{k_B T}} \tag{AIII.10}$$

If the Equation AIII.7 condition is applied to Equation AIII.6 and resultant relation is inserted to Equation AIII.10, it leads to:

$$D_c = \frac{nl^2}{2\alpha}\frac{k_B T}{h} e^{\frac{-E_a}{k_B T}} \tag{AIII.11}$$

As the diffusion coefficient and mobility relation were given in Equation AIII.8, if we equate the diffusion coefficient in Equation AIII.11, we can obtain the final mobility relation.

$$\frac{nl^2}{2\alpha}\frac{k_B T}{h} e^{\frac{-E_a}{k_B T}} = D_c = \frac{\mu_e k_B T}{q} \tag{AIII.12}$$

$$\mu_e = \frac{qnl^2}{2\alpha h} e^{\frac{-E_a}{k_B T}} \tag{AIII.13}$$

Equation AIII.13 reveals the bulk activation barrier and mobility relation depending on the hopping distance, l, and potential neighbouring locations that it can happen to. To correlate the time constant associated with charge carrier migration, τ^*, and mobility, we can use the diffusion relation [109] and one can write the generalized mobility, *i.e.*, $\mu = \mu_e/q$, as the ratio of a particle's terminal drift velocity, v_d, to the applied force, F.

$$\mu = \frac{v_d}{F} \tag{AIII.14}$$

In our case, the drift velocity is the electron drift velocity caused by the electric field. The force is the electrical force applied through the created electric field over the sample surface by the tip-sample bias voltage. Hence, the electrical force, F_e, is represented as:

$$F = F_e = Eq \tag{AIII.15}$$

where E is the magnitude of the applied electric field. If Equation AIII.15 is substituted into Equation AIII.14, we obtain the electrical mobility.

$$\mu_e = \frac{v_d}{E} \tag{AIII.16}$$

Also, the drift velocity can be stated in terms of τ^*, the effective mass of the particle, m, and F_e in the following form. [268, 269]

$$v_d = \frac{\tau^* Eq}{m} \tag{AIII.17}$$

As a result of Equations AIII.16 and AIII.17, it is possible to correlate the measured τ^*changes with mobility variations, which then can be interpreted for charge carrier motion analysis and optimization.

APPENDIX IV

SUPPLEMENTARY INFORMATION OF THE ARTICLE "ULTRAVIOLET IRRADIATION PENETRATION DEPTH ON TiO_2"

Bugrahan Guner[a], Mohammad Safikhani-Mahmoudi[a], Fengmiao Li[b,c], Ke Zou[b,c], and Omur E. Dagdeviren[a]

[a]Department of Mechanical Engineering, École de Technologie Supérieure, 1100 Notre-Dame West, Montreal, Quebec, Canada H3C 1K3

[b]Department of Physics and Astronomy, University of British Columbia, Vancouver, British Columbia, Canada, V6T 1Z1

[b]Quantum Matter Institute, University of British Columbia, Vancouver, British Columbia, Canada, V6T 1Z4

Paper published in *Communications Chemistry*[9], March 2025

Appendix IV.A – X-ray Diffraction Measurements

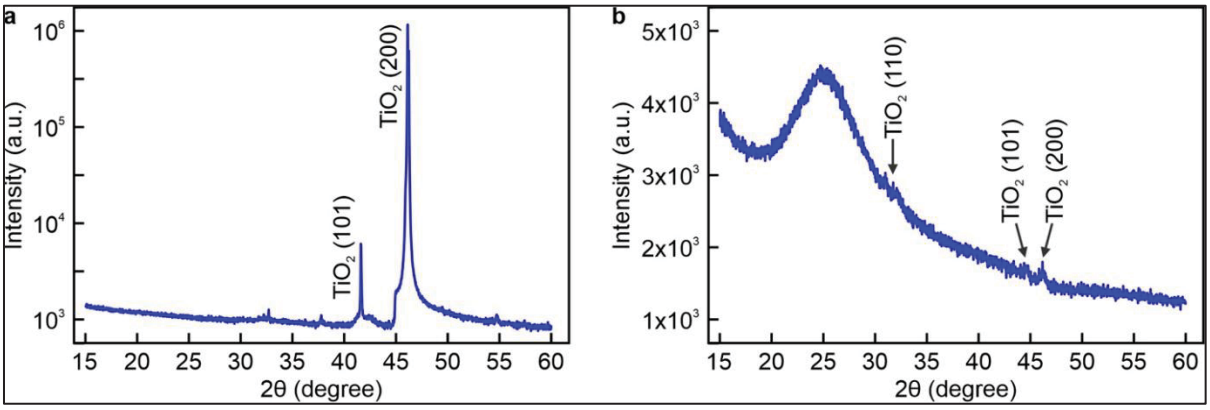

Figure-A IV.1 X-ray diffraction measurements of single crystal TiO_2 and 46-nm thick TiO_2 film grown on quartz

X-ray diffraction (XRD) measurements were performed by employing a PANalytical X'Pert PRO, which was operated with a Co X-ray source with Co K_{α_1} (λ= 1.78901 Å) and Co K_{α_2} (λ=

[9] Bugrahan Guner (2025, *p.* 83)

1.7929 Å) emitted with an intensity ratio (K_{α_2} / K_{α_1}) of 0.5 at a resolution of 0.0167° by employing a generator voltage of 45 kV and tube current of 40 mA at 200 seconds per step sampling rate.

Figure-A IV.1a shows the XRD measurements of the single-crystal TiO_2 sample. The supplier, MSE Supplies LLC, reported that the TiO_2 crystal has (100) orientation, confirmed by our XRD measurements, revealing a sharp, intense peak at $2\theta \approx 46°$. [359, 360] Due to destructive interference (a.k.a., systematic absence), the (100) peak of TiO_2 is suppressed. [360] A second peak is visible at $2\theta \approx 42°$, corresponding to the (101) plane; however, it has two orders of magnitude less intensity than the (200) peak. [359, 361-363] The powder form of rutile would ordinarily give (110) and (101) the most intense peaks. However, these peaks are absent relative to the (200) peak. These observations support the supplier report of the (100) surface. The lattice constant corresponding to the most dominant peak, i.e., (200), is calculated as 4.5786 Å, while the tetragonal lattice constant ($a = b \neq c$) of rutile TiO_2 is $a = 4.5937$ Å. [364]

Figure-A IV.1b shows the XRD measurement of 46-nm thick, polycrystalline TiO_2 film on the quartz substrate. The XRD data have a background due to the quartz substrate, e.g., ~25° peak, which is consistent with the literature. [35] Distinct reflections appear around 31°, 44°, and 46°, which are relevant to polycrystalline rutile TiO_2, specifically the (110), (101), and (200) planes. [359, 361-363] The thin-film nature (~46 nm) and polycrystalline microstructure cause these peaks to be broad and low-intensity, in contrast to the stronger reflections typically observed in bulk. [365] We did not observe characteristics of anatase, indicating that the film is predominantly rutile.

LIST OF BIBLIOGRAPHICAL REFERENCES

[1] R. Boyle, *The sceptical chymist*. London : Dent; New York : Dutton, [1964], 1964.

[2] A. L. Lavoisier, *Elements of chemistry : in a new systematic order, containing all the modern discoveries*. Edinburgh : W. Creech, 1790., 1790.

[3] P. Duhem, "The Law of Definite Proportions," in *Mixture and Chemical Combination: And Related Essays*, P. Duhem Ed. Dordrecht: Springer Netherlands, 2002, pp. 34-42.

[4] J. Dalton, *A New System of Chemical Philosophy*. Manchester, England: Executors of S. Russell (in English).

[5] J. J. Thomson, "XL. Cathode Rays," *The London, Edinburgh, and Dublin Philosophical Magazine and Journal of Science,* vol. 44, no. 269, pp. 293-316, 1897/10/01 1897, doi: 10.1080/14786449708621070.

[6] E. Rutherford, "The scattering of α and β particles by matter and the structure of the atom," *Philosophical Magazine,* vol. 92, no. 4, pp. 379-398, 2012/02/01 2012, doi: 10.1080/14786435.2011.617037.

[7] N. Bohr, "I. On the constitution of atoms and molecules," *The London, Edinburgh, and Dublin Philosophical Magazine and Journal of Science,* vol. 26, no. 151, pp. 1-25, 1913/07/01 1913, doi: 10.1080/14786441308634955.

[8] H. Kragh, *Quantum generations : a history of physics in the twentieth century*, Princeton, N.J.: Princeton University Press, 1999. [Online]. Available: https://search.ebscohost.com/login.aspx?direct=true&scope=site&db=nlebk&db=nlabk&AN=2444779.

[9] G. Binnig and H. Rohrer, "Scanning tunneling microscopy," *Helvetica Physica Acta,* vol. 55, no. 6, p. 726, 1982, doi: 10.5169/seals-115309.

[10] G. Binnig, C. F. Quate, and C. Gerber, "Atomic Force Microscope," *Physical Review Letters,* vol. 56, no. 9, pp. 930-933, 03/03/ 1986, doi: 10.1103/PhysRevLett.56.930.

[11] Y. Zhou *et al.*, "Defect engineering of metal–oxide interface for proximity of photooxidation and photoreduction," *Proceedings of the National Academy of Sciences,* vol. 116, no. 21, pp. 10232-10237, 2019, doi: doi:10.1073/pnas.1901631116.

[12] Y. Zeng, Z. Lai, Y. Han, H. Zhang, S. Xie, and X. Lu, "Oxygen-Vacancy and Surface Modulation of Ultrathin Nickel Cobaltite Nanosheets as a High-Energy Cathode for Advanced Zn-Ion Batteries," *Advanced Materials,* vol. 30, no. 33, p. 1802396, 2018, doi: https://doi.org/10.1002/adma.201802396.

[13] S. Ben-Jaber *et al.*, "Photo-induced enhanced Raman spectroscopy for universal ultra-trace detection of explosives, pollutants and biomolecules," *Nature Communications,* vol. 7, no. 1, p. 12189, 2016/07/14 2016, doi: 10.1038/ncomms12189.

[14] D. Glass *et al.*, "Dynamics of Photo-Induced Surface Oxygen Vacancies in Metal-Oxide Semiconductors Studied Under Ambient Conditions," (in eng), *Adv Sci (Weinh),* vol. 6, no. 22, p. 1901841, Nov 2019, doi: 10.1002/advs.201901841.

[15] H. Wu, H. Wang, and G. Li, "Metal oxide semiconductor SERS-active substrates by defect engineering," *Analyst,* 10.1039/C6AN01959E vol. 142, no. 2, pp. 326-335, 2017, doi: 10.1039/C6AN01959E.

[16] G. Kiriakidis and V. Binas, "Metal oxide semiconductors as visible light photocatalysts," *Journal of the Korean Physical Society,* vol. 65, no. 3, pp. 297-302, 2014/08/01 2014, doi: 10.3938/jkps.65.297.

[17] J. L. Holechek, H. M. E. Geli, M. N. Sawalhah, and R. Valdez, "A Global Assessment: Can Renewable Energy Replace Fossil Fuels by 2050?," *Sustainability,* vol. 14, no. 8, p. 4792, 2022. [Online]. Available: https://www.mdpi.com/2071-1050/14/8/4792.

[18] A. O. M. Maka and J. M. Alabid, "Solar energy technology and its roles in sustainable development," *Clean Energy,* vol. 6, no. 3, pp. 476-483, 2022, doi: 10.1093/ce/zkac023.

[19] J. Liu, N. Ma, W. Wu, and Q. He, "Recent progress on photocatalytic heterostructures with full solar spectral responses," *Chemical Engineering Journal,* vol. 393, pp. 124719-124719, 2020, doi: 10.1016/j.cej.2020.124719.

[20] S. Sathish *et al.*, "Latest avenues on solar light-driven photocatalytic hydrogen generation using surface modified nanomaterials towards sustainable environment and circular bioeconomy," *Fuel,* vol. 340, pp. 127398-127398, 2023, doi: 10.1016/j.fuel.2023.127398.

[21] F. Wang, Q. Li, and D. Xu, "Recent progress in semiconductor-based nanocomposite photocatalysts for solar-to-chemical energy conversion," *Advanced Energy Materials,* vol. 7, no. 23, pp. 1700529-1700529, 2017.

[22] X. H. Chen, K. Tee, M. Elnahass, and R. Ahmed, "Assessing the environmental impacts of renewable energy sources: A case study on air pollution and carbon emissions in China," *Journal of Environmental Management,* vol. 345, p. 118525, 2023/11/01/ 2023, doi: https://doi.org/10.1016/j.jenvman.2023.118525.

[23] A. I. Osman *et al.*, "Cost, environmental impact, and resilience of renewable energy under a changing climate: a review," *Environmental Chemistry Letters,* vol. 21, no. 2, pp. 741-764, 2023/04/01 2023, doi: 10.1007/s10311-022-01532-8.

[24] Z. Li *et al.*, "Scalable fabrication of perovskite solar cells," *Nature Reviews Materials,* vol. 3, no. 4, p. 18017, 2018/03/27 2018, doi: 10.1038/natrevmats.2018.17.

[25] P. P. Boix, K. Nonomura, N. Mathews, and S. G. Mhaisalkar, "Current progress and future perspectives for organic/inorganic perovskite solar cells," *Materials Today,* vol. 17, no. 1, pp. 16-23, 2014/01/01/ 2014, doi: https://doi.org/10.1016/j.mattod.2013.12.002.

[26] T. Leijtens, K. A. Bush, R. Prasanna, and M. D. McGehee, "Opportunities and challenges for tandem solar cells using metal halide perovskite semiconductors," (in En), *Nature Energy,* ReviewPaper vol. 3, no. 10, pp. 828-838, 2018-07-09 2018, doi: doi:10.1038/s41560-018-0190-4.

[27] X. Yu, T. J. Marks, and A. Facchetti, "Metal oxides for optoelectronic applications," (in En), *Nature Materials,* ReviewPaper vol. 15, no. 4, pp. 383-396, 2016-03-23 2016, doi: doi:10.1038/nmat4599.

[28] H. Eidsvåg, S. Bentouba, P. Vajeeston, S. Yohi, and D. Velauthapillai, "TiO(2) as a Photocatalyst for Water Splitting-An Experimental and Theoretical Review," (in eng), *Molecules,* vol. 26, no. 6, Mar 17 2021, doi: 10.3390/molecules26061687.

[29] K. Perović *et al.*, "Recent Achievements in Development of TiO2-Based Composite Photocatalytic Materials for Solar Driven Water Purification and Water Splitting,"

Materials, vol. 13, no. 6, p. 1338, 2020. [Online]. Available: https://www.mdpi.com/1996-1944/13/6/1338.

[30] M. Rafique *et al.*, "Hydrogen Production Using TiO2-Based Photocatalysts: A Comprehensive Review," *ACS Omega,* vol. 8, no. 29, pp. 25640-25648, 2023/07/25 2023, doi: 10.1021/acsomega.3c00963.

[31] N. Shehzad, M. Tahir, K. Johari, T. Murugesan, and M. Hussain, "A critical review on TiO2 based photocatalytic CO2 reduction system: Strategies to improve efficiency," *Journal of CO2 Utilization,* vol. 26, pp. 98-122, 2018/07/01/ 2018, doi: https://doi.org/10.1016/j.jcou.2018.04.026.

[32] Q. Fatima, A. A. Haidry, H. Zhang, A. El Jery, and M. Aldrdery, "A critical review on advancement and challenges in using TiO2 as electron transport layer for perovskite solar cell," *Materials Today Sustainability,* vol. 27, p. 100857, 2024/09/01/ 2024, doi: https://doi.org/10.1016/j.mtsust.2024.100857.

[33] S. Paul, M. A. Rahman, S. B. Sharif, J.-H. Kim, S.-E.-T. Siddiqui, and M. A. M. Hossain, "TiO2 as an Anode of High-Performance Lithium-Ion Batteries: A Comprehensive Review towards Practical Application," *Nanomaterials,* vol. 12, no. 12, p. 2034, 2022. [Online]. Available: https://www.mdpi.com/2079-4991/12/12/2034.

[34] A. M. Elshahawy, S. M. Elkatlawy, M. S. Shalaby, C. Guan, and J. Wang, "Surface-Engineered TiO2 for High-Performance Flexible Supercapacitor Applications," *Journal of Electronic Materials,* vol. 52, no. 2, pp. 1347-1356, 2023/02/01 2023, doi: 10.1007/s11664-022-10084-0.

[35] O. E. Dagdeviren *et al.*, "The effect of photoinduced surface oxygen vacancies on the charge carrier dynamics in TiO2 films," *Nano Letters,* vol. 21, no. 19, pp. 8348-8354, 2021.

[36] F. Chen, T. Ma, T. Zhang, Y. Zhang, and H. Huang, "Atomic-Level Charge Separation Strategies in Semiconductor-Based Photocatalysts," *Advanced Materials,* vol. 33, no. 10, p. 2005256, 2021, doi: https://doi.org/10.1002/adma.202005256.

[37] D. Schweke, Y. Mordehovitz, M. Halabi, L. Shelly, and S. Hayun, "Defect Chemistry of Oxides for Energy Applications," *Advanced Materials,* vol. 30, no. 41, p. 1706300, 2018, doi: https://doi.org/10.1002/adma.201706300.

[38] B. Guner, O. Dincer, and O. E. Dagdeviren, "Fast and Slow Time-Scale Effects of Photoinduced Surface Oxygen Vacancies on the Charge Carrier Dynamics of TiO2," *ACS Applied Energy Materials,* vol. 7, no. 6, pp. 2292-2298, 2024/03/25 2024, doi: 10.1021/acsaem.3c03040.

[39] B. Guner and O. E. Dagdeviren, "Multidimensionality of the Contact Potential Difference at the Nanoscale in Inorganic Oxides," *ACS Applied Electronic Materials,* vol. 4, no. 8, pp. 4085-4093, 2022/08/23 2022, doi: 10.1021/acsaelm.2c00713.

[40] O. Dincer, B. Guner, and O. E. Dagdeviren, "Effect of methanol and photoinduced surface oxygen vacancies on the charge carrier dynamics in TiO2," *APL Materials,* vol. 12, no. 2, 2024, doi: 10.1063/5.0192058.

[41] O. E. Dagdeviren, A. Mascaro, S. Yuan, J. Shirani, K. H. Bevan, and P. Grütter, "Ergodic and Nonergodic Dynamics of Oxygen Vacancy Migration at the Nanoscale in Inorganic Perovskites," *Nano Letters,* vol. 20, no. 10, pp. 7530-7535, 2020/10/14 2020, doi: 10.1021/acs.nanolett.0c03002.

[42] S. Bai, N. Zhang, C. Gao, and Y. Xiong, "Defect engineering in photocatalytic materials," *Nano Energy,* vol. 53, pp. 296-336, 2018/11/01/ 2018, doi: https://doi.org/10.1016/j.nanoen.2018.08.058.

[43] A. Mascaro *et al.*, "Measuring Spatially Resolved Collective Ionic Transport on Lithium Battery Cathodes Using Atomic Force Microscopy," *Nano Letters,* vol. 17, no. 7, pp. 4489-4496, 2017/07/12 2017, doi: 10.1021/acs.nanolett.7b01857.

[44] D. Glass *et al.*, "Probing the Role of Atomic Defects in Photocatalytic Systems through Photoinduced Enhanced Raman Scattering," *ACS Energy Letters,* vol. 6, no. 12, pp. 4273-4281, 2021/12/10 2021, doi: 10.1021/acsenergylett.1c01772.

[45] R. Qian *et al.*, "Charge carrier trapping, recombination and transfer during TiO2 photocatalysis: An overview," *Catalysis Today,* vol. 335, pp. 78-90, 2019/09/01/ 2019, doi: https://doi.org/10.1016/j.cattod.2018.10.053.

[46] L. Zhang, H. H. Mohamed, R. Dillert, and D. Bahnemann, "Kinetics and mechanisms of charge transfer processes in photocatalytic systems: A review," *Journal of Photochemistry and Photobiology C: Photochemistry Reviews,* vol. 13, no. 4, pp. 263-276, 2012.

[47] H. L. Tan, F. F. Abdi, and Y. H. Ng, "Heterogeneous photocatalysts: an overview of classic and modern approaches for optical, electronic, and charge dynamics evaluation," *Chem Soc Rev,* vol. 48, no. 5, pp. 1255-1271, Mar 4 2019, doi: 10.1039/c8cs00882e.

[48] A. Litke, Y. Su, I. Tranca, T. Weber, E. J. M. Hensen, and J. P. Hofmann, "Role of Adsorbed Water on Charge Carrier Dynamics in Photoexcited TiO2," *The Journal of Physical Chemistry C,* vol. 121, no. 13, pp. 7514-7524, 2017/04/06 2017, doi: 10.1021/acs.jpcc.7b00472.

[49] C. Kranz and M. Wachtler, "Characterizing photocatalysts for water splitting: from atoms to bulk and from slow to ultrafast processes," *Chem Soc Rev,* vol. 50, no. 2, pp. 1407-1437, Jan 21 2021, doi: 10.1039/d0cs00526f.

[50] C. S. Ponseca, Jr., P. Chabera, J. Uhlig, P. Persson, and V. Sundstrom, "Ultrafast Electron Dynamics in Solar Energy Conversion," *Chem Rev,* vol. 117, no. 16, pp. 10940-11024, Aug 23 2017, doi: 10.1021/acs.chemrev.6b00807.

[51] R. A. De Souza, "Oxygen Diffusion in SrTiO3 and Related Perovskite Oxides," *Advanced Functional Materials,* vol. 25, no. 40, pp. 6326-6342, 2015, doi: https://doi.org/10.1002/adfm.201500827.

[52] N. Tsvetkov, Q. Lu, L. Sun, E. J. Crumlin, and B. Yildiz, "Improved chemical and electrochemical stability of perovskite oxides with less reducible cations at the surface," *Nature Materials,* vol. 15, no. 9, pp. 1010-1016, 2016, doi: 10.1038/nmat4659.

[53] M. Riva *et al.*, "Influence of surface atomic structure demonstrated on oxygen incorporation mechanism at a model perovskite oxide," *Nature Communications,* vol. 9, no. 1, p. 3710, 2018/09/13 2018, doi: 10.1038/s41467-018-05685-5.

[54] K. Szot, W. Speier, G. Bihlmayer, and R. Waser, "Switching the electrical resistance of individual dislocations in single-crystalline SrTiO3," *Nature Materials,* vol. 5, no. 4, pp. 312-320, 2006/04/01 2006, doi: 10.1038/nmat1614.

[55] A. Kumar *et al.*, "Probing Surface and Bulk Electrochemical Processes on the LaAlO3–SrTiO3 Interface," *ACS Nano,* vol. 6, no. 5, pp. 3841-3852, 2012/05/22 2012, doi: 10.1021/nn204960c.

[56] Y. Yang, X. Zhang, L. Qin, Q. Zeng, X. Qiu, and R. Huang, "Probing nanoscale oxygen ion motion in memristive systems," *Nature Communications,* vol. 8, no. 1, p. 15173, 2017/05/04 2017, doi: 10.1038/ncomms15173.

[57] A. Schirmeisen *et al.*, "Probing ion transport at the nanoscale: Time-domain electrostatic force spectroscopy on glassy electrolytes," *Applied Physics Letters,* vol. 85, no. 11, pp. 2053-2055, 2004, doi: 10.1063/1.1790034.

[58] D. U. Karatay, J. S. Harrison, M. S. Glaz, R. Giridharagopal, and D. S. Ginger, "Fast time-resolved electrostatic force microscopy: Achieving sub-cycle time resolution," *Review of Scientific Instruments,* vol. 87, no. 5, 2016, doi: 10.1063/1.4948396.

[59] R. Giridharagopal *et al.*, "Submicrosecond Time Resolution Atomic Force Microscopy for Probing Nanoscale Dynamics," *Nano Letters,* vol. 12, no. 2, pp. 893-898, 2012/02/08 2012, doi: 10.1021/nl203956q.

[60] B. Guner, M. Safikhani-Mahmoudi, F. Li, K. Zou, and O. E. Dagdeviren, "Ultraviolet irradiation penetration depth on TiO2," *Communications Chemistry,* vol. 8, no. 1, p. 83, 2025/03/16 2025, doi: 10.1038/s42004-025-01487-1.

[61] B. Guner, S. Laflamme, and O. E. Dagdeviren, "Customization of an atomic force microscope for multidimensional measurements under environmental conditions," *Review of Scientific Instruments,* vol. 94, no. 6, 2023, doi: 10.1063/5.0147331.

[62] F. J. Giessibl, "Advances in atomic force microscopy," *Reviews of Modern Physics,* vol. 75, no. 3, pp. 949-983, 07/29/ 2003, doi: 10.1103/RevModPhys.75.949.

[63] Y. Seo and W. Jhe, "Atomic force microscopy and spectroscopy," *Reports on Progress in Physics,* vol. 71, no. 1, p. 016101, 2007/12/17 2008, doi: 10.1088/0034-4885/71/1/016101.

[64] J. A. Dagata, "Scanning force microscopy with applications to electric, magnetic and atomic forces by Dror Sarid Oxford University Press, 1991," *Scanning,* vol. 14, no. 2, pp. 118-120, 1992, doi: https://doi.org/10.1002/sca.4950140211.

[65] B. W. Hoogenboom, "AFM in Liquids," in *Encyclopedia of Nanotechnology*, B. Bhushan Ed. Dordrecht: Springer Netherlands, 2012, pp. 83-89.

[66] G. R. Heath *et al.*, "Localization atomic force microscopy," *Nature,* vol. 594, no. 7863, pp. 385-390, 2021/06/01 2021, doi: 10.1038/s41586-021-03551-x.

[67] E. Lipiec, K. Sofińska, S. Seweryn, N. Wilkosz, and M. Szymonski, "Revealing DNA Structure at Liquid/Solid Interfaces by AFM-Based High-Resolution Imaging and Molecular Spectroscopy," (in eng), *Molecules,* vol. 26, no. 21, Oct 27 2021, doi: 10.3390/molecules26216476.

[68] U. D. Schwarz, H. Hölscher, and R. Wiesendanger, "Atomic resolution in scanning force microscopy: Concepts, requirements, contrast mechanisms, and image interpretation," *Physical Review B,* vol. 62, no. 19, pp. 13089-13097, 11/15/ 2000, doi: 10.1103/PhysRevB.62.13089.

[69] A. Schwarz, U. D. Schwarz, S. Langkat, H. Hölscher, W. Allers, and R. Wiesendanger, "Dynamic force microscopy with atomic resolution at low temperatures," *Applied Surface Science,* vol. 188, no. 3, pp. 245-251, 2002/03/28/ 2002, doi: https://doi.org/10.1016/S0169-4332(02)00146-0.

[70] R. García and R. Pérez, "Dynamic atomic force microscopy methods," *Surface Science Reports,* vol. 47, no. 6, pp. 197-301, 2002/09/01/ 2002, doi: https://doi.org/10.1016/S0167-5729(02)00077-8.

[71] R. Garcia, *Amplitude Modulation Atomic Force Microscopy*. Singapore: Wiley-VCH, 2010.

[72] T. R. Albrecht, P. Grütter, D. Horne, and D. Rugar, "Frequency modulation detection using high-Q cantilevers for enhanced force microscope sensitivity," *Journal of Applied Physics,* vol. 69, no. 2, pp. 668-673, 1991, doi: 10.1063/1.347347.

[73] H. Hölscher and U. D. Schwarz, "Theory of amplitude modulation atomic force microscopy with and without Q-Control," *International Journal of Non-Linear Mechanics,* vol. 42, no. 4, pp. 608-625, 2007/05/01/ 2007, doi: https://doi.org/10.1016/j.ijnonlinmec.2007.01.018.

[74] J. Lübbe *et al.*, "Achieving high effective Q-factors in ultra-high vacuum dynamic force microscopy," *Measurement Science and Technology,* vol. 21, no. 12, p. 125501, 2010/11/04 2010, doi: 10.1088/0957-0233/21/12/125501.

[75] O. E. Dagdeviren, C. Zhou, E. I. Altman, and U. D. Schwarz, "Quantifying Tip-Sample Interactions in Vacuum Using Cantilever-Based Sensors: An Analysis," *Physical Review Applied,* vol. 9, no. 4, p. 044040, 04/26/ 2018, doi: 10.1103/PhysRevApplied.9.044040.

[76] L. Schwab *et al.*, "Very-high-frequency probes for atomic force microscopy with silicon optomechanics," *Microsystems & Nanoengineering,* vol. 8, no. 1, p. 32, 2022/03/18 2022, doi: 10.1038/s41378-022-00364-4.

[77] K. L. Ngai, Y. N. Wang, and L. B. Magalas, "Theoretical basis and general applicability of the coupling model to relaxations in coupled systems," *Journal of Alloys and Compounds,* vol. 211-212, pp. 327-332, 1994/09/01/ 1994, doi: https://doi.org/10.1016/0925-8388(94)90513-4.

[78] K. L. Ngai and O. Kanert, "Comparisons between the coupling model predictions, Monte Carlo simulations and some recent experimental data of conductivity relaxations in glassy ionics," *Solid State Ionics,* vol. 53-56, pp. 936-946, 1992/07/01/ 1992, doi: https://doi.org/10.1016/0167-2738(92)90275-T.

[79] K. Funke, "Jump relaxation in solid electrolytes," *Progress in Solid State Chemistry,* vol. 22, no. 2, pp. 111-195, 1993/01/01/ 1993, doi: https://doi.org/10.1016/0079-6786(93)90002-9.

[80] S. Arrhenius, "Über die Dissociationswärme und den Einfluss der Temperatur auf den Dissociationsgrad der Elektrolyte," *Zeitschrift für Physikalische Chemie,* vol. 4U, pp. 116 - 96, 1889.

[81] S. Arrhenius, "Über die Reaktionsgeschwindigkeit bei der Inversion von Rohrzucker durch Säuren," *Zeitschrift für Physikalische Chemie,* vol. 4U, no. 1, pp. 226-248, 1889, doi: doi:10.1515/zpch-1889-0416.

[82] G. T. S. How, A. Pandikumar, H. N. Ming, and L. H. Ngee, "Highly exposed {001} facets of titanium dioxide modified with reduced graphene oxide for dopamine sensing," *Scientific Reports,* vol. 4, no. 1, p. 5044, 2014/05/23 2014, doi: 10.1038/srep05044.

[83] R. Ghamarpoor, A. Fallah, and M. Jamshidi, "Investigating the use of titanium dioxide (TiO2) nanoparticles on the amount of protection against UV irradiation," *Scientific Reports,* vol. 13, no. 1, p. 9793, 2023/06/16 2023, doi: 10.1038/s41598-023-37057-5.

[84] W. Souza *et al.*, "The two faces of titanium dioxide nanoparticles bio-camouflage in 3D bone spheroids," *Scientific Reports,* vol. 9, no. 1, p. 9309, 2019/06/27 2019, doi: 10.1038/s41598-019-45797-6.

[85] J. Bai and B. Zhou, "Titanium Dioxide Nanomaterials for Sensor Applications," *Chemical Reviews,* vol. 114, no. 19, pp. 10131-10176, 2014/10/08 2014, doi: 10.1021/cr400625j.

[86] M. Vasilopoulou *et al.*, "Hydrogen and nitrogen codoping of anatase TiO2 for efficiency enhancement in organic solar cells," *Scientific Reports,* vol. 7, no. 1, p. 17839, 2017/12/19 2017, doi: 10.1038/s41598-017-18051-0.

[87] U. Diebold, "The surface science of titanium dioxide," *Surface Science Reports,* vol. 48, no. 5-8, pp. 53-229, 2003, doi: 10.1016/s0167-5729(02)00100-0.

[88] X. Du *et al.*, "One-step Preparation of Nanoarchitectured TiO2 on Porous Al as Integrated Anode for High-performance Lithium-ion Batteries," *Scientific Reports,* vol. 6, no. 1, p. 20138, 2016/02/04 2016, doi: 10.1038/srep20138.

[89] H. H. Pham and L.-W. Wang, "Oxygen vacancy and hole conduction in amorphous TiO2," *Physical Chemistry Chemical Physics,* 10.1039/C4CP04209C vol. 17, no. 1, pp. 541-550, 2015, doi: 10.1039/C4CP04209C.

[90] A. Stevanovic, M. Büttner, Z. Zhang, and J. T. Yates, Jr., "Photoluminescence of TiO2: Effect of UV Light and Adsorbed Molecules on Surface Band Structure," *Journal of the American Chemical Society,* vol. 134, no. 1, pp. 324-332, 2012/01/11 2012, doi: 10.1021/ja2072737.

[91] P. Y. Yu and M. Cardona, *Fundamentals of Semiconductors: Physics and Materials Properties*, 4 ed. Springer-Verlag Berlin Heidelberg, 2010.

[92] D. A. Neamen, *Semiconductor Physics and Devices: Basic Principles*, 4 ed. McGraw-Hill Education, 2011.

[93] X. Pan, M.-Q. Yang, X. Fu, N. Zhang, and Y.-J. Xu, "Defective TiO2 with oxygen vacancies: synthesis, properties and photocatalytic applications," *Nanoscale,* 10.1039/C3NR00476G vol. 5, no. 9, pp. 3601-3614, 2013, doi: 10.1039/C3NR00476G.

[94] N. Rahimi, R. A. Pax, and E. M. Gray, "Review of functional titanium oxides. I: TiO2 and its modifications," *Progress in Solid State Chemistry,* vol. 44, no. 3, pp. 86-105, 2016/09/01/ 2016, doi: https://doi.org/10.1016/j.progsolidstchem.2016.07.002.

[95] B. J. Morgan and G. W. Watson, "Polaronic trapping of electrons and holes by native defects in anatase TiO2," *Physical Review B,* vol. 80, no. 23, p. 233102, 12/16/ 2009, doi: 10.1103/PhysRevB.80.233102.

[96] S. Yang, A. T. Brant, and L. E. Halliburton, "Photoinduced self-trapped hole center in TiO2 crystals," *Physical Review B,* vol. 82, no. 3, p. 035209, 07/21/ 2010, doi: 10.1103/PhysRevB.82.035209.

[97] B. Liu, X. Zhao, J. Yu, I. P. Parkin, A. Fujishima, and K. Nakata, "Intrinsic intermediate gap states of TiO2 materials and their roles in charge carrier kinetics," *Journal of Photochemistry and Photobiology C: Photochemistry Reviews,* vol. 39, pp. 1-57, 2019/06/01/ 2019, doi: https://doi.org/10.1016/j.jphotochemrev.2019.02.001.

[98] Y. Nam, L. Li, J. Y. Lee, and O. V. Prezhdo, "Strong Influence of Oxygen Vacancy Location on Charge Carrier Losses in Reduced TiO2 Nanoparticles," *The Journal of Physical Chemistry Letters,* vol. 10, no. 11, pp. 2676-2683, 2019/06/06 2019, doi: 10.1021/acs.jpclett.9b00987.

[99] T. Berger *et al.*, "Light-Induced Charge Separation in Anatase TiO2 Particles," *The Journal of Physical Chemistry B,* vol. 109, no. 13, pp. 6061-6068, 2005/04/01 2005, doi: 10.1021/jp0404293.

[100] O. B. J. Williams, K. Katsiev, B. Baek, G. Harrison, G. Thornton, and H. Idriss, "Direct Visualization of a Gold Nanoparticle Electron Trapping Effect," *Journal of the American Chemical Society,* vol. 144, no. 2, pp. 1034-1044, 2022/01/19 2022, doi: 10.1021/jacs.1c12197.

[101] T. L. Thompson and J. T. Yates, "Monitoring Hole Trapping in Photoexcited TiO2(110) Using a Surface Photoreaction," *The Journal of Physical Chemistry B,* vol. 109, no. 39, pp. 18230-18236, 2005/10/01 2005, doi: 10.1021/jp0530451.

[102] L. T. Banner, A. G. Richter, and E. Pinkhassik, "Pinhole-free large-grained atomically smooth Au(111) substrates prepared by flame-annealed template stripping," *Surface and Interface Analysis,* vol. 41, 2009.

[103] A. Roy-Gobeil, Y. Miyahara, and P. Grutter, "Revealing energy level structure of individual quantum dots by tunneling rate measured by single-electron sensitive electrostatic force spectroscopy," (in eng), *Nano Lett,* vol. 15, no. 4, pp. 2324-8, Apr 8 2015, doi: 10.1021/nl504468a.

[104] C. Kittel and D. F. Holcomb, "Introduction to Solid State Physics," *American Journal of Physics,* vol. 35, no. 6, pp. 547-548, 1967, doi: 10.1119/1.1974177.

[105] N. W. Ashcroft and N. D. Mermin, *Solid State Physics*. New York: Sounders College: Philadelphia (in eng), 1981.

[106] S. Sadewasser and T. Glatzel, "Kelvin Probe Force Microscopy: Measuring and Compensating Electrostatic Forces," *Kelvin Probe Force Microscopy,* 2012.

[107] B. Liu, X. Zhao, I. P. Parkin, and K. Nakata, "Chapter 4 - Charge carrier transfer in photocatalysis," in *Interface Science and Technology*, vol. 31, J. Yu, M. Jaroniec, and C. Jiang Eds.: Elsevier, 2020, pp. 103-159.

[108] T. Bak, M. Nowotny, L. Sheppard, and J. Nowotny, "Mobility of Electronic Charge Carriers in Titanium Dioxide," *The Journal of Physical Chemistry C,* vol. 112, 07/23 2008, doi: 10.1021/jp801028j.

[109] A. Einstein, "Über die von der molekularkinetischen Theorie der Wärme geforderte Bewegung von in ruhenden Flüssigkeiten suspendierten Teilchen," *Annalen der Physik,* vol. 322, no. 8, pp. 549-560, 1905, doi: https://doi.org/10.1002/andp.19053220806.

[110] J. Crank, *The Mathematics of Diffusion*, 2 ed. Oxford University Press, 1975.

[111] W. Jost, *Diffusion in Solids, Liquids, Gases*. Academic Press, 1960.

[112] A. Janotti, J. B. Varley, M. Choi, and C. G. Van de Walle, "Vacancies and small polarons in SrTiO3," *Physical Review B,* vol. 90, no. 8, p. 085202, 08/18/ 2014, doi: 10.1103/PhysRevB.90.085202.

[113] L. Hüttenhofer *et al.*, "Anapole Excitations in Oxygen-Vacancy-Rich TiO2–x Nanoresonators: Tuning the Absorption for Photocatalysis in the Visible Spectrum,"

ACS Nano, vol. 14, no. 2, pp. 2456-2464, 2020/02/25 2020, doi: 10.1021/acsnano.9b09987.

[114] A. Fujishima, X. Zhang, and D. A. Tryk, "TiO2 photocatalysis and related surface phenomena," *Surface Science Reports,* vol. 63, no. 12, pp. 515-582, 2008/12/15/ 2008, doi: https://doi.org/10.1016/j.surfrep.2008.10.001.

[115] J. Schneider *et al.*, "Understanding TiO2 Photocatalysis: Mechanisms and Materials," *Chemical Reviews,* vol. 114, no. 19, pp. 9919-9986, 2014/10/08 2014, doi: 10.1021/cr5001892.

[116] Y. Zhang, C. Harris, P. Wallenmeyer, J. Murowchick, and X. Chen, "Asymmetric Lattice Vibrational Characteristics of Rutile TiO2 as Revealed by Laser Power Dependent Raman Spectroscopy," *The Journal of Physical Chemistry C,* vol. 117, pp. 24015–24022, 11/01 2013, doi: 10.1021/jp406948e.

[117] H. Kuramochi and T. Tahara, "Tracking Ultrafast Structural Dynamics by Time-Domain Raman Spectroscopy," *Journal of the American Chemical Society,* vol. 143, no. 26, pp. 9699-9717, 2021/07/07 2021, doi: 10.1021/jacs.1c02545.

[118] X. Wang *et al.*, "Trap states and carrier dynamics of TiO2 studied by photoluminescence spectroscopy under weak excitation condition," *Physical Chemistry Chemical Physics,* 10.1039/B925277K vol. 12, no. 26, pp. 7083-7090, 2010, doi: 10.1039/B925277K.

[119] J. A. Quirk and K. P. McKenna, "Small-polaron mediated recombination in titanium dioxide from first principles," *Physical Review Research,* vol. 5, no. 2, p. 023072, 05/01/ 2023, doi: 10.1103/PhysRevResearch.5.023072.

[120] D. Wrana *et al.*, "Photoluminescence imaging of defects in TiO2: The influence of grain boundaries and doping on charge carrier dynamics," *Applied Surface Science,* vol. 569, p. 150909, 2021/12/15/ 2021, doi: https://doi.org/10.1016/j.apsusc.2021.150909.

[121] R. Yalavarthi *et al.*, "Radiative and Non-Radiative Recombination Pathways in Mixed-Phase TiO2 Nanotubes for PEC Water-Splitting," *Catalysts,* vol. 9, no. 2, p. 204, 2019. [Online]. Available: https://www.mdpi.com/2073-4344/9/2/204.

[122] H. M. Abd El-Lateef, M. M. Khalaf, V. D. Dao, and I. M. A. Mohamed, "Electrochemical Impedance Investigation of Dye-Sensitized Solar Cells Based on Electrospun TiO(2) Nanofibers Photoanodes," (in eng), *Materials (Basel),* vol. 15, no. 17, Sep 5 2022, doi: 10.3390/ma15176175.

[123] F. Schauer, V. Nádaždy, and K. Gmucová, "Electrochemical impedance spectroscopy for study of electronic structure in disordered organic semiconductors—Possibilities and limitations," *Journal of Applied Physics,* vol. 123, no. 16, 2018, doi: 10.1063/1.5008830.

[124] M. Krawczyk, R. Korbutowicz, and P. Suchorska-Woźniak, "Impedance Spectroscopy Study of Charge Transfer in the Bulk and Across the Interface in Networked SnO2/Ga2O3 Core–Shell Nanobelts in Ambient Air," *Sensors,* vol. 24, no. 19, p. 6173, 2024. [Online]. Available: https://www.mdpi.com/1424-8220/24/19/6173.

[125] B. L. Gorman and M. L. Kraft, "High-Resolution Secondary Ion Mass Spectrometry Analysis of Cell Membranes," *Analytical Chemistry,* vol. 92, no. 2, pp. 1645-1652, 2020/01/21 2020, doi: 10.1021/acs.analchem.9b04492.

[126] H. F. Arlinghaus, "Possibilities and limitations of high-resolution mass spectrometry in life sciences," *Applied Surface Science,* vol. 255, no. 4, pp. 1058-1063, 2008/12/15/ 2008, doi: https://doi.org/10.1016/j.apsusc.2008.05.047.

[127] S. Mishra, A. Gurjar, and A. K. De, "Elucidating Effect of Surface-Passivation on Charge-Carrier Relaxation Dynamics in Cs4CuSb2Cl12 Microcrystals," *The Journal of Physical Chemistry C,* vol. 129, no. 10, pp. 5156-5163, 2025/03/13 2025, doi: 10.1021/acs.jpcc.5c00090.

[128] Q. Deng, S. Lv, Z. Li, K. Tan, X. Liang, and S. Shen, "The impact of flexoelectricity on materials, devices, and physics," *Journal of Applied Physics,* vol. 128, no. 8, 2020, doi: 10.1063/5.0015987.

[129] J. Peng, Y. Chen, K. Zheng, T. Pullerits, and Z. Liang, "Insights into charge carrier dynamics in organo-metal halide perovskites: from neat films to solar cells," *Chemical Society Reviews,* 10.1039/C6CS00942E vol. 46, no. 19, pp. 5714-5729, 2017, doi: 10.1039/C6CS00942E.

[130] S. Neppl and O. Gessner, "Time-resolved X-ray photoelectron spectroscopy techniques for the study of interfacial charge dynamics," *Journal of Electron Spectroscopy and Related Phenomena,* vol. 200, pp. 64-77, 2015/04/01/ 2015, doi: https://doi.org/10.1016/j.elspec.2015.03.002.

[131] B. Sheng, D. Cao, S. Chen, N. Zhang, J. Wang, and L. Song, "Advanced X-ray absorption spectroscopy for probing dynamics in CO2 reduction reaction electrocatalysts," *Communications Materials,* vol. 6, no. 1, p. 64, 2025/04/04 2025, doi: 10.1038/s43246-025-00779-2.

[132] N. L. Tolman, R. Bai, and H. Liu, "Hydrocarbons in the Meniscus: Effects on Conductive Atomic Force Microscopy," *Langmuir,* vol. 39, no. 12, pp. 4274-4281, 2023/03/28 2023, doi: 10.1021/acs.langmuir.2c03222.

[133] L. Jiang *et al.*, "Understanding Current Instabilities in Conductive Atomic Force Microscopy," *Materials,* vol. 12, no. 3, p. 459, 2019. [Online]. Available: https://www.mdpi.com/1996-1944/12/3/459.

[134] D. A. Bonnell *et al.*, "Imaging physical phenomena with local probes: From electrons to photons," *Reviews of Modern Physics,* vol. 84, no. 3, pp. 1343-1381, 09/26/ 2012, doi: 10.1103/RevModPhys.84.1343.

[135] T. Glatzel, S. Sadewasser, and M. C. Lux-Steiner, "Amplitude or frequency modulation-detection in Kelvin probe force microscopy," *Applied Surface Science,* vol. 210, no. 1, pp. 84-89, 2003/03/31/ 2003, doi: https://doi.org/10.1016/S0169-4332(02)01484-8.

[136] N. A. Burnham, R. J. Colton, and H. M. Pollock, "Interpretation of force curves in force microscopy," *Nanotechnology,* vol. 4, no. 2, p. 64, 1993/04/01 1993, doi: 10.1088/0957-4484/4/2/002.

[137] E. I. Altman, M. Z. Baykara, and U. D. Schwarz, "Noncontact Atomic Force Microscopy: An Emerging Tool for Fundamental Catalysis Research," *Accounts of Chemical Research,* vol. 48, no. 9, pp. 2640-2648, 2015/09/15 2015, doi: 10.1021/acs.accounts.5b00166.

[138] C. Bustamante and D. Keller, "Scanning Force Microscopy in Biology," *Physics Today,* vol. 48, no. 12, pp. 32-38, 1995, doi: 10.1063/1.881478.

[139] F. J. Giessibl, H. Bielefeldt, S. Hembacher, and J. Mannhart, "Calculation of the optimal imaging parameters for frequency modulation atomic force microscopy," *Applied Surface Science,* vol. 140, no. 3, pp. 352-357, 1999/02/01/ 1999, doi: https://doi.org/10.1016/S0169-4332(98)00553-4.

[140] N. A. Burnham and R. J. Colton, "Measuring the nanomechanical properties and surface forces of materials using an atomic force microscope," *Journal of Vacuum Science & Technology A,* vol. 7, no. 4, pp. 2906-2913, 1989, doi: 10.1116/1.576168.

[141] S. Kawai and H. Kawakatsu, "Atomically resolved amplitude modulation dynamic force microscopy with a high-frequency and high-quality factor cantilever," *Applied Physics Letters,* vol. 89, no. 1, p. 013108, 2006, doi: 10.1063/1.2219415.

[142] O. E. Dagdeviren, J. Götzen, H. Hölscher, E. I. Altman, and U. D. Schwarz, "Robust high-resolution imaging and quantitative force measurement with tuned-oscillator atomic force microscopy," *Nanotechnology,* vol. 27, no. 6, p. 065703, 2016/01/12 2016, doi: 10.1088/0957-4484/27/6/065703.

[143] K. Umeda *et al.*, "Author Correction: Atomic-resolution three-dimensional hydration structures on a heterogeneously charged surface," *Nature Communications,* vol. 9, no. 1, p. 2099, 2018/05/23 2018, doi: 10.1038/s41467-018-04401-7.

[144] R. Garcia and E. T. Herruzo, "The emergence of multifrequency force microscopy," *Nature Nanotechnology,* vol. 7, no. 4, pp. 217-226, 2012/04/01 2012, doi: 10.1038/nnano.2012.38.

[145] K. Kimura *et al.*, "Visualizing water molecule distribution by atomic force microscopy," *The Journal of Chemical Physics,* vol. 132, no. 19, p. 194705, 2010, doi: 10.1063/1.3408289.

[146] T. Fukuma, Y. Ueda, S. Yoshioka, and H. Asakawa, "Atomic-Scale Distribution of Water Molecules at the Mica-Water Interface Visualized by Three-Dimensional Scanning Force Microscopy," *Physical Review Letters,* vol. 104, no. 1, p. 016101, 01/06/ 2010, doi: 10.1103/PhysRevLett.104.016101.

[147] A. J. Weymouth, D. Wastl, and F. J. Giessibl, "Advances in AFM: Seeing Atoms in Ambient Conditions," *e-Journal of Surface Science and Nanotechnology,* vol. 16, pp. 351-355, 2018, doi: 10.1380/ejssnt.2018.351.

[148] B. J. Albers *et al.*, "Three-dimensional imaging of short-range chemical forces with picometre resolution," *Nature Nanotechnology,* vol. 4, no. 5, pp. 307-310, 2009/05/01 2009, doi: 10.1038/nnano.2009.57.

[149] S. Kawai *et al.*, "Van der Waals interactions and the limits of isolated atom models at interfaces," (in eng), *Nat Commun,* vol. 7, p. 11559, May 13 2016, doi: 10.1038/ncomms11559.

[150] A. J. Weymouth, T. Hofmann, and F. J. Giessibl, "Quantifying molecular stiffness and interaction with lateral force microscopy," (in eng), *Science,* vol. 343, no. 6175, pp. 1120-2, Mar 7 2014, doi: 10.1126/science.1249502.

[151] H. Mönig *et al.*, "Quantitative assessment of intermolecular interactions by atomic force microscopy imaging using copper oxide tips," (in eng), *Nat Nanotechnol,* vol. 13, no. 5, pp. 371-375, May 2018, doi: 10.1038/s41565-018-0104-4.

[152] S. Kawai *et al.*, "Direct quantitative measurement of the C═O···H–C bond by atomic force microscopy," *Science Advances,* vol. 3, no. 5, p. e1603258, 2017, doi: doi:10.1126/sciadv.1603258.

[153] H. Mönig *et al.*, "Submolecular Imaging by Noncontact Atomic Force Microscopy with an Oxygen Atom Rigidly Connected to a Metallic Probe," *ACS Nano,* vol. 10, no. 1, pp. 1201-1209, 2016/01/26 2016, doi: 10.1021/acsnano.5b06513.

[154] L. Gross, F. Mohn, N. Moll, P. Liljeroth, and G. Meyer, "The Chemical Structure of a Molecule Resolved by Atomic Force Microscopy," *Science,* vol. 325, no. 5944, pp. 1110-1114, 2009, doi: doi:10.1126/science.1176210.

[155] Z. Schumacher *et al.*, "Nanoscale force sensing of an ultrafast nonlinear optical response," *Proceedings of the National Academy of Sciences,* vol. 117, no. 33, pp. 19773-19779, 2020, doi: doi:10.1073/pnas.2003945117.

[156] R. J. Hamers and D. G. Cahill, "Ultrafast time resolution in scanned probe microscopies: Surface photovoltage on Si(111)–(7×7)," *Journal of Vacuum Science & Technology B: Microelectronics and Nanometer Structures Processing, Measurement, and Phenomena,* vol. 9, no. 2, pp. 514-518, 1991, doi: 10.1116/1.585559.

[157] R. J. Hamers and D. G. Cahill, "Ultrafast time resolution in scanned probe microscopies," *Applied Physics Letters,* vol. 57, no. 19, pp. 2031-2033, 1990, doi: 10.1063/1.103997.

[158] S. Rode *et al.*, "Modification of a commercial atomic force microscopy for low-noise, high-resolution frequency-modulation imaging in liquid environment," *Review of Scientific Instruments,* vol. 82, no. 7, p. 073703, 2011, doi: 10.1063/1.3606399.

[159] P. Zahl, M. Bierkandt, S. Schröder, and A. Klust, "The flexible and modern open source scanning probe microscopy software package GXSM," *Review of Scientific Instruments,* vol. 74, no. 3, pp. 1222-1227, 2003, doi: 10.1063/1.1540718.

[160] J. L. Hutter and J. Bechhoefer, "Calibration of atomic-force microscope tips," *Review of Scientific Instruments,* vol. 64, pp. 1868-1873, July 01, 1993 1993, doi: 10.1063/1.1143970.

[161] J. E. Sader, I. Larson, P. Mulvaney, and L. R. White, "Method for the calibration of atomic force microscope cantilevers," *Review of Scientific Instruments,* vol. 66, no. 7, pp. 3789-3798, 1995, doi: 10.1063/1.1145439.

[162] A. Mascaro, Y. Miyahara, O. E. Dagdeviren, and P. Grütter, "Eliminating the effect of acoustic noise on cantilever spring constant calibration," *Applied Physics Letters,* vol. 113, no. 23, p. 233105, 2018, doi: 10.1063/1.5063992.

[163] Z. Ye and A. Martini, "Atomic friction at exposed and buried graphite step edges: Experiments and simulations," *Applied Physics Letters,* vol. 106, no. 23, p. 231603, 2015, doi: 10.1063/1.4922485.

[164] Z. Chen, A. Khajeh, A. Martini, and S. H. Kim, "Identifying Physical and Chemical Contributions to Friction: A Comparative Study of Chemically Inert and Active Graphene Step Edges," *ACS Applied Materials & Interfaces,* vol. 12, no. 26, pp. 30007-30015, 2020/07/01 2020, doi: 10.1021/acsami.0c08121.

[165] L. Chen *et al.*, "Friction at single-layer graphene step edges due to chemical and topographic interactions," *Carbon,* vol. 154, pp. 67-73, 2019/12/01/ 2019, doi: https://doi.org/10.1016/j.carbon.2019.07.081.

[166] J. E. Sader and S. P. Jarvis, "Accurate formulas for interaction force and energy in frequency modulation force spectroscopy," *Applied Physics Letters,* vol. 84, no. 10, pp. 1801-1803, 2004, doi: 10.1063/1.1667267.

[167] L. Collins, M. Ahmadi, T. Wu, B. Hu, S. V. Kalinin, and S. Jesse, "Breaking the Time Barrier in Kelvin Probe Force Microscopy: Fast Free Force Reconstruction Using the G-Mode Platform," *ACS Nano,* vol. 11, no. 9, pp. 8717-8729, 2017/09/26 2017, doi: 10.1021/acsnano.7b02114.

[168] R.-P. Stomp, "Dissipative and electrostatic force spectroscopy of indium arsenide quantum dots by non-contact atomic force microscopy," McGill University, Canada, 2006. [Online]. Available: https://ui.adsabs.harvard.edu/abs/2006PhDT.....370S

[169] H. Lang, Y. Peng, X. Zeng, X. a. Cao, L. Liu, and K. Zou, "Effect of relative humidity on the frictional properties of graphene at atomic-scale steps," *Carbon,* vol. 137, pp. 519-526, 2018/10/01/ 2018, doi: https://doi.org/10.1016/j.carbon.2018.05.069.

[170] Z. Chen, A. Khajeh, A. Martini, and S. H. Kim, "Chemical and physical origins of friction on surfaces with atomic steps," *Science Advances,* vol. 5, no. 8, p. eaaw0513, 2019, doi: doi:10.1126/sciadv.aaw0513.

[171] H. G. Yang *et al.*, "Anatase TiO2 single crystals with a large percentage of reactive facets," *Nature,* vol. 453, no. 7195, pp. 638-641, 2008/05/01 2008, doi: 10.1038/nature06964.

[172] E. J. W. Crossland, N. Noel, V. Sivaram, T. Leijtens, J. A. Alexander-Webber, and H. J. Snaith, "Mesoporous TiO2 single crystals delivering enhanced mobility and optoelectronic device performance," *Nature,* vol. 495, no. 7440, pp. 215-219, 2013/03/01 2013, doi: 10.1038/nature11936.

[173] B. O'Regan and M. Grätzel, "A low-cost, high-efficiency solar cell based on dye-sensitized colloidal TiO2 films," *Nature,* vol. 353, no. 6346, pp. 737-740, 1991/10/01 1991, doi: 10.1038/353737a0.

[174] U. Bach *et al.*, "Solid-state dye-sensitized mesoporous TiO2 solar cells with high photon-to-electron conversion efficiencies," *Nature,* vol. 395, no. 6702, pp. 583-585, 1998/10/01 1998, doi: 10.1038/26936.

[175] D. Huang and J. E. Hoffman, "Monolayer FeSe on SrTiO3," *Annual Review of Condensed Matter Physics,* vol. 8, no. 1, pp. 311-336, 2017, doi: 10.1146/annurev-conmatphys-031016-025242.

[176] W. Qing-Yan *et al.*, "Interface-Induced High-Temperature Superconductivity in Single Unit-Cell FeSe Films on SrTiO 3," *Chinese Physics Letters,* vol. 29, no. 3, p. 037402, 2012. [Online]. Available: http://stacks.iop.org/0256-307X/29/i=3/a=037402.

[177] Z. Li *et al.*, "Molecular beam epitaxy growth and post-growth annealing of FeSe films on SrTiO 3 : a scanning tunneling microscopy study," *Journal of Physics: Condensed Matter,* vol. 26, no. 26, p. 265002, 2014. [Online]. Available: http://stacks.iop.org/0953-8984/26/i=26/a=265002
http://iopscience.iop.org/0953-8984/26/26/265002/pdf/0953-8984_26_26_265002.pdf.

[178] Y. Li *et al.*, "Observation of superconductivity in structure-selected Ti2O3 thin films," (in En), *NPG Asia Materials,* OriginalPaper vol. 10, no. 6, pp. 522-532, 2018-06-06 2018, doi: doi:10.1038/s41427-018-0050-5.

[179] H. Ding *et al.*, "High-Temperature Superconductivity in Single-Unit-Cell FeSe Films on AnataseTiO2(001)," *Physical Review Letters,* vol. 117, no. 6, 2016, doi: 10.1103/physrevlett.117.067001.

[180] K. Zou *et al.*, "Role of doubleTiO2layers at the interface of FeSe/SrTiO3superconductors," *Physical Review B,* vol. 93, no. 18, 2016, doi: 10.1103/physrevb.93.180506.

[181] A. G. Ricciardulli, S. Yang, J. H. Smet, and M. Saliba, "Emerging perovskite monolayers," *Nature Materials,* vol. 20, no. 10, pp. 1325-1336, 2021/10/01 2021, doi: 10.1038/s41563-021-01029-9.

[182] G. Grancini and M. K. Nazeeruddin, "Dimensional tailoring of hybrid perovskites for photovoltaics," *Nature Reviews Materials,* vol. 4, no. 1, pp. 4-22, 2019/01/01 2019, doi: 10.1038/s41578-018-0065-0.

[183] J. Y. Huh, J. Lee, S. Z. A. Bukhari, J.-H. Ha, and I.-H. Song, "Development of TiO2-coated YSZ/silica nanofiber membranes with excellent photocatalytic degradation ability for water purification," (in En), *Scientific Reports,* OriginalPaper vol. 10, no. 1, pp. 1-12, 2020-10-20 2020, doi: doi:10.1038/s41598-020-74637-1.

[184] B. C. Hodges, E. L. Cates, and J.-H. Kim, "Challenges and prospects of advanced oxidation water treatment processes using catalytic nanomaterials," *Nature Nanotechnology,* vol. 13, no. 8, pp. 642-650, 2018/08/01 2018, doi: 10.1038/s41565-018-0216-x.

[185] Y. Jiang, W.-N. Wang, P. Biswas, and J. D. Fortner, "Facile Aerosol Synthesis and Characterization of Ternary Crumpled Graphene–TiO2–Magnetite Nanocomposites for Advanced Water Treatment," *ACS Applied Materials & Interfaces,* vol. 6, no. 14, pp. 11766-11774, 2014/07/23 2014, doi: 10.1021/am5025275.

[186] Q. Yang, H. Choi, and D. D. Dionysiou, "Nanocrystalline cobalt oxide immobilized on titanium dioxide nanoparticles for the heterogeneous activation of peroxymonosulfate," *Applied Catalysis B: Environmental,* vol. 74, no. 1, pp. 170-178, 2007/06/18/ 2007, doi: https://doi.org/10.1016/j.apcatb.2007.02.001.

[187] Y. Yang and R. Huang, "Probing memristive switching in nanoionic devices," (in En), *Nature Electronics,* ReviewPaper vol. 1, no. 5, pp. 274-287, 2018-05-14 2018, doi: doi:10.1038/s41928-018-0069-1.

[188] B. D. Hoskins *et al.*, "Stateful characterization of resistive switching TiO2 with electron beam induced currents," (in En), *Nature Communications,* OriginalPaper vol. 8, no. 1, pp. 1-11, 2017-12-07 2017, doi: doi:10.1038/s41467-017-02116-9.

[189] A. Regoutz *et al.*, "Role and Optimization of the Active Oxide Layer in TiO 2 -Based RRAM," *Advanced Functional Materials,* vol. 26, no. 4, pp. 507-513, 2016, doi: 10.1002/adfm.201503522.

[190] D.-H. Kwon *et al.*, "Atomic structure of conducting nanofilaments in TiO2 resistive switching memory," (in En), *Nature Nanotechnology,* OriginalPaper vol. 5, no. 2, pp. 148-153, 2010-01-17 2010, doi: doi:10.1038/nnano.2009.456.

[191] K. Leng, W. Fu, Y. Liu, M. Chhowalla, and K. P. Loh, "From bulk to molecularly thin hybrid perovskites," *Nature Reviews Materials,* vol. 5, no. 7, pp. 482-500, 2020/07/01 2020, doi: 10.1038/s41578-020-0185-1.

[192] Q. D. Jiang and J. Zegenhagen, "c(6×2) and c(4×2) reconstruction of SrTiO3(001)," *Surface Science,* vol. 425, no. 2–3, pp. 343-354, 4/20/ 1999, doi: http://dx.doi.org/10.1016/S0039-6028(99)00223-X. Surface Science.

[193] Q. Tai, K.-C. Tang, and F. Yan, "Recent progress of inorganic perovskite solar cells," *Energy & Environmental Science,* 10.1039/C9EE01479A vol. 12, no. 8, pp. 2375-2405, 2019, doi: 10.1039/C9EE01479A.

[194] K. Liu, Z.-Y. Lu, and T. Xiang, "Atomic and electronic structures of FeSe monolayer and bilayer thin films on SrTiO3 (001): First-principles study," *Physical Review B,* vol. 85, no. 23, p. 235123, 06/14/ 2012. [Online]. Available: http://link.aps.org/doi/10.1103/PhysRevB.85.235123.

[195] M.-G. Han *et al.*, "Interface-induced nonswitchable domains in ferroelectric thin films," *Nat Commun,* Article vol. 5, 08/18/online 2014, doi: 10.1038/ncomms5693.

[196] C. J. Lu, Z. L. Wang, C. Kwon, and Q. X. Jia, "Microstructure of epitaxial La0.7Ca0.3MnO3 thin films grown on LaAlO3 and SrTiO3," *Journal of Applied Physics,* vol. 88, no. 7, pp. 4032-4043, 2000, doi: doi:http://dx.doi.org/10.1063/1.1290741.

[197] Q. Gan, R. A. Rao, C. B. Eom, J. L. Garrett, and M. Lee, "Direct measurement of strain effects on magnetic and electrical properties of epitaxial SrRuO3 thin films," *Applied Physics Letters,* vol. 72, no. 8, pp. 978-980, 1998, doi: doi:http://dx.doi.org/10.1063/1.120603.

[198] A. Grutter, F. Wong, E. Arenholz, M. Liberati, A. Vailionis, and Y. Suzuki, "Enhanced magnetism in epitaxial SrRuO3 thin films," *Applied Physics Letters,* vol. 96, no. 8, p. 082509, 2010, doi: doi:http://dx.doi.org/10.1063/1.3327512.

[199] H. Yang *et al.*, "Temperature-dependent leakage mechanisms of Pt/BiFeO3/SrRuO3 thin film capacitors," *Applied Physics Letters,* vol. 91, no. 7, p. 072911, 2007, doi: doi:http://dx.doi.org/10.1063/1.2772666.

[200] M. R. Islam, M. A. Zubair, M. S. Bashar, and A. K. M. B. Rashid, "Bi0.9Ho0.1FeO3/TiO2 Composite Thin Films: Synthesis and Study of Optical, Electrical and Magnetic Properties," *Scientific Reports,* vol. 9, no. 1, p. 5205, 2019/03/26 2019, doi: 10.1038/s41598-019-41570-x.

[201] E. Kumi-Barimah, R. Penhale-Jones, A. Salimian, H. Upadhyaya, A. Hasnath, and G. Jose, "Phase evolution, morphological, optical and electrical properties of femtosecond pulsed laser deposited TiO2 thin films," *Scientific Reports,* vol. 10, no. 1, p. 10144, 2020/06/23 2020, doi: 10.1038/s41598-020-67367-x.

[202] X. F. Song *et al.*, "Electrical level of defects in single-layer two-dimensional TiO2," *Scientific Reports,* vol. 5, no. 1, p. 15989, 2015/11/02 2015, doi: 10.1038/srep15989.

[203] X. Ning *et al.*, "Outstanding supercapacitive properties of Mn-doped TiO2 micro/nanostructure porous film prepared by anodization method," *Scientific Reports,* vol. 6, no. 1, p. 22634, 2016/03/04 2016, doi: 10.1038/srep22634.

[204] S. J. Song *et al.*, "Real-time identification of the evolution of conducting nano-filaments in TiO2 thin film ReRAM," *Scientific Reports,* vol. 3, no. 1, p. 3443, 2013/12/06 2013, doi: 10.1038/srep03443.

[205] Gyanan, S. Mondal, and A. Kumar, "Tunable dielectric properties of TiO2 thin film based MOS systems for application in microelectronics," *Superlattices and Microstructures,* vol. 100, pp. 876-885, 2016/12/01/ 2016, doi: https://doi.org/10.1016/j.spmi.2016.10.054.

[206] O. E. Dagdeviren *et al.*, "Surface phase, morphology, and charge distribution transitions on vacuum and ambient annealed SrTiO3(100)," *Physical Review B,* vol.

93, no. 19, p. 195303, 05/04/ 2016. [Online]. Available: http://link.aps.org/doi/10.1103/PhysRevB.93.195303.

[207] S. A. Chambers, T. C. Droubay, C. Capan, and G. Y. Sun, "Unintentional F doping of SrTiO3(001) etched in HF acid-structure and electronic properties," *Surface Science,* vol. 606, no. 3, pp. 554-558, 2012/02/01/ 2012, doi: https://doi.org/10.1016/j.susc.2011.11.029.

[208] H. Zhang and J. F. Banfield, "Thermodynamic analysis of phase stability of nanocrystalline titania," *Journal of Materials Chemistry,* 10.1039/A802619J vol. 8, no. 9, pp. 2073-2076, 1998, doi: 10.1039/A802619J.

[209] J. Muscat, V. Swamy, and N. M. Harrison, "First-principles calculations of the phase stability ofTiO2," *Physical Review B,* vol. 65, no. 22, 2002, doi: 10.1103/physrevb.65.224112.

[210] S. J. Smith *et al.*, "Heat capacities and thermodynamic functions of TiO2 anatase and rutile: Analysis of phase stability," *American Mineralogist,* vol. 94, no. 2-3, pp. 236-243, 2009, doi: doi:10.2138/am.2009.3050.

[211] D. A. H. Hanaor and C. C. Sorrell, "Review of the anatase to rutile phase transformation," (in En), *Journal of Materials Science,* ReviewPaper vol. 46, no. 4, pp. 855-874, 2010-12-08 2010, doi: doi:10.1007/s10853-010-5113-0.

[212] J. Augustynski, "The role of the surface intermediates in the photoelectrochemical behaviour of anatase and rutile TiO2," *Electrochimica Acta,* vol. 38, no. 1, pp. 43–46, 1993. [Online]. Available: https://doi.org/10.1016/0013-4686(93)80008-N.

[213] A. Sclafani and J. M. Herrmann, "Comparison of the Photoelectronic and Photocatalytic Activities of Various Anatase and Rutile Forms of Titania in Pure Liquid Organic Phases and in Aqueous Solutions," *The Journal of Physical Chemistry,* vol. 100, no. 32, pp. 13655-13661, 1996/01/01 1996, doi: 10.1021/jp9533584.

[214] S. Bhansali *et al.*, "Enhanced thermoelectric properties of lightly Nb doped SrTiO3 thin films," *Nanoscale Advances,* vol. 1, no. 9, pp. 3647-3653, 2019, doi: 10.1039/c9na00361d.

[215] Q. Jie, L. Hui-Bin, J. Kui-Juan, L. Guo-Zhen, and Y. Guo-Zhen, "Transport Behaviour of La 0.8 Sr 0.2 AlO 3 Thin Film on Oxygen Deficient SrTiO 3 Substrate," *Chinese Physics Letters,* vol. 25, no. 6, pp. 2206-2208, 2008/05/29 2008, doi: 10.1088/0256-307x/25/6/077.

[216] A. Lübcke, "Time-resolved X-ray diffraction study on superconducting YBa2Cu3O7 epitaxially grown on SrTiO3," Jena, 2007. [Online]. Available: https://www.db-thueringen.de/receive/dbt_mods_00010296
http://uri.gbv.de/document/gvk:ppn:561085587

[217] R. Chaurasia, K. Asokan, K. Kumar, and A. K. Pramanik, "Low-temperature ferromagnetism in perovskite SrIrO3 films," *Physical Review B,* vol. 103, no. 6, 2021, doi: 10.1103/physrevb.103.064418.

[218] E. Chernova, O. Pacherova, T. Kocourek, M. Jelinek, A. Dejneka, and M. Tyunina, "Optical Properties of Ferroelectric Epitaxial K0.5Na0.5NbO3 Films in Visible to Ultraviolet Range," *PLOS ONE,* vol. 11, no. 4, p. e0153261, 2016, doi: 10.1371/journal.pone.0153261.

[219] O. E. Dagdeviren *et al.*, "Length Scale and Dimensionality of Defects in Epitaxial SnTe Topological Crystalline Insulator Films," *Advanced Materials Interfaces,* vol. 4, no. 2, p. 1601011, 2017, doi: https://doi.org/10.1002/admi.201601011.

[220] E. A. Patterson, M. Major, W. Donner, K. Durst, K. G. Webber, and J. Rödel, "Temperature-Dependent Deformation and Dislocation Density in SrTiO3 (001) Single Crystals," *Journal of the American Ceramic Society,* vol. 99, no. 10, pp. 3411-3420, 2016, doi: https://doi.org/10.1111/jace.14352.

[221] D. de Ligny and P. Richet, "High-temperature heat capacity and thermal expansion of SrTiO3 and SrZrO3 perovskites," *Physical Review B,* vol. 53, no. 6, pp. 3013-3022, 02/01/ 1996, doi: 10.1103/PhysRevB.53.3013.

[222] T. Tadano and S. Tsuneyuki, "Ab initio prediction of structural phase-transition temperature of SrTiO3 from finite-temperature phonon calculation," *Journal of the Ceramic Society of Japan,* vol. 127, no. 6, pp. 404-408, 2019, doi: 10.2109/jcersj2.18216.

[223] R. A. Cowley, "The Phase Transition of Strontium Titanate," *Philosophical Transactions: Mathematical, Physical and Engineering Sciences,* vol. 354, no. 1720, pp. 2799-2814, 1996. [Online]. Available: http://www.jstor.org/stable/54703.

[224] Z. Zhang *et al.*, "Manipulating the carrier concentration and phase transition via Nb content in SrTiO3," *Scientific Reports,* vol. 12, no. 1, 2022, doi: 10.1038/s41598-021-03199-7.

[225] X. Fang, "Phase Transitions in Strontium Titanate," 2013.

[226] R. He *et al.*, "Structural phase transitions in SrTiO3 from deep potential molecular dynamics," *Physical Review B,* vol. 105, no. 6, p. 064104, 02/15/ 2022, doi: 10.1103/PhysRevB.105.064104.

[227] M. Nonnenmacher, M. P. O'Boyle, and H. K. Wickramasinghe, "Kelvin probe force microscopy," *Applied Physics Letters,* vol. 58, no. 25, pp. 2921-2923, 1991, doi: 10.1063/1.105227.

[228] W. Melitz, J. Shen, A. C. Kummel, and S. Lee, "Kelvin probe force microscopy and its application," *Surface Science Reports,* vol. 66, no. 1, pp. 1-27, 2011/01/01/ 2011, doi: https://doi.org/10.1016/j.surfrep.2010.10.001.

[229] L. Collins, J. I. Kilpatrick, S. V. Kalinin, and B. J. Rodriguez, "Towards nanoscale electrical measurements in liquid by advanced KPFM techniques: a review," (in eng), *Rep Prog Phys,* vol. 81, no. 8, p. 086101, Aug 2018, doi: 10.1088/1361-6633/aab560.

[230] S. A. Burke, J. M. LeDue, Y. Miyahara, J. M. Topple, S. Fostner, and P. Grütter, "Determination of the local contact potential difference of PTCDA on NaCl: a comparison of techniques," (in eng), *Nanotechnology,* vol. 20, no. 26, p. 264012, Jul 1 2009, doi: 10.1088/0957-4484/20/26/264012.

[231] O. E. Dagdeviren, "Confronting interatomic force measurements," *Review of Scientific Instruments,* vol. 92, no. 6, p. 063703, 2021, doi: 10.1063/5.0052126.

[232] V. Solokha *et al.*, "Water Splitting on Ti-Oxide-Terminated SrTiO3(001)," *The Journal of Physical Chemistry C,* vol. 123, no. 28, pp. 17232-17238, 2019/07/18 2019, doi: 10.1021/acs.jpcc.9b01730.

[233] L.-Q. Wang, K. F. Ferris, and G. S. Herman, "Interactions of H2O with SrTiO3(100) surfaces," *Journal of Vacuum Science & Technology A,* vol. 20, no. 1, pp. 239-244, 2002, doi: 10.1116/1.1430246.

[234] R. Garcia-Diaz, M. T. Romero de la Cruz, R. Ochoa Valiente, J. Guerrero-Sanchez, and G. Hernández Cocoletzi, "DFT study for OH radical formation on SrTiO3(001) surface and the effect of Bi," *Applied Surface Science,* vol. 487, pp. 1394-1402, 2019/09/01/ 2019, doi: https://doi.org/10.1016/j.apsusc.2019.05.134.

[235] R. Shimizu *et al.*, "Effect of oxygen deficiency on SrTiO3(001) surface reconstructions," *Applied Physics Letters,* vol. 100, no. 26, p. 263106, 2012, doi: doi:http://dx.doi.org/10.1063/1.4730409.

[236] I. Sokolović, M. Schmid, U. Diebold, and M. Setvin, "Incipient ferroelectricity: A route towards bulk-terminated SrTiO3," *Physical Review Materials,* vol. 3, no. 3, p. 034407, 03/14/ 2019, doi: 10.1103/PhysRevMaterials.3.034407.

[237] I. Sokolović *et al.*, "Quest for a pristine unreconstructed SrTiO3 (001) surface: An atomically resolved study via noncontact atomic force microscopy," *Physical Review B,* vol. 103, no. 24, p. L241406, 06/10/ 2021, doi: 10.1103/PhysRevB.103.L241406.

[238] I. Sokolović *et al.*, "Resolving the adsorption of molecular O2 on the rutile TiO2 (110) surface by noncontact atomic force microscopy," *Proceedings of the National Academy of Sciences,* vol. 117, no. 26, pp. 14827-14837, 2020, doi: doi:10.1073/pnas.1922452117.

[239] M. Reticcioli, I. Sokolović, M. Schmid, U. Diebold, M. Setvin, and C. Franchini, "Interplay between Adsorbates and Polarons: CO on Rutile TiO2 (110)," *Physical Review Letters,* vol. 122, no. 1, p. 016805, 01/09/ 2019, doi: 10.1103/PhysRevLett.122.016805.

[240] J. Heinrichs, "Theory of van der Waals interactions between metal surfaces," *Physical Review B,* vol. 11, no. 10, pp. 3625-3636, 05/15/ 1975, doi: 10.1103/PhysRevB.11.3625.

[241] W. Buhl, "On the Theory of Van der Waals Interaction," *Z. Physik B,* vol. 23, pp. 221-232, 1976.

[242] G. L. Klimchitskaya, U. Mohideen, and V. M. Mostepanenko, "Casimir and van der Waals forces between two plates or a sphere (lens) above a plate made of real metals," *Physical Review A,* vol. 61, no. 6, p. 062107, 05/17/ 2000, doi: 10.1103/PhysRevA.61.062107.

[243] M. Z. Baykara *et al.*, "Atom-specific forces and defect identification on surface-oxidized Cu(100) with combined 3D-AFM and STM measurements," *Physical Review B,* vol. 87, no. 15, p. 155414, 04/12/ 2013. [Online]. Available: http://link.aps.org/doi/10.1103/PhysRevB.87.155414.

[244] J. E. Hoffman *et al.*, "Imaging Quasiparticle Interference in Bi2Sr2CaCu2O8+δ," *Science,* vol. 297, no. 5584, pp. 1148-1151, 2002-08-16 00:00:00 2002, doi: 10.1126/science.1072640.

[245] B. J. Morgan and G. W. Watson, "Intrinsic n-type Defect Formation in TiO2: A Comparison of Rutile and Anatase from GGA+U Calculations," *The Journal of Physical Chemistry C,* vol. 114, no. 5, pp. 2321-2328, 2010/02/11 2010, doi: 10.1021/jp9088047.

[246] C. Passiu, A. Rossi, M. Weinert, W. Tysoe, and N. D. Spencer, "Probing the outermost layer of thin gold films by XPS and density functional theory," *Applied Surface Science,* vol. 507, p. 145084, 2020/03/30/ 2020, doi: https://doi.org/10.1016/j.apsusc.2019.145084.

[247] D. I. Yakubovsky, A. V. Arsenin, Y. V. Stebunov, D. Y. Fedyanin, and V. S. Volkov, "Optical constants and structural properties of thin gold films," *Opt. Express,* vol. 25, no. 21, pp. 25574-25587, 2017/10/16 2017, doi: 10.1364/OE.25.025574.

[248] A. L. Linsebigler, G. Lu, and J. T. Yates, "Photocatalysis on TiO2 Surfaces: Principles, Mechanisms, and Selected Results," *Chemical Reviews,* vol. 95, pp. 735-758, 1995.

[249] F. Gunkel, D. V. Christensen, Y. Z. Chen, and N. Pryds, "Oxygen vacancies: The (in)visible friend of oxide electronics," *Applied Physics Letters,* vol. 116, no. 12, 2020, doi: 10.1063/1.5143309.

[250] G. Pacchioni, "Oxygen Vacancy: The Invisible Agent on Oxide Surfaces," *ChemPhysChem,* vol. 4, no. 10, pp. 1041-1047, 2003, doi: https://doi.org/10.1002/cphc.200300835.

[251] G. Rothenberger, J. Moser, M. Graetzel, N. Serpone, and D. K. Sharma, "Charge carrier trapping and recombination dynamics in small semiconductor particles," *Journal of the American Chemical Society,* vol. 107, no. 26, pp. 8054-8059, 1985/12/01 1985, doi: 10.1021/ja00312a043.

[252] M. Borgwardt *et al.*, "Photoinduced Charge Carrier Dynamics and Electron Injection Efficiencies in Au Nanoparticle-Sensitized TiO2 Determined with Picosecond Time-Resolved X-ray Photoelectron Spectroscopy," *The Journal of Physical Chemistry Letters,* vol. 11, no. 14, pp. 5476-5481, 2020/07/16 2020, doi: 10.1021/acs.jpclett.0c00825.

[253] T. Zubkov, D. Stahl, T. L. Thompson, D. Panayotov, O. Diwald, and J. T. Yates, "Ultraviolet Light-Induced Hydrophilicity Effect on TiO2(110)(1×1). Dominant Role of the Photooxidation of Adsorbed Hydrocarbons Causing Wetting by Water Droplets," *The Journal of Physical Chemistry B,* vol. 109, no. 32, pp. 15454-15462, 2005/08/01 2005, doi: 10.1021/jp058101c.

[254] J. Zhang *et al.*, "Reconstruction of the (001) surface of TiO2 nanosheets induced by the fluorine-surfactant removal process under UV-irradiation for dye-sensitized solar cells," *Physical Chemistry Chemical Physics,* 10.1039/C2CP24039D vol. 14, no. 14, pp. 4763-4769, 2012, doi: 10.1039/C2CP24039D.

[255] S.-G. Wang, X.-D. Wen, D.-B. Cao, Y.-W. Li, J. Wang, and H. Jiao, "Formation of oxygen vacancies on the TiO2(110) surfaces," *Surface Science,* vol. 577, no. 1, pp. 69-76, 2005/02/20/ 2005, doi: https://doi.org/10.1016/j.susc.2004.12.017.

[256] P. Deák, B. Aradi, and T. Frauenheim, "Quantitative theory of the oxygen vacancy and carrier self-trapping in bulk TiO2," *Physical Review B,* vol. 86, no. 19, p. 195206, 11/15/ 2012, doi: 10.1103/PhysRevB.86.195206.

[257] A. Ruiz Puigdollers, P. Schlexer, S. Tosoni, and G. Pacchioni, "Increasing Oxide Reducibility: The Role of Metal/Oxide Interfaces in the Formation of Oxygen Vacancies," *ACS Catalysis,* vol. 7, no. 10, pp. 6493-6513, 2017/10/06 2017, doi: 10.1021/acscatal.7b01913.

[258] A. Mascaro, Y. Miyahara, T. Enright, O. E. Dagdeviren, and P. Grütter, "Review of time-resolved non-contact electrostatic force microscopy techniques with applications to ionic transport measurements," *Beilstein Journal of Nanotechnology,* vol. 10, pp. 617-633, 2019.

[259] T. L. Thompson and J. T. Yates, "Surface Science Studies of the Photoactivation of TiO2New Photochemical Processes," *Chemical Reviews,* vol. 106, no. 10, pp. 4428-4453, 2006/10/01 2006, doi: 10.1021/cr050172k.
[260] L. D. Landau, E. M. Lifšic, and L. P. Pitaevskij, *Electrodynamics of continuous media*, 2. , rev. and enlarged, repr ed. Amsterdam: Elsevier Butterworth-Heinemann Amsterdam (in eng), 2009.
[261] C. Kittel, *Introduction to Solid State Physics*. Wiley: New York, 2004.
[262] A. Taskiran, A. Schirmeisen, H. Fuchs, H. Bracht, and B. Roling, "Time-domain electrostatic force spectroscopy on nanostructured lithium-ion conducting glass ceramics: analysis and interpretation of relaxation times," *Physical Chemistry Chemical Physics,* 10.1039/B900175C vol. 11, no. 26, pp. 5499-5505, 2009, doi: 10.1039/B900175C.
[263] A. Schirmeisen, A. Taskiran, H. Fuchs, H. Bracht, S. Murugavel, and B. Roling, "Fast Interfacial Ionic Conduction in Nanostructured Glass Ceramics," *Physical Review Letters,* vol. 98, no. 22, p. 225901, 05/29/ 2007, doi: 10.1103/PhysRevLett.98.225901.
[264] A. Schirmeisen, A. Taskiran, H. Bracht, and B. Roling, "Ion Jump Dynamics in Nanoscopic Subvolumes Analyzed by Electrostatic Force Spectroscopy," *Zeitschrift für Physikalische Chemie,* vol. 224, pp. 1831-1852, 11/01 2010, doi: 10.1524/zpch.2010.0016.
[265] M. K. Nowotny, L. R. Sheppard, T. Bak, and J. Nowotny, "Defect Chemistry of Titanium Dioxide. Application of Defect Engineering in Processing of TiO2-Based Photocatalysts," *The Journal of Physical Chemistry C,* vol. 112, no. 14, pp. 5275-5300, 2008/04/01 2008, doi: 10.1021/jp077275m.
[266] D. Freedman, R. Pisani, and R. Purves, *Statistics*, 3rd ed. New York: W.W. Norton New York (in eng), 1998.
[267] D. C. Montgomery, G. C. Runger, and N. F. Hubele, *Engineering Statistics, 5th Edition*. John Wiley & Sons, Incorporated, 2010.
[268] A. P. D. Goetzberger, J. Knobloch, and B. Voß, *Crystalline Silicon Solar Cells*. John Wiley & Sons, 1998.
[269] M. A. Green, "Solar Cells : Operating Principles, Technology and System Applications," 1981.
[270] J. Zhuang *et al.*, "Photocatalytic Degradation of RhB over TiO2 Bilayer Films: Effect of Defects and Their Location," *Langmuir,* vol. 26, no. 12, pp. 9686-9694, 2010/06/15 2010, doi: 10.1021/la100302m.
[271] M. Kong *et al.*, "Tuning the Relative Concentration Ratio of Bulk Defects to Surface Defects in TiO2 Nanocrystals Leads to High Photocatalytic Efficiency," *Journal of the American Chemical Society,* vol. 133, no. 41, pp. 16414-16417, 2011/10/19 2011, doi: 10.1021/ja207826q.
[272] L. Zhang, W. Chu, Q. Zheng, and J. Zhao, "Effects of oxygen vacancies on the photoexcited carrier lifetime in rutile TiO2," *Physical Chemistry Chemical Physics,* 10.1039/D1CP04248C vol. 24, no. 8, pp. 4743-4750, 2022, doi: 10.1039/D1CP04248C.
[273] C. Franchini, M. Reticcioli, M. Setvin, and U. Diebold, "Polarons in materials," *Nature Reviews Materials,* vol. 6, no. 7, pp. 560-586, 2021/07/01 2021, doi: 10.1038/s41578-021-00289-w.

[274] H. Kisch, "Semiconductor photocatalysis--mechanistic and synthetic aspects," *Angew Chem Int Ed Engl,* vol. 52, no. 3, pp. 812-47, Jan 14 2013, doi: 10.1002/anie.201201200.

[275] D. Zhu and Q. Zhou, "Action and mechanism of semiconductor photocatalysis on degradation of organic pollutants in water treatment: A review," *Environmental Nanotechnology, Monitoring & Management,* vol. 12, pp. 100255-100255, 2019.

[276] S. K. Dutta, S. K. Mehetor, and N. Pradhan, "Metal Semiconductor Heterostructures for Photocatalytic Conversion of Light Energy," *J Phys Chem Lett,* vol. 6, no. 6, pp. 936-44, Mar 19 2015, doi: 10.1021/acs.jpclett.5b00113.

[277] N. Serpone and A. V. Emeline, "Semiconductor Photocatalysis Past, Present, and Future Outlook," in *The journal of physical chemistry letters* vol. 3, ed: ACS Publications, 2012, pp. 673-677.

[278] I. Arora, H. Chawla, A. Chandra, S. Sagadevan, and S. Garg, "Advances in the strategies for enhancing the photocatalytic activity of TiO2: Conversion from UV-light active to visible-light active photocatalyst," *Inorganic Chemistry Communications,* vol. 143, pp. 109700-109700, 2022.

[279] Y. Liang *et al.*, "Structure and Reactivity of Methanol Adsorbed on Rutile TiO2(011) Surface," *The Journal of Physical Chemistry C,* vol. 122, no. 42, pp. 24202-24208, 2018/10// 2018, doi: 10.1021/acs.jpcc.8b08399.

[280] W. J. Ong, L. L. Tan, S. P. Chai, S. T. Yong, and A. R. Mohamed, "Facet-dependent photocatalytic properties of TiO2-based composites for energy conversion and environmental remediation," *ChemSusChem,* vol. 7, no. 3, pp. 690-719, 2014.

[281] Q. Guo *et al.*, "Stepwise photocatalytic dissociation of methanol and water on TiO2 (110)," *Journal of the American Chemical Society,* vol. 134, no. 32, pp. 13366-13373, 2012.

[282] S. Lettieri, M. Pavone, A. Fioravanti, L. Santamaria Amato, and P. Maddalena, "Charge carrier processes and optical properties in TiO2 and TiO2-based heterojunction photocatalysts: A review," *Materials,* vol. 14, no. 7, pp. 1645-1645, 2021.

[283] P. Maity, O. F. Mohammed, K. Katsiev, and H. Idriss, "Study of the bulk charge carrier dynamics in anatase and rutile TiO2 single crystals by femtosecond time-resolved spectroscopy," *The Journal of Physical Chemistry C,* vol. 122, no. 16, pp. 8925-8932, 2018.

[284] S. Koppen and W. Langel, "Adsorption of small organic molecules on anatase and rutile surfaces: a theoretical study," *Phys Chem Chem Phys,* vol. 10, no. 14, pp. 1907-15, Apr 14 2008, doi: 10.1039/b719098k.

[285] C. L. Pang, R. Lindsay, and G. Thornton, "Chemical reactions on rutile TiO 2 (110)," *Chemical Society Reviews,* vol. 37, no. 10, pp. 2328-2353, 2008.

[286] F. Dalena, A. Senatore, A. Marino, A. Gordano, M. Basile, and A. Basile, "Methanol Production and Applications: An Overview," in *Methanol*: Elsevier, 2018, pp. 3-28.

[287] A. Lais, M. A. Gondal, M. A. Dastageer, and F. F. Al-Adel, "Experimental parameters affecting the photocatalytic reduction performance of CO2 to methanol: A review," in *International Journal of Energy Research* vol. 42, ed: John Wiley and Sons Ltd, 2018, pp. 2031-2049.

[288] J. Zhao, R. Shi, Z. Li, C. Zhou, and T. Zhang, "How to make use of methanol in green catalytic hydrogen production?," *Nano Select,* vol. 1, no. 1, pp. 12-29, 2020/7// 2020, doi: 10.1002/nano.202000010.
[289] S. Dong *et al.*, "Origin of the adsorption-state-dependent photoactivity of methanol on TiO2 (110)," *ACS Catalysis,* vol. 11, no. 5, pp. 2620-2630, 2021.
[290] M. A. Henderson and I. Lyubinetsky, "Molecular-level insights into photocatalysis from scanning probe microscopy studies on TiO2 (110)," *Chemical Reviews,* vol. 113, no. 6, pp. 4428-4455, 2013.
[291] D. A. Panayotov, S. P. Burrows, and J. R. Morris, "Photooxidation Mechanism of Methanol on Rutile TiO2 Nanoparticles," *The Journal of Physical Chemistry C,* vol. 116, no. 11, pp. 6623-6635, 2012/3// 2012, doi: 10.1021/jp209215c.
[292] M. Setvin *et al.*, "Methanol on anatase TiO2 (101): Mechanistic insights into photocatalysis," *ACS catalysis,* vol. 7, no. 10, pp. 7081-7091, 2017.
[293] J. Li and N. Wu, "Semiconductor-based photocatalysts and photoelectrochemical cells for solar fuel generation: a review," *Catalysis Science & Technology,* vol. 5, no. 3, pp. 1360-1384, 2015.
[294] L. Chang, S.-T. Yong, S.-P. Chai, L. Putri, L.-L. Tan, and A. Mohamed, "A review of methanol photoreforming: elucidating the mechanisms, photocatalysts and recent advancement strategies," *Materials Today Chemistry,* vol. 27, p. 101334, 2023.
[295] G. N. Nomikos, P. Panagiotopoulou, D. I. Kondarides, and X. E. Verykios, "Kinetic and mechanistic study of the photocatalytic reforming of methanol over Pt/TiO2 catalyst," *Applied Catalysis B: Environmental,* vol. 146, pp. 249-257, 2014/03/01/ 2014, doi: https://doi.org/10.1016/j.apcatb.2013.03.018.
[296] A. Wahl and J. Augustynski, "Charge Carrier Transport in Nanostructured Anatase TiO2 Films Assisted by the Self-Doping of Nanoparticles," *The Journal of Physical Chemistry B,* vol. 102, no. 40, pp. 7820-7828, 1998/10/01 1998, doi: 10.1021/jp9814000.
[297] K. Fujihara, S. Izumi, T. Ohno, and M. Matsumura, "Time-resolved photoluminescence of particulate TiO2 photocatalysts suspended in aqueous solutions," *Journal of Photochemistry and Photobiology A: Chemistry,* vol. 132, no. 1, pp. 99-104, 2000/03/20/ 2000, doi: https://doi.org/10.1016/S1010-6030(00)00204-5.
[298] F. Xiao *et al.*, "Engineering oxygen vacancy on rutile TiO2 for efficient electron-hole separation and high solar-driven photocatalytic hydrogen evolution," *Science China Materials,* vol. 61, no. 6, pp. 822-830, 2018/06/01 2018, doi: 10.1007/s40843-018-9222-4.
[299] A. V. Akimov, A. J. Neukirch, and O. V. Prezhdo, "Theoretical insights into photoinduced charge transfer and catalysis at oxide interfaces," *Chemical reviews,* vol. 113, no. 6, pp. 4496-4565, 2013.
[300] F. Gunkel, D. V. Christensen, and N. Pryds, "Charge-transfer engineering strategies for tailored ionic conductivity at oxide interfaces," *Journal of Materials Chemistry C,* vol. 8, no. 33, pp. 11354-11359, 2020.
[301] K. V. Vokhmintcev, P. S. Samokhvalov, and I. Nabiev, "Charge transfer and separation in photoexcited quantum dot-based systems," *Nano Today,* vol. 11, no. 2, pp. 189-211, 2016.

[302] Y. Nosaka and A. Y. Nosaka, "Reconsideration of Intrinsic Band Alignments within Anatase and Rutile TiO2," *The Journal of Physical Chemistry Letters,* vol. 7, no. 3, pp. 431-434, 2016/02/04 2016, doi: 10.1021/acs.jpclett.5b02804.

[303] A. Furube, T. Asahi, H. Masuhara, H. Yamashita, and M. Anpo, "Charge carrier dynamics of standard TiO2 catalysts revealed by femtosecond diffuse reflectance spectroscopy," *The Journal of Physical Chemistry B,* vol. 103, no. 16, pp. 3120-3127, 1999.

[304] P. Zawadzki, "Semiconductor Photocatalysis: Electronic Hole Trapping in TiO2," 2011.

[305] M. J. Tillotson, P. M. Brett, R. A. Bennett, and R. Grau-Crespo, "Adsorption of organic molecules at the TiO2 (110) surface: the effect of van der Waals interactions," *Surface Science,* vol. 632, pp. 142-153, 2015.

[306] K. S. Kim and M. A. Barteau, "Reactions of methanol on TiO2 (001) single crystal surfaces," *Surface science,* vol. 223, no. 1-2, pp. 13-32, 1989.

[307] M. Shen and M. A. Henderson, "Identification of the active species in photochemical hole scavenging reactions of methanol on TiO2," *The Journal of Physical Chemistry Letters,* vol. 2, no. 21, pp. 2707-2710, 2011.

[308] L.-Q. Wang, K. F. Ferris, J. P. Winokur, A. N. Shultz, D. R. Baer, and M. H. Engelhard, "Interactions of methanol with stoichiometric and defective TiO 2 (110) and (100) surfaces," *Journal of Vacuum Science & Technology A: Vacuum, Surfaces, and Films,* vol. 16, no. 5, pp. 3034-3040, 1998.

[309] D. A. Panayotov, S. Burrows, M. Mihaylov, K. Hadjiivanov, B. M. Tissue, and J. R. Morris, "Effect of methanol on the Lewis acidity of rutile TiO2 nanoparticles probed through vibrational spectroscopy of coadsorbed CO," *Langmuir,* vol. 26, no. 11, pp. 8106-8112, 2010.

[310] E. A. Taylor and G. L. Griffin, "Product selectivity during methanol decomposition on titania powders," *The Journal of Physical Chemistry,* vol. 92, no. 2, pp. 477-481, 1988.

[311] A. Yamakata, T.-a. Ishibashi, and H. Onishi, "Electron-and hole-capture reactions on Pt/TiO2 photocatalyst exposed to methanol vapor studied with time-resolved infrared absorption spectroscopy," *The Journal of Physical Chemistry B,* vol. 106, no. 35, pp. 9122-9125, 2002.

[312] C. Fu *et al.*, "Site Sensitivity of Interfacial Charge Transfer and Photocatalytic Efficiency in Photocatalysis: Methanol Oxidation on Anatase TiO2 Nanocrystals," *Angewandte Chemie International Edition,* vol. 60, no. 11, pp. 6160-6169, 2021/03/08 2021, doi: https://doi.org/10.1002/anie.202014037.

[313] D. A. Panayotov and J. R. Morris, "Surface chemistry of Au/TiO2: Thermally and photolytically activated reactions," *Surface Science Reports,* vol. 71, no. 1, pp. 77-271, 2016/03/01/ 2016, doi: https://doi.org/10.1016/j.surfrep.2016.01.002.

[314] D. A. Panayotov *et al.*, "Ultraviolet and Visible Photochemistry of Methanol at 3D Mesoporous Networks: TiO2 and Au–TiO2," *The Journal of Physical Chemistry C,* vol. 117, no. 29, pp. 15035-15049, 2013/07/25 2013, doi: 10.1021/jp312583w.

[315] R. Sellappan, M. G. Nielsen, F. González-Posada, P. C. K. Vesborg, I. Chorkendorff, and D. Chakarov, "Effects of plasmon excitation on photocatalytic activity of Ag/TiO2 and Au/TiO2 nanocomposites," *Journal of Catalysis,* vol. 307, pp. 214-221, 2013/11/01/ 2013, doi: https://doi.org/10.1016/j.jcat.2013.07.024.

[316] E. Farfan-Arribas and R. J. Madix, "Different binding sites for methanol dehydrogenation and deoxygenation on stoichiometric and defective TiO2 (1 1 0) surfaces," *Surface science,* vol. 544, no. 2-3, pp. 241-260, 2003.
[317] M. A. Henderson, S. Otero-Tapia, and M. E. Castro, "The chemistry of methanol on the TiO 2 (110) surface: the influence of vacancies and coadsorbed species," *Faraday Discussions,* vol. 114, pp. 313-329, 1999.
[318] Q. Yuan *et al.*, "Photocatalytic cross-coupling of methanol and formaldehyde on a rutile TiO2 (110) surface," *Journal of the American Chemical Society,* vol. 135, no. 13, pp. 5212-5219, 2013.
[319] X. Lang, B. Wen, C. Zhou, Z. Ren, and L.-M. Liu, "First-principles study of methanol oxidation into methyl formate on rutile TiO2 (110)," *The Journal of Physical Chemistry C,* vol. 118, no. 34, pp. 19859-19868, 2014.
[320] A. Y. Ahmed, T. A. Kandiel, T. Oekermann, and D. Bahnemann, "Photocatalytic Activities of Different Well-defined Single Crystal TiO2 Surfaces: Anatase versus Rutile," *The Journal of Physical Chemistry Letters,* vol. 2, no. 19, pp. 2461-2465, 2011/10/06 2011, doi: 10.1021/jz201156b.
[321] T. A. Kandiel, R. Dillert, and D. W. Bahnemann, "Enhanced photocatalytic production of molecular hydrogen on TiO2 modified with Pt–polypyrrole nanocomposites," *Photochemical & Photobiological Sciences,* vol. 8, no. 5, pp. 683-690, 2009/05/01 2009, doi: 10.1039/b817456c.
[322] M. Cardona and G. Harbeke, "Optical Properties and Band Structure of Wurtzite-Type Crystals and Rutile," *Physical Review,* vol. 137, no. 5A, pp. A1467-A1476, 03/01/ 1965, doi: 10.1103/PhysRev.137.A1467.
[323] G. Ghosh, *Handbook of optical constants of solids*. Orlando : Academic Press, 1985., 1985.
[324] I. Tanabe and Y. Ozaki, "Far- and deep-ultraviolet spectroscopic investigations for titanium dioxide: electronic absorption, Rayleigh scattering, and Raman spectroscopy," *Journal of Materials Chemistry C,* 10.1039/C6TC02368A vol. 4, no. 33, pp. 7706-7717, 2016, doi: 10.1039/C6TC02368A.
[325] T. Siefke *et al.*, "Materials Pushing the Application Limits of Wire Grid Polarizers further into the Deep Ultraviolet Spectral Range," *Advanced Optical Materials,* vol. 4, no. 11, pp. 1780-1786, 2016, doi: https://doi.org/10.1002/adom.201600250.
[326] J. Zheng *et al.*, "Crystalline TiO2 protective layer with graded oxygen defects for efficient and stable silicon-based photocathode," *Nature Communications,* vol. 9, no. 1, p. 3572, 2018/09/03 2018, doi: 10.1038/s41467-018-05580-z.
[327] R. Engel-Herbert, B. Jalan, J. Cagnon, and S. Stemmer, "Microstructure of epitaxial rutile TiO2 films grown by molecular beam epitaxy on r-plane Al2O3," *Journal of Crystal Growth,* vol. 312, no. 1, pp. 149-153, 2009/12/15/ 2009, doi: https://doi.org/10.1016/j.jcrysgro.2009.10.005.
[328] X. Weng, P. Fisher, M. Skowronski, P. A. Salvador, and O. Maksimov, "Structural characterization of TiO2 films grown on LaAlO3 and SrTiO3 substrates using reactive molecular beam epitaxy," *Journal of Crystal Growth,* vol. 310, no. 3, pp. 545-550, 2008/02/01/ 2008, doi: https://doi.org/10.1016/j.jcrysgro.2007.10.084.
[329] F. Maleki, G. Di Liberto, and G. Pacchioni, "pH- and Facet-Dependent Surface Chemistry of TiO2 in Aqueous Environment from First Principles," *ACS Applied*

Materials & Interfaces, vol. 15, no. 8, pp. 11216-11224, 2023/03/01 2023, doi: 10.1021/acsami.2c19273.

[330] B. J. Morgan and G. W. Watson, "A DFT+U description of oxygen vacancies at the TiO2 rutile (110) surface," *Surface Science,* vol. 601, no. 21, pp. 5034-5041, 2007/11/01/ 2007, doi: https://doi.org/10.1016/j.susc.2007.08.025.

[331] B. Wei, F. Tielens, and M. Calatayud, "Understanding the Role of Rutile TiO2 Surface Orientation on Molecular Hydrogen Activation," *Nanomaterials,* vol. 9, no. 9, p. 1199, 2019. [Online]. Available: https://www.mdpi.com/2079-4991/9/9/1199.

[332] H. Yaghoubi *et al.*, "Toward a Visible Light-Driven Photocatalyst: The Effect of Midgap-States-Induced Energy Gap of Undoped TiO2 Nanoparticles," *ACS Catalysis,* vol. 5, no. 1, pp. 327-335, 2015/01/02 2015, doi: 10.1021/cs501539q.

[333] D. Meroni *et al.*, "Oxygen vacancies in the Spotlight: On the engineering of intrinsic defects in highly defective TiO2 photocatalysts," *Journal of Photochemistry and Photobiology A: Chemistry,* vol. 444, p. 114916, 2023/10/01/ 2023, doi: https://doi.org/10.1016/j.jphotochem.2023.114916.

[334] V. Etacheri, C. Di Valentin, J. Schneider, D. Bahnemann, and S. C. Pillai, "Visible-light activation of TiO2 photocatalysts: Advances in theory and experiments," *Journal of Photochemistry and Photobiology C: Photochemistry Reviews,* vol. 25, pp. 1-29, 2015/12/01/ 2015, doi: https://doi.org/10.1016/j.jphotochemrev.2015.08.003.

[335] Z. Pei *et al.*, "Facile synthesis of defect-mediated TiO2−x with enhanced visible light photocatalytic activity," *Journal of Materials Chemistry A,* 10.1039/C3TA12062G vol. 1, no. 35, pp. 10099-10102, 2013, doi: 10.1039/C3TA12062G.

[336] X. Kang, X.-Z. Song, Y. Han, J. Cao, and Z. Tan, "Defect-engineered TiO2 Hollow Spiny Nanocubes for Phenol Degradation under Visible Light Irradiation," *Scientific Reports,* vol. 8, no. 1, p. 5904, 2018/04/12 2018, doi: 10.1038/s41598-018-24353-8.

[337] J. Zhang, C. Y. Toe, P. Kumar, J. Scott, and R. Amal, "Engineering defects in TiO2 for the simultaneous production of hydrogen and organic products," *Applied Catalysis B: Environment and Energy,* vol. 333, p. 122765, 2023/09/15/ 2023, doi: https://doi.org/10.1016/j.apcatb.2023.122765.

[338] M. K. Nowotny, T. Bak, and J. Nowotny, "Electrical Properties and Defect Chemistry of TiO2 Single Crystal. I. Electrical Conductivity," *The Journal of Physical Chemistry B,* vol. 110, no. 33, pp. 16270-16282, 2006/08/01 2006, doi: 10.1021/jp0606210.

[339] H. Huang *et al.*, "TiO2 surface oxygen vacancy passivation towards mitigated interfacial lattice distortion and efficient perovskite solar cell," *Applied Surface Science,* vol. 544, p. 148583, 2021/04/01/ 2021, doi: https://doi.org/10.1016/j.apsusc.2020.148583.

[340] A. Klasen *et al.*, "Removal of Surface Oxygen Vacancies Increases Conductance Through TiO(2) Thin Films for Perovskite Solar Cells," (in eng), *J Phys Chem C Nanomater Interfaces,* vol. 123, no. 22, pp. 13458-13466, Jun 6 2019, doi: 10.1021/acs.jpcc.9b02371.

[341] A. C. Papageorgiou *et al.*, "Electron traps and their effect on the surface chemistry of TiO2 (110)," *Proceedings of the National Academy of Sciences,* vol. 107, no. 6, pp. 2391-2396, 2010, doi: doi:10.1073/pnas.0911349107.

[342] G. Horowitz and M. E. Hajlaoui, "Grain size dependent mobility in polycrystalline organic field-effect transistors," *Synthetic Metals,* vol. 122, no. 1, pp. 185-189, 2001/05/01/ 2001, doi: https://doi.org/10.1016/S0379-6779(00)01351-5.

[343] S. Emin, E. Pavlica, H. Okuyucu, M. Valant, and G. Bratina, "Charge carrier transport in polycrystalline CH3NH3PbI3 perovskite thin films in a lateral direction characterized by time-of-flight photoconductivity," *Materials Chemistry and Physics,* vol. 220, pp. 182-189, 2018/12/01/ 2018, doi: https://doi.org/10.1016/j.matchemphys.2018.08.012.

[344] R. T. Weitz *et al.*, "The Importance of Grain Boundaries for the Time-Dependent Mobility Degradation in Organic Thin-Film Transistors," *Chemistry of Materials,* vol. 21, no. 20, pp. 4949-4954, 2009/10/27 2009, doi: 10.1021/cm902145x.

[345] I. Jelovica Badovinac *et al.*, "Grain size effect on photocatalytic activity of TiO2 thin films grown by atomic layer deposition," *Thin Solid Films,* vol. 709, p. 138215, 2020/09/01/ 2020, doi: https://doi.org/10.1016/j.tsf.2020.138215.

[346] M. C. K. Sellers and E. G. Seebauer, "Manipulation of polycrystalline TiO2 carrier concentration via electrically active native defects," *Journal of Vacuum Science & Technology A,* vol. 29, no. 6, 2011, doi: 10.1116/1.3635373.

[347] J. Quirk, M. Rothmann, W. Li, D. Abou-Ras, and K. P. McKenna, "Grain boundaries in polycrystalline materials for energy applications: First principles modeling and electron microscopy," *Applied Physics Reviews,* vol. 11, no. 1, 2024, doi: 10.1063/5.0175150.

[348] T. Bak, D. Chu, A. R. Francis, W. Li, and J. Nowotny, "Concentration of electrons at grain boundaries in TiO2 (rutile): Impact on charge transport and reactivity," *Catalysis Today,* vol. 224, pp. 200-208, 2014/04/01/ 2014, doi: https://doi.org/10.1016/j.cattod.2013.11.039.

[349] F. Y. Bruno *et al.*, "Band Structure and Spin–Orbital Texture of the (111)-KTaO3 2D Electron Gas," *Advanced Electronic Materials,* vol. 5, no. 5, p. 1800860, 2019, doi: https://doi.org/10.1002/aelm.201800860.

[350] W. Meevasana *et al.*, "Creation and control of a two-dimensional electron liquid at the bare SrTiO3 surface," *Nature Materials,* vol. 10, no. 2, pp. 114-118, 2011/02/01 2011, doi: 10.1038/nmat2943.

[351] S. M. Walker *et al.*, "Carrier-Density Control of the SrTiO3 (001) Surface 2D Electron Gas studied by ARPES," *Advanced Materials,* vol. 27, no. 26, pp. 3894-3899, 2015, doi: https://doi.org/10.1002/adma.201501556.

[352] A. S. Herrmann and M. J, "Comparison of the Photoelectronic and Photocatalytic Activities of Various Anatase and Rutile Forms of Titania in Pure Liquid Organic Phases and in Aqueous Solutions," (in en), *The Journal of Physical Chemistry,* research-article August 8, 1996 1996, doi: 10.1021/jp9533584.

[353] Y. Liao, "Practical electron microscopy and database," *An Online Book,* 2006.

[354] M. T. Postek, "An approach to the reduction of hydrocarbon contamination in the scanning electron microscope," *Scanning,* vol. 18, no. 4, pp. 269-274, 1996, doi: https://doi.org/10.1002/sca.1996.4950180402.

[355] G. Vineyard, "Frequency factors and isotope effects in solid state rate processes," *Journal of Physics and Chemistry of Solids,* vol. 3, pp. 121-127, January 01, 1957 1957, doi: 10.1016/0022-3697(57)90059-8.

[356] G. Antczak and G. Ehrlich, "Surface Diffusion: Metals, Metal Atoms, and Clusters," 2010.
[357] J. Maier, "Physical Chemistry of Ionic Materials: Ions and Electrons in Solid," 01/28 2005, doi: 10.1002/0470020229.ch1.
[358] U. Kürpick, A. Kara, and T. S. Rahman, "Role of Lattice Vibrations in Adatom Diffusion," *Physical Review Letters,* vol. 78, no. 6, pp. 1086-1089, 02/10/ 1997, doi: 10.1103/PhysRevLett.78.1086.
[359] T. Degen, M. Sadki, E. Bron, U. König, and G. Nénert, "The highscore suite," *Powder diffraction,* vol. 29, no. S2, pp. S13-S18, 2014.
[360] T. Hahn, U. Shmueli, and J. W. Arthur, *International tables for crystallography*. Reidel Dordrecht, 1983.
[361] T. Al-Dhahir, "Quantitative phase analysis for titanium dioxide from X-ray powder diffraction data using the Rietveld method," *Diyala journal for pure sciences,* vol. 2, no. 9, pp. 108-119, 2013.
[362] M. N. Khan, K. Shahzad, and J. Bashir, "Thermal atomic displacements in nanocrystalline titanium dioxide studied by synchrotron x-ray diffraction," *Journal of Physics D: Applied Physics,* vol. 41, no. 8, p. 085409, 2008.
[363] O. Le Bacq, E. Salinas, A. Pisch, C. Bernard, and A. Pasturel, "First-principles structural stability in the strontium–titanium–oxygen system," *Philosophical Magazine,* vol. 86, no. 15, pp. 2283-2292, 2006.
[364] R. B. Cook, "Handbook of mineralogy," *Rocks and Minerals,* vol. 76, no. 4, p. 278, 2001.
[365] B. D. Cullity and R. Smoluchowski, "Elements of X-ray Diffraction," *Physics Today,* vol. 10, no. 3, pp. 50-50, 1957.